UNIVERSITÀ DEGLI STUDI DI PADOVA

DEPARTMENT OF INFORMATION ENGINEERING

Ph.D. Course on Information Engineering

Curriculum: Information Science and Technologies

XXX Series

RELIABILITY OF III-V LASER DIODES AND LEDS FOR LIGHTING AND TELECOMMUNICATION APPLICATIONS

Ph.D Student

Matteo Buffolo

Supervisor

Dr. Matteo Meneghini

Coordinator

Ch.mo Prof. Andrea Neviani

ACADEMIC YEAR 2016/2017

Contents

Acknowledgments

The work presented in chapter 8 of this thesis is partially supported by the New Energy and Industrial Technology Development Organization (NEDO), Japan, under the Strategic Innovation Program for Energy Conservation Technologies.

Abstract

The research in optoelectronics has recently shown impressive advancements, thanks to the development of disruptive technologies, such as Gallium Nitride LEDs and lasers - that are enabling novel lighting devices - and Silicon photonics - that will change the paradigm in broadband data transmission. Industrial laboratories and academic researchers are working towards the improvement of device performance and reliability. This goal is complicated by the complex nature of optoelectronic devices and systems: a deep knowledge on material properties, device characteristics and system optimization is needed to identify the physical mechanisms that limit the lifetime of the devices, and to address possible solutions. The aim of this thesis is to report on a detailed study of the physical factors that limit the performance and reliability of innovative optoelectronic technologies based on nitrides and arsenides. The investigation was conducted by means of purposely planned Accelerated Life Test (ALT) experiments and short-term stress tests on selected state-of-the-art devices, which let us identify the main physical processes responsible for the long-term degradation of the devices, and pinpointed the weaknesses of modern LEDs when temporary operated outside their Safe Operating Area (SOA) as a consequence of Electrical Over-Stress (EOS) events.

With regard to Gallium Nitride (GaN)-based white and visible monochromatic LEDs, we found that under constant near-breakdown reverse bias the devices exhibit a time-dependent degradation phenomenon, which promotes the increase of the leakage current of the device, eventually leading to its catastrophic failure. The peculiar failure statistics, as well as the electro-luminescence and leakage-current data acquired during stress, could be interpreted by considering that highly-depleted GaN under reverse bias may behave like a partially-leaking dielectric that degrades over time due to a defect percolation process, similar to the dielectric degradation-driven breakdown process affecting Silicon MOS devices.

On the other hand, high forward-current short-term step-stress on high-power LEDs revealed that sustained operation at driving currents above the maximum rating of the devices can rapidly induce failure in correspondence of a major current injection point, dependent on the specific chip structure, as a consequence of the localized power dissipation and temperature reached due to extreme current crowding effects and to the degradation of the conductivity of extended device regions.

A clear dependence of the failure mode on the chip structure and device layout could also be found during the investigation on the effects of single short EOS events of increasing amplitude on high-power white LEDs. The experimental data helped identifying the best LED design to be employed in an electrically critical environment, also showing that EOS-related reliability issues tend to arise more from extrinsic elements of the LED system rather than from the semiconductor chip.

Unlike High-Brightness (HB) state-of-the-art LEDs, whose main reliability concern is represented by EOS events, cost-effective mid-power LEDs for lighting applications were found to suffer from gradual degradation processes impacting in the long term on both the electrical an optical characteristics of the device. Moreover, the results of the ALTs highlighted the role of the plastic package in the degradation of the optical properties of the emitted light.

The long-term reliability of mid-power LEDs was further investigated at system level by performing a lifetime analysis of commercial LED bulbs employing these devices as primary light sources. The increased complexity of the system under stress negatively impacted on the stability over time of the luminous performances of the luminaries, which was severely affected by the degradation of extrinsic elements like the diffusing dome or the current driver.

In Part II of this work, our system-level analysis continued with an extensive investigation on the reliability of blue-emitting phosphors for near-UV laser excitation, as part of a research project performed in collaboration with the New Energy and Industrial Technology Development Organization (NEDO), Japan. By means of a series of pure thermal stress experiments and stress under high levels of optical excitation, we have been able to identify the physical process responsible for the degradation of the phosphors under extreme and more conservative operating conditions. In particular, while the phosphors demonstrated good stability during pure thermal treatment in air up to 300 °C, for temperatures equal to or greater than 450 °C the material exhibited a time-dependent drop in the photo-luminescence, which was attributed to the thermally-induced autoionization of the Eu^{2+} optically active centers. By means of different material characterization techniques, evidence of this degradation process was also found on samples stressed under moderate $3\,W/mm^2$ - $405\,nm$ optical excitation. This indicated that the optically (and thermally) induced ionization of the optically-active species is the most critical degradation process for this family of phosphorescent material.

The operating limits of an improved second generation luminescent material were also investigated by means of short term stress under $405\,nm$ optical excitation. The experimental data showed that, for a given deposition condition, a threshold excitation intensity for continuous pumping exists. Above this threshold, decay of the steady-state photo-luminescence performances and degradation of the material were found to take place, which suggested that the material was being operated in an unuseful excitation regime, mainly limited by the thermal management capabilities of the carrier substrate employed for our experimental purposes rather than from intrinsic properties of the phosphor.

Part III of this thesis is devoted to the analysis of the degradation processes of heterogeneous III-V/Silicon infrared (IR) laser diodes designed for integrated telecommunications and interconnects. By submitting the devices to a series of constant current stress tests, a gradual degradation of the main device parameters was observed. In particular, in every stress scenario the devices under test showed (*i*) an increase in the threshold current, (*ii*) a decrease in the turn-on voltage, and (*iii*) an increase in the apparent carrier concentration within the space charge region. The variation of the electrical parameters was found to be significantly correlated to the optical degradation for long stress times; the results support the hypothesis that degradation originates from an increase in the non-radiative recombination rate, possibly due to the diffusion of defects towards the active region of the devices.

In order to further investigate the physical origin of the diffusing defects, capacitance Deep-Level Transient Spectroscopy (C-DLTS) analysis was performed. The results indicate the presence of several deep levels, with a main trap located around $0.43\,eV$ above the valence band energy. This trap was found to be compatible with an interface defect characteristic of the quaternary material employed to grow the active region of the device.

The above-mentioned experimental results represent the most relevant and original outcomes of the three-years research activity of the Ph.D student. The following section lists the scientific contributions co-authored by the candidate based on those results.

Sommario

L'ultimo decennio di ricerca nell'ambito dei dispositivi optoelettronici ha contribuito allo sviluppo e alla successiva introduzione sul mercato di rivoluzionarie tecnologie, sia in ambito illuminotecnico, grazie agli innovativi sistemi di illuminazione basati su LED e laser in Nitruro di Gallio, che in ambito telecomunicazioni, dove la Silicon photonics promette di stravolgere l'odierno approccio alla trasmissione a larga banda. Innumerevoli laboratori di ricerca universitari e privati concorrono nell'incrementare le performance e l'affidabilità dei dispositivi. Tale obbiettivo, tuttavia, è ostacolato dalla complessa natura dei dispositivi optoelettronici e, ancor più, dei sistemi su di essi basati. Una conoscenza approfondita dei materiali, delle proprietà dei dispositivi e dell'ottimizzazione a livello di sistema risultano essere indispensabili per l'identificazione dei meccanismi fisici che limitano il tempo di vita utile dei dispositivi, e per lo sviluppo di possibili soluzioni. Scopo di questa tesi è descrive i risultati di un'estesa analisi finalizzata ad identificare i processi fisici che limitano l'affidabilità e le prestazioni degli innovativi sistemi optoelettronici basati su semiconduttori III-V. Per tale scopo sono stati realizzati specifici esperimenti di degrado accelerato e stress a breve termine su dispositivi allo stato dell'arte, che hanno permesso di individuare i processi fisici responsabili del degrado, graduale o catastrofico, cui possono essere soggetti i moderni dispositivi optoelettronici durante la propria vita operativa.

Nello specifico, le analisi condotte su LED ad emissione nel visibile basati su Nitruro di Gallio (GaN) hanno innanzitutto rivelato che la prolungata polarizzazione del dispositivo con tensioni inverse vicine al valore critico di breakdown è accompagnata dall'instaurarsi di un processo di degrado tempo-dipendente che induce l'aumento della corrente di leakage del LED, portandolo eventualmente alla failure catastrofica. La peculiare distribuzione statistica del tempo di failure, unita all'andamento temporale di corrente e segnale di elettro-luminescenza durante lo stress in inversa, sono stati interpretati supponendo che il Nitruro di Gallio, portato in svuotamento spinto dalle elevate tensioni inverse, possa comportarsi come un dielettrico con perdite che degrada nel tempo a causa della percolazione di difetti, con un processo del tutto simile al

breakdown tempo-dipendente del dielettrico presente nei MOS in Silicio.

Lo studio sugli effetti a breve termine di elevate correnti di polarizzazione su LED in GaN ad alta potenza ha invece evidenziato una localizzazione della failure dei dispositivi in prossimità dei principali punti di iniezione di corrente, specificatamente associabili alla particolare struttura del dispositivo in analisi. Tale tipologia di stress si è inoltre rivelata altamente dannosa anche per la struttura epitassiale del dispositivo, che, a causa delle elevate temperature e densità di corrente in gioco, ha mostrato incrementi di resistività localizzati.

Una più marcata dipendenza delle modalità e delle condizioni di failure dalla struttura e dal layout superficiale è emersa dall'analisi degli effetti di eventi di overstress di breve durata su LED bianchi ad alta potenza. I risultati sperimentali hanno portato all'identificazione della tipologia di LED più adeguata da adottare in ambienti soggetti a disturbi elettrici, mostrando inoltre come le problematiche relative ad eventi di overstress elettrico siano determinate più dalle debolezze di elementi estrinseci del LED che dal chip di semiconduttore.

L'attività di ricerca ha poi evidenziato come per LED bianchi a media potenza in condizioni operative limite i processi di degrado graduale delle caratteristiche ottiche ed elettriche del dispositivo, ed in particolar modo relativi al package plastico, possano risultare deleteri per l'affidabilità a lungo termine della sorgente allo stato solido.

L'analisi affidabilistica su tale tipologia di LED è stata poi estesa a livello di sistema, andando ad investigare i meccanismi di degrado che interessano le comuni lampadine a bulbo basate per l'appunto su LED bianchi a media potenza. La maggiore complessità del sistema illuminante sotto stress ha impattato negativamente sulle performance a lungo termine del bulbo, la cui affidabilità è risultata essere per lo più limitata da elementi estrinseci al LED, quali la cupola diffusiva oppure il driver di corrente.

Nella seconda parte di questa tesi sono state analizzate le proprietà affidabilistiche di uno di questi elementi estrinseci: i fosfori. In collaborazione con l'organizzazione per lo sviluppo delle nuove energie e delle tecnologie industriali del Giappone (NEDO), è stata condotta un'estesa ricerca sull'affidabilità di fosfori ad emissione nel blu per eccitazione nel vicino UV tramite sorgenti a stato solido, in particolare laser. Attraverso una serie di stress termici e/o sotto fascio ottico ad elevate intensità, è stato possibile identificare il principale meccanismo fisico responsabile del degrado delle performance di fotoluminescenza del materiale fosforescente in esame. Nello specifico, correlando quest'ultimo fenomeno con le variazioni delle proprietà chimico-fisiche del materiale, è stato possibile identificare nell'autoionizzazione otticamente e/o termicamente indotta dei centri otticamente attivi di Eu^{2+} la principale causa di degrado del fosforo.

La stress ottico a breve termine su pigmento luminescente di seconda generazione ha poi permesso di identificare un valore limite di intensità per il pompaggio ottico continuo. Oltre tale soglia, le performance del materiale luminescente calano per effetto congiunto della perdita di efficienza dovuta alle alte temperature di esercizio e al degrado non reversibile del materiale stesso.

Nella terza parte di questa tesi vengono analizzati i meccanismi di degrado di diodi laser IR ibridi basati su semiconduttori III-V e Silicio progettati per sistemi di telecomunicazione e di interconnessione integrati. Esperimenti di degrado accelerato condotti a corrente costante hanno permesso l'identificazione di diversi processi di degrado graduale, tra i quali: (*i*) l'aumento della corrente di soglia, (*ii*) la decrescita della tensione di turn-on del diodo (*iii*) e l'incremento della concentrazione di carica apparente in prossimità della regione attiva. Sulla base della correlazione tra tali processi, è stata formulata l'ipotesi secondo la quale l'origine del degrado ottico del dispositivo risieda nell'aumento del rate di ricombinazione non radiativa, possibilmente dovuto alla diffusione di difetti verso la regione attiva.

Al fine di investigare l'origine della specie diffondente sono state impiegate tecniche di analisi spettroscopica che hanno permesso l'identificazione di diversi livelli trappola all'interno del dispositivo, il principale dei quali, localizzato $0.43\,eV$ al di sopra della banda di valenza, è risultato essere compatibile con un difetto d'interfaccia caratteristico del materiale semiconduttore utilizzato per la crescita della regione attiva dei dispositivi in esame.

Quanto sopra esposto è rappresentativo dei risultati sperimentali originali più importati conseguiti dallo studente di dottorato durante la propria attività di ricerca. Nella sezione seguente viene riportata una lista dei contributi scientifici basati su tali risultati di cui il canditato è co-autore.

Publications

International journal papers

1. M. Buffolo, C. De Santi, M. Meneghini, D. Rigon, G. Meneghesso, E. Zanoni "*Long-Term Degradation Mechanisms of Mid-Power LEDs for Lighting Applications*", Microelectronics Reliability 55 (9-10), pp. 1754-1758, (2015), DOI: 10.1016/j.microrel.2015.06.098

2. M. Buffolo, M. Meneghini, A. Munaretto, C. De Santi, G. Meneghesso and E. Zanoni, "*Failure of High Power LEDs Submitted to EOS: Dependence on Device Layout and Pulse Properties*" in IEEE Transactions on Device and Materials Reliability, vol. 17, no. 1, pp. 191-196, March 2017. DOI: 10.1109/TDMR.2016.2642167

3. M. Buffolo, M. Meneghini, C. De Santi, H. Felber, N. Renso, G. Meneghesso, E. Zanoni, "*Experimental observation of TDDB-like behavior in reverse-biased green InGaN LEDs*", Microelectronics Reliability, Volume 64, 2016, Pages 610-613, ISSN 0026-2714, DOI: 10.1016/j.microrel.2016.07.103

4. M. Buffolo, M. Meneghini, C. De Santi, M. Davenport, J. Bowers, G. Meneghesso, E. Zanoni, "*Degradation Mechanisms of Heterogeneous III-V/Silicon 1.55 μm DBR Laser Diodes*" in IEEE Journal of Quantum Electronics, vol. 53, no. 4, pp. 1-8, Aug. 2017. DOI: 10.1109/JQE.2017.2714582

5. C. De Santi, M. Meneghini, M. Buffolo, G. Meneghesso and E. Zanoni, "*Experimental Demonstration of Time-Dependent Breakdown in GaN-Based Light Emitting Diodes*" in IEEE Electron Device Letters, vol. 37, no. 5, pp. 611-614, May 2016. DOI: 10.1109/LED.2016.2543805

6. N. Renso, M. Meneghini, M. Buffolo, C. De Santi, G. Meneghesso, E. Zanoni, "*Understanding the degradation processes of GaN based LEDs submitted to extremely high current density*", Microelectronics Reliability, 2017, ISSN 0026-2714, DOI: 10.1016/j.microrel.2017.06.044

7. C. De Santi, M. Dal Lago, M. Buffolo, D. Monti, M. Meneghini, G. Meneghesso, E. Zanoni "*Failure causes and mechanisms of retrofit LED lamps*", Microelectronics Reliability 55 (9-10), pp. 1765-1769, (2015). DOI: 10.1016/j.microrel.2015.06.080
8. N. Trivellin, M. Yushchenko, M. Buffolo, C. De Santi, M. Meneghini, E. Zanoni, G. Meneghesso "*Laser-based lighting: Experimental Analysis and Perspectives*", Materials 2017, 10(10), 1166, DOI:10.3390/ma10101166

Papers in conference proceedings

1. M. Buffolo, C. De Santi, M. Meneghini, G. Meneghesso, E. Zanoni "*Mid-power LEDs for lighting applications: degradation mechanisms and kinetics*", proceedings of WOCSDICE 2015
2. M. Buffolo, C. De Santi, M. Meneghini, G. Meneghesso, E. Zanoni, "*Reliability of mid-power LEDs for lighting applications*", proceedings of FOTONICA 2016
3. M. Buffolo, N. Trivellin, M. Meneghini, D. Barbisan, N. Ferretti, G. Meneghesso, E. Zanoni, "*Electrical overstress robustness of latest generation LEDs for general lighting*", proceedings of LED Professional symposium 2016, Bregenz (Austria)
4. M. Buffolo, M. Meneghini, G. Meneghesso, E. Zanoni, "*EOS-related failures of modern High-Brightness white LEDs: failure limits and correlation with device structure*", proceedings of LS15, Kyoto (Japan)
5. M. Dal Lago, M. Buffolo, C. De Santi, N. Trivellin, M. Meneghini, G. Meneghesso, E. Zanoni "*High-Temperature Reliability of Retrofit LED Bulbs*", proceedings of LpS 2015
6. C. De Santi, M. Dal Lago, M. Buffolo, M. Meneghini, G. Meneghesso, E. Zanoni "*Analysis of the mechanisms limiting the reliability of retrofit LED lamps*", proceeding of RTSI 2015
7. M. Buffolo, M. Meneghini, C. De Santi, M. Davenport, J. Bowers, G. Meneghesso, E. Zanoni, "*Degradation Mechanisms of Heterogeneous III-V/Silicon 1.55 μm DBR Laser Diodes*", accepted for publication in SPIE Photonics West conference proceedings
8. C. De Santi, M. Meneghini, M. Buffolo, G. Meneghesso, E. Zanoni "*Time-Dependent Breakdown in GaN-Based LEDs—Description and Physical Origin*", proceedings of IWN 2016 conference, Orlando, Florida (USA)

9. E. Zanoni, N. Trivellin, M. Meneghini, G. Meneghesso, D. Barbisan, C. De Santi, M. Ferretti, M. Buffolo, "*LED lighting: nuove piattaforme tecnologiche per l'illuminazione ad alta efficienza*", proceedings of Luce e Design 2016 (Italy)
10. C. De Santi, M. Meneghini, N.Renso, M. Buffolo, N. Trivellin, G. Mura, M. Vanzi, A. Migliori, V. Morandi, G. Meneghesso, E. Zanoni, "*Investigation of the time-dependent failure of InGaN-based LEDs submitted to reverse-bias stress*", PSPIE 10124, Light-Emitting Diodes: Materials, Devices, and Applications for Solid State Lighting XXI, 2017, DOI: 10.1117/12.2256023
11. N. Trivellin, M. Buffolo, M. Meneghini, E. Zanoni, G. Meneghesso, "*White light source based on GaN laser diode*", proceedings of WOCSDICE 2017
12. E. Zanoni, M. Meneghini, G. Meneghesso, C. De Santi, M. La Grassa, M. Buffolo, N. Trivellin, D. Monti, "*Aging behavior, reliability, and failure physics of GaN-based optoelectronic components*", Proceedings Volume 9768, Light-Emitting Diodes: Materials, Devices, and Applications for Solid State Lighting XX, 97681E (2016), DOI: 10.1117/12.2225128
13. M. Meneghini, C. De Santi, M. Buffolo, A. Munaretto, G. Meneghesso and E. Zanoni, "*Towards high reliability GaN LEDs: Understanding the physical origin of gradual and catastrophic failure*", 2015 12th China International Forum on Solid State Lighting (SSLCHINA), Shenzhen, 2015, pp. 63-66. DOI: 10.1109/SSLCHINA.2015.7360690
14. M. Meneghini, G. Meneghesso E. Zanoni, N. Trivellin, C. De Santi, M. Buffolo, M. Dal Lago, D. Barbisan, A. Munaretto, M. Ferretti, "*Reliability of high power LEDs: from gradual to catastrophic failure*", proceedings of LED professionl sysmposium, 2015

Introduction

Direct-gap semiconductor alloys based on group III and group V elements of the periodic table are the most widely employed materials for the fabrication of optoeletronic devices, such as Laser Diodes (LD), Light-Emitting Diodes (LEDs), solar cells and photodectors. Thanks to the availability of mature III-V hetero-epitaxy growing techniques and to the possibility of tuning the alloy properties with an appropriate *bandgap engineering*, efficient optoelectronic devices with emission and absoprtion wavelengths ranging from the UV-C to the medium infrared spectrum can be obtained [1]. In particular, wide-bandgap short emission wavelength devices are based on the Gallium Nitride (GaN) - Aluminum Nitride (AlN) - Indium Nitride (InN) material system. White light-emitting diodes based on the phosphor-conversion of the blue light emitted by InGaN/GaN semiconductor chips have revolutionized the lighting industry, introducing a more efficient and durable alternative to the conventional light sources [2]. More than two decades of scientific and industrial research efforts have greatly improved the reliability of those devices [3], making it possible for state-of-the art LEDs to be now rated for useful lifetimes in excess of $50\,kh$ to $70\,kh$ at junction temperatures up to $150\,°\mathrm{C}$ [4]. However, while gradual current-driven and/or temperature-accelerated degradation mechanisms have been mostly mitigated, the performance and the reliability of LEDs can still be affected by unpredictable events of Electrical Over-Stress (EOS) [5], which are not so uncommon once the solid-state luminaire has been deployed on the field. Thus, one of the goals of this thesis is to investigate the robustness of modern GaN LEDs towards EOS events, focusing on the failure modes, conditions and mechanisms that are peculiar for each specific device structure.

Of course, gradual degradation processes may still be an issues when lower-tiered devices are operated at the limits of their Safe Operating Area [6]. However, the reliability of modern solid-state luminaries becomes more affected by extrinsic elements rather than by the primary emitters as the complexity of lighting system is increased. As shown in chapter 6, this is the case of the retrofit LED light bulbs commonly employed for home lighting, whose emission intensity and color point showed strong dependence on the degradation of the optics and the electronics of the bulb system.

The improvements in the III-N semiconductors growing techniques and the optimization of the device structures also contributed to the fabrication of green, blue and near-UV highly efficient and reliable laser diodes. Such devices found their way on several market segments, ranging from media projection to laser cutting. However, the most promising application for blue and UV-A emitters is laser-based lighting [7]. Due to the lower efficiency droop at high current density regimes of laser diodes with respect to LEDs [8], and to the simplified optical design of lighting systems based on small emitting area sources, Laser Activated Remote Phosphors (LARP) systems are set to replace LED-based lighting sources in medium/long distance white light projection applications, such as car headlights and street lamps. For those systems, the reliability of the phosphorescent material, rather than the robustness of the source, is the key factor in determining the long-term lifetime. High optical excitation densities and operating temperature can induce permanent worsening of the photo-luminescence efficiency of the material [9, 10], thus lowering the optical performance of the LARP system even if the emission of the solid-state source remains stable. For this reason, in Part II of this thesis the robustness and the degradation mechanisms affecting the reliability of blue-emitting phosphors for near-UV excitation have been investigated. The results of the experimental activity, carried out as part of a research project in collaboration with the New Energy and Industrial Technology Development Organization of Japan (NEDO), are discussed in Chapter 8.

Within the III-V based phosphides (III-P), arsenides (III-As) and atimonides (III-Sb) semiconductor material systems, opto-electronic devices with emission wavelengths ranging from green to the mid-infrared can be designed and manufactured. Semiconductor lasers emitting in the $1.31\,\mu m$ and $1.55\,\mu m$ windows are of primary interest for telecommunication applications, since those wavelength ranges represent the so-called *absorption windows* where the IR light attenuation due to the materials typically employed for optical fibers is minimum [11]. In particular, in the $1.55\,\mu m$ optical window absorption losses are minimized, and chromatic dispersion has only a minor influence on the transmission bandwidth. Devices tuned for this particular emission wavelength usually employ active regions based on quaternary InGaAsP or InAlGaAs alloys, grown in lattice-matching conditions on Indium Phosphide (InP) substrates. Those families of devices have been studied for decades, both in terms of performance optimization and reliability. However, in a recent push towards the integration and efficiency increase of telecommunications systems, AlInGaAs-based III-V emitters are now being directly integrated on a Silicon-On-Insulator (SOI) substrate, which serves as a platform for signal routing, filtering and conditioning through passive elements [12]. To this aim, the semiconductor epitaxy, separately grown on a specific III-V growth process, is first removed from its substrate and then bonded onto the SOI wafer by means of appropriate wafer bonding techniques. Former studies have demonstrated that this added processing step does not induce the formation of extended defects within the semiconductor region [13]. However, the impact of the generation/propagation of point defects on the long-term reliability of such devices has not been investigated, yet. With this goal, in Part III we describe the results of an investigation on heterogeneous III-V/Silicon $1.55\,\mu m$ experimental laser diodes, aimed at understanding the gradual degradation mechanisms affecting this novel class of opto-electronic devices.

Part I

Long-term aging and catastrophic failure of GaN-based LEDs submitted to electrical overstress

Introduction to Part I

Thanks to the technological improvements in the epitaxial growing techniques and to years of reliability-oriented research studies, the lifetime of solid-state sources for lighting applications has greatly improved since their introduction to the market. Nowadays, state-of-the-art high-power GaN LEDs rated for more than $50\,kh$ of useful lifetime at a junction temperature of up to $150\,^{\circ}\mathrm{C}$ can be commonly found. Moreover, since the gradual degradation of LEDs is typically accelerated by current (linear or superlinear dependence on current) and temperature (Arrhenius-like dependence), the effects of gradual degradation processes on both the semiconductor chip and the device package can be further mitigated by tuning the driving conditions and by improving the thermal management capabilities of the illuminator. For this reasons, the main reliability concern for those modern light sources is the effect of unpredictable electrical overdrive events, such as EOS or ESDs, that can induce sudden failure of the devices during normal operation. While several reports exist on the effects of ESD events on the performance and reliability of GaN LEDs [14, 15, 16], the literature on the effects of EOS events is very restricted. In light of these considerations, in part I of this thesis we investigated the effects of various electrical over-stress regimes on the electro-optical characteristics and on the reliability of GaN LEDs. As will be described in the following chapters, by submitting different kinds of LEDs to transient or continuous electrical overstress, we have been able to relate the specific failure modes of the LEDs under test to device structure-related failure conditions, which helped identifying the weaknesses of modern solid state sources towards electrically critical environment and unwanted out-of-specs operation.

While for state-of-the-art high-power devices the gradual degradation processes play a minor role in determining the robustness of the solid-state luminaire on the field, lower-tiered devices can still be affected by such problems. For instance, mid-power LEDs generally offer a good trade-off between lumen output and cost, but at the price of a reduced thermal and optical design of the package and a less evolved semiconductor chip structure. Those features not only impact on the performance of this class of LEDs, but can also increase the sensitivity towards high operating temperature. Thus, with the aim of analyzing the degradation mechanism that limit the reliability of mid-power LEDs subjected to a high-temperature operation, we performed a series of accelerated ageing experiments, whose outcomes are reported in chapter 5.

Due to their high lumen-to-cost ratio, mid-power white LEDs are usually employed in retrofit LED light bulbs. While the integration of those devices into the commonly adopted light bulb represents the best way to push towards the domestic adoption of SSL solutions, the added optical, mechanical and electrical components in a space and thermally-limited system can negatively impact on the lifetime of the solid-state luminaire if a proper thermal design is not implemented. Since this would reduce, if not neglect, the return on investment for a lighting product that costs considerably more with respect to conventional light sources, an analysis of the possible degradation processes that can reduce the lifetime of the LED bulb is needed. To this aim, a $20\,kh$ long lifetime experiment on four different commercial LED bulbs was carried out. The results of this system-level reliability investigation are reported in chapter 6.

Chapter 1

Working principles of LEDs

The physical process exploited by LEDs in order to generate light is the spontaneous emission. Through this process, an electron in an excited state loses its excess energy by emitting it as photon. Peculiar semiconductor structures based on *pn* junctions are employed in order to maximize the number of electrons (and holes) the undergo this process, thus maximizing the light output and efficiency of the device. This chapter provides a brief overview of the basic working principles of LEDs, their typical structure, and the basic electrical and optical properties, whose variation during aging provides fundamental information for the identification of the physical mechanisms responsible for the degradation of the devices.

1.1 Recombination processes

From a macroscopic point of view, the interaction between electro-magnetic radiation and matter is ruled by the Maxwell equations, which must be solved by imposing specific boundary conditions for the propagation inside a medium characterized by its conductibility, its dielectric permittivity and the magnetic permeability. On the other hand, the EM interaction with a semiconductor material is determined by the band-to-band processes that, depending on the energy difference between the interacting photon ($E_{ph} = hf$) and the energy-gap of the material (E_g), may occur. In particular:

- $E_{ph} < E_g$: weak interaction, no band-to-band processes, only the "dielectric" response of the material is interested (intraband transitions). Examples: RF, microwaves and long IR radiation.
- $E_{ph} \approx E_g$ e $E_{ph} > E_g$: strong interaction through band-to-band processes that induce the generation/recombination of $(e - h)$ pairs, typically due to the inter-

action with UV, visible and near-IR light.

- $E_{ph} \gg E_g$: high-energy ionizing radiation, like X-rays.

From a microscopic point of view, three main (optical) band-to-band processes, involving at least one electron-hole pair and a photon, can be identified 1.1:

- **Absorption** The energy of a photon is transferred to an electron which is promoted to the conduction band, generating a hole in the valence band.
- **Stimulated emission** A photon stimulates the recombination of an $(e-h)$ pair. This process generates a second photon, having the same frequency and *wave-vector* k of the incident photon. Since the second photon is *coherent* with the incident EM radiation, its amplitude is increased.
- **Spontaneous emission** A photon is spontaneously emitted as a consequence of an $(e-h)$ recombination. Since the emission is incoherent, a new EM field with a (relatively) large spectrum is generated.

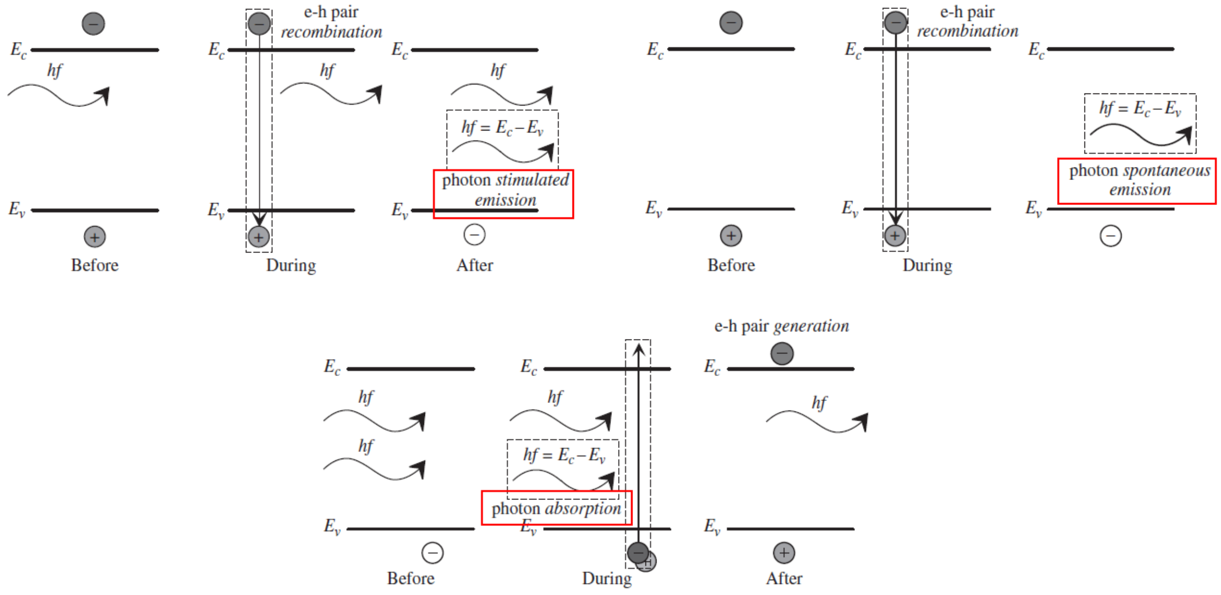

Figure 1.1: Simple view of stimulated emission, spontaneous emission and (spontaneous) absorption

The rules for the photon-electron interaction are defined by quantum-mechanical principles based on the *theory of perturbations*. Those restrictions, paired with the density of available states, define the absorption/emission profile of a specific semiconductor material.

1.1.1 Radiative recombination

In a non-degenerately doped semiconductor material at thermal equilibrium, the carrier concentrations n (electrons) and p (holes) are determined by the so-called *mass-action law*:

$$n_0 \, p_0 = n_i^2 \tag{1.1}$$

where n_0 and p_0 are the carrier concentrations at equilibrium, while n_i is the intrinsic carrier concentration. In order for an $(e-h)$ recombination event to take place, two conditions must be met: the presence of an excited electron in the conduction band, and an available empty energy state must exist in the valence band (hole). Hence, the carrier recombination rate per unit volume R must be proportional to the concentration of both carriers:

$$R = -\frac{dn}{dt} = -\frac{dp}{dt} = Bnp \tag{1.2}$$

where B is called *molecular recombination coefficient.* Typical values of B for III-V direct-gap semiconductors of interest for opto-electronic devices range from 10^{-11} to 10^{-9} cm^3/s.

At equilibrium, the recombination rate $R_0 = Bn_i^2$ equals generation G_0, hence the net recombination rate $R_{net} = R - G = R_0 - G_0$ is zero. In order to have a non-zero net recombination and attain spontaneous emission, the device must be brought out of equilibrium by the injection of free carriers into the quantum wells active region. In this condition, the concentration of carriers become:

$$p = p_0 + \Delta p \qquad n = n_o + \Delta n \tag{1.3}$$

where $\Delta p(t) = \Delta n(t)$, since also in high-injection condition carries are generate and annihilated in pairs. Employing (1.3) in (1.2) the recombination rate becomes

$$R = B[n_o + \Delta n][p_0 + \Delta p] \tag{1.4}$$

To further interpret this equation, assumption must be made regarding the effective amount of the excess free carriers injected.

In **low excitation** condition, $\Delta n \ll n_0 + p_0$, Eq. (1.4) becomes:

$$R = Bn_i^2 + B[n_o + p_0]\Delta n(t) = R_0 + R_{exc} \tag{1.5}$$

thus, the time-dependent concentration of electrons is given by

$$\frac{dn(t)}{dt} = G - R = (G_0 + G_{exc}) - (R_0 + R_{exc}) = G_{exc} - R_{exc} \tag{1.6}$$

If the excitation/injection process is turned-off at $t = 0$, then ($G_{exc} = 0$). By employing in (1.6) the value for R_{exc} found in (1.5) we obtain the following differential equation:

$$\frac{dn(t)}{dt} = -B[n_o + p_0]\Delta n(t) \tag{1.7}$$

whose exact analytical solution is given by

$$\Delta n(t) = \Delta n_0 e^{-B[n_o+p_0]t} = \Delta n_0 e^{-t/\tau} \quad \text{with} \quad \tau = \frac{1}{B[n_o + p_0]} \tag{1.8}$$

The time constant τ, also called *carrier lifetime*, is a characteristic parameter of the semiconductor material, which determines its radiative efficiency.
If we consider the trend over time of the concentration of carriers for a p-type semiconductor under moderate excitation (Fig. 1.2a), we can see that at $t = 0$ both species of carriers start decaying with the same time constant τ, equal to $1/BN_A$. However, only a small amount of majority carriers recombine, since their lifetime is much longer compared to the minority carrier lifetime, which is the limiting factor for the dynamic performance of the device. The reduction of the lifetime can be achieved by increasing the doping level in the active region, the injection level or by increasing the carrier confinement through the band-structure engineering by means of *quantum-well* structures.

In case of **high injection**, $\Delta n \gg n_0 + p_0$, the bimolecular rate equation (1.2) becomes

$$R = -\frac{dn}{dt} = -B\Delta n^2 \tag{1.9}$$

whose exact analytic solutions and (pseudo) time constant are given by:

$$\Delta n(t) = \frac{1}{Bt + \Delta n_o^{-1}} \qquad \tau(t) = \frac{-\Delta n(t)}{\frac{d\Delta n(t)}{dt}} = t + \frac{1}{B\Delta n_0} \tag{1.10}$$

which shows that the carrier decay rate after the injection pulse slows down with time, reaching an exponential trend only once the excess carrier population has reached the low-excitation condition $1/B(n_0 + p_0)$ (see Fig. 1.2b).

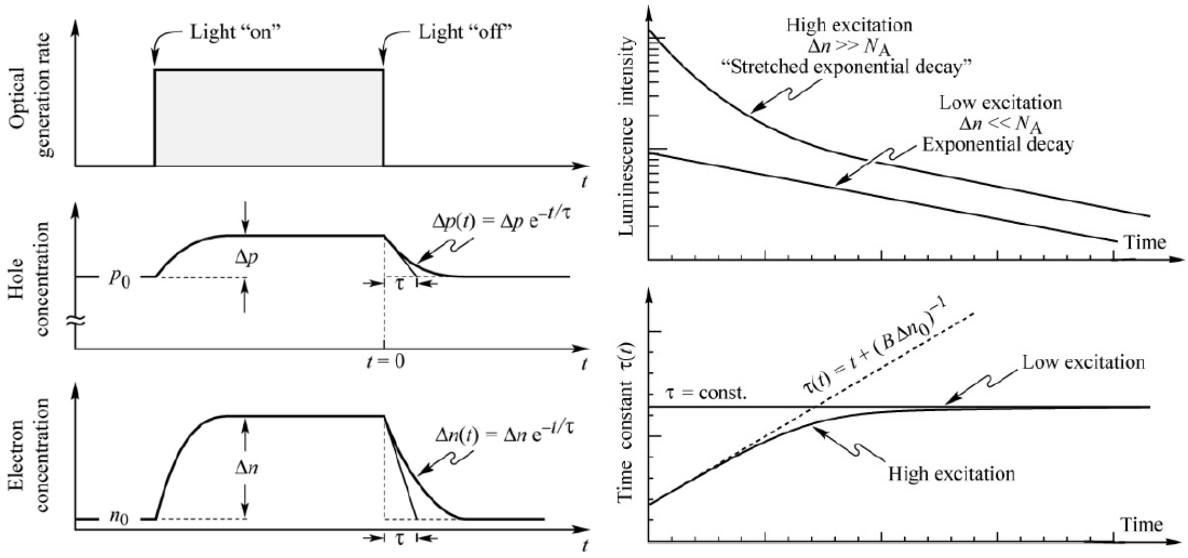

(a) (b)

Figure 1.2: Time-dependent concentration of carriers in a p-type ($n_o \ll p_0$) semiconductor under low excitation (a). Trend over time of luminescence and of the time constant for a semiconductor under high optical excitation levels (b).

1.1.2 Non-radiative recombination mechanisms

Within optoelectronic semiconductor devices, several physical process may concur to the non-radiative recombination of the free carriers contained in the active region, thus reducing the spontaneous recombination rate and the luminous efficiency of the device. Due to these processes, the excess energy of a charge carrier in a excited states is not emitted as photon, but is rather transferred to the crystal lattice as a quantum of vibrational energy, called (*phonon*), i.e. as heat (Fig. 1.3).

The most relevant non-radiative recombination mechanism is the **recombination**

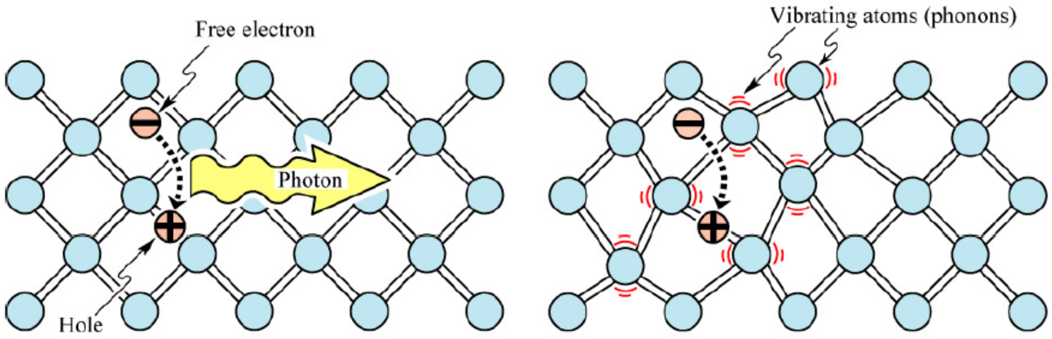

Figure 1.3: Schematic view of radiative (left) e non-radiative (right) recombination processes inside the crystal lattice.

through deep-levels, which are available energy states within the energy gap of the material whose origin is related to the atomic-level imperfections of the crystal lattice structure.

The recombination through deep-levels was first theorized by Shocley, Read [17] and Hall [18] in 1952. They showed that the rate of non-radiative recombination through a deep-level with (energy) depth E_T and concentration N_T is equal to

$$R_{shr} = \frac{p_0\Delta n + n_0\Delta p + \Delta n\Delta p}{(N_T\nu_p\sigma_p)^{-1}(n_0 + n_1 + \Delta n) + (N_T\nu_n\sigma_n)^{-1}(p_0 + p_1 + \Delta p)} \tag{1.11}$$

where ν_n and ν_p are electrons and holes thermal velocities, while σ_n and σ_p are the effective capture cross sections of the traps. Parameters n_1 and p_1 represent the electrons and holes concentration assuming a Fermi level equal to E_T. Those can be expressed as

$$n_1 = n_i \exp\left(\frac{E_T - E_{Fi}}{kT}\right) \qquad p_1 = n_i \exp\left(\frac{E_{Fi} - E_T}{kT}\right) \tag{1.12}$$

where E_{Fi} indicates the position of the intrinsic Fermi level.

Considering that $R_{shr} = \Delta n/\tau$, the non-radiative lifetime due to excess electrons is given by

$$\frac{1}{\tau} = \frac{p_0 + n_0 + \Delta n}{(N_T\nu_p\sigma_p)^{-1}(n_0 + n_1 + \Delta n) + (N_T\nu_n\sigma_n)^{-1}(p_0 + p_1 + \Delta p)} \tag{1.13}$$

In order to clarify the interpretation of the former equation, let us consider the case of p-doped semiconductor, $(p_0 \gg n_0, p_1)$, whit a minimal deviation from the equilibrium condition $(n - n_o \ll p_0)$: the minority-carrier lifetime and the related recombination rate, in low-excitation condition, can written as

$$\frac{1}{\tau} = \frac{1}{\tau_{n_0}} = N_T\nu_n\sigma_n \qquad R_n = \frac{n - n_0}{\tau_{n_0}} \tag{1.14}$$

whereas for an n-type semiconductor, $(n_0 \gg p_0, n_1)$, we have that

$$\frac{1}{\tau} = \frac{1}{\tau_{p_0}} = N_T\nu_p\sigma_p \qquad R_p = \frac{p - p_0}{\tau_{p_0}} \tag{1.15}$$

The former set of equations reveals that the SHR recombination rate is limited by the minority-carrier capture rate from the deep-levels. Assuming $\nu_n = \nu_p = \nu$, $\sigma_n = \sigma_p$ and low-injection, the average minority carrier lifetime can be expressed as

$$\tau_n = \frac{n_0 + p_0 + n_i \, cosh\left(\frac{E_T - E_{Fi}}{kT}\right)}{n_0 + p_0}\tau_0 \tag{1.16}$$

Equation 1.16 highlights two important properties of the recombination through deep-levels:

- The efficiency of deep-levels as non-radiative recombination centers increases as the trap level gets closer to mid-gap (the hyperbolic cosine function at the denominator has a minimum for $E_T = E_{Fi}$).
- The rate of SHR recombination increases as temperature increases.

The recombination through deep-levels is not strictly a non-radiative recombination process. Depending on the specific defect, a small probability exists that a photon can be generated as a consequence of the electronic transitions associated with the related deep-level. That is the case of the so-called *yellow luminescence* of Gallium Nitrides, whose energy level is assocaited with the formation of complexes between Galium vacancies and impurities like O or Si [19].

A second important non-radiative recombination mechanism is the **Auger recombination**. Due to this process, the excess energy released after an $(e-h)$ recombination event contributes to the promotion of another electron (hole) deeper into the conduction (valence) band. The excited carriers then lose their energy through subsequent emission of phonons, until the energy level of the band-edge is reached. The Auger recombination rate is given by

$$R_{aug} = (nC_n + pC_p)\left(np - n_i^2\right) \tag{1.17}$$

where C_n and C_p are the electrons and holes Auger recombination coefficient, whose typical value for III-V semiconductor ranges between $10^{-29} - 10^{-28} cm^6/s$. The temperature dependence of those coefficients is given by

$$C_{n,p}(T) = C_0 e^{\frac{-E_a}{k_b T}} \tag{1.18}$$

where E_a is an activation energy. Since two carriers of one type, plus one of the other, are needed for an Auger recombination process to occur, a quadratic dependence on the concentration of a specific carrier exists. This means that while in low-excitation condition the probability of Auger recombination is low, in high injection condition, where the dependence on carrier density expressed in (1.17) becomes cubic, this added non-radiative recombination process can severely impact the radiative efficiency of opto-electronic devices.

1.1.3 The internal quantum efficiency

In the previous section we showed how several non-radiative recombination processes can impact the luminous efficiency of opto-electronic devices by reducing the effective amount of injected carrier that undergo spontaneous recombination. This effect can be quantitatively evaluated by introducing the concept of *Internal Quantum Efficiency* (IQE). This parameter represent the ratio between the number of radiative recombination events and the total number of recombination events within the active region of the semiconductor device (per unit time). The partial contribution of each non-radiative recombination process can be expressed in terms of a characteristic recombination lifetime τ_i, associated with the specific mechanism. Following Matthiessen rule, the process-related lifetimes can be combined, thus attaining the average lifetime of carrier subjected to recombination. For the non-radiative recombination processes, we have that:

$$\frac{1}{\tau_{nr}} = \sum_i \frac{1}{\tau_i} = \frac{1}{\tau_{shr}} + \frac{1}{\tau_{aug}} \tag{1.19}$$

which takes into account both the Auger and the SHR recombination. Thus, the internal quantum efficiency can be calculated as

$$\eta_{IQE} = \frac{\tau_r^{-1}}{\tau_r^{-1} + \tau_{nr}^{-1}} \tag{1.20}$$

where τ_r is the average carrier lifetime for spontaneous emission. The carrier to photons conversion ratio is not the only limiting factor for the efficiency of an LED. Not only carrier transport and injection-related issues exist, but also the extraction of photons from the semiconductor chip and from the device package can limit the amount of light emitted by the device.

1.2 Electrical properties of LEDs

The p-n junction is the basic semiconductor building-block on which almost every kind of otpo-electronic device is based. Thanks to the very-high electrons and holes concentrations that can be simultaneously injected near the junction, p-n diode-based semiconductor devices have a clear advantages as soon as a high radiative emission rate is to be attained.

1.2.1 The p-n junction

An homo-junction p-n diode is a peculiar semiconductor system formed by two differently doped semiconductor layers brought in contact. In order to simplify its description, the following assumptions must be made:

- Abrupt junction: step variation in the dopant concentrations.
- Complete dopant ionization: the carrier concentrations at the p and n side are respectively $p = N_A$ e $n = N_D$, where N_A and N_D are the acceptor and donor dopant concentrations.
- No dopant compensation due to impurities.

Due to the gradient of carriers concentrations in proximity of the boundary of the two semiconductor layers, diffusion of majority carriers towards the region of opposite polarity occurs. As the diffused carriers recombine, the fixed charge of the ionized doping atoms is not compensated anymore. As a consequence, a *built-in* electric field that opposes to the flux of free carriers builds up. Once the magnitude of the electric field completely compensates the diffusion process, equilibrium is reached. In this situation the semiconductor region closer to the junction is completely emptied of free carriers, and the fixed charge defines the so-called *space-charge region* (SCR), on which a potential drop ϕ_i exists (Fig. 1.4b).

The built-in potential value is given by

$$\Phi_i = \frac{kT}{q} \ln \frac{N_A N_D}{n_i^2} \tag{1.21}$$

and represent the potential barrier that the carrier have to overcome in order to reach the semiconductor region of opposite polarity. The width of the SCR can be easily calculated by solving the Poisson equation:

$$W_D = \sqrt{\frac{2\varepsilon}{q}(\phi_i - V)\left(\frac{1}{N_A} + \frac{1}{N_D}\right)} \tag{1.22}$$

where $\varepsilon = \varepsilon_r \varepsilon_0$ is the specific dielectric permittivity of the semiconductor material, while V is the external potential applied between the two sides of the junction. Due to the high-resistivity of the SCR, whose free carriers concentration is very low, such

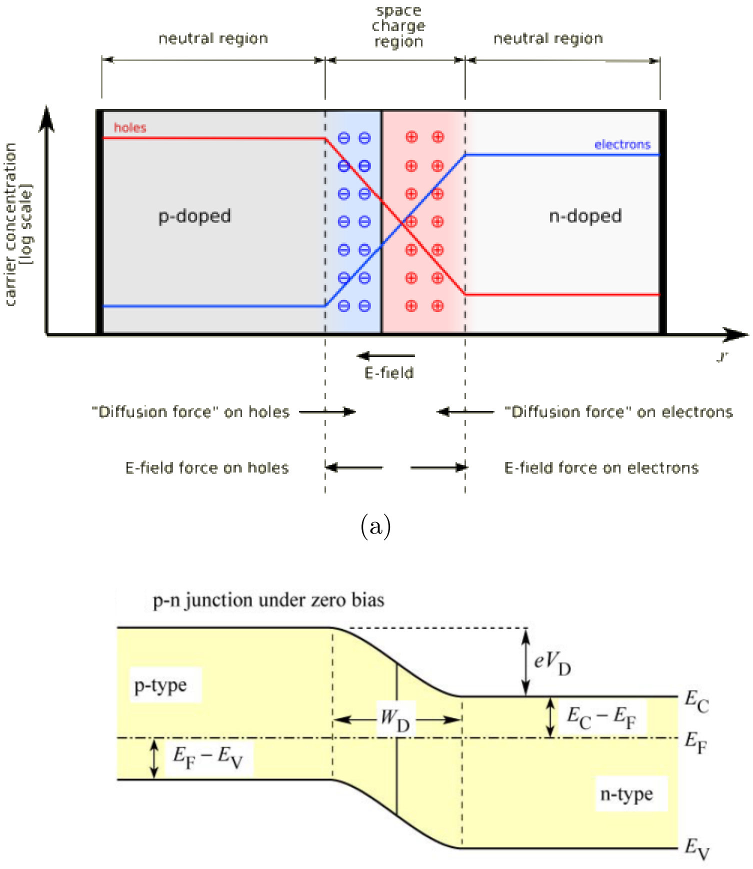

(a)

(b)

Figure 1.4: Distribution of free and fixed charge in an abrupt p-n junction at equilibrium (a). Band-diagram at 0 V (qV_D corresponds to ϕ_i) (b).

potential falls entirely on this region, inducing a change $\phi_i \longrightarrow \phi_i - V$ in the effective potential barrier seen by the diffusing carriers. If a forward bias is applied, $V > 0\,V$, a reduction of the potential barriers occurs, thus promoting the diffusion of carriers towards the neutral region of opposite polarity, where they recombine, eventually emitting a photon. The current-voltage characteristic of a p-n diode is described by the *Shockley equation*:

$$I_D = I_S \left(e^{qV/kT} - 1\right) \qquad \text{with} \qquad I_S = qA \left(\sqrt{\frac{D_p}{\tau_p}} \frac{n_i^2}{N_D} + \sqrt{\frac{D_n}{\tau_n}} \frac{n_i^2}{N_A} \right) \tag{1.23}$$

where A is the junction area, $D_{n,p}$ is the diffusion constant for electrons and holes, $\tau_{n,p}$ is the average minority-carrier lifetime and the pre-factor I_S (1.23) is the reverse-bias *saturation current.*

For forward-bias polarization values $V \gg kT/q$ ($\approx 25\,mV$ at room temperature) the I-V characteristic is exponential. The voltage value discriminating the high current conduction regime, named threshold or turn-on voltage, can be determined by substituting (1.21) into (1.23):

$$I_D = qA\left(\sqrt{\frac{D_p}{\tau_p}}N_A + \sqrt{\frac{D_n}{\tau_n}}N_D\right)\left(e^{q(V-\phi_i)/kT} - 1\right) \tag{1.24}$$

Equation (1.24) shows that for applied voltages close to the built-in junction potential current rapidly increases. In particular, for highly doped junction where the Fermi level in the quasi-neutral p and n regions lies right below (above) the conduction (valence) band, the threshold voltage $V_{th} \approx \phi_i \approx Eg/q$ depends directly on the energy-gap of the materials. As a consequence, the turn-on voltage of a diode inherits the (quite high) temperature dependence of the energy-gap of the semiconductor, that can be described by the experimental relation given by *Varshni's law*:

$$E_g(T) = E_g(0K) - \frac{\alpha T^2}{T+\beta} \tag{1.25}$$

where α e β are appropriate fitting parameters. Equation (1.25) shows that as temperatures increases, the energy-gap of the material, and thus the turn-on voltage of the diode, decreases. The intrinsic dependence of the I-V characteristic of a diode on temperature, and the direct proportionality of the Output Power (OP) of an LED on its driving current, implicates that a constant-current bias scheme is mandatory for those kind of devices.

1.2.2 Heterojunction diodes

In the previous paragraphs we saw how the built-in potential barrier can be lowered by applying an external bias, thus increasing the amount of diffusing carrier. Once they reach the quasi-neutral regions of opposite polarity, where they act as minority carriers, the average distance covered prior recombination, called *diffusion length*, can be quantitatively estimated to be

$$L_n = \sqrt{D_n\tau_n} \qquad \text{and} \qquad L_p = \sqrt{D_p\tau_p} \tag{1.26}$$

where $\tau_{n,p}$ is the average minority carrier lifetime. Since this length is in the order of microns, the diffused minority carrier are spread over a wide region, in decreasing concentration with increasing distance (see Fig. 1.5a).

Since the radiative recombination strictly depends on the simultaneous presence of

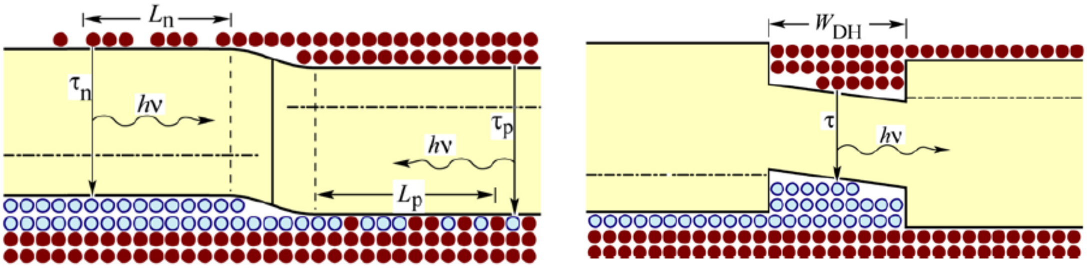

(a)

(b)

Figure 1.5: Carrier distribution in proximity of a forward-biased p-n junction for a homojunction (a) and a double heterostructure diode (b).

a high concentration of both electrons and holes, homojunction diodes are far from optimal structures to be employed for the realization of efficient LEDs. Instead, modern light-emitting diodes employ heterostructures in order to attain strong spatial confinement of both electrons and holes. In particular, alternating semiconductor layers with high (barriers) and low (wells) energy gap are employed in order to create potential wells both in valence and conduction bands, as shown in 1.5b. The strong localization of both species of carriers dramatically increases the radiative recombination rate in terms of number of (useful) recombination events per second and per unit volume, thus increasing the efficiency and the luminous output of the device.

Quantum Wells

In a semiconductor material, the carrier density $n(E)$ is proportional to the product of the *density of states* $g(E)$ and the *probability of occupation* given by the Fermi-Dirac distribution $f_n(E)$: while the latter is a well-defined function, depending only on the absolute temperature, the former parameter can be exploited in order to design innovative and more efficient micro-electronic devices.

The density of states function $g(E)$ for a specific charge carrier can be shaped by confining with potential barriers the carrier itself. While energetic confinement always leads to the quantization of the available energy states, the shape of the $g(E)$ functions strictly depends on the kind of carrier confinement that is being employed, as shown in Fig. 1.6.

Among these reduced dimensionality structures, the Quantum Wells (QWs) are the most commonly employed. With regard to LEDs, the carrier are trapped in the potential well that is formed in the band-diagram due to presence of the double heterostructure (Fig. 1.7a), which limits the movement of carriers in the direction perpendicular to it. For sufficiently narrow QWs, quantization of the energy levels within the wells

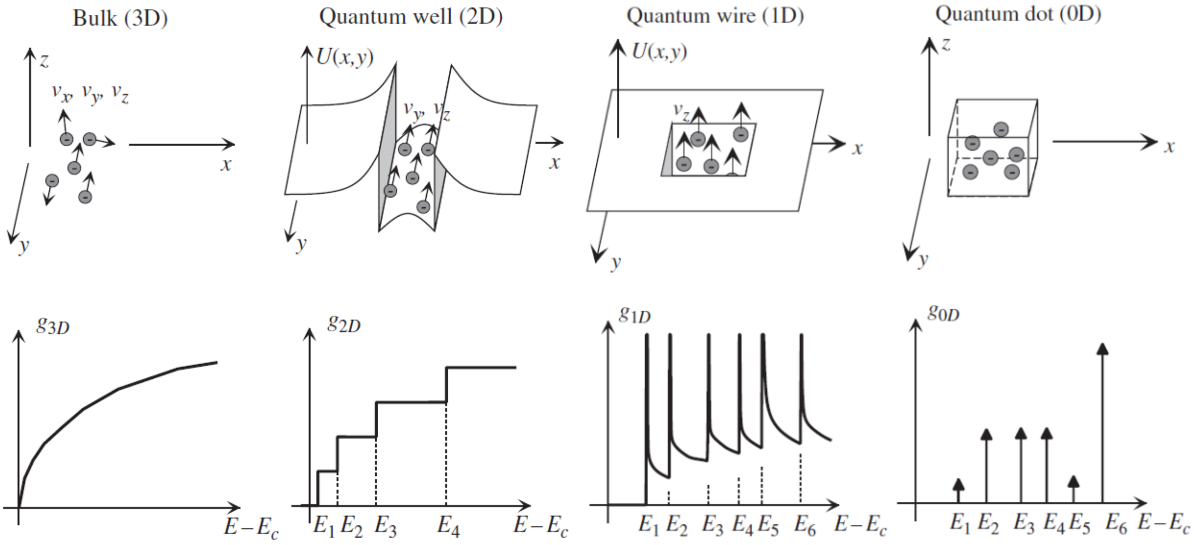

Figure 1.6: Degrees of freedom for an electron subjected to four different kinds of confinement (top), and related density of states function (bottom).

occurs, thus generating new sub-bands with parabolic dispersion relation (Fig. 1.7b). In particular, for a QW defined in the Cartesian space, the wave function of a particle can be expressed within the effective mass approximations as the product of three factors:

$$\psi(x, y, z) = \phi(x) \exp(-jk_y y) \exp(-jk_z z) \tag{1.27}$$

For a particle in steady-state ($k_y = 0, k_z = 0$) the wave function reduces to $\psi(x, y, z)$, the *envelope function*, that derived from the solution of the uni-dimensional Shrödinger equation inside a potential well (Fig. 1.7a). Since $|\psi(x, y, z|^2 = |\phi(x)|^2$, the probability density associated to the particle only depends on the envelope function, and in particular on its functional dependence on the x coordinate, which determines the energy distribution of the particle within the well. If we consider E_i as the available energy states in this peculiar potential, the total energy of the particle can be expressed as

$$E = E_k + E_i = E_i + \frac{\hbar^2}{2m^*}(k_y^2 + k_z^2) \tag{1.28}$$

where E_k is the kinetic energy and m^* is the effective mass of the particle. Since this relation holds for every energy state i, the potential well modifies the conduction and valence band structure by introducing a series of sub-bands, whose dispersion relation, as previously stated, is approximately parabolic, as for a free particle (Fig. 1.7b). Since the motion of the particles is limited in the z direction while being free in the (x, y) plane, particles contained within a (2D) potential well are referred to as 2D *gas*.

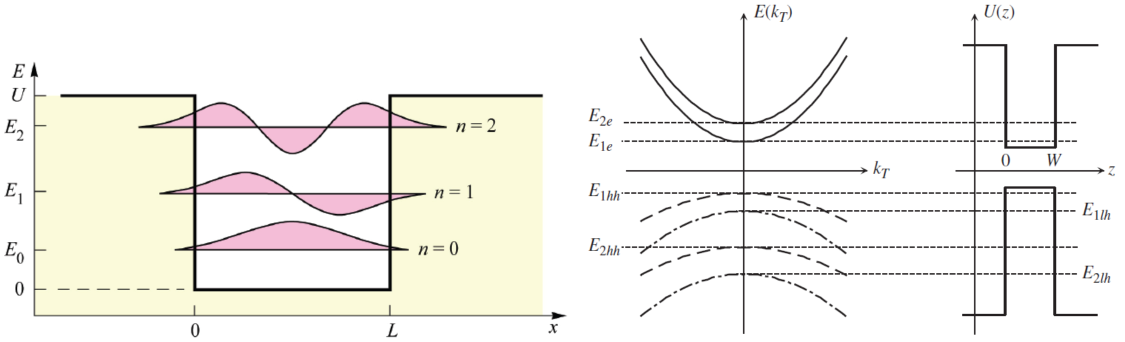

(a) (b)

Figure 1.7: Wave function of a particle confined in a symmetric potential well with finite barriers (a). Approximate dispersion relation for the sub-bands of a QW (b).

1.2.3 I-V characteristic of an LED: non idealities

Temperature is not the only factor influencing the current-voltage characteristic of a diode, which can be affected by several non-idealities. Firstly, the Shockley equation (1.23) describes the theoretical behavior of an ideal diode. In order to better interpret real experimental data, the following equation is usually employed:

$$I_D = I_S \exp \frac{qV}{n_{id}kT} \tag{1.29}$$

where n_{id} is the *ideality factor* of the diode, that is equal to 1 for an ideal homojunction diode. In real diodes, the value of this parameter ranges from 1.1 to 2, whereas for heterojunction diodes values even greater than 4 can be reached. Generally speaking, an higher value of the (bias-dependent) ideality factor implies a less steeper I-V characteristic, which identifies a less efficient conduction mechanism. High values of n_{id} can also be interpreted by considering other factors:

- The SRH recombination within the space charge region of the diode (Fig. 1.8a). This conduction mechanism is characterized by an ideality factor equal to 2.
- Tunneling-assisted conduction mechanisms.
- The contribution of the several heterojunctions forming the device: the total ideality factor is the sum of all the ideality factors related to the rectifying junctions present within the epitaxial structure (Fig. 1.8b), [20].

A real diode is also affected by parasitic resistive paths, either in series or in parallel with the junction, that can be modeled as resistor properly connected to the ideal

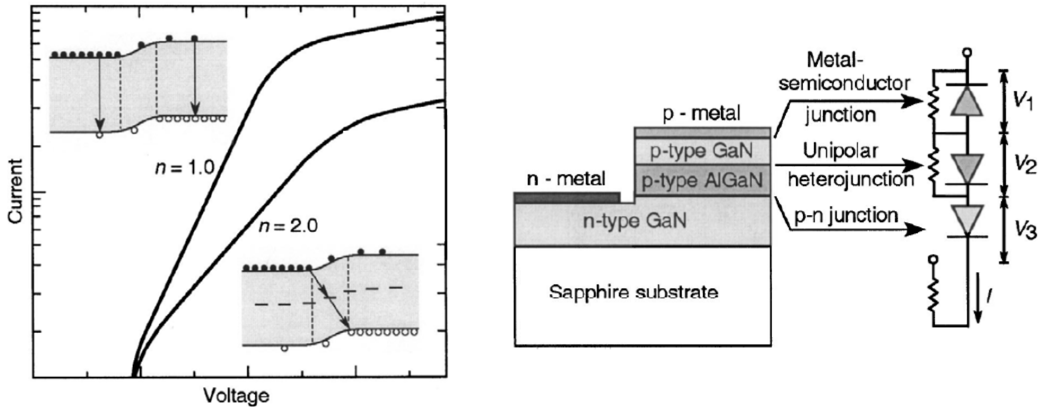

(a) (b)

Figure 1.8: Conduction mechanisms in an ideal homojunction diode (a). Heterojunction diode seen as the composition of several diodes, each one identifying e specific heterointerface (b).

diode. In particular, factors like the resistivity of the quasi-neutral regions, of the heterointerfaces and of the ohmic contacts contribute to the *series resistance* of the diode, whereas parasitic conduction paths bypassing the junction contribute to the so-called *parallel resistance*. An increased series resistance component leads to an higher operating voltage of the device and increased losses due to Joule effect. On the other hand, parallel conduction paths are symptom of an increased conduction through the surface of the device or of defect-assisted conduction through the active region. Figure 1.9 shows the impact of those parasitic components on the ideal I-V characteristic of a diode.

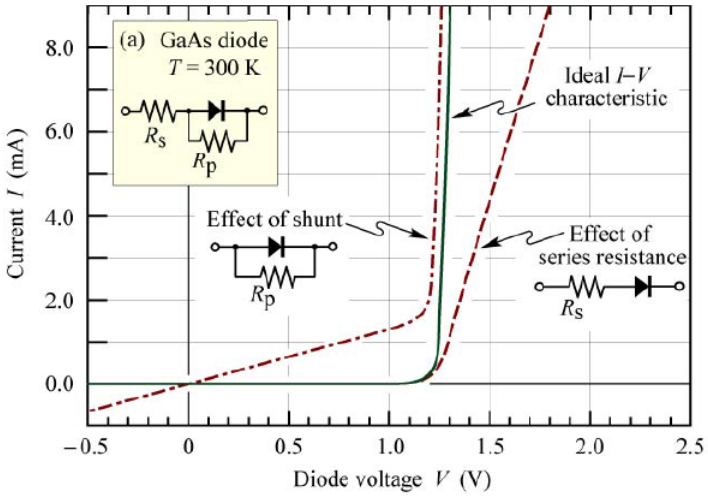

Figure 1.9: Effect of the parasitic series and parallel resistances on the I-V characteristic of a diode.

In order to take into account those parasitic resistances, the Shockley equation (1.29) must be properly modified, thus obtaining

$$I - \frac{V - R_s I}{R_P} = I_S \exp \frac{q(V - R_s I)}{n_{id} kT} \tag{1.30}$$

1.2.4 I-V characteristic of an LED: electron transport mechanisms

The variation of the I-V characteristic during stress/operation can provide fundamental information regarding the degradation mechanisms affecting the lifetime of the device. Since for each bias regime of the diode the electronic conduction is dominated by a specific conduction mechanism, the analysis of the evolution of the I-V characteristics over time can help interpreting the physical origin of the ongoing degradation process.

Forward-bias regime

Let us now consider the I-V characteristic of a generic GaN-based LED in forward bias reported in Fig. 1.10 (from Ref. [21], chapter 8). Depending on temperature and applied bias, several conduction mechanisms can be identified.

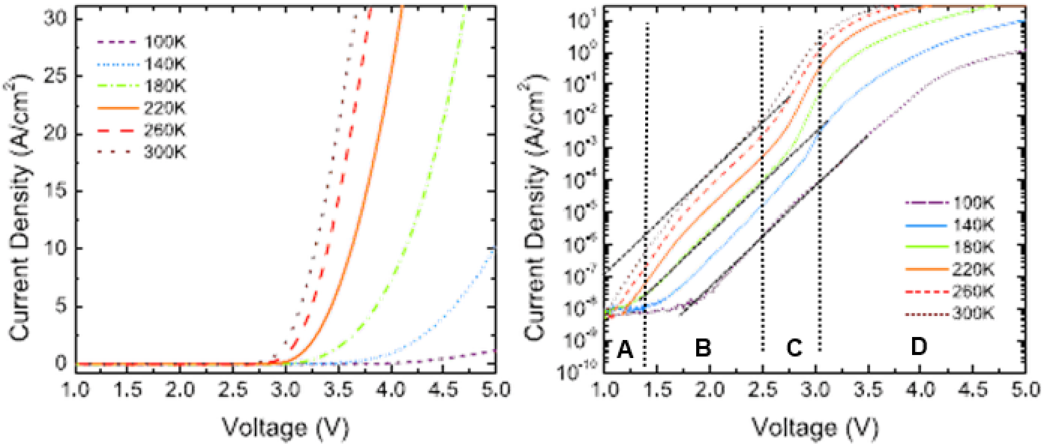

Figure 1.10: Current-voltage characteristic of a GaN LED based on a multi-QW structure measured at different temperatures.

- **Region A** In the low forward-bias regime the current-voltage relation can be approximated by $I \approx R_{sur}/V$, where R_{sur} is a parallel resistance taking into account the leakage current due to surface recombination. For low temperatures the conduction is dominated by *hopping* between localized nearby states, and becomes influenced by the field-dependent Poole-Frenkel effect (see section 9.2.2 in chapter 9) for higher temperatures. This phenomenon also affects the reverse-bias I-V characteristics in the low voltage region.

- **Region B** For moderate bias, in our example between 1.5 and 2.5 V, tunneling components starts prevailing. In this condition the I-V relation can be expresses as

  $$I = I_0 \exp\left(\frac{qV}{E}\right) \tag{1.31}$$

  where E is a fitting parameter that takes into account the transparency of the barriers towards carrier flow, featuring a very low temperature dependence. Among the several tunneling mechanism that can affect conduction in GaN-based LEDs we can find tunneling of holes towards the active region, electron tunneling assisted by localized states within the barriers or diagonal tunneling. Since tunneling processes are largely field-dependent and weakly dependent on temperature, the slope of the I-V curve in region B is not affected by temperature variations.

- **Region C** With increasing bias, $2.5 < V < 3$, the electron transport gets progressively dominated by the generation/recombination currents within the active region of the device first, and then by diffusion of carriers over the potential barrier offered by the junction. In this situation the I-V characteristic, already expresses in (1.29), is given by

  $$I = I_S \exp\left(\frac{qV}{n_{id}kT}\right) \tag{1.32}$$

- **Region D** In high injection condition the voltage drop across the quasi-neutral regions increases, thus the I-V characteristic becomes dominated by the series resistance of the device.

1.2.5 I-V characteristic in reverse-bias

The Shockley equation of an ideal diode (1.23) shows that for high reverse-bias values the current of the device saturates at the value I_S, previously defined. However, real devices deviate from this ideal blocking behavior, showing both exponential (1.31) and n-th power dependency of reverse-current on voltage ($I \propto V^n$). For low values of reverse voltage the leakage current is dominated by the surface conduction, as for the low forward-bias region. Moreover, the influence of tunneling mechanisms on the reverse-bias conduction is usually testified by temperature independence of the slope of

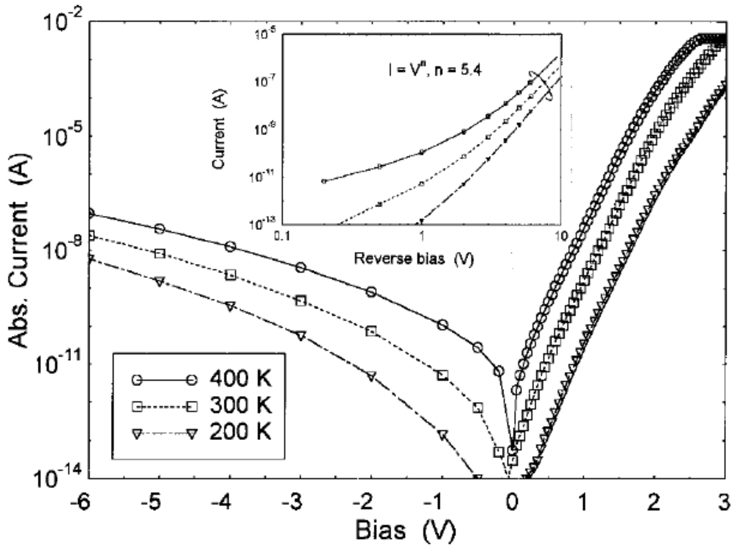

Figure 1.11: I-V characteristic in semi-log scale of a single QW InGaN LED measured at different temperatures [22].

the I-V curve, as shown in Fig. 1.11. In that operating condition, for GaN and InGaN-based diodes, conduction is usually assisted by the defects related to dislocations, which are linear (1D) defects propagating through the epitaxial structure. This topic will be further explored in the next chapter, where the behavior and the degradation mechanisms of GaN LEDs submitted to reverse-bias stress will be explored.

1.3 Optical properties of LEDs

This section will focus on the description of the main optical properties of LEDs, including the standard emission spectrum, the L-I characteristic and the chip geometries aimed at maximizing the extraction of photons emitted within the active layer.

1.3.1 Emission spectrum

The spontaneous emission process relies on the recombination between an electron in the conduction band and a hole in the valence band. Carriers are energetically distributed following an approximately parabolic dispersion relation $E(k)$ given by

$$E_e = E_C + \frac{\hbar^2 k^2}{2m_e^*} \qquad \text{and} \qquad E_h = E_V - \frac{\hbar^2 k^2}{2m_h^*} \tag{1.33}$$

and showed in Figure 1.12a.

Considering the emission process, the momentum $p = \hbar k \approx E_g/c$ of the emit-

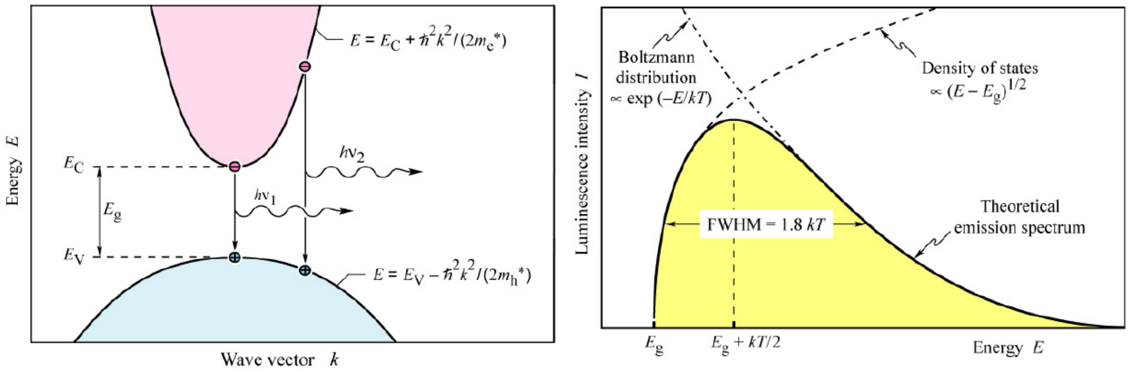

(a) (b)

Figure 1.12: Dispersion relation for electrons and holes in a bulk semiconductor (a). Theoretical emission spectrum of an homo-junction LED (b).

ted photon is much lower (several orders of magnitude) respect to the momentum of the particles undergoing recombination, which is equal to $\sqrt{2m^*kT}$. Hence, since the quantum-mechanical transition rules require the conservation of the momentum, in LEDs based on direct-gap semiconductor material "vertical" transitions are much more likely to occur. Following that assumption, the energy of the emitted photon can be calculated as

$$E_{ph} = h\nu = E_e - E_h = E_g + \frac{\hbar^2 k^2}{2m_r^*} \tag{1.34}$$

where m_r^* is the *reduced effective mass* defined as ${m_r^*}^{-1} = {m_e^*}^{-1} + {m_h^*}^{-1}$.

By employing the joint dispersion relation (1.34), the joint density of states for a bulk semiconductor can be computed as

$$g_{3D}(E) = \frac{1}{2\pi^2}\left(\frac{2m_r^*}{\hbar^2}\right)^{3/2}\sqrt{E - E_g} \tag{1.35}$$

which can be multiplied by the occupation probability given by Boltzmann statistics, $f_B(E) = \exp(-E/kT)$, attaining an approximate relation for the intensity Vs. energy of the emitted photons from the semiconductor:

$$I(E) \propto \sqrt{E - E_g}\,\exp\left(-\frac{E}{kT}\right) \tag{1.36}$$

which is plotted in Figure 1.12b. This maximum emission intensity is attained for a photon energy equal to $E_g + kT/2$, with a FWHM of $1.8\,kT$, corresponding to a $\Delta\lambda = 1.8\,kT\lambda^2/(hc)$. Since the emitted light has a relatively narrow spectral bandwidth, around 28 nm for a GaAs-based device with emission at 870 nm at room temperature, the emission of an LED is perceived by the human eye as monochromatic.

From an experimental point of view, fluctuations in the composition of the semiconductor are found to induce a broadening of the theoretical shape of the emission spectrum described by 1.36, which can be better approximated by a Gaussian distribution. Moreover, since radiative recombination takes place within the quantum wells rather than in the bulk semiconductor, the former relation must be adapted to take into account the electronic transition between the sub-bands of the conduction and valence bands wells.

1.3.2 Extraction of photons

Within the active region of the device photons are isotropically emitted. Due to the high mismatch between the refraction indexes of the semiconductor material and air, part of the emitted radiation is trapped within the crystal by total reflection (Fig. 1.13a). In particular, *Snell's law* let us numerically determine the *critical incidence angle* ϕ_c above which this phenomenon occurs:

$$\phi_c = arcsin\frac{n_{air}}{n_s} \approx \frac{n_{air}}{n_s} \tag{1.37}$$

where n_{air} and n_s are the refractive indexes of air, or more generally of the material surrounding the chip, and of the semiconductor material. The second inequality in (1.37) derives from the high (> 2.5) refractive index usually employed for opto-electronic devices. Assuming a point-like light source within the semiconductor material and computing the portion of spherical surface covered by the escape cone (Fig. 1.13b), it is possible to estimate the relative amount of outgoing optical power. In particular, considering a total emitted power P_{src}, the amount of light escaping from the chip is

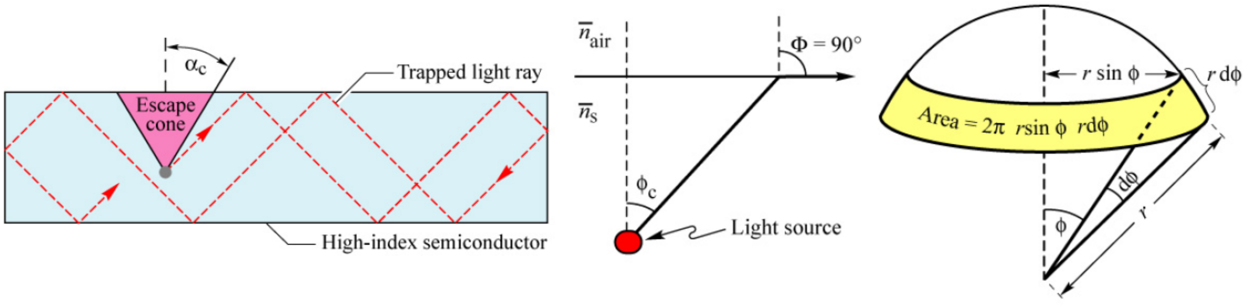

(a) (b)

Figure 1.13: Total reflection in a semiconductor chip (a). Representation of the critical angle and of the escape cone of light (b).

equal to

$$P_{esc} = P_{src} \frac{2\pi r^2 (1 - cos\phi_c)}{4\pi r^2} \tag{1.38}$$

which can be related to the total emitted power obtaining

$$\frac{P_{esc}}{P_{src}} = \eta_{extr} = \frac{1}{2}(1 - cos\phi_c) \approx \frac{1}{4} \frac{n_{air}^2}{n_s^2} \tag{1.39}$$

Equation (1.39) shows that the extraction efficiency of planar LED based on high refractive index semiconductors is rather low. Thus, in order the increase the global efficiency of the device, tweaks to the geometry and to the composition of both the package and the chip must be implemented:

- **Shaping of the encapsulant material** Shaping of the Lambertian emission pattern can be easily attained by employing a dome-shaped encapsulation layer with high refraction index. This solution not only reduces the losses related to total reflection at the semiconductor-encapsulant interface, bu also provides a primary optics to the lighting source.

- **Shaping of the semiconductor** Due to its reduced cost, the most commonly employed semiconductor chips feature a planar rectangular geometry (Figure 1.14a). For this particular structure, six light escape cones can be identified. However, five of those cones partially or totally interact with the susbstrate, which may absorb part of the radiation. Moreover, the cone on the top surface suffers from shadowing from the surface contact. In order to overcome the intrinsically low extraction efficiency of this kind of structure, several chips geometries have been studied and developed, like the truncated inverted-pyramid shape reported in Fig. 1.14b. Thanks to the reduced internal reflections, and to the reduced light re-absorption due to the decreased average free photons path in the semiconductor, an increase of a factor of two in η_{ext} can be achieved with respect to the standard rectangular geometry.

- **Texturing of the semiconductor surface** Within the device, the semiconductor/encapsulant and the semiconductor/substrate interfaces act as a waveguide which reduces the amount of photons emitted from the active region. This effect can be mitigated by texturing the surface of the semiconductor material, thus making it more diffusive. With regards to Gallium-Nitride, specific chemical processes have been developed in order to etch the material from different crystallographic planes and obtain a surface texture based on micro-pyramids, able to increase the extraction efficiency up to 50%.

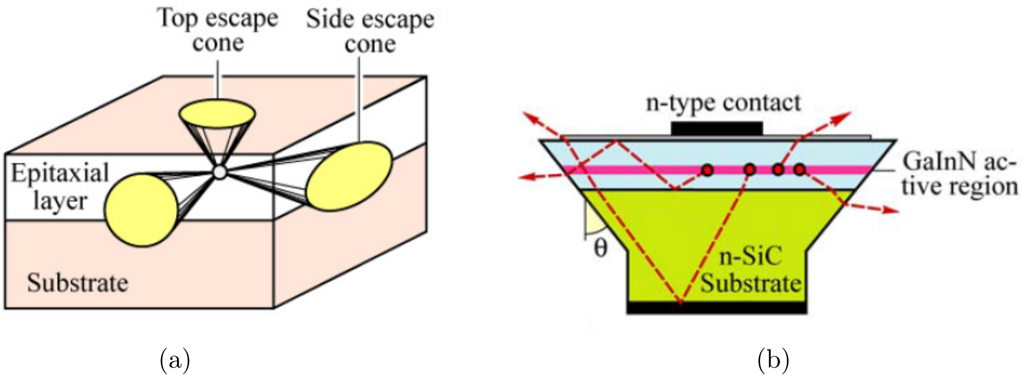

Figure 1.14: Semiconductor chip with rectangular (a) and pedestal-like (b) geometry.

- **Patterning of the Sapphire substrate** A similar approach can be employed in order to reduce reflections and increase photons scattering at the semiconductor/substrate interface. Firstly proposed by Tadatomo in 2001 [23], GaN growth on PSS (*Patterned Sapphire Substrate*) can provide up to 70% increase in the extraction efficiency. Since the semiconductor is epitaxially grown on a highly irregular surface, *Selective Area Growth* (SAG) growth techniques need to be employed in order to reduced the density of dislocation in the epitaxial layer.

1.3.3 Evolution of the LED structure

The improvements in the chip/packages geometry described in the former section all refer to the *Conventional Chip* (CC) LED structure, whose functionality for a single QW apporach was firstly demostrated by Nakamura in 1993 [24]. In this kind of structure both ohmic contacts face upwards and the *n*-type material is accessed by means of selective etching of the epitaxial layers.

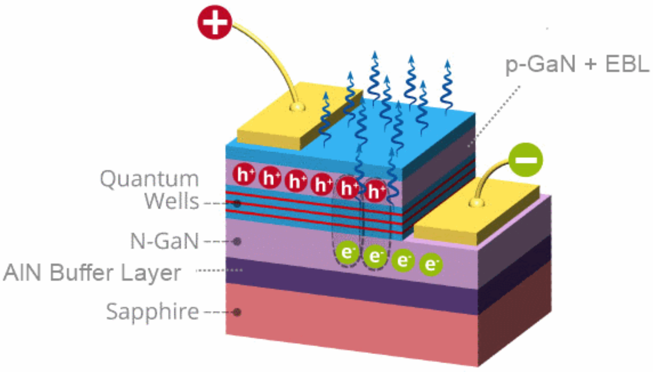

Figure 1.15: Structure of a Convetional-Chip LED.

Since the *p*-contact covers part of the exposed semiconductor surface, a trade-off between this shadowing effect and the reduced current spread due to the reduction in the dimensions of the metal lines exists. Since this approach leads to the increase of the *current crowding* effect, which limits the efficiency and increases the self-heating of the device, current-spreading is usually achieved by means of a low-resistivity semi-transparent *current spreading layer* made of NiAu or ITO. However, even with those tweaks, the geometry of CC-LEDs limits the extraction efficiency to a mere $\eta_{extr} \approx 30\%$.

Flip-Chip LEDs In order to overcome the trade-off between current distribution and photon extraction, the Flip-Chip (FC) LED structure was developed. In this case, the epi stack (and the sapphire substrate) are first flipped and then properly attached to a secondary support structure (Fig. 1.16a). This baseplate is usually made of Silicon, which greatly improves the thermal management capabilities of the FC structure, limited in CC-LEDs by the low thermal conductivity of the Sapphire substrate ($\approx 0.3\, W/cm\, K$). Since no bonding wires are required, FC LEDs have a lower production cost and can be easily arranged in matrix in order to obtain integrated multi-chip single-package high-intensity sources, like the *Chip On Board* (COB) LED shown in figure 1.16b. By properly calibrating the distance between the active region and the (highly-reflective) p-contact, also η_{extr} can be greatly improved with respect to the conventional rectangular structure. However, since a high step between the refractive indexes of the semiconductor material and of the substrate exists, the losses due to internal reflection still represent a limiting factor for this kind of configuration.

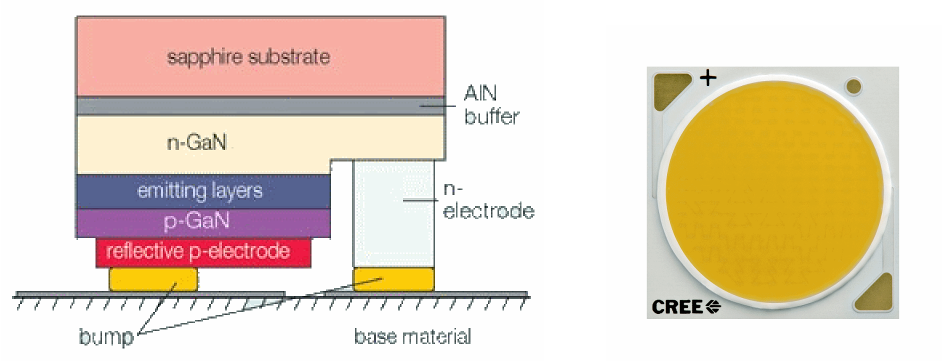

(a) (b)

Figure 1.16: Structure of a FC-LED (a). Chip-on-board LED (b).

Vertical Thin-Film LEDs In Vertical Thin Film (VTF) LEDs, Total Internal Reflection (TIR) losses related to the semiconductor-substrate interface are avoided by completely removing the substrate through laser *lift-off* techniques. The epitaxial structure is then transferred and bonded at the p-side to a thermally conductive carrier substrate featuring a highly reflecting metallization. TIR losses are then further reduced by roughening of the exposed n-type semiconductor. With this improved LED structure, reported in Figure 1.17a, extraction efficiencies as high as 75% can be attained.

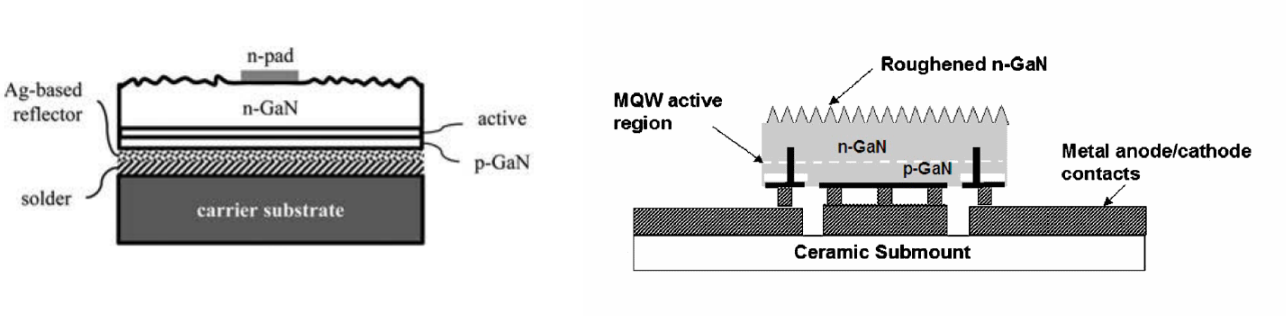

(a) (b)

Figure 1.17: Structure of VTF (a) and a TFFC LED (b).

Thin-Film Flip-Chip LEDs As suggested by the name, this kind of approach combines the thermal performances of FC-LEDs with the high extraction efficiency and homogeneity in the current distribution attainable with VTF-LEDs. This kind of LEDs, whose structure is reported in Fig. 1.17b, are manufactured as follows: once the hetero-epitaxy and the ohmic contacts are formed, the semiconductor chip is bonded to the support baseplate and the Sapphire substrate is removed. Bonding wires-free electrical contacts to the n-GaN are then formed by means of laterally insulated vias. Finally, TIR losses are reduced by texturing of the exposed n-type semiconductor. LEDs based on the TFFC structure can benefit from an extraction efficiency as high as 80 % [25], thus making it the most commonly adopted design for single-chip high-power LEDs.

1.3.4 Interpretation of the L-I characteristic of an LED

The analysis of the optical power Vs. current characteristic of a ligth-emitting diode provides useful information regarding the dominant recombination mechanisms at a specific injection density value. In the former sections, we showed that the main recombination mechanisms in LEDs are radiative recombination, SHR and Auger recombination, whose recombination rate is respectively proportional to Bn^2, An e Cn^3, where n is the carrier density. If we apply the principle of charge neutrality when a current density J is flowing through the active region of the device, and consider the presence of a leakage current J_L, the equation of the recombination rate becomes

$$\frac{dn}{dt} = \frac{J}{ql} - AnN_T - Bnp - Cn^3 - \frac{J_L}{qL_m} \tag{1.40}$$

where l, L_m, N_T are the thickness of the active region, the diffusion length of the minority carriers and the trap states density, respectively. In steady-state conditions, with $dn/dt = 0$, Eq. (1.40) becomes

$$\frac{J}{ql} = AnN_T + Bnp + Cn^3 + \frac{J_L}{qL_m} \tag{1.41}$$

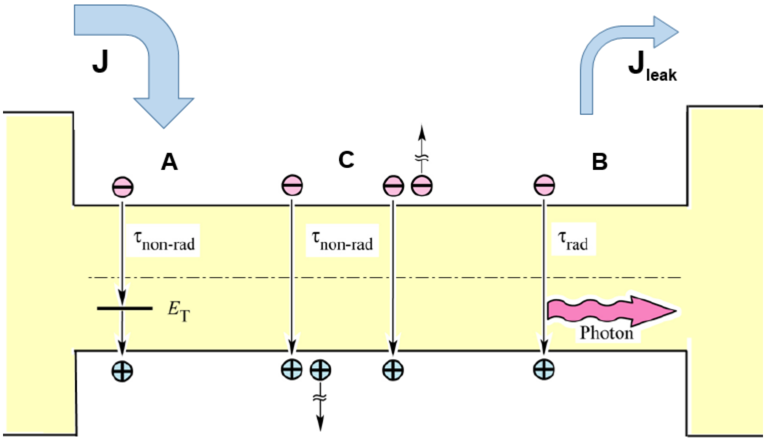

Figure 1.18: Dynamic balance of the charge within the active region of the device.

conceptually represented in Figure 1.18. For lightly-doped semiconductor, $n = p > N_A, N_D$, with negligible contribution of the Auger recombination (which is actually smaller for large-gap materials) and of the leakage current, Equation (1.41) can be rewritten as

$$\frac{J}{ql} \approx AnN_T + Bn^2 \tag{1.42}$$

In high-injection condition, where $n \approx p \gg N_A, N_D$, we have that $AnN_T \ll Bn^2$, meaning that the radiative recombination is prevailing on the non radiative recombination. Hence, equation (1.42) becomes

$$\frac{J}{ql} \approx Bn^2 \tag{1.43}$$

Since the luminous intensity L is proportional to the sole radiative recombination, $L \propto Bn^2$, Eq. (1.43) shows that in that bias condition a liner dependence of emitted OP on injected current exists.

On the other hand, in low-injection regime, the non-radiative SHR recombination processes prevail ($AnN_T \gg Bn^2$). Thus, equation (1.42) becomes

$$\frac{J}{ql} \approx AnN_T \qquad \text{meaning that} \qquad L \propto Bn^2 \approx \frac{B}{A^2}\left(\frac{J}{ql}\right)^2 \tag{1.44}$$

where a quadratic dependence of the luminous output on the injection current is highlighted. The threshold between bias regimes dominated by non-radiative and radiative recombination processes can be experimentally observed by evaluating the slope on the L-I curve plotted in log-log scale: as the saturation of the non-radiative recombination paths is reached, the slope of the L-I plot approaches the value of one. For higher current densities the L-I characteristic shows a sub-linear trend, mainly limited by the self-heating of the device (see Fig. 1.19).

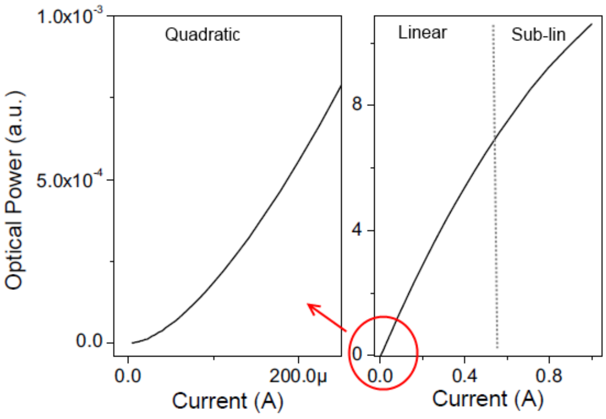

Figure 1.19: Example of an experimental L-I curve where the functional dependencies between emitted optical power and current have been highlighted.

Chapter 2

Experimental observation of TDDB-like behavior in reverse-biased green InGaN LEDs

The investigation on the impact of electrical overstress on the reliability of modern GaN LEDs begins with a comprehensive analysis of the failure mode of commercial green LEDs submitted to prolonged reverse-bias stress. In particular, the outcome of the experiments described in this chapter showed that green LEDs submitted to reverse bias *i*) show a time-dependent failure when they are submitted to constant (reverse) voltage stress, at a bias point smaller than the Breakdown Voltage (BDV); *ii*) experience an increase in the reverse-bias electro-luminescence signal, well-correlated with the increase of the reverse leakage current; *iii*) the TTF (Time-To-Failure) related to the time-dependent breakdown process has an exponential dependence on stress voltage; *iv*) the TTF is Weibull distributed. These results provide the experimental demonstration of time-dependent failure of GaN LEDs.

2.1 Introduction and motivation

Time-Dependent Dielectric Breakdown (TDDB) is a well-known statistical phenomenon that affects the reliability of dielectrics in semiconductor devices exposed to high internal electric fields. While extensive studies have proven the physical models and mechanisms involved in the breakdown of Silicon MOS devices [26], more recent observations of time-dependent breakdown in GaN-based devices have not been clarified yet. The classic dielectric breakdown model explains the failure of GaN-based devices with a dielectric, e.g. MIS HEMTs [27]; on the other hand, it does not fit with the Weibull-distributed TTF found for dielectric-free forward-biased p-GaN gate transistors [28] or for reverse-biased Schottky junctions [29].

Since such a TTF distribution is typical for a dielectric degradation-driven breakdown process, the above observations suggest that the failure is rather due to the highly-depleted GaN, which – when submitted to high voltages - may behave like a leaky dielectric.

The aim of this experimental activity is to demonstrate the existence of a time-dependent breakdown process in GaN-based LEDs submitted to reverse bias stress. The observed TTF of the devices was found to be Weibull-distributed, indicating that also in those dielectric-free structures the semiconductor, when exposed to high electric-fields, experiences a time-dependent (dielectric-like) degradation process.

This work also gives a first insight into the reliability issues that LEDs directly driven by AC in driverless lighting solutions may face during their lifetime [30]. This family of inexpensive light engines features two LEDs stripes connected in an anti-parallel configuration. Depending on the polarity of the supply voltage wave, only one of the two stripes is alternatively forward biased during each semi-period of the power line. Since the devices belonging to the reverse-biased stripe may be exposed to high levels of reverse voltage, the effects of such a bias condition need to be investigated. In particular, while it is a well known fact that reverse-bias stress may have a negative impact on the optical performance of the device and on its long-term reliability [31], the bias and time dependencies of this kind of degradation phenomenon have not been deeply analyzed, yet.

2.2 Experimental details

For the experiments described in the following paragraphs, low-power commercial green LEDs based on InGaN quantum well structures were analyzed. Three sets of samples

– referred to as A1, A2 and B - were employed. All the devices have a square GaN chip design with a $240\,\mu m - 250\,\mu m$ junction-area side, a vertical epitaxial structure with p-GaN on top and an emission wavelength in the range of $520\,nm - 530\,nm$. While groups A1 and A2 consisted of fully-packaged LED devices, samples of group B included bare semiconductor chips: as will be shown in the next paragraph, the absence of the encapsulant material let us perform more in-depth investigations on the effects of prolonged reverse-bias stress.

Electrical characterization and stress tests were performed by employing either an Agilent E5263 parameter analyzer or a Keithley 2612 source-meter. In the worst-case, the leakage-current noise floor introduced by the experimental setup was in the order of $5\,nA$: since it was only related to our constant reverse-bias stress setup, the magnitude of this unwanted current fell well-below the minimum $10\,\mu A$ LED leakage current measured during this kind of stress. Temperature control was obtained by means of a Voetsch climate chamber. Finally, an Andor EMCCD camera was used to carry out spatially and time-resolved reverse-bias electroluminescence measurements.

2.3 Failure characterization

2.3.1 Reverse-voltage stress

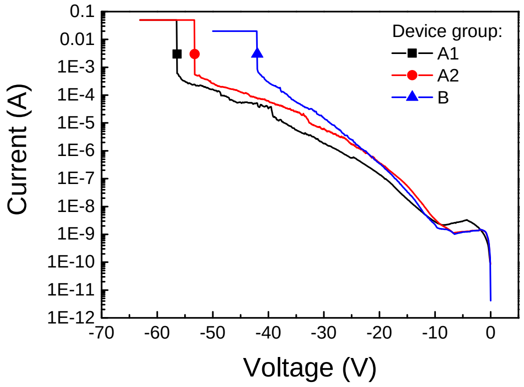

Figure 2.1: Reverse-bias I-V measurements on an untreated sample of each group. The observed breakdown voltage was in the order of $-56.4\,V$, $-53.3\,V$ and $-42\,V$ for groups A1, A2 and B, respectively.

As a preliminary characterization, we carried out an I-V measurement in reverse bias until the catastrophic failure condition, typically a short-like state, was reached (Fig. 2.1). The DC breakdown characteristics revealed a “soft” breakdown behaviour, as well as a sharp increase of the reverse leakage current once the breakdown phenomenon takes place. The inconsistency of BDVs between different device groups visible in Fig. 2.1 is probably due to the different distribution of the electric field inside the active region of devices grown with dissimilar epitaxial structures and crystalline quality.

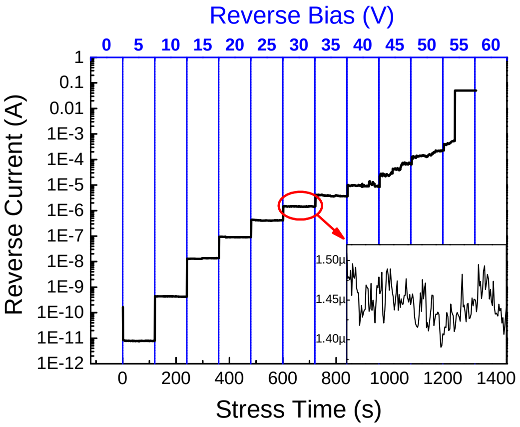

Figure 2.2: Reverse leakage current recorded during the step-stress experiment on an LED of group A1. Inset graph shows the current variation during a single bias step, whose period was set to 120 s.

Once we found the typical BDV of the samples under test, we executed a step-stress experiment aimed at finding the short-term impact of reverse-bias stress on the electrical performance of the device. The results reported in Fig. 2.2 revealed that the continuous exposure to bias levels close to the BDV induces a non-instantaneous time and bias-dependent leakage current increase, which eventually leads to the catastrophic failure of the device. Moreover, the measured leakage current was found to be quite noisy, especially for high bias levels. This is a common behavior for defect-assisted conduction, since the continuous generation/annihilation of leakage paths directly influences the magnitude of the reverse current of the light-emitting diode. In fact, recent reports indicated that for operating temperatures typically greater than 250 K, the reverse-leakage current of a GaN LED is driven either by thermally-assisted multi-step tunnelling (for low to medium bias) or by direct band-to-band tunnelling (for higher bias) [32, 33, 34, 35]. In a highly defective material, like the active region of an heavily stressed GaN LED, the first of the two phenomena may prevail [32], thus the leakage current strictly depends on the density of defects, i.e. deep-levels, involved in the tunnelling process. In GaN, leakage paths may be related to dislocations threading through the epitaxial structure [36]. Those line-defects, which depending on their structural nature may or may not be electrically or optically active [33, 37] are also known to be a preferential site for the propagation/generation of defects of lower dimensionality, like vacancies and anti-site defects. Since this phenomenon can be accelerated by temperature and current flow, while being reversible on a small scale (lattice re-absorption of point defects may also occur), a noisy current trend in moderate to high reverse bias regimes is to be expected.

2.3.2 Reverse-bias luminescence

In order to better clarify this behaviour, and to characterize the time-dependent defect-generation phenomenon observed, the reverse-bias experiments were further improved by employing spatially-resolved electro-luminesce (EL) measurements. With the formerly described EMCCD camera we have been able to acquire a reasonable EL map of the reverse-bias luminescence starting from $-15\,V$, assuming a maximum exposure time of $120\,s$. By dynamically adjusting this parameter, and normalizing the per-pixel photon count to the effective value employed, the complete time and bias dependent EL characteristic was measured.

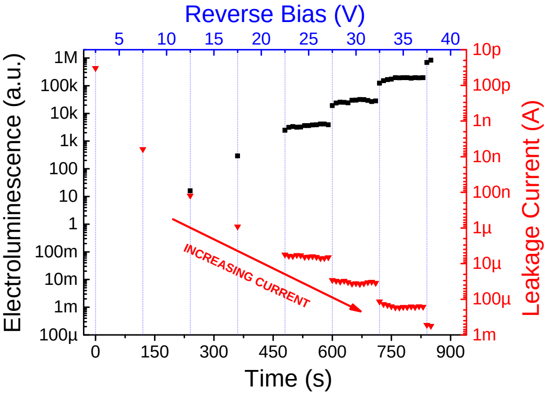

Figure 2.3: Variation of leakage-current and integrated EL signal during the step-stress on group B LED.

EL monitoring during a step-stress experiment (Fig.2.3) revealed that there is a strict correlation between the reverse-leakage current and the EL signal (Fig.2.4). This correlation is maintained either between different bias conditions and during a single stress step. Thus, despite the physical origin of the reverse-bias luminescence is still unclear, this experimental result shows that while this radiative phenomenon seems to be quite insensitive on the energy of the charged carrier(s) involved in the process, it is strictly dependent on the magnitude of the absolute current flow. Fig. 2.4 also reports the I-V measurements carried out after each stress step: for stress voltages higher than $-20\,V$, a monotonic increase of the leakage current (measured for example at $-15\,V$) is observed. This behavior further confirms the role of high internal electric fields in the generation of leakage paths [38].

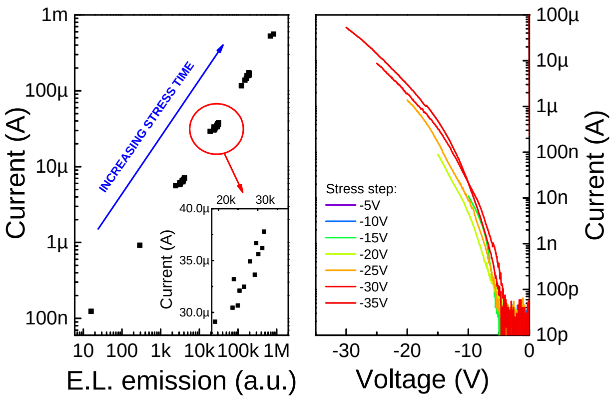

Figure 2.4: Correlation between reverse-leakage current and EL signal during the entire stress reported in Fig. 2.3 (left). I-V curves carried-out after each stress step (right). In order not to induce further degradation, a maximum reverse voltage 5 V smaller than the actual stress step bias was employed during the electrical characterization.

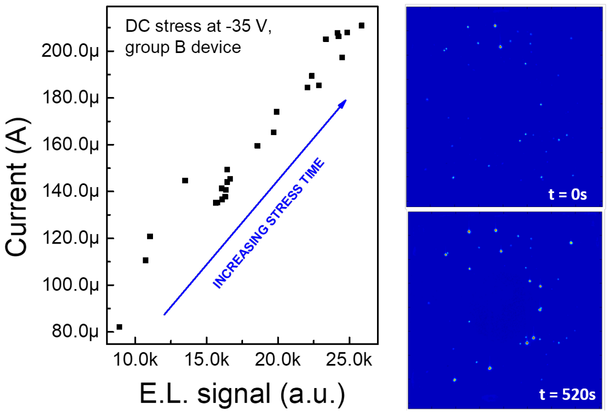

Figure 2.5: Group B device stressed at a constant bias of $-35\,V$: correlation between EL signal and leakage current. On the right, reverse-bias luminescence map acquired at the beginning of the stress and right before the device failure.

Correlation between leakage current and reverse-bias luminescence could also be clearly identified during constant reverse-bias stress (Fig. 2.5). Moreover, the evolution of the EL maps reveals that a sustained reverse polarization condition induces an increase in the number and intensity of luminescence spots, i.e, of leakage paths. Eventually, if the stress is continued for a sufficient amount of time, localized failure of the device, usually in correspondence of one of the dominant emission spots, occurs.
As can be seen in Fig. 2.6 for the previously analyzed sample of group B submitted to step-stress (Fig. 2.3 and 2.4), the failure spot visually appears as a melted surface area

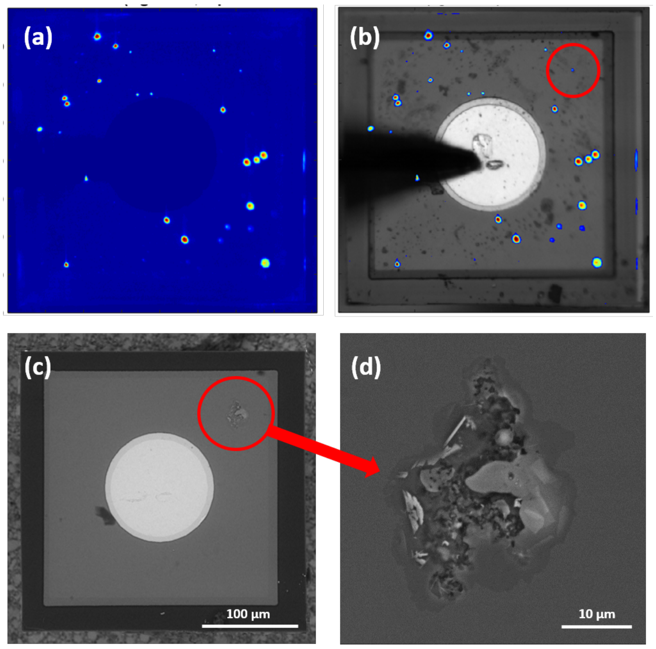

Figure 2.6: Superposition of the last emission image taken before failure (a) on the micrograph of untreated sample (b). ESEM (back-scattered electrons) image of the failed LED chip (c) with magnification of the failure spot (d).

(Fig. 2.6(d)). This outcome suggests that during the final stages of the degradation the high temperature reached due to current flow through nanometer-sized leakage paths is the main driving force of the failure process.

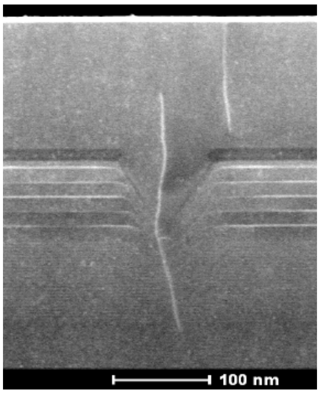

Figure 2.7: Transmission electron microscopy image of a lamella extracted in correspondence of a device region showing localized RBL signal ("hot-spots") on a stressed LED.

In devices stressed for a sufficient amount of time to increase the number and intensity of RBL spots without inducing catastrophic failure, transmission electron microscopy analysis of a region corresponding to an emission spot shows the presence of a V-pit (Fig. 2.7). While this result suggests that a correlation between certain dislocations-related defects and the RBL in GaN may exist, their origin and their role in the degradation of GaN LEDs submitted to reverse-bias need to be further investigated.

2.4 Statistical analysis

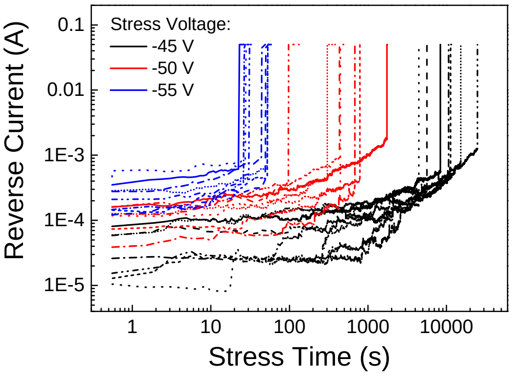

Figure 2.8: Trend over time of the leakage current of group A1 samples submitted to constant reverse-bias stress.

A set of constant voltage stress experiments was carried out in order to perform a statistical analysis of the distribution of the TTF and to look for possible correlations between the TTF and the stress condition. The results of the constant-voltage stress tests on group A1, summarized in Fig. 2.9, demonstrate that the devices under analysis show a time-dependent breakdown process, even when they are stressed below the breakdown voltage identified by DC measurements. Neither the initial or the pre-failure leakage current were found to be correlated with the recorded TTF: this behavior can be explained by considering that the magnitude of reverse current is not a suitable parameter to globally describe defect-related spot-like conduction. Indeed, as suggested in the previous paragraph, it is the density of the current flowing through localized leakage paths that mainly determines the onset of catastrophic failure of the device. Thus, leakage-current measurements cannot be effectively used to predict the lifetime of GaN LEDs submitted to reverse-bias operation. Nevertheless, it remains a good figure of merit as soon as structural lattice quality and robustness towards ESD events are concerned [39].

As can be seen from Fig. 2.9, TTF has an exponential dependence on the applied reverse bias. Given the good linearity of the mean log(TTF) to applied reverse-voltage relation, the extrapolation of the TTF at reduced stress voltages appears to be mathematically feasible. However, although this may be very important for the lifetime estimation of devices employed in driverless AC-driven LED luminaires, it may not be

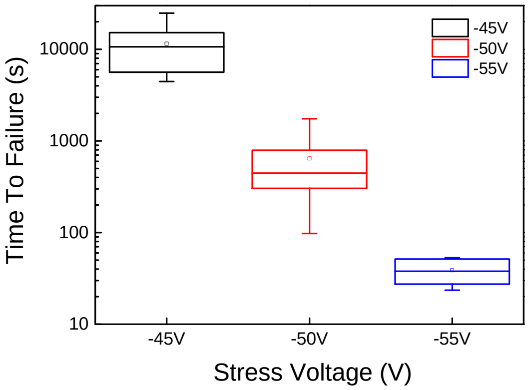

Figure 2.9: Dependence of the TTF on the stress voltage. Box graph shows minimum and maximum values (whiskers), mean (dot) and 25-75 percentiles (edges of the inner box).

a formally correct procedure since different degradation mechanisms may dominate in the low bias regime.

In addition to this bias dependence, the recorded time-to-failure was found to be Weibull distributed, with extrapolated shape factors β relative to a 99% confidence interval in the range of 0.9 – 2.34 (Fig. 2.10).

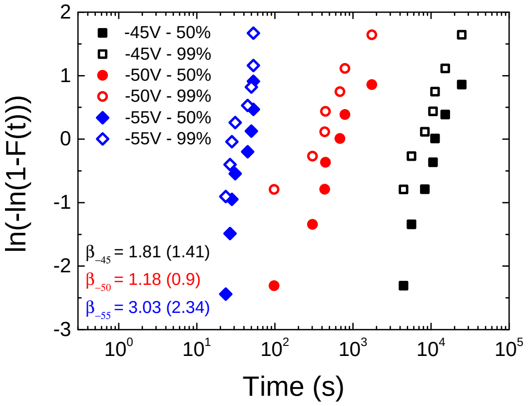

Figure 2.10: Weibull plot of the recorded TTF for group A1 samples stressed at 25 °C. The extrapolated shape parameters β relative to 50% and 99% confidence intervals, the latter within brackets, are reported in the lower left corner.

Considering the intrinsic variability of commercial devices, and considering that the failure is strictly correlated with the generation of leakage paths, this range of β values is consistent with a wear-out induced failure [40]. The same statistical analysis was performed on a different set of samples (group A2) to ensure the consistency of our experimental results: indeed, we were able to observe again a Weibull distributed TTF. This particular failure time distribution is a core characteristic predicted by the percolation model usually employed to describe the breakdown behavior of thin oxide layers submitted to high electric fields.

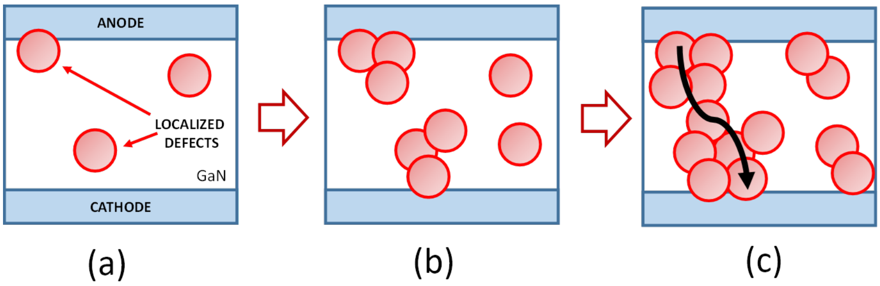

Figure 2.11: Classic percolation model: (a) initial condition, isolated defects; (b) clustering of defects; (c) creation of a percolation path.

If we adapt this model to our specific case of study, the time-dependent failure is therefore explained by considering that when the devices are exposed to high reverse bias, the GaN layer reaches a deep depletion; once depleted, it behaves as a leaky dielectric, thus showing a time-dependent failure similar to that observed in dielectrics. In particular, the defect generation process, initially aided by the electric-field, tends to increase the concentration of defects in proximity of pre-existing disordered crystal regions, mainly dislocations. Once the accumulation of defects creates a sufficient amount of deep-levels spread inside the energy-gap, a reverse leakage path is created (Fig. 2.11). Degradation of those preferential leakage spots is then progressively increased by current-flow and temperature, which eventually leads to the shortening of the device.

2.5 Conclusions

Within this chapter the behavior of green GaN-based LEDs subjected to near-breakdown reverse-bias levels was analyzed. Constant voltage stress tests revealed the presence of a time-dependent degradation phenomenon, which promotes the increase of the leakage current of the device and eventually leads to a catastrophic failure. The Weibull-like distribution of the TTF, and its exponential dependence on the stress voltage, closely resembled the statistics of a TDDB process, which suggests that highly-depleted GaN under reverse bias may behave like a partially-leaking dielectric that degrades over time due to a defect percolation process.

Chapter 3

Failure of High Power LEDs Submitted to EOS: Dependence on Device Layout and Pulse Properties

This chapter extends the analysis of the degradation processes induced on GaN LEDs by electrical overstress (EOS) events by considering the effects of short high forward-current pulses on the reliability of modern high-power LEDs. By employing a custom EOS simulator, capable of generating current pulses up to $40\,A$ with duration between $50\,\mu s$ and $5\,ms$, four different kinds of power LEDs having different layouts were characterized: horizontal structure with bonding wires, vertical structure with via-holes through the insulating substrate, and flip chip-structure with isolated vias. The results described in this chapter demonstrate that: (i) state-of-the-art LEDs rated for a maximum current of $1-1.5\,A$ can withstand EOS current levels in excess of $35\,A$, corresponding to power densities of $350\,W/mm^2$. (ii) dependently on the layout of the devices, the failure mechanisms include: fusion of the bonding wires, migration/degradation of the metal lines, failure of the insulated vias, cracking the semiconductor material. (iii) the EOS failure level strongly depends on the pulse duration and on the layout of the package/chip. The devices with flip-chip structure showed the highest robustness, while the use of bonding wires was found to severely limit the stability of the devices.

3.1 introduction and motivation

Over the last few years, the reliability of GaN-based LEDs has shown impressive improvements; thanks to the optimization of the growth, processing and packaging technology it is now possible to fabricate LEDs with expected lifetime in excess of $30-50\,kh$ [41]. In several cases [3, 42, 43], LEDs submitted to constant current stress show a gradual degradation of the optical power (OP), that can be associated to changes in the spectral properties (in the case of phosphor-converted white LEDs) and in modifications of the electrical characteristics (increase in reverse leakage, increase in series resistance) [44]. The decrease in optical power is typically ascribed to the generation of non-radiative defects within the active region [45, 46], while the changes in the spectral properties are associated to the degradation of the phosphors, of the silicone matrix and of the package material [47, 48, 49]. The gradual degradation of LEDs is typically accelerated by current (linear or superlinear dependence on current [50, 51]) and temperature (Arrhenius-like dependence) [52].

In most of the cases, the effects of gradual degradation can be reduced by optimizing the driving conditions and the thermal management at system level. For this reason, the general understanding is that LED-based lamps can be considered highly-reliable light sources. However, besides gradual degradation, in the final application the devices can show a catastrophic (sudden) failure, whenever they are exposed to extrinsic factors, such as electrostatic discharges (ESD) and electrical overstress (EOS) [53, 54]. In several cases, it is difficult to predict how and when the devices will be subject to ESD and EOS during operation; for this reason, it is of fundamental importance to study the impact of ESD/EOS on the electro-optical performance of the devices, and to understand how the robustness depends on the structure of the devices. Several papers have recently investigated the effect of ESD on the performance and reliability of LEDs [14, 15, 16]; on the other hand, to date only few papers on the effects of EOS have been published in the literature, mostly white papers and application notes from device manufacturers [55, 56, 57, 58].

The aim of experimental activity described in this chapter is to contribute to the understanding of the impact of EOS on the reliability of white light-emitting diodes for power application. This was achieved by submitting different groups of commercial HB-LEDs to a series of voltage/current pulses of increasing magnitude, until the catastrophic failure of the device was reached. The results of the investigation, reported in the following paragraphs, highlighted the various failure mechanisms that can affect LEDs submitted to this kind of electrical overstress, and the dependence of the failure current on the specific structure of the devices.

3.2 Experimental details

3.2.1 Devices under test

The analysis focused on four different kinds of commercial High-Power white LEDs, fabricated by four different industry-leading manufacturers. All the families of LEDs, which will be referred to as groups A, B, C and D, have absolute maximum current rating ranging from 1000 mA (groups B, C, D) to 1500 mA (group A), as well as the same 3535 ceramic package (3.5 mm x 3.5 mm). Three of the four families were found to differ both in terms of chip layout and current spreading structures.

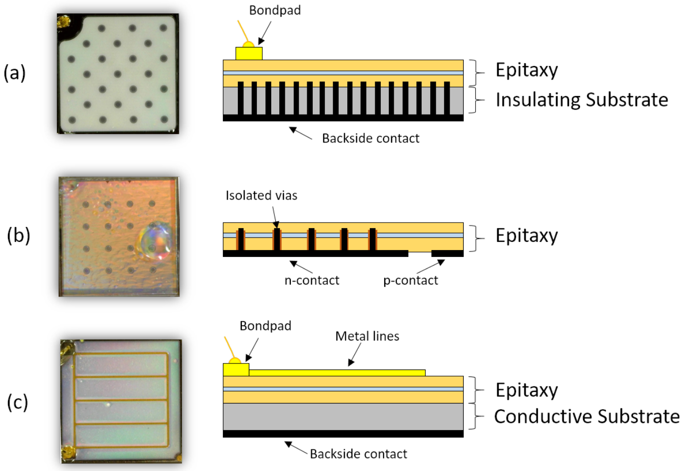

Figure 3.1: Images of the semiconductor chips of untreated LEDs after the de-processing procedure (left) and approximate drawing of the chip section (right). Devices from A, B and C+D families respectively showed a vertical structure with via-holes through insulating substrate (a), a flip-chip structure with isolated vias (b) and an horizontal structure with bonding wires and surface metallization grid (c).

The devices of group A have a vertical structure, whose top ohmic contact has been fabricated with via-holes through an insulating substrate (see Fig. 3.1 (a)). The absence of a surface metallization helps those kind of devices to increase their extraction efficiency, thus improving the current-spreading uniformity as-well. Despite no metal lines are present on the surface of the semiconductor, the devices of this group employ bonding wires in order to contact the metal pads on the upper surface of the package substrate: as we will see in the next section, this layout decreases the stability against EOS, since every metal structure is prone to undergo catastrophic failure when high currents are reached or slow events are triggered. Conversely, the LEDs of group B are characterized by the complete absence of bonding wires and metallization (Fig. 3.1 (b)). Those state-of-the-art flip-chip LEDs [59] have both electrodes on the back, from where contacts are routed to the pads through metallizations directly deposited on the top of the package. On the contrary, the last two groups of devices employ a horizontal structure where both bonding wires and current-spreading metal grid are present (Fig. 3.1 (c)).

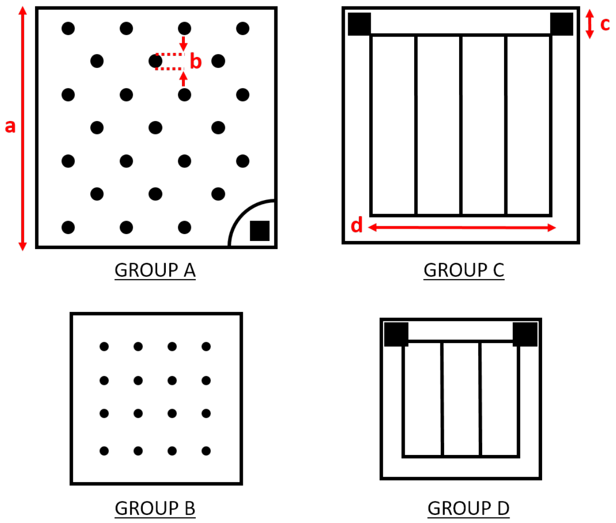

Figure 3.2: Scaled sketches of the layouts of the four different groups of devices under test. Main LED layout parameters extrapolated from optical and SEM-based imaging, including a) chip size (side length), b) via diameter, c) pad size and d) metal lines length, are reported in Table 3.1.

Group	**(a) Chip size** (μm)	**(b) Via diameter** (μm)	**(c) Pad size** (μm)	**(d) Metal length** (μm)	**Metal width** (μm)	**Approx. active area** (μm^2)
A	1405	78	117	-	-	1.57
B	993	53	-	-	-	0.96
C	1380	-	137	1070	20	1.74
D	936	-	144	675	7.5	0.95

Table 3.1: Main layout parameters, referred to Figure 3.2.

Optical and ESEM-based inspection of de-processed samples was employed in order to estimate the main layout parameters, here reported in Table 3.1 with reference to the scaled sketches of the layouts depicted in Fig. 3.2. All the DUTs shared a squared GaN chip with active areas ranging from about $1\,mm^2$ to $1.74\,mm^2$. The number of vias and the area coverage of the surface metallizations scales with the total size of the chip. The relatively high mismatch in the metal lines width observed between group C and group D samples may be detrimental for high current pulses related reliability issues, unfortunately no data regarding the height, hence the total section of the metal lines, could be obtained.

3.2.2 Experimental setup

An electrical overstress event consists of a temporary bias condition during which the maximum (electrical) ratings of the device are exceeded. Since a common waveform/pulse generator is not able to source the amount of current that a forward-biased high-power LED is able to sustain, a custom EOS simulator, based on the concept preliminary proposed by Tuttle et al. in [19], was designed.

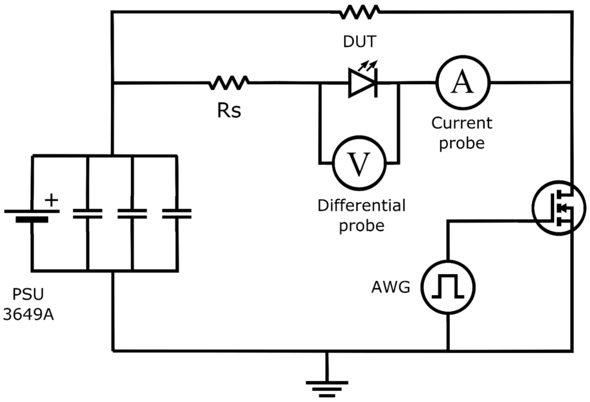

Figure 3.3: Functional electrical scheme of the custom EOS simulator employed for the testing purposes of this work.

As depicted in Fig. 3.3, the setup employs a charged capacitor to apply a duration and amplitude-variable voltage pulse to the LED under test. Voltage control is implemented by varying the charge voltage of the capacitors connected to the power supply (an Agilent 3649A): since the electrical behavior of a light-emitting diode is dominated by the series resistance, the pulse current changes almost linearly with the applied voltage. Moreover, this current has a strong dependence on the effective series resistance of the discharge branch of the circuit: given the limited supply voltage and the need to generate EOS events with (relatively) small current steps, this observation let us obtain the desired range of stress conditions just by adding and trimming a power resistance, named R_S in Fig. 3.3, in series to the DUT. The EOS event was triggered by turning on the nMOS placed in series to discharge circuit. An arbitrary waveform generator was used to drive the solid-state switch, which let us obtain pulse widths ranging from $50\,\mu s$ to $5\,ms$. While the lower bound was set by the transient response of the overall circuit, the maximum pulse duration was limited by the discharge time constant of the overall

RC circuit. Nevertheless, the maximum attainable pulse width is well representative of the most common EOS-induced LED failures in field conditions. Inrush current, for instance, which is the over-current event that may occur when the LED driver is switched on, can be as high as three times the steady-state (set-point) value, and last several milliseconds, if a proper soft-start algorithm is not implemented by the driver manufacturer [21].

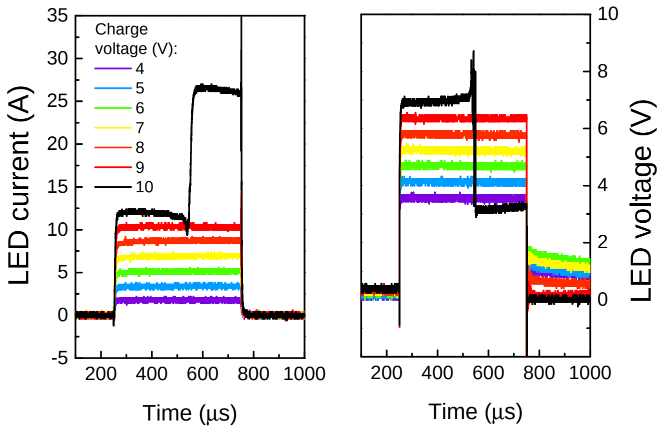

Figure 3.4: Examples of LED current and voltage waveforms acquired during subsequent EOS events applied to the same device. Failure occurred for a pulse power of around 110 W, and induced a sudden decrease of the LED equivalent series resistance. The visible positive current spikes are probably originated from the recirculating current in the upper loop of the circuit at the beginning of the off-phase, whereas negative voltage undershoots are generated from a capacitive coupling phenomenon related to the large power n-MOS employed for our experimental purposes.

The waveform generator was synced wih a Tektronix TDS5052B oscilloscope, equipped with a current probe and a differential high-bandwidth voltage probe, in order to be able to record the complete evolution of voltage and current during the stress pulse (Fig. 3.4): since non-completely matched transmission lines have been employed, partial waveforms distortion has been experienced. Pulsed I-V characteristics have then been extrapolated by averaging the acquired waveforms within the 45% - 55% pulse interval: as previously mentioned, for very high forward bias the pulsed I-V characteristic is essentially linear (see Fig. 3.5). After each pulse, the current-voltage characteristics were measured by means of a source-meter, in order to quantitatively describe the impact of EOS events on the electrical performance of the devices. In order not to interfere with the discharge circuit and to perform a correct measurement of the DUT, its electrical connection to the source-meter was interrupted after every pulse by means of a relay (not shown in the Figure 3.3). The connection was then automatically re-established after carrying out the I-V curve.

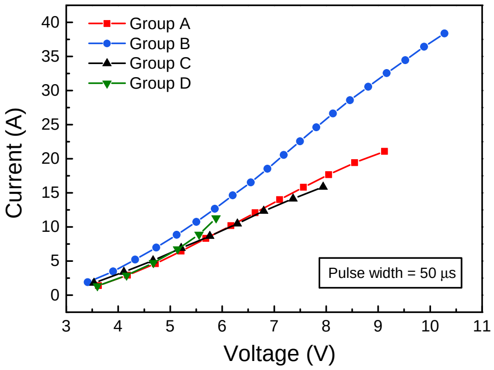

Figure 3.5: Examples of pulsed I-V curves extrapolated from the 45% to 55% averaging of the current and voltage waveforms acquired during subsequent 50 μs pulses.

3.2.3 Methodology

The formerly described experimental setup was employed to perform two different sets of measurements. Firstly, a statistical analysis on the failure conditions was carried out. This first activity was targeted at finding how the magnitude and duration of the simulated EOS events affect the failure of the device, and whether there is correlation among equally-stressed samples of the same group or not. Once we could verify how a specific overstress condition affects the reliability of the device, i.e. the maximum duration and magnitude of the pulse sustainable by a specific group of devices, a more in-depth investigation on the failure mechanisms was started. To this aim, microscope-based visual inspection on de-processed samples was employed: as explained in the next section, the de-processing of the semiconductor chip (and surrounding structures) let us identify the specific weaknesses of each LED group and chip topology towards EOS events. In the end, the same damaged structures were analyzed through an ESEM (Environmental Scanning-Electron Microscope), which provided further proofs about the physical processes responsible for the failure of the devices.

3.3 Experimental results

Each device under test was submitted to a series of voltage pulses of increasing amplitude, until the catastrophic failure condition was reached. The starting line voltage (i.e. capacitor charge voltage) was set at $4\,V$, which on average led to a starting pulse current in the order of $1-2\,A$, depending of the specific equivalent “on-state” series resistance of the device under test. Several failure mechanisms were identified, which were found to be heavily dependent on both the duration of the EOS event and the structure of the LEDs.

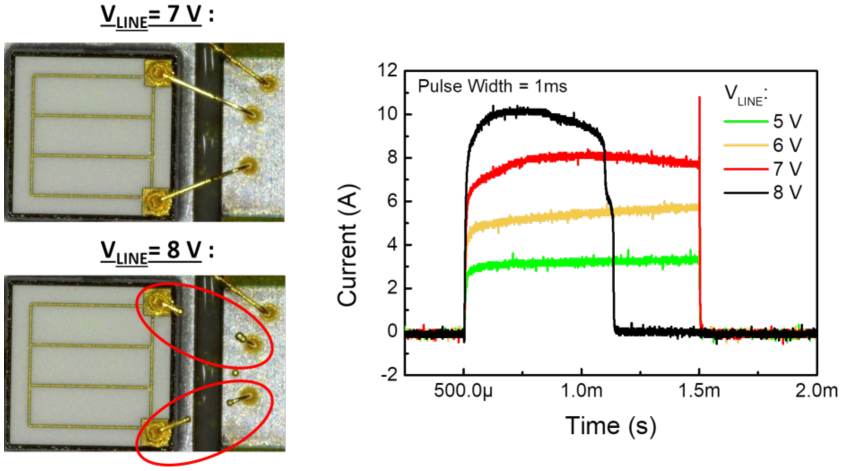

Figure 3.6: Effect of low-amplitude long ($1\,ms$) EOS events on group D LEDs. Prolonged high power dissipation causes the fusion of the bonding wires, as well as the partial melting of the bonding pads.

As shown in Figure 3.6, the most common failure mechanism for relatively long ($\geq 1\,ms$) pulses at medium to high currents ($> 3 - 7\,A$) was the fusion of the bonding wires. The open circuit-like failure can be clearly recognized as a sudden drop in the discharge current of the waveforms acquired during the EOS simulation, here reported in Fig. 3.6 for a sample of group D submitted to $1\,ms$ pulses. The figure also reports the micrographs of the LEDs before and after the EOS event that led to the failure. It is worth noticing that also group A LEDs, that employ bonding wires in combination with a via-based structure, experienced the same kind of failure when submitted to equivalent stress conditions. Since the failure happened for the same magnitude of current pulse (3 to $7\,A$ for a $1 - 5\,ms$ long pulse), we can state that for longer EOS events the main weakness of the devices under test lies in the power handling capability of the gold-made bonding wires. Higher tolerance towards that class of EOS can be attained by increasing the section of the wires (and thus the related shadowing effect).

A second degradation mechanism, which affects the metal-lines used for current spreading, was identified by submitting the devices to EOS pulses with short duration ($50 - 300\,\mu s$). More specifically, for sub $300\,\mu s$ pulse periods the experiment revealed that the main elements to be affected by the over-stress event are surface metal lines and bonding pads, as depicted in Fig. 3.7. The I-V curves reported, together with the sequence of optical images of the sample taken after every pulse, provided a hint on the physical origin of failure. The images show a partial degradation of the metal lines near the bonding pads after the $\mathrm{V_{LINE}}$=12 V pulse. The reduced current spreading capability of the device probably triggered a current crowding phenomenon under the

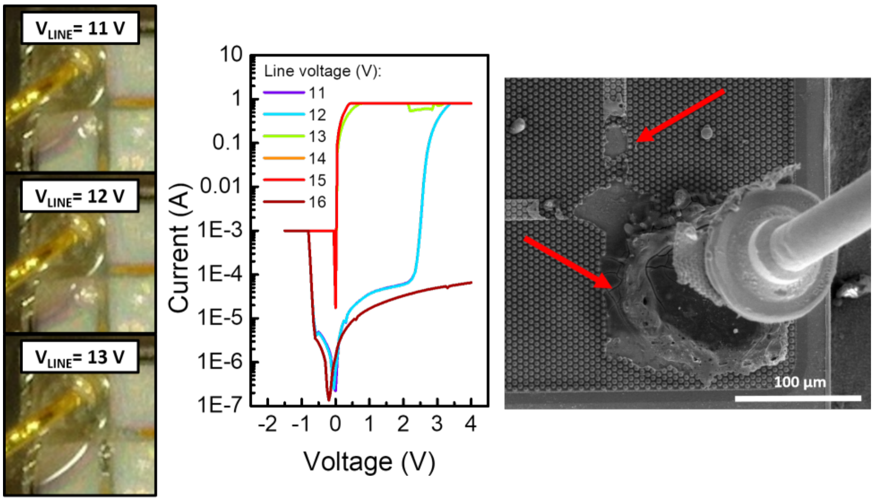

Figure 3.7: Group C device submitted to $50\,\mu s$ pulses. From left to right: detailed view of the bonding pad and the surface metallizations; evolution of the I-V characteristic; ESEM image of the failures of metal grid and bonding pad. .

bonding pad, which caused the shortening of the device during the $\mathrm{V_{LINE}}$ =13 V pulse. This short-like state was then maintained until the $\mathrm{V_{LINE}}$ =16 V pulse, which caused the total detachment of the boding pad from the semiconductor surface, leading the device to the high impedance condition testified by the I-V curves and the ESEM image in Fig. 3.7.

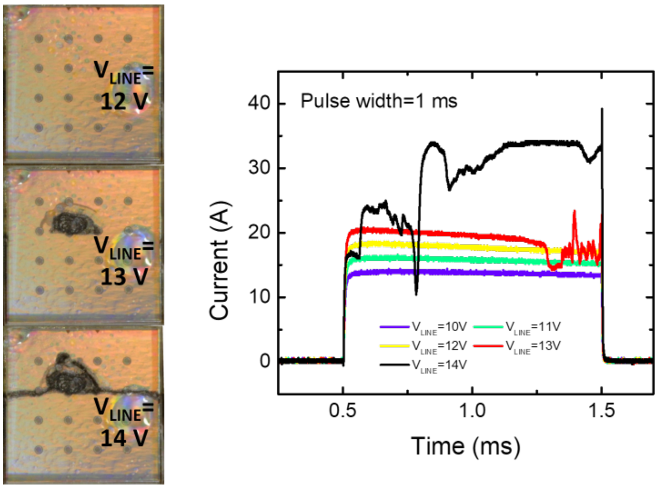

Figure 3.8: Effects of $1\,ms$ repeated EOS pulses on a flip-chip LED of group B. High-power dissipation, and currents in excess of $20\,A/mm^2$, produced a localized failure near a central via. The liquid drop visible on the right side of the semiconductor chip is a leftover of the de-polymerizing agent employed to remove the encapsulant material.

So far only bonding and metallization-related issues have been analyzed. However, the analyses carried out on group B LEDs, whose flip-chip structure and package are free from any kind of metal-based current distribution lines (see type (b) in Fig. 3.1), permitted to identify further degradation mechanisms. In particular, long ($\geq$ 1ms) EOS pulses revealed that devices of this kind are able to withstand currents and power dissipation levels more than double with respect to the other groups of devices. As reported in Fig. 3.8, the failure is now localized in proximity of a central via, whose thermally induced degradation first causes the shortening of the devices, and then, as the overstress is carried on, the cracking of the semiconductor chip itself. Even in this scenario, it is an extrinsic structure that undergoes failure rather than the semiconductor itself.

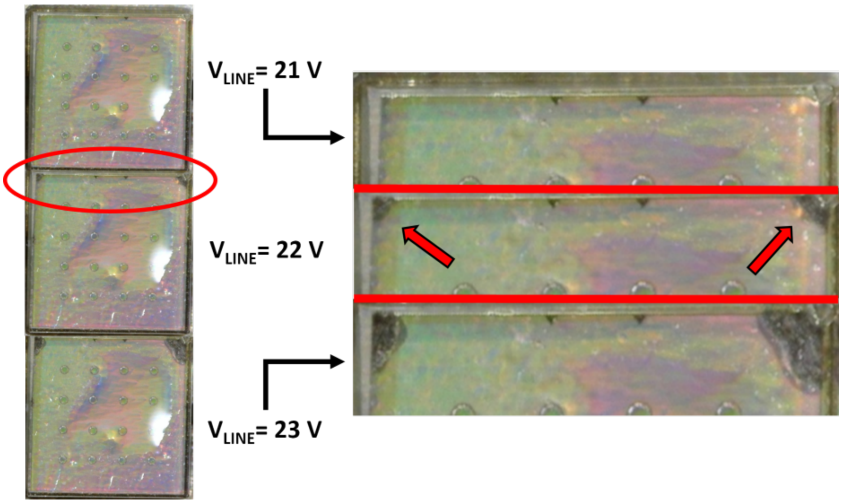

Figure 3.9: Effect of high-energy (high-power, short width) pulses on the semiconductor chip of group B LEDs. The liquid drop visible on the center of the device is a leftover of the de-polymerizing agent employed to remove the encapsulant material.

The outcome of the experiments performed on group B samples changes when shorter pulses are employed. As we can see from Figure 3.9, which shows the damage caused by 350 W and 50 μs long pulses on the aforementioned LEDs, the EOS was found to induce degradation of the upper edges of the semiconductor chip. Since this phenomenon was observed only for very high current and voltage levels ($\approx$ 37 A and 10 V for V_{LINE} = 22 V), and since it was limited to the corners of the device, we may assume that this specific failure process was driven by the strong electric field located near those spots. Nonetheless, chip corners are also a preferential site for surface leakage current conduction. So, despite the passivation and the electrical isolation of the edges, also the progressive increase of current density through the surface may have led the device to the short-circuit condition.

High DUT voltages, like the ones reached in this last particular experiment, may be detrimental for a correct interpretation of the failure data, since such bias levels can trigger the ESD protection structures embedded in the LED package. While the maximum forward voltage reached by our samples ($\approx 10\,V$) should not carry typical protection devices into breakdown state, the aim of this work is to test the robustness against EOS events of the whole LED system, including the integrated ESD protection structures: for this reason, the results provided are well representative of the robustness of state-of-the-art commercial LEDs.

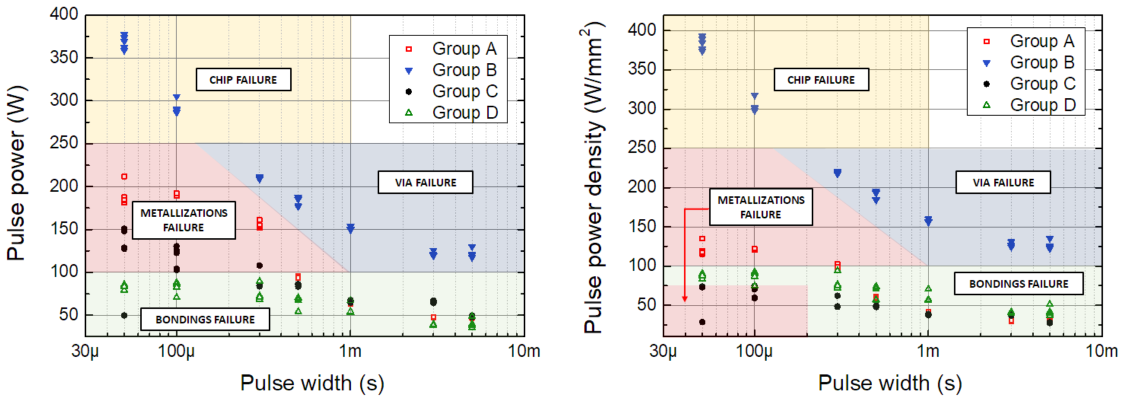

(a) (b)

Figure 3.10: Pulse power-to-failure (a) and pulse power density-to-failure (b) in function of the pulse width measured for all the 140 samples put-through the EOS simulation experiment.

All the above observations are summarized in the graph of Fig. 3.10a, which shows the failure condition for each of the 140 stressed devices (5 samples for 7 different pulse widths were analyzed from the four families of LEDs under test). The EOS robustness of devices without metal lines (group B) is higher for every pulse duration, with current handling capabilities for 5 ms pulses more than doubled with respect to the other families of devices. The devices of groups A, C and D not only suffer from the same bonding wires melting-related issue, but they also share the same pulse power-to-fail trend. For shorter pulses group A increases its EOS handling capability, probably thanks to the absence of the surface current spreading metallization grid, which proved to be another source of potential failure for LEDs.

It is also worth noticing that families sharing the same package/device layout (groups C and D) have different behaviors towards EOS events of the same duration, with the devices of group D performing noticeably worse than all the other DUTs. This may suggest that even the epitaxy or the geometry of the current distribution system has a consistent impact when electrical overstress is concerned. By looking at the power density-to-failure trend reported in Figure 3.10b, we can see a reduction in the spread of the failure threshold for shorter pulse widths between devices of groups A, C and D. In particular, since only group A and C LEDs share the same failure mode for short EOS events, i.e. metallization or bonding pad degradation, this behavior may indicate that the robustness of those structures is probably limited by the power (or current) density handling capability of the ohmic contacts or of the metal-lines employed in modern GaN-based HB-LEDs.

3.4 Conclusions

In summary, within this chapter the robustness of state-of-the-art high-power LEDs towards EOS events was investigated. A custom-made EOS simulator was used to generate $50\,\mu s$ to $5\,ms$ long pulses, with magnitudes in excess of $350\,W - 35\,A$ for the shorter ones. More than 140 different samples from four different manufactures were submitted to EOS of increasing magnitude, until the failure condition was reached. The good statistics of the pulse current/power-to-fail revealed a clear dependence of the EOS handling capability of the devices on their specific structures and on the duration of the overstress event. Flip-chip LEDs without metal lines showed the best robustness among the devices under test; this is the best choice whenever a high level of immunity towards electrically critical environment is required. The remaining three groups of LEDs, which shared common elements like bonding wires or current-spreading contact grids, faced similar failure modes, both for long and for short pulse widths (fusion of the bonding wires, melting of the bonding pads, degradation of the surface metallization lines).

The registered behavior of the tested samples showed that EOS-related reliability issues tend to arise more from extrinsic elements of the LED system rather than from the GaN chip, which was found to be capable of withstanding for brief periods power densities in excess of $350\,W/mm^2$.

Chapter 4

Catastrophic failure of high-power blue GaN LEDs submitted to high temperature and current stress

This chapter reports an extensive analysis of the short-term effects of high driving current and self-heating on the performance and reliability of commercial high-power blue LEDs. To this aim, five different groups of devices, having different structures and chip areas, were submitted to increasing levels of bias current, until catastrophic failure was reached. The experimental results showed that device failure usually occurred in correspondence of a major current injection point, as a consequence of the localized power dissipation and temperature reached due to extreme current crowding effects and to the degradation of the conductivity of extended device regions.

4.1 Introduction and motivation

With the increasing demand for high power and efficient optical sources by the general lighting market, novel generations of High-Brightness GaN Light-Emitting Diodes (HB-LEDs) have been introduced. The improvements in the growth techniques and the years of reliability-oriented scientific research led to the development of devices capable of withstanding junction-temperatures in excess of 150 °C and current densities of more than $1.5\,A/mm^2$. Since high current operation is desirable to drive down the cost of LED luminaires while maintaining high the luminous output, the effects of extreme operating conditions on the reliability of modern HB solid-state sources needs to be evaluated.

The aim of the work described in this chapter is to analyze the physical limits of modern high-power LEDs when submitted to excessive temperature and driving current levels, and to study the dependence on device structure and layout of the failure modes. By means of a series of current step-stresses performed on different device structures and with varying ambient temperature, both the limiting factors and the LED performances under high driving current levels were explored. This chapter is outlined as follows: after a brief description of the employed experimental setup and of the results of the thermal characterization of the samples, the outcomes of the current step-stress at 25 °C will be reported. Attention will then be focused on the analysis of the failed devices, carried out by means of optical and electron microscopy. After that, the changes induced by short-term high-current stress on the emission pattern of the LED chip will be thoroughly examined and correlated with the observed degradation kinetics and failure modes. Finally, the role of temperature in the degradation process will be evaluated.

4.2 Experimental details

GROUP	**Device Area** (mm^2)	**LED Structure**	**SOA** (°C)
A1	1.76	Flip-chip (25x vias)	150
A2	0.88	Flip-chip (16x vias)	135
B1	0.89	Horizontal structure (single metal line)	135
B2	0.89	Horizontal structure (single metal line)	150
C	0.82	Horizontal structure (metal grid)	150

Table 4.1: Relevant properties of the five different groups of devices under analysis. Group A LEDs differ in term of total device area and vias number. Group B LEDs share the same semiconductor die while differing in packaging.

Five different groups of state-of-the-art commercially-available High-Brightness (HB) LEDs were analyzed for this experimental activity. All the Devices Under Test (DUTs) have a nominal emission wavelength of around 455 nm (at T_j=25 °C) and are rated for a maximum DC current of 1 A. The devices differ in terms of device area, chip structure, metallization geometry/vias number and packaging (see Table 4.1). In particular, group A devices exhibit a flip-chip structure with isolated vias, whereas group B and group C LEDs employ a conventional horizontal structure with bonding wires and surface metallizations. For our experimental purposes, the devices were soldered to Metal-Core PCB substrates, which were attached to a TEC-controlled copper baseplate. This assembly was then put inside a 65" wide integrating sphere (model LMS-650 from LabSphere), where the LEDs were submitted to the stress procedure and to periodic electrical (I-V) and optical (absolute irradiance) characterizations.

4.3 Results of current step-stress

In order to estimate the junction temperature of the devices during stress, a preliminary thermal characterization was carried out by means of the forward voltage method proposed by Xi and Schubert in [60]. As expected, devices employing a more advanced ceramic substrate, with larger footprint and a dedicated thermal pad (A1, B1 and C) exhibited a lower thermal resistance (R_{th}) with respect to smaller-sized LEDs lacking a proper thermal pad (A2) or to devices featuring a less thermally-conducting plastic package (B2) (Fig. 4.1).

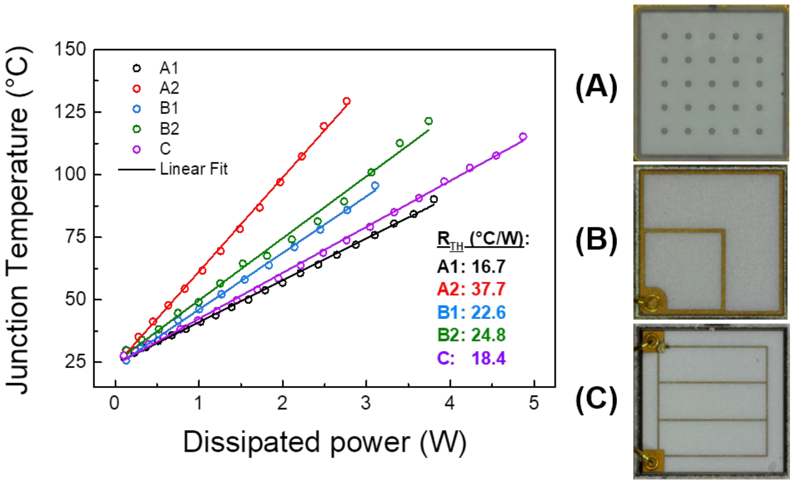

Figure 4.1: Typical thermal resistance (junction to cold-plate) plot for the five different groups of devices under test. On the right, detailed view of the three different chip layouts.

With the aim of evaluating the short-term impact of high driving current and high temperature on the reliability of HB-LEDs, a current step-stress was performed on different devices of each group. With a fixed baseplate temperature ranging from 25 °C to 125 °C, the LEDs were submitted to 120 s long stress steps. The in-situ stressing procedure let us constantly monitor the optical parameters of the devices (absolute irradiance spectrum), the forward voltage and thermals, as reported in Fig. 4.2 for a group A1 sample.

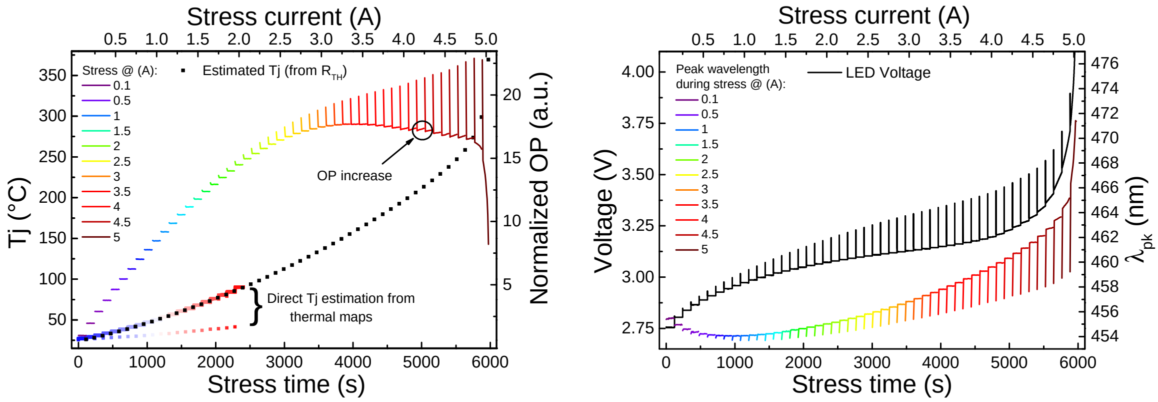

(a) (b)

Figure 4.2: Detailed evolution of (a) junction temperature and optical power, (b) LED voltage and peak emission wavelength of group A1 device submitted to a current step-stress experiment at $T_{AMB} = 25\,°C$. OP is normalized to the total LED emission measured at the beginning of the first stress step ($I_{BIAS} = 100\,mA$).

The slight decrease in the emission wavelength observed up to bias levels of $1\,A$ is ascribed to the QWs band-filling phenomenon and to the screening of the Quantum-Confined Stark Effect (QCSE) by injected carriers [61]. Above this current threshold, the emission wavelength starts to increase due to the increased self-heating of the device. This is testified by the simultaneous drop in the LED voltage, OP and by the emission wavelength increase measured after the beginning of each step. With regard to the trend of the optical power, all the DUTs stressed at a baseplate temperature of 25 °C experienced a characteristic behavior. Above a specific injection current level, around $2.75\,A$ for the group A1 sample analyzed in Fig. 4.2, the slope of the L-I curve extrapolated from the first measurement of each stress step decreases, revealing a noticeable drop in the LED efficiency. This behavior can be explained by considering the concurrent action of two physical processes: a) at high injection currents, fewer empty carrier states are available inside the QWs due to band filling. Therefore, the number of carrier escaping from inside the QWs prior to recombination increases due to the reduced effective barrier height. b) At higher stress current levels a stronger non-radiative recombination is present, due to the enhanced Shockley-Read-Hall (SRH) recombination, and this reduces the quantum efficiency of the devices. At very high driving currents and junction temperatures, above $3.75\,A$ and $T_j = 150\,°C$ for the group A1 sample in Fig. 4.2, a noticeable increase in the operating voltage, due to degradation of the LED series resistance, occurs during each constant bias stress step. This phenomenon may originate from the increase in the resistivity of the ohmic contacts or of the (p-type) semiconductor areas subjected to extreme current crowding levels. A localized increase in current density lowers the LED emission efficiency, by locally increasing the device temperature and thus the resistivity of the semiconductor, increasing even more the current-crowding effect and the degradation rate. Once a specific power dissipation level is reached, the degradation process/self-heating of the device enters a positive feedback loop, that ultimately leads to the catastrophic failure of the LED.

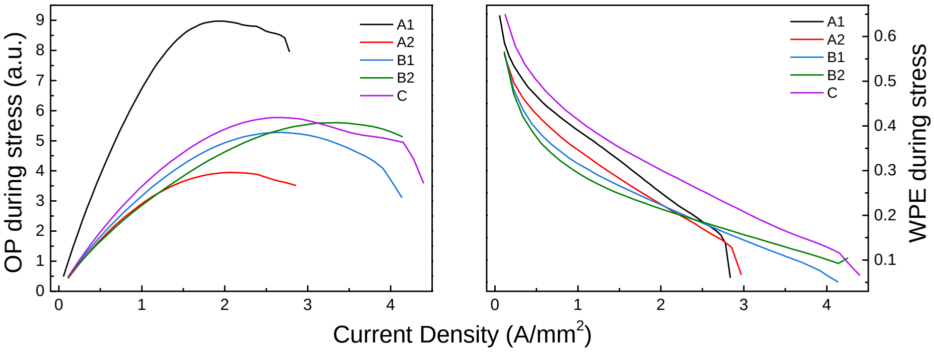

Figure 4.3: Optical power (left) and Wall-Plug Efficiency (right) in function of the current density registered during the current step-stress for one sample of each group.

In figure 4.3 the trends of the optical power and of the Wall-Plug Efficiency (WPE) in function of the current density of the five different groups of LEDs are compared. As expected, the highest optical emission is reached by group A1 LEDs, which features an active area doubled with respect to the other devices. On the other hand, group A2 LED shows the worst OP, probably due to the poor thermal performances of the smaller sized package, lacking a proper thermal pad, employed by those devices. Interestingly, both group A flip-chip LEDs experienced catastrophic failure around $3\,A/mm^2$, which probably suggests that a critical current density exists for this specific device structure. With regard to the trend of the wall-plug efficiency during stress, the horizontal structure devices of group C show significant advantage over the entire range of current (densities) scanned by this experiment, despite group A1 devices employ a more optically-advanced advanced flip-chip structure and feature an extended ceramic package.

4.4 Failure analysis

The specific failure modes of the DUTs have been analyzed by means of optical and electron microscopy. Samples of groups A1 and A2, Fig. 4.4 and 4.5, which share the same chip structure but differ in device areas and packaging, were both found to be affected by strong degradation of (i) the semiconductor material near the upper chip

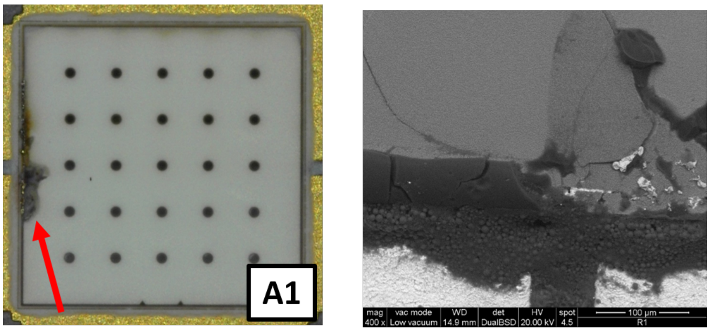

Figure 4.4: Optical inspection and ESEM back-scattered electrons analysis of group A1 de-packaged device failed during current step-stress. Red markings indicate the degraded parts of the device analyzed with high-resolution electron microscopy.

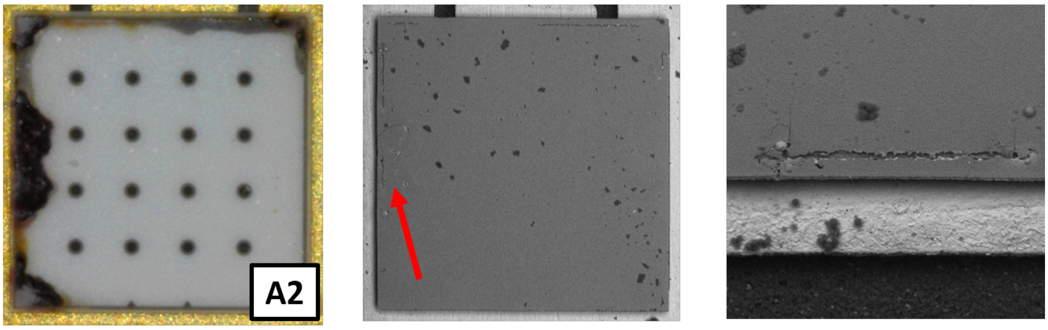

Figure 4.5: Optical inspection and ESEM back-scattered electrons analysis of group A2 de-packaged device failed during current step-stress. Red markings indicate the degraded parts of the device analyzed with high-resolution electron microscopy.

edge, testified by the localized darkening of the surface, (*ii*) of the insulated vias, which visually appear darker in the aged device, (*ii*) and of the vertical conduction paths along the mesa border, whose melting ultimately led to the shorting and to the catastrophic failure of the light-emitting diode. ESEM imaging revealed that cracking of semiconductor chip occurred in correspondence of the highly degraded upper and left chip sides. In particular, with respected to a non critically-damaged device area, EDX analysis showed the presence of conglomerates with very-high content of Si or Au near the failure point marked in Fig. 4.4, meaning that the strong localized power dissipation induced melting and migration of both the semiconductor passivating layer and of the metal lines underneath the semiconductor chip.

With regard to the other sets of LEDs under analysis, optical inspection revealed that both group B2 and group C devices experienced a severe deterioration of the metallization near the bonding bad, possibly due to the high temperature and the high current densities reached in proximity of the main carrier injection point. In particular, group B2 devices experienced fusion of the surface metal line, which led to the

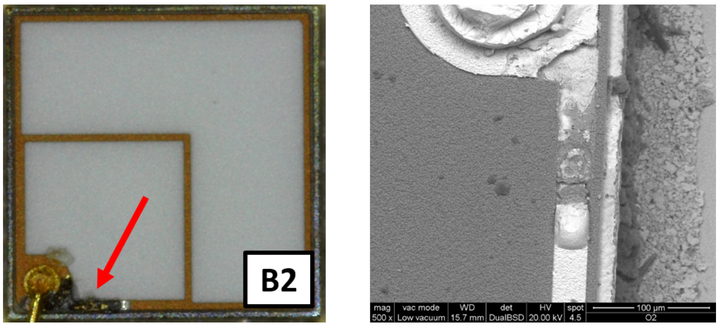

Figure 4.6: Optical inspection and ESEM back-scattered electrons analysis of group B2 de-packaged device failed during current step-stress. Red markings indicate the degraded parts of the device analyzed with high resolution electron microscopy.

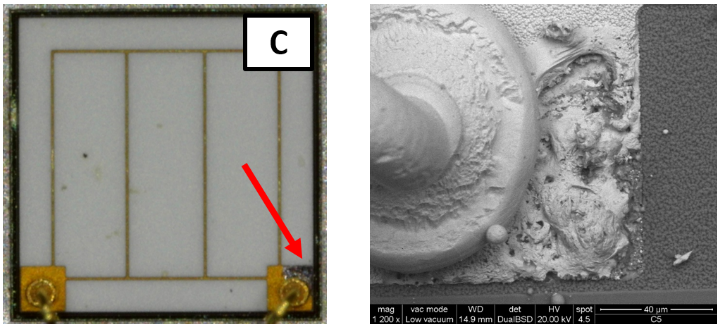

Figure 4.7: Optical inspection and ESEM back-scattered electrons analysis of group C de-packaged devices failed during current step-stress. Red markings indicate the degraded parts of the device analyzed with high resolution electron microscopy.

exposure of the epitaxial layers underneath forming the ohmic contact and the current spreading layer, as testified by the presence on Ni an Ti in the EDX spectra measured in correspondence of the area previously covered by the gold line. For group C devices, on the other hand, the failure is localized in the bonding pad area, as testified by the optical and ESEM images reported in Figure 4.7 and highlighting the melting of the surface metal layer.

Interestingly, group B1 devices failed due to fusion of the bonding wire (Fig. 4.8), whereas devices of group B2, apparently sharing the same kind of semiconductor die and of bonding wires, failed around the same current injection level of $3.7\,A$ due to degradation of the metal lines. This behavior indicates that also the thermal management properties of the encapsulant material, as well as of the rest of the LED package, may limit the expected lifetime of HB-LEDs submitted to sustained high temperature and high current operating conditions.

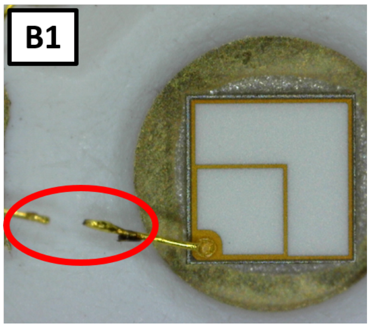

Figure 4.8: Optical inspection of group B1 de-packaged device failed during current step-stress.

4.5 Spatially-resolved EL analysis

Flip-chip LEDs

In order to investigate the dynamics of the failure mechanism, spatially resolved EL imaging was performed during current step-stress. Figure 4.9 shows the normalized EL maps acquired during each stress step on a group A1 sample, whose lens/encapsulating material was removed in order to gain optical access to the (planar) chip surface. The reported evolution of the emission pattern of the device under increasing bias highlights the progressive crowding of the electro-luminescence, and thus of the current, around the electrically-conductive edges of the device and in correspondence of the vias. For bias currents higher than 3.6 A, the relative EL signal around the upper three rows of vias starts increasing, probably due to a temperature-enhanced crowding effect close to the anode pad, which is located exactly underneath the upper portion of the LED chip. Around 4.6 A the crowding process is inverted, and the average EL emission moves towards the lower part of the LED, as testified by the trend during stress time of the upper-to-lower LED chip emission reported in Figure 4.10. For stress currents higher than 4.8 A, the darkening of the chip edges and of the areas surrounding the vias that previously affected the upper portion of the light-emitting diode starts to impact on the emission pattern at the lower side as well. Finally, at 4.9 A the high driving current and the extremely-high temperatures reached by the device induce an extreme localization of the optical emission (frame (h)) and the rapid short-like failure of the LED.

In order to discriminate between the permanent effects of the ongoing degradation process from temporary worsening of the emission characteristics of the device due to the high current densities and operating temperatures, EL mapping at a (moderate) fixed bias current of 1 A was performed after each stress step (Fig. 4.11). The EL maps

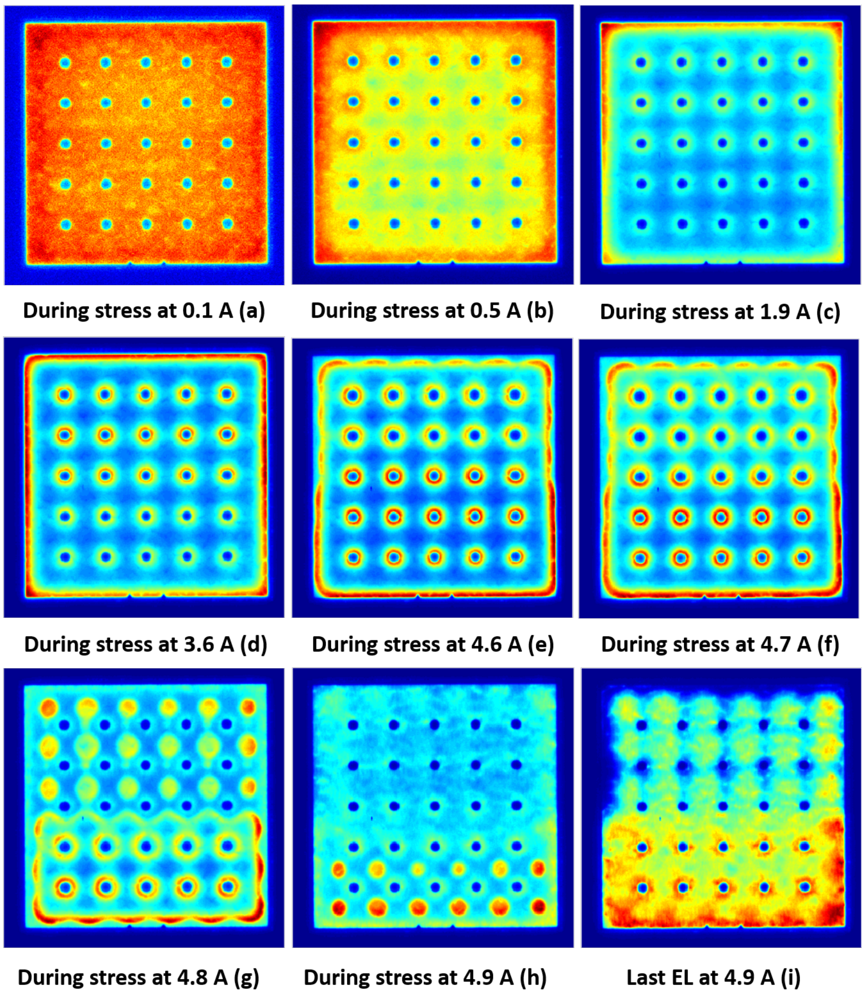

Figure 4.9: Spatially-resolved Electro-Luminescence images taken during the step-stress experiment on a group A1 sample ($T_{AMB} = 25\,°C$). The EL maps are normalized to the respective maxima in order to highlight the stress-induced changes in the emission pattern of the device.

reveal that up to a stress current of $1.9\,A$, the LED emission pattern remains stable, showing the expected current crowding effect around the vias and the vertically conducting mesa edges. Then, after the stress step at $4.3\,A$, the emission crowding starts to increase around the upper three rows of vias (closer to the anode), while decreasing near the upper edges of the device. This effect is correlated with the increase in the LED series resistance. Severe degradation of the vias and/or of the surrounding p-type semiconductor material occurs after $120\,s$ of stress at $4.6\,A$. As a consequence of the reduced current spreading capability of the upper part of the device, injected carrier become more prone to reach the lower region. The reduction in the effective injection area, in conjunction with the increase in the stress current and device temperature, accelerated the degradation of the lower vias and/or the surrounding material,

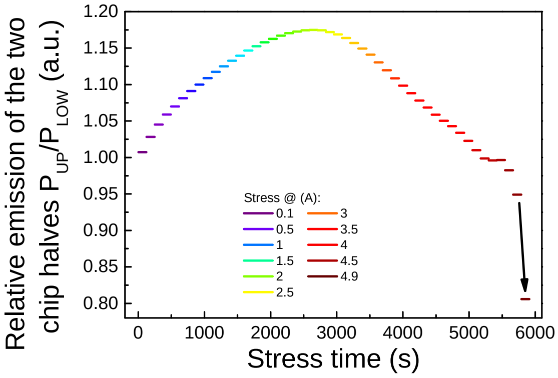

Figure 4.10: Trend during stress time of the upper-to-lower LED chip emission for a group A1 sample submitted to current step-stress (T_{AMB} = 25 °C).

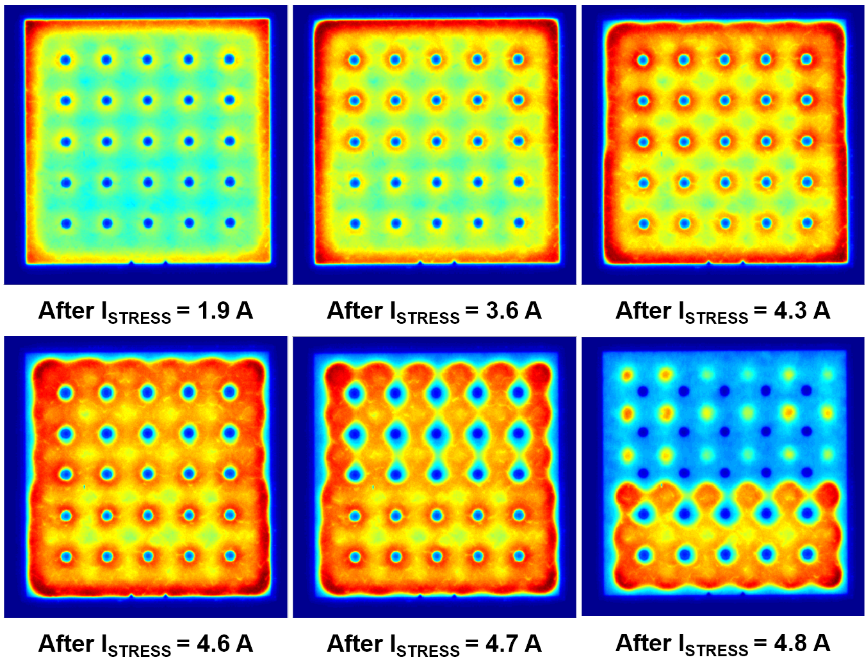

Figure 4.11: Spatially-resolved Electro-Luminescence imaging of the reference EL-I measurement taken at $I_{BIAS} = 1\,A$ after every stress cycle on a group A1 sample (T_{AMB} = 25 °C). The EL maps are normalized to the respective maxima in order to highlight the stress-induced changes in the emission pattern of the device.

as previously observed for the upper three rows of vias. Finally, due to the highly degraded conductivity of the entire semiconductor chip, current injected from the anode pad starts to flow almost entirely through the lower resistance path offered by the conducting mesa edges. At this point, the vertical conducting paths on the left side of the device melted, due to the high localized dissipated power (see first frame in Fig. 4.4); this led to the shorting and catastrophic failure of the light-emitting diode.

Horizontal structure LEDs

The effects of short-term high-current stress on the EL pattern were also evaluated for the horizontal structure LEDs of group C.

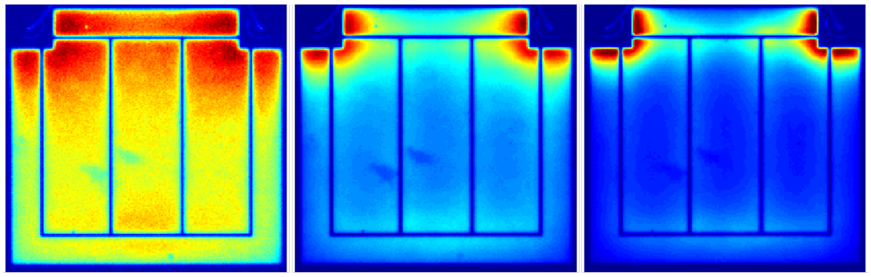

During stress at 0.1 A (a) During stress at 1 A (b) During stress at 2 A (c)

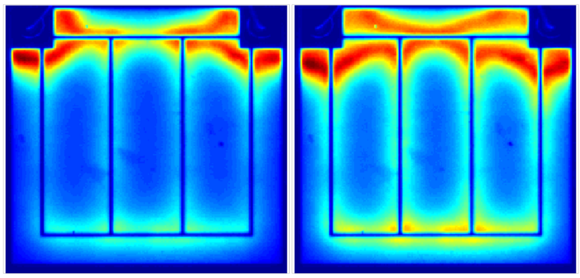

During stress at 2.5 A (d) During stress at 2.7 A (e)

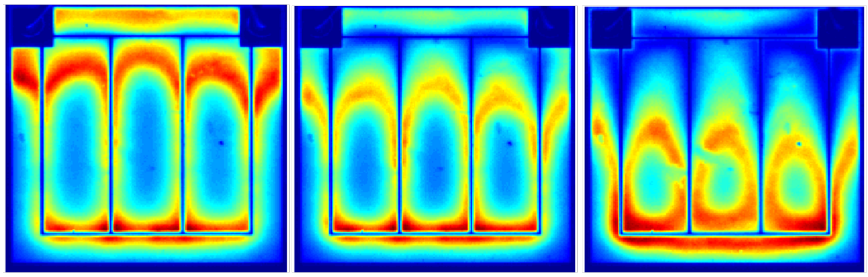

During stress at 2.9 A t = 3470 s (g) During stress at 2.9 A t = 3560 s (h) During stress at 3 A t = 3613 s (f)

Figure 4.12: Spatially-resolved Electro-Luminescence images taken during the step-stress experiment on group C sample ($T_{\mathrm{AMB}} = 25\,^{\circ}\mathrm{C}$). The EL maps are normalized to the respective maxima in order to highlight the stress-induced changes in the emission pattern of the device.

Figure 4.12 shows trend during stress time of the normalized emission map. Up to a stress current of $2\,A$, the experimental data reveal a progressive emission crowding around the bonding pad areas, which are the main current injection point for this specific device structure. Above $2.5\,A$, the emission around the bonding pad weakens and starts spreading along the surface metallization lines. During the stress step at $2.9\,A$, the emission undergoes a rapid relocalization towards the bottom side of the LED chip, whereas the upper part of the device shows a rapid decrease of its brightness.

Finally, at 3 *A* the luminescence originates mostly from the bottom portion of the GaN chip and catastrophic failure of the device occurs due to the melting of a portion of right-side bonding pad, which probably was not designed to sustain for prolonged intervals high current densities at the very high temperatures ($T_j > 200\,°C$) reached by the device during the final stages of the step-stress experiment.

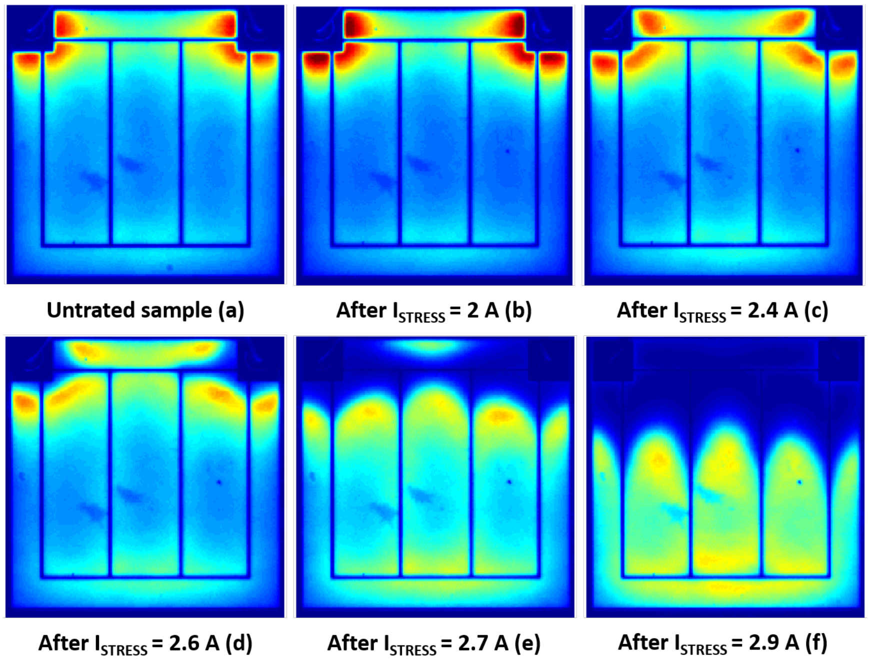

Figure 4.13: Spatially-resolved Electro-Luminescence imaging of the reference EL-I measurement taken at $I_{BIAS} = 1\,A$ after every stress cycle on a group C sample ($T_{AMB} = 25\,°C$). The EL maps are normalized to the respective maxima in order to highlight the stress-induced changes in the emission pattern of the device.

This characteristic degradation of the high driving current EL maps can be interpreted by looking at the EL-I maps acquired after each stress cycle and reported in Figure 4.13. The correlation between the progressive darkening of the upper portion of the EL-I maps at 1 *A* and the previously observed relocalization of the peak chip emission during high-temperature high-current operation suggests that this latter phenomenon is mostly related to a permanent, and localized, degradation of extended portions the semiconductor chip rather than to a temporary and spatially-defined loss in the radiative efficiency. The minor differences in the (relative) emission patterns registered during and after high current stress can be explained by considering that high temperatures increase the crowding effect, thus increasing the current density in device regions closer to the current injection point, i.e. the bonding pads (see frame (*e*) of Figures 4.12 and 4.13).

4.6 Role of temperature and positive aging

As pointed out in the former paragraphs, temperature played a major role in the final stages of degradation during prolonged high-current operation. To further evaluate the effect of temperature on the reliability of HB-LEDs operated at high current densities, the step stress experiment was repeated increasing the baseplate temperature up to 75 °C and 125 °C.

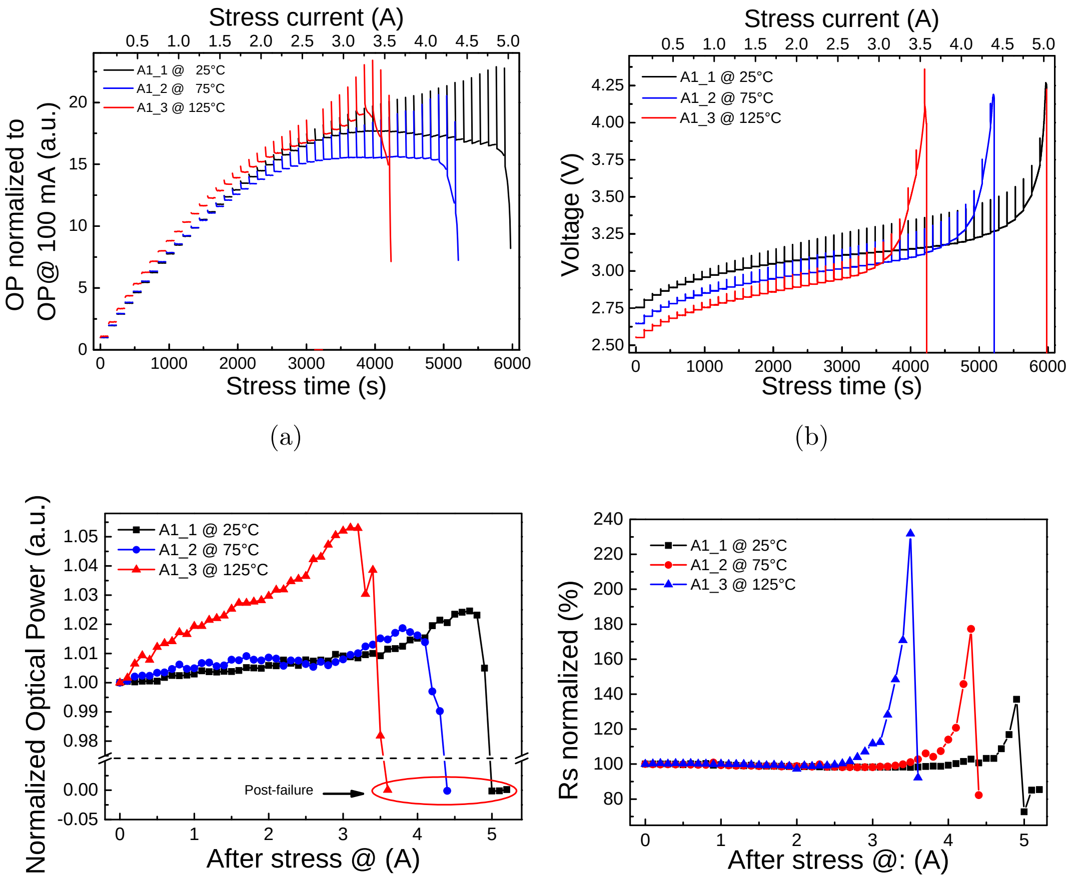

(a) (b)

(c) (d)

Figure 4.14: Trend of the optical power (a) and of the LED voltage (b) of three group A1 devices submitted to current step-stress at baseplate temperatures equal to 25 °C, 75 °C and 125 °C. The two bottom graphs show respectively the degradation kinetics of the OP (at 1 A) (c) and of the series resistance (d) extracted from the I-V and L-I characterizations performed after each stress step.

The results, reported in Figure 4.14, show that temperature is an accelerating factor for the observed RS increase degradation phenomenon, whose root causes may be found in the degradation of the p-type GaN or of the ohmic contacts [52]. On the other hand, the failure modes of the devices were note affected by temperature. High temperature ($T_{AMB} = 125\,°C$) and current stress was also found to accelerate the OP increase observed on every device under analysis during high driving current stress (see Fig. 4.14c, and the OP trend during stress in Fig. 4.2 for stress currents greater than $4\,A$). This “positive ageing” effect, often observed in the early stages of operation of GaN LEDs, may be due to the annealing of defects, to the activation of the p-dopant [62] or to the improvement of the electrical properties of the ohmic contacts. It is worth noticing that since the current-driven temperature-activated OP increase was found to be more prominent ad high injection currents, where the non-radiative recombination paths are saturated, the decrease in the number of deep-levels inside the active region of the device does not appear to be the driving force of the observed positive ageing process.

To further investigate this positive aging process, a series of constant current stresses at baseplate temperatures of 25 °C, 50 °C and 75 °C were carried out on group A1 LEDs. The bias point of $3.9\,A$ was chosen considering that during the previously reported current step-stress at room temperature (Fig. 4.2) this was the smallest driving current which induced significant increase in the emitted OP, both during stress and L-I characterization, without triggering the rapid degradation process observed for higher currents. The stress experiment was regularly interrupted in order to measure the electrical (I-V) and optical (L-I) characteristics of the devices (at 25 °C).

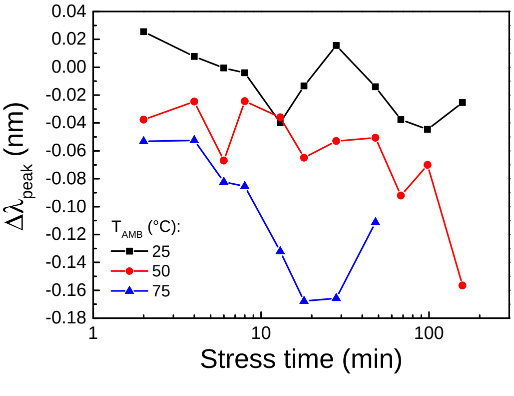

Figure 4.15: Trend of the peak emission wavelength measured at $1\,A$ - 25 °C of the A1 LEDs stressed at a constant current of $3.9\,A$ at different base-plate temperatures.

Interestingly, the adopted stress condition was found to induce a slight (max $0.2\,nm$) stress temperature-dependent decrease of the peak emission wavelength at $1\,A$, as shown in Figure 4.15. This minor increase in the energy of the emitted photons suggest that the short-term high-current stress induced a variation in the concentration and/or distribution of carriers which undergo radiative recombination within the active layer.

Conclusions

Within this chapter, the failure modes of high-power blue GaN LEDs submitted to very high current and temperature stress were investigated. The three different families of devices submitted to current step-stress showed different kinds of structure/layout-related failures, and a common set of epitaxy-related degradation processes. In particular, short-term high temperature and current stress induced the worsening of the conductivity of large portions of the semiconductor, by increasing the current crowding effect, and consequently power dissipation, in correspondence of the major current transport elements (vias, bonding pads and metal lines). Due to excessive levels of temperature reached during stress, those structures melted, causing the shorting and the catastrophic failure of the LED.

Chapter 5

Long-term degradation mechanisms of mid-power LEDs for lighting applications

The EOS-related device failures described in the previous chapters have become the major reliability issue for modern state-of-the-art LEDs. However, with regard to lower-tier less-engineered devices like the $0.3\,W$ mid-power LEDs designed for lighting and back-lighting applications, the gradual degradation processes affecting both the semiconductor chip and the package are still of main concern for the long-term operation of those light sources. This chapter reports the results of a reliability investigation performed on four different groups of commercially-available mid-power white LEDs. In order to determine the robustness of this continuously growing class of lighting devices we arranged an experiment of accelerated ageing: the four groups of LEDs (from different manufacturers) were submitted to a series of stress tests in environmental chambers with set-point temperatures ranging from 45 °C to 105 °C, in accordance to the IES LM-80-08 lumen maintenance measurement standard. The experimental data gathered all along the 4000 hours of total stress time suggest the presence of multiple degradation mechanisms that may limit the useful lifespan of the light-emitting diodes under test. In particular we observed the following phenomena: *i*) a decay of the luminous flux; *ii*) an increase in the reverse and forward leakage current; *iii*) the worsening of the chromatic properties of the emitted light; *iv*) the presence of a thermally activated degradation mechanism. The results provide a first insight into the reliability of those widely used LEDs; the results on the temperature-dependence of the degradation kinetics can be used as a guideline for the thermal design of modern distributed-light lamps.

5.1 Introduction and motivation

Over the last years, Solid State Lighting (SSL) gained a considerable market share over conventional light sources like halogen, incandescent or Cold-Cathode Fluorescent (CCF) lamps. Thanks to the superior lifetime, efficiency and color rendering capabilities of GaN-based white Light-Emitting Diodes (LEDs), this lighting approach is set to be the reference standard for the nearest future.

A modern LED lamp designed for general lighting purposes usually features a small number of High-Brightness devices (HB-LED) located in an appropriate frame, whose structure and material composition is the result of rigorous thermal and optical analyses finalized to maximize both the heat and light extraction from the source devices. Typically, these are state-of-the-art LEDs, supported by a solid background of reliability studies and equipped with a thermally advanced (ceramic) package. In the last few years, however, the need for costs reduction and for a simpler design of distributed light systems pushed towards the implementation of the so-called mid-power LEDs in place of the less cost-effective HB devices.

Those mid-power LEDs, whose (electrical) power rating ranges from 0.2 to $0.5\,W$, generally offer a good trade-off between lumen output and cost. This comes at the price of a reduced thermal and optical design of the package, which usually features a plastic housing that lacks of an optical element and, in some cases, of a dedicated thermal pad. Thus, despite the lower power dissipation, the increased sensitivity of this class of LEDs towards environmental temperature may turn out to be a major reliability issue.

The aim of this paper is to analyze the degradation mechanism that limit the reliability of mid-power LEDs subjected to a high-temperature operating regime. To this aim, we arranged an accelerated ageing experiment which revealed the following phenomena: 1) a strong and generalized decay of the luminous flux for junction temperatures above 120 °C; 2) an increase in the reverse and forward leakage current; 3) the worsening of the chromatic properties of the emitted light; 4) the presence of a thermally activated degradation mechanism.

5.2 Experimental details

The mid-power LEDs analyzed within this work have been selected based on the following criteria: a color temperature of 3000 K, a nominal current of 100 ± 20 mA and a Color Rendering Index (CRI) > 80. Four families of LEDs (which from now on will be referred to as groups A, B, C and D) fabricated by four different leading manufacturers were chosen. Three of the four groups (namely A,B and C) were selected within the highly popular 5630 (5.6×3.0 mm) class of mid-power LEDs, while the fourth one, group D, presents a smaller-sized package (2.0×0.8 mm) inherited from the typical devices designed for backlighting purposes. Four single devices of each group were connected in series on a MCPCB (Metal-Core PCB) which was tightly anchored to an aluminium heatsink; a thin graphite layer served as thermal interface material. The peculiar series connection was adopted to provide a good signal-to-noise ratio during L-I measurements performed with our optical characterization setup, which will be described later on. The electro-optical characterizations were carried out on the whole series, therefore only one effective sample per group and per stress condition was analysed.

GROUP	**Nominal/stress current (mA)**	**Mean R_{th} (°C/W)**	**T_j Max (°C)**	**SOA (°C)**
A	100	9.7	119.9	125
B	100	14.2	126.5	115
C	120	19	138.7	110
D	80	39	151.8	120

Table 5.1: Main properties of the four different families of devices under analysis. T_j Max is the maximum junction-temperature reached during stress by a specific group. The last column reports the maximum T_j suggested on the datasheets.

5.3 Thermal characterization and stress conditions

In order to define the thermal behaviour of the four different LEDs' families under analysis, we carried out a complete thermal characterization on untreated samples. The junction-temperatures were estimated following the diode "forward voltage method" proposed by Xi et Schubert [60]. The results, summarized in Fig. 5.1, show the following facts: a) a quite good thermal resistance for the 5630 package-based samples (specific values range from about 9 to 20 °C/W; b) a thermal disadvantage of D group's LEDs, due to the absence of a dedicated thermal pad and the reduced thermal design of the device; c) an almost linear relationship between environmental stress temperature and junction-temperature, whose maximum value of 152 °C is reached from group D

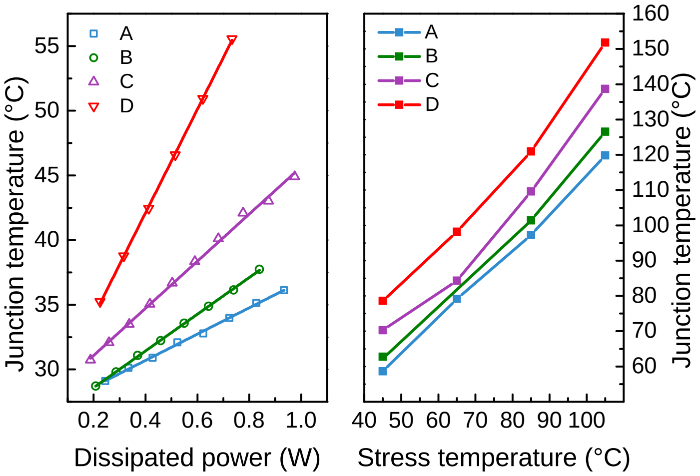

Figure 5.1: Results of the thermal characterization performed on the four families of mid-power LEDs under analysis. On the left side: junction-temperature vs. thermal dissipation curves at room temperature (25 °C) obtained through the diode "forward voltage method" for one sample of each. On the right side: experimentally acquired values of the junction-temperature reached by the devices during the stress tests (maximum T_j is reported in Table 5.1).

samples stressed at $T_{AMB} = 105\,°C$. For this stress temperature, the four families of devices were operating outside the SOA (Safe-Operating Area) for T_j advised from the manufacturers (see Table 5.1).

The elevated temperatures reached by modern GaN-based light-emitting diodes during operation are still one of the major limiting factor for their long-term reliability [63, 64], both at chip or at package level. With the aim of testing the robustness of the mid-power LEDs under analysis against thermally activated and/or current driven degradation mechanisms, the devices were actively stressed at nominal current inside climatic chambers whose temperatures were set at 45, 65, 85 and 105 °C. The stress cycles were regularly interrupted in order to perform a complete electrical and optical characterization. For the latter we exploited a fully power and wavelength-calibrated setup constituted of a 65" large integrating sphere (model LMS-650 from LabSphere) fiber-coupled to an OceanOptics USB2000+ spectrometer. A Keithley 2614B source-meter provided the polarization for the samples. On the other hand, the voltage-current characteristics were measured through an HP4155A parameter analyzer, whose accuracy, even if affected by the non-ideal connection system used, let us spot current variations down to the pA range (see Fig. 5.3a).

The measurement and stress methodologies described above fulfil the common IES LM-80-08 lumen maintenance measurement standard.

5.4 Results of the accelerated ageing experiment

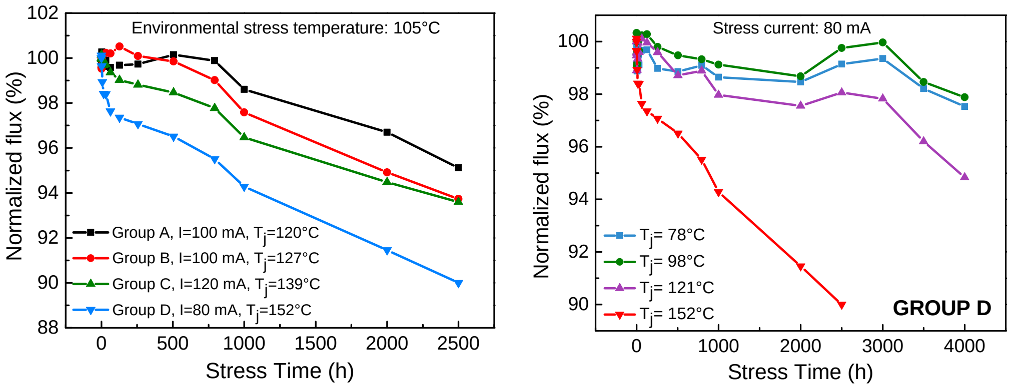

(a) (b)

Figure 5.2: Luminous flux trend registered during the active stress at the highest temperature ($T_{AMB} = 105\,°C$) of all the four families of devices (a) and relative to the smaller-sized LEDs belonging to group D (b) .

The degradation kinetics of the analyzed LEDs are reported in Figure 5.2. Linear lifetime extrapolation for a 10 % decrease of the output flux produced expected values of useful device life between 2500 and 5000 hours: considering that a common market requirement for a $TTF_{70\,\%}$ (usually referred to as L70) stands around 40.000h, we can state that our samples, probably, are not suited to be operated at junction temperatures above-120 °C, which, as already pointed out, is the average upper bound of the SOA for the LEDs under test. The aforementioned lifetime values are intended to be used only for the evaluation of activation energies, not for an accurate estimation of the expected lifetime of the device: not only this would require more data points, i.e. more hours of stress, but also a more sophisticated extrapolation algorithm, like the widely adopted IESNA TM-21.

As we can see from Fig. 5.2b, the kinetics of flux decay are highly temperature dependent, which suggest the presence of a temperature activated degradation process. Nonetheless, the luminous flux trends provide a useful guideline for an appropriate design of the lamp thermal management, which should guarantee a maximum junction-temperature below the extrapolated critical level.

In order to identify the physical mechanisms responsible for the flux decay, a deep investigation about the degradation of the chromatic and electrical characteristics was carried out. For the LEDs of group A, the increase in forward leakage current shows an approximately linear correlation with the flux decay, as reported in semi-log scale in Fig. 5.3b. Since one the main electronic transport processes in the low forward bias

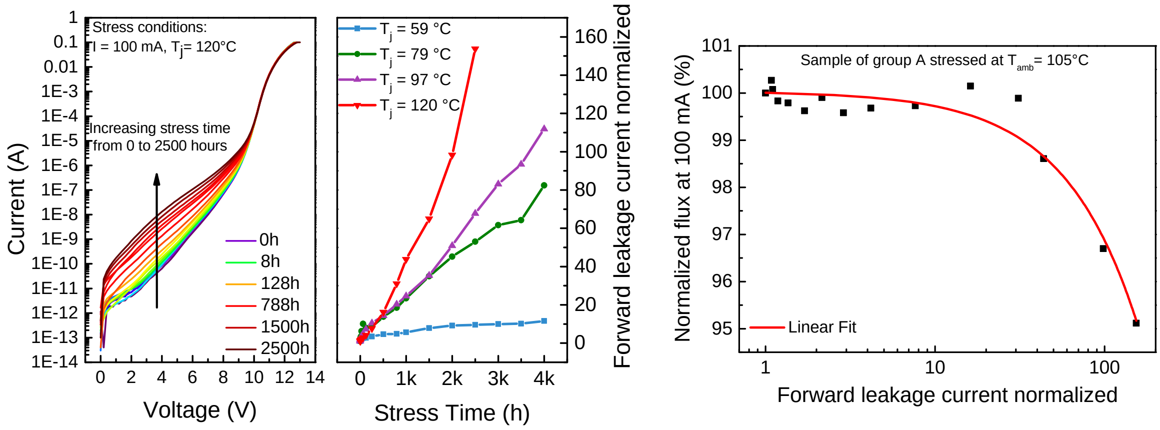

(a) (b)

Figure 5.3: Plot (a): degradation of the electrical characteristic of the A group devices stressed at the highest ambient temperature (105 °C). On the left, in a semi-log scale, an increase in the forward leakage current is clearly visible, while its temperature dependent kinetics (measured at $4\,V$) are reported in the graph on the right hand. The measurements were carried out on a series of four identical samples. Plot (b): normalized luminous flux plotted against normalized forward leakage current (measured at $4\,V$) for the samples of group A stressed at $\mathrm{T_{AMB}} = 105\,°\mathrm{C}$. The red line represents the linear fits of the experimental data.

region is trap-assisted tunneling [65], and since the rate of non-radiative recombination is directly proportional to the concentration of defect-related deep-levels inside the energy gap, the experimental data suggest the presence of an ongoing process of crystal defect generation inside the active region of the device. The observed phenomenon showed a remarkable temperature dependence.

Another relevant variation of the current-voltage characteristic was exhibited by D group LEDs (Fig. 5.4). The reverse leakage current of those devices experienced a temperature-dependent increase over time. Since leakage current strongly depends on the density of defects, a gradual worsening of crystal quality is to be expected [35, 66]. Moreover, in the forward conduction region, those LEDs registered a maximum increase of the forward voltage of about 63 mV, well above the average 30 mV gained from the other samples under analysis. The forward voltage increase was found to be temperature dependent and well correlated with the gradual rise of the series resistance, as shown in Fig. 5.5.

This suggests a partial degradation of the ohmic contacts and/or a resistivity increase of the quasi-neutral regions due to the high current density [67] and temperature of the operating regime. Such behavior, which may be the result of a “current-crowding” phenomenon [3], is critical when LEDs are employed in modules, where the voltage in-

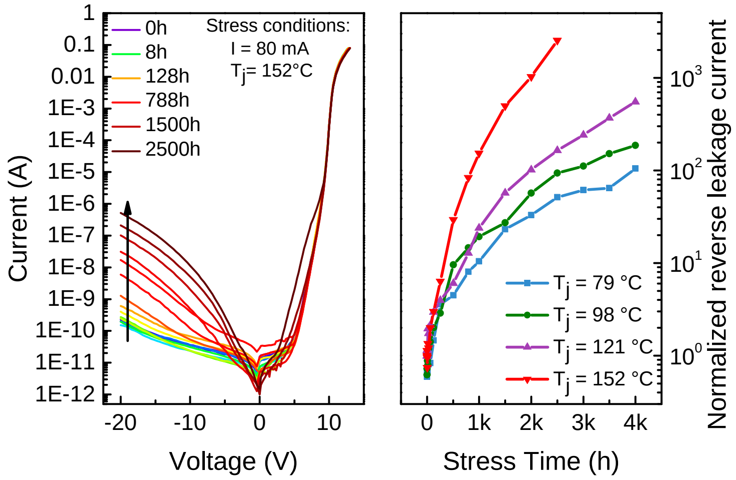

Figure 5.4: On the left: current-voltage characteristics of group D devices stressed at 105 °C (ambient temperature). On the right: kinetics of the leakage current, measured at $-20\,V$ ($-5\,V$ per LED), of the samples stressed at all the four environmental conditions.

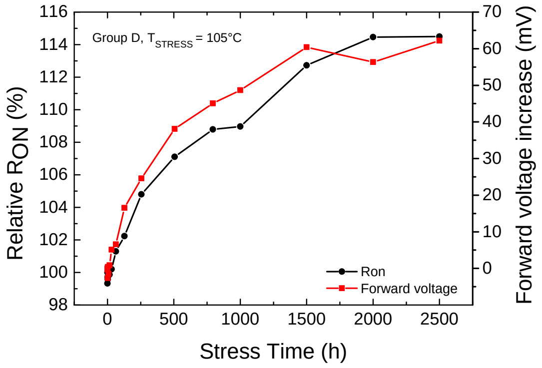

Figure 5.5: Relative R_{ON} and voltage increase for D group samples aged at 105 °C.

crease V_F of a single device lowers the limited voltage headroom of the current driver by an amount nV_F, where n is the number of devices in series.

Group D LEDs suffered from a noticeable chromaticity shift, which, for instance, led to a maximum 55 K increase of the CCT point within the whole 4000 h period of ageing. The chromatic degradation process takes place mostly during the first stress hours, after which the yellow to blue emission peak ratio suddenly slows its decay. This phenomenon is clearly visible in Fig. 5.6a. A similar behavior, but with different time constants, was experienced from the samples stressed at lower temperatures (Fig. 5.7): the strict correlation between stress temperature and the kinetics of the observed chromatic shift suggest the presence of a thermally activated degradation process, which probably involves the plastic package [68], the yellow phosphors [69] or the encapsulating material [47].

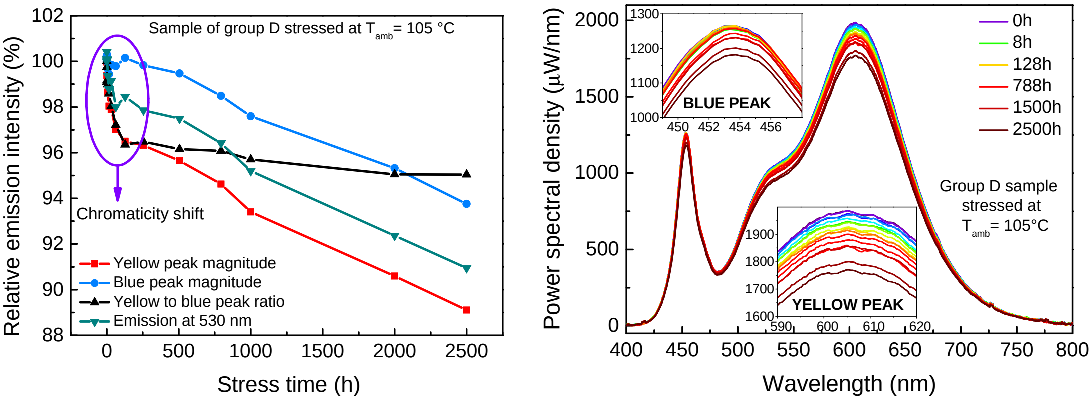

(a) (b)

Figure 5.6: Evolution of the chromatic characteristics of D group devices stressed at $\mathrm{T_{AMB}} = 105\,°\mathrm{C}$: (a) relative emission intensities registered for the blue and yellow spectral peaks; PSD (Power Spectra Density) trend at 530 nm and yellow to blue ratio are included as well. Plot (b): EL spectra at nominal current; inset graphs provide a more accurate vision of the specific degradation of the phosphor's (yellow peak) and GaN chip's (blue peak) emissions during the stress.

The simultaneous presence of a high-temperature environment (> 100 °C) and of a low-wavelength optical radiation is a well-known condition that triggers both the decay of the phosphor conversion efficiency and the worsening of the optical properties of the polymeric encapsulants. As a matter of fact, those materials tend to assume an amorphous phase above their "glass-transition" temperature ($\mathrm{T_G}$), which not only promotes the discoloring by VOCs (Volatile Organic Compounds) but also reduces their optical transmissivity in the low-wavelength range. Since our samples did not seem to suffer from this "red shift", and since the power-normalized spectra of untreated samples showed a remarkably different phosphor composition for D group LEDs, the "blue

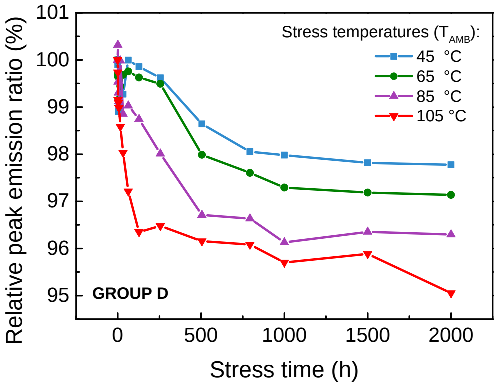

Figure 5.7: Relative yellow to blue peak emission ratio for the D group samples stressed in all the four environmental conditions.

shift" of the chromaticity point, which affected in a relevant way only the aforementioned devices, is probably due to a conversion efficiency loss of the phosphor species.

One last package-related degradation mechanism, which was not considered so far, is the tarnishing of the Ag reflective coating. This metallic layer, covering the lead frame and/or the plastic housing, is usually employed in mid-power LEDs in order to increase the overall light extraction efficiency. However, sulphur and chlorine-rich pollutants, released from different sources, may diffuse through the silicone encapsulant and react with the Ag atoms, forming AgS and AgCl complexes [70]. This may lead to an unrecoverable chromaticity shift and/or a decay of the emitted optical power. In order to evaluate this hypothesis, we de-processed the stressed samples with a depolymerizer agent and compared them with untreated samples. Visual inspection did not reveal any particular sign of sulfurization, though in-depth analyses, like EDS, may provide us more accurate results.

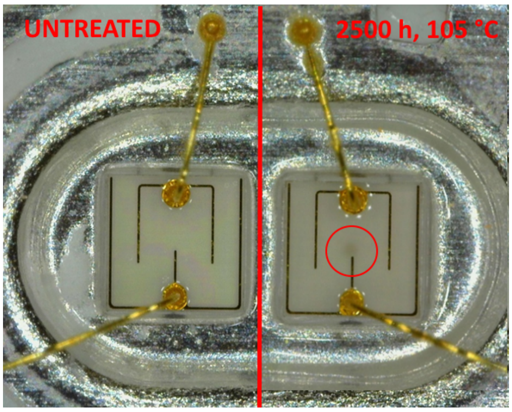

Figure 5.8: De-processed samples of group A: untreated sample (left) and device stressed at 105 °C for 2500 hours (right). Left and right chips are respectively shown.

Inspection of the de-processed devices belonging to the other three groups did not reveal proofs of degradation either, except for the samples of group A. As we can see in Fig. 5.8, those two-dice based LEDs showed a little darkening of the chip area near the lower surface contact. While this may be an evidence of an ongoing current crowding process, no correlation with the (slight) forward-voltage increase was found.

As an additional analysis, the activation energies of the registered lumen decay processes was estimated. From the L90 lifetime data, energy values of the degradation process ranging from 0.38 to 0.6 eV were extrapolated, indicating the presence of a temperature-activated process. The Arrhenius plots, reported in Fig. 5.9 for group C devices, did not show any bending for high temperature values, which suggests that no new processes were activated for junction-temperatures above 120 °C.

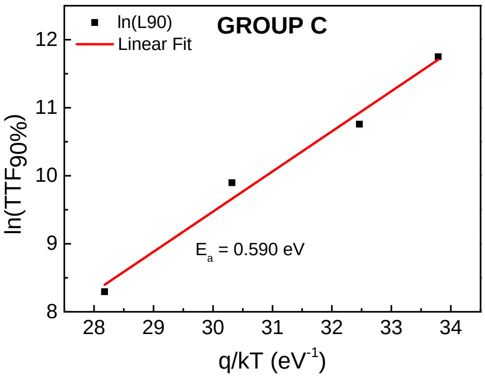

Figure 5.9: Arrhenius plot of the 90 % TTF (Time To Failure) for C group LEDs. The failure criterion, which corresponds to a 10 % decrease of the luminous flux at nominal current, has been chosen in order to guarantee the best possible coherence between the (linearly) extrapolated lifetime and the experimental data acquired so far, whose linear fit is represented by the red line showed above.

5.5 Conclusions

In summary, within this chapter a comprehensive study on the typical degradation mechanisms that may limit the long-term reliability of mid-power white LEDs was presented. The experimental data gathered during the accelerated aging experiments allowed to identify several degradation mechanisms, related both to the semiconductor chip (generation of defects within the active region of the devices, degradation of the electrical characteristics) and to the package/phosphors system (worsening of the chromatic properties of the emitted light). Despite those reliability issues, the LEDs under test showed a good robustness for junction temperatures belonging to the advised Safe Operating Area (SOA). Within these operating bounds, the analyzed devices are expected to have a useful lifetime, relative to a $\mathrm{TTF}_{70\%}$ flux decay process, adequate enough to fulfil nowadays market requirements.

Chapter 6

Failure causes and mechanisms of retrofit LED lamps

Years of reliability-oriented research and the technological improvements in the epitaxial growth techniques have greatly improved the lifetime of light-emitting diodes for general lighting applications. However, the stability and the performance of the solid-state light source are not the only factors impacting on the reliability of the whole LED-based lamp, since extrinsic elements like the current driver, the optics and the heat management system may degrade over time as well. In order to understand the limiting factors for the reliability of LED-based lighting systems, this chapter focuses on the analysis of the long-term degradation of retrofit light bulbs based on white GaN mid-power LEDs. The results of the long-term aging experiment performed on commercially-available bulbs from four different manufacturers showed that (i) long-term stress causes a change in the chromatic properties of the lamps, which is ascribed to the degradation of the phosphors or to the inner LED reflector; (ii) gradual and/or catastrophic failure of the LED driver may occur; (iii) a proper thermal design reduces the degradation rate; (iv) worsening of the transmissivity of diffusive optical element may occur, probably due to the combined effect of short wavelength radiation and high environmental temperature. These outcomes indicate that the lifetime of these LED-based luminaries relies mostly on the stability of the driver and optical elements, rather than on the robustness of the LED chips.

6.1 Introduction and motivation

Modern solid-state lighting solutions are based on white LEDs, which exploit the yellow conversion of the blue light emitted by GaN chips through appropriate phosphorescent materials. The reliability and stability of those devices has been proved up to tens of thousands hours [71, 64]. Thanks to their greater efficiency and longer lifetime, SSL solutions are being adopted in every segment of the general lighting market. In particular, with regard to the home lighting, several countries and associations are promoting the production of LED retrofit light bulbs, able to fit in a common Edison screw socket. This push towards home adoption is testified by several government funding projects, like the "L Prize" competition run in 2008 by the United States Department of Energy with a 10 million USdoll prize fund [72].

Nowdays, retrofit light bulbs can be easily found in common retail stores. However, since the customers need to face an higher retail price compared to conventional lighting solutins like fluorescent lamps, the return-on-investment must be granted by taking advantage of the reduced power consumption and longer lifetimes of LED-based luminaries, thus ensuring that the intensity and chromatic properties remain stable over the usable lifetime [73].

The aim of this chapter is to analyze the degradation mechanisms that may affect the long-term reliability of commercially-available lamps; the experimental results highlighted the critical parts of the overall system, whose failure modes were correlated with specific failure mechanisms. In particular, (i) operating temperature was found to be an accelerating factor for the degradation processes, that are related to (ii) the darkening of the plastic diffusive bulb, to (iii) the change in the chromatic properties of the inner phosphor and/or reflector and to (iv) the degradation of the LED driver.

6.2 Experimental details

Four different groups of commercially-available retrofit light bulbs from four different manufacturers, named A to D in the following, were submitted to lifetime tests at room temperature (RT) and accelerated tests at higher temperature (HT). The bulbs under investigation have a luminous flux between 765 lm and 810 lm, and a correlated color temperature of 2700 - 3000 K. The actual stress temperature varies due to the different driving and heat dissipation strategies adopted by the manufacturers: on average, the temperature of the HT lamps is 15 °C higher than the RT lamps (see Table 6.1 for a comparison of the average temperatures in different regions of the light bulb for each manufacturer and test temperature; these temperatures were measured by using a FLIR Systems i50 infrared thermal camera). During the stress the lamps were biased in their normal operating condition, i.e. screwed in a socket and connected to a mains wall plug. Characterization was performed in a repeatable way right after each stress cycle, in order to avoid the unpredictable warm-up times of the driving electronics and to reduce the time interval needed to reach thermal equilibrium during the absolute irradiance measurements.

	RT		**HT**	
	Bulb T (°C)	**Heatsink T (°C)**	**Bulb T (°C)**	**Heatsink T (°C)**
A	38.1	82.6	42.6	98.5
B	35.2	75.3	38.1	89.1
C	39.2	64.4	42	80.7
D	36	88.1	38.4	99.8

Table 6.1: Operating temperatures of different lamp regions for each manufacturer during stress at room temperature (RT) or high temperature (HT).

After each stress step a complete optical and spectral characterization was carried out in a 1.5 m diameter Labsphere LMS-650 integrating sphere by using a Ocean Optics USB2000 spectrometer. A radiometric calibration of the whole setup was performed in order to obtain an accurate estimation of the optical power at different wavelengths and the correct power spectral density in $\mu W/nm$. Moreover, after every stress period the electrical power consumption of the complete system, i.e. the power absorbed by the LED driver from the electrical distribution network in order to operate the LEDs, was measured by means of a Rohde& Schwarz HAMEG HM8115-2 power meter.

6.3 Degradation kinetics

In Figures 6.1 and 6.2 the degradation kinetics of the output optical power for all the samples under test at room temperature and at high temperature are reported. In figures 6.1a and 6.2a each line represents the average trend of all the lamps from the same manufacturer stressed at the same external temperature. The reliability of groups A and B devices under nominal operating conditions at room temperature is good, showing a maximum 18% drop after approximately 20 kh (19400) with no catastrophic failures registered. Degradation rate was found to be correlated with the

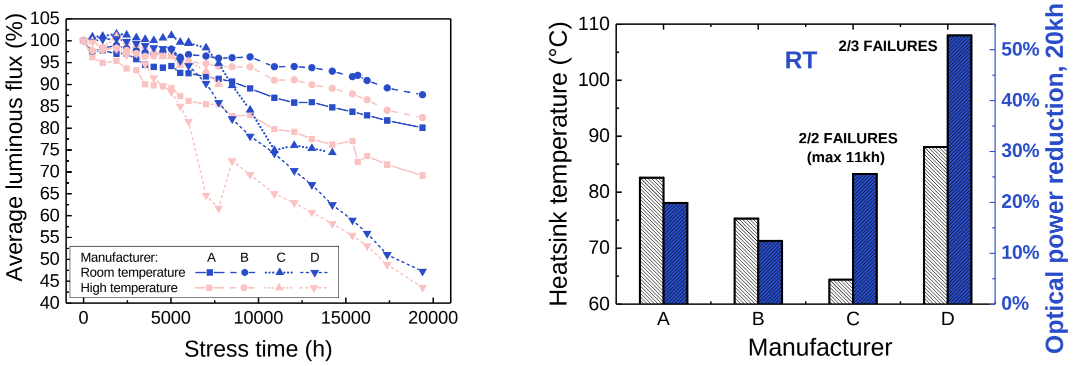

(a) (b)

Figure 6.1: Stress at room temperature: OP reduction of the light bulbs over time (a) and total (average) OP reduction Vs. bulb temperature (b).

(heat-sink) operating temperature, i.e. the lower the temperature the lesser is the flux drop registered during the aging experiment. These figures highlight a general improvement of the systems if compared to preliminary reports on the degradation of retrofit bulbs produced during previous iterations of the technological process [74]. Nevertheless, the outcome of the RT lifetime test changes when considering group C and group D devices. In particular, all the bulbs of group C failed after a maximum of 11 kh (see Fig. 6.1b), whereas only one out of three group D samples managed to survive up to 20 kh, with a consistent 52 % drop in the emitted luminous flux.

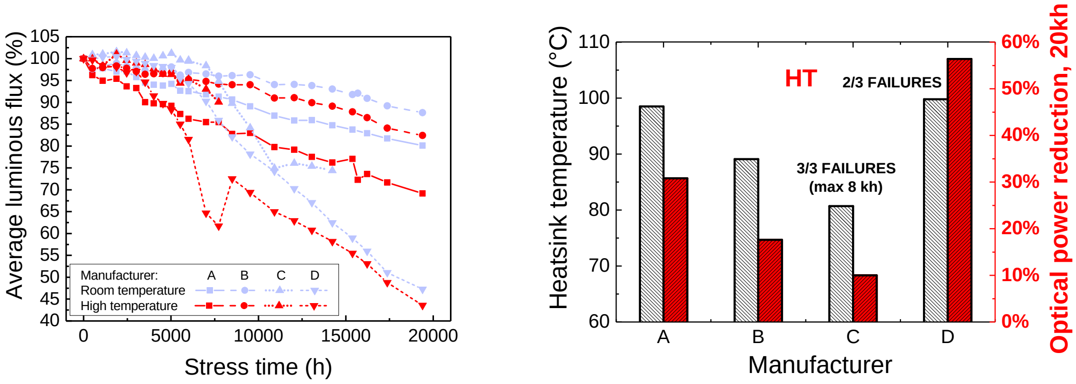

(a) (b)

Figure 6.2: Stress at high temperature: OP reduction of the light bulbs over time (a) and total (average) OP reduction Vs. bulb temperature (b). The dip in the trend of group D devices around 7500 h results from the averaging of a heavily degraded sample which failed after that specific stress step.

High operating temperature was found to negatively affect the lifetime of the devices from all the manufacturers under analysis. This highlights the importance of temperature as a degradation accelerating factor, which was reported for all the components of the LED systems, namely the GaN chip [75], the phosphors [76] and reflector [77]. In order to gain further information regarding the operating temperature of the bulb system, the temperature distribution in the luminaries was measured by means of IR thermography.

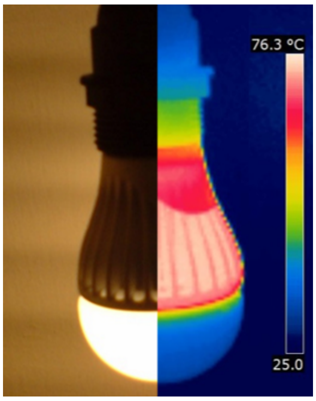

Figure 6.3: IR thermography of a group B sample taken during room-temperature stress.

The results, here presented in Figure 6.3 alongside an optical photography for a group B sample, show that even if the diffusive bulb temperature differs lightly from room temperature, the heat-sink of the device can reach very high temperatures (75 °C or more). Therefore, a junction temperature for the LEDs higher than this value is to be expected: this can pose serious reliability issues to the whole system, since the mid-power LEDs typically employed in these systems are usually rated for maximum T_j values up to 125 °C [6], and state-of-the-art HB LEDs should not be operated at junction temperatures higher than 150-170 °C [78].

6.4 Diffusive bulb darkening

A progressive darkening of the diffusive bulb over stress time for lamps of manufacturer D was detected. In Figure 6.4a an untreated bulb is compared to a dome belonging to a failed device stressed for 2500 hours. A non-uniform variation in the color of the dome surface is clearly visible. The effect was found to be stronger at the center and weaker at the borders: this suggests that degradation is probably related to the short-wavelength radiation shone onto the diffusive bulb, whose intensity is higher in the direction normal to the surface of the LED due to its typical lambertian emission

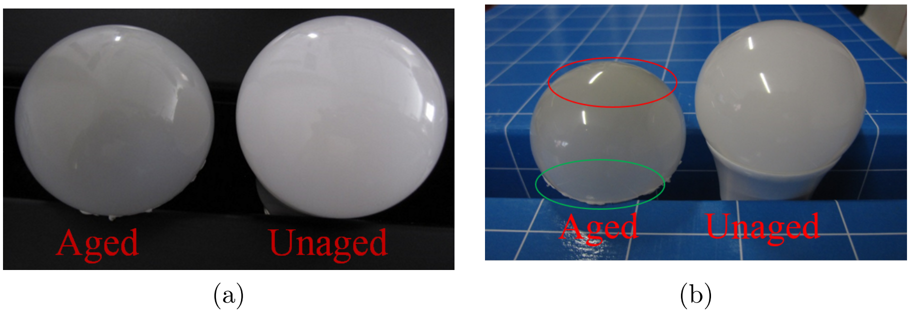

(a) (b)

Figure 6.4: Comparison between an unaged and a 2500h aged diffusive dome of two group D samples. In (b) a diffused darkening of the surface is clearly visible. In figure (a) an uneven amount of darkening is pointed out by the green oval (low darkening) and by the red oval (high darkening). Both bulbs belong to the same lamp set: in the figure the aged one looks smaller because it was cut from the main body in order to expose the underlying LEDs for visual inspection.

profile. The role of temperature as the sole cause of degradation can be excluded, since the hotter areas of the dome are found in correspondence of the edges of the dome (see Figure 6.3), where the darkening was found to be lower Figure 6.4b.

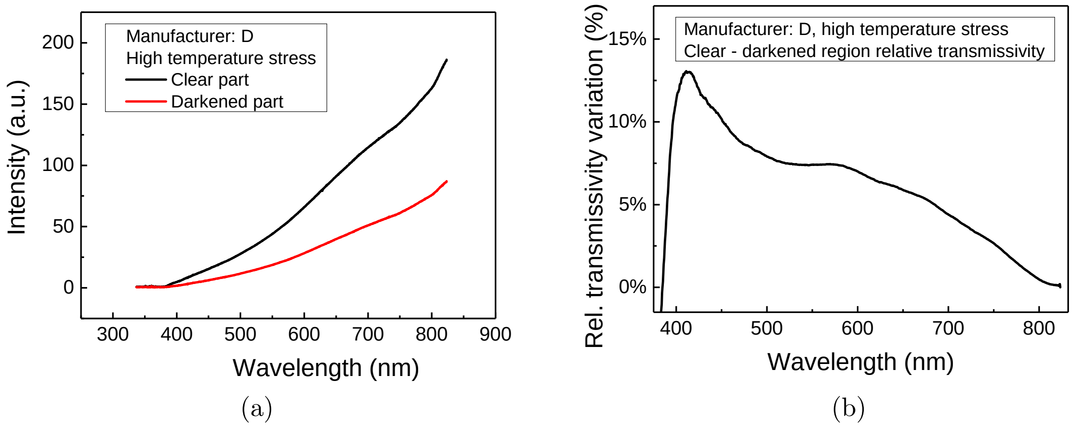

(a) (b)

Figure 6.5: Transmissivity measurements on aged Vs. unaged group D samples. Transmissivity curves (a) and (b) variation in the relative transmissivities.

Figure 6.5a shows the results of a transmissivity measurement performed on both a darkened (red region in Figure 6.4b) and a clear (green region in Figure 6.4b) part of the same aged bulb. The analysis was carried out by illuminating the sample with an external Ocean Optics LS-1-CAL radiometric calibration lamp, which prevented any effect related to the LEDs or to their driver from influencing the validity of the acquired data. The darkening was found to effectively reduce the transmissivity of the dome and is therefore a major responsible in the decrease of the luminous flux.

In order to estimate the effect of the darkening on the chromatic properties of the lamp, the curves of Figure 6.5a and the lamp spectrum provided by the manufacturer were normalized at their highest value. By dividing the curves of the two dome parts by the curve of the lamp the percentage variation of the transmissivity, relative to its maximum value, was obtained. Then, by subtracting the two relative transmissivities the spectral distortion induced by the darkening process, reported in Figure 6.5b, was obtained. The experimental data show that the degradation of the dome causes not only a reduction of the absolute transmissivity but also a distortion of the transmitted spectrum, leading to a change in the chromatic properties of the lamp.

6.5 Chromatic variations

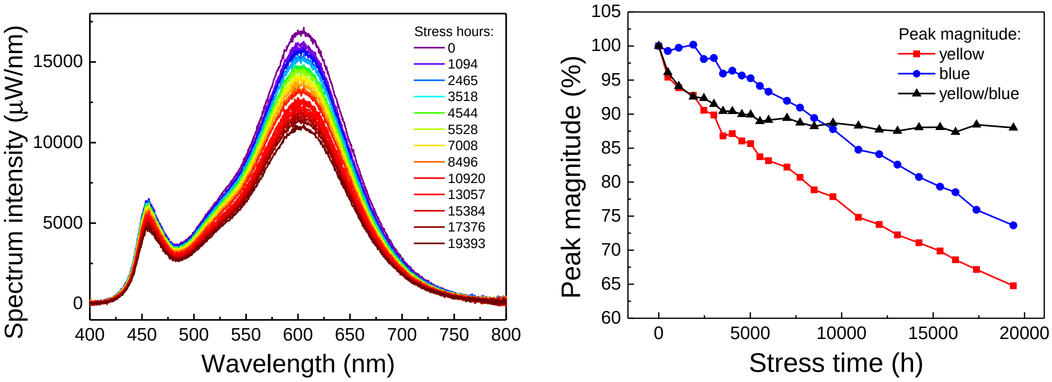

(a) (b)

Figure 6.6: Variation in the chromatic properties of the light of a group A bulb submitted to HT stress: emission spectra (a) and trend of the peak magnitude during stress time (b).

For lamps of group A, the most relevant degradation mechanism is the variation of the relative contributions in the output spectra, reported for a representative sample in Figure 6.6a. By looking at the trend of the yellow and blue peaks and of their ratio in Figure 6.6b, it is clearly visible how the stress induced a variation in the chromatic properties of the emitted light, due to an uneven decay of the yellow and blue peaks during the first 5000 h of high-temperature aging. The worsening of the yellow emission may originate from three different mechanisms: a change in the spectral response of the diffusive bulb (see section 6.4), the decrease in the phosphor conversion efficiency or the oxidation/darkening of the inner reflector. From the experimental results presented

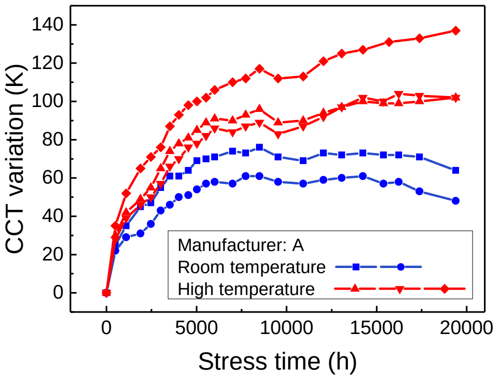

Figure 6.7: Variation of the CCT of group A samples during stress time.

in the former paragraph, the hypothesis regarding the diffusive bulb may probably be ruled out: as a matter of fact, no relevant darkening is detected in lamps of group A, contrary to the case of group D devices. In addition, the dome darkening was found to impact more at shorter wavelengths (see Figure 6.5b), whereas in Figure 6.6a the spectral decay was found to be more prominent at the low energy side. In the long term, also the LED emission at 455 nm varies with the same trend of the phosphor emission, suggesting that the GaN chip is probably undergoing degradation due to the high-temperature operation.

The strong decrease of the yellow luminescence during the first 5000 hours of stress is also testified by the trend of the Correlated Color Temperature (CCT) reported in Figure 6.7. The experimental data show that the decrease in the yellow contribution is correlated with a gradual increase of the CCT towards more hot, i.e. bluish, equivalent black body temperatures. This CCT increase process, which was found to be accelerated by temperature, can be a problem for the end user since even though the bulb is still functional, the shift towards a colder perceived light may induce the early substitution of the LED light source.

6.6 Driver performance

There is one more light bulb subsystem which was found to affect the lamp performance: the LED driver. This apparatus includes all the additional circuitry required in order to convert the electrical power drawn at high voltage (230 V_{RMS}) from the mains to a lower level, compatible with the limited operating voltage and current of the white LED matrix.

For lamps of manufacturer D, the trend of the output optical power during the first 3000 to 5000 hours of HT stress was found to be well correlated with the decrease

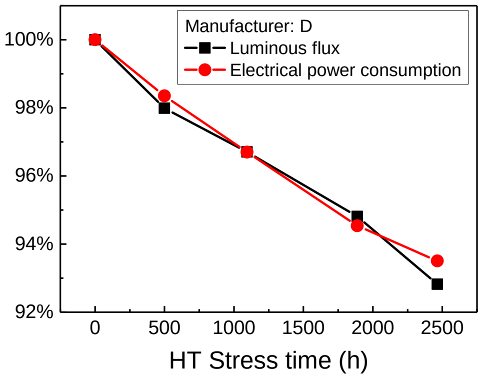

Figure 6.8: Correlation between the decrease of the luminous flux and the reduction in the electrical power consumption in one of the group D light-bulbs under investigation.

of the electrical power consumption, as reported in Figure 6.8. This effect suggests that the reduced optical emission is probably related to a decrease in the electrical power provided to the LEDs rather than to the degradation of the optical source or of the diffusive dome. A linear decrease with time of the absorbed electrical power was experienced by all the devices of group D submitted to high temperature stress. Since previous reports suggest that this kind of behavior may be related to the worsening of the electrolytic input capacitor [79], we decided to investigate this degradation mode by analyzing a failed device belonging to group D, whose OP Vs. power draw trend is the one reported in Fig. 6.8.

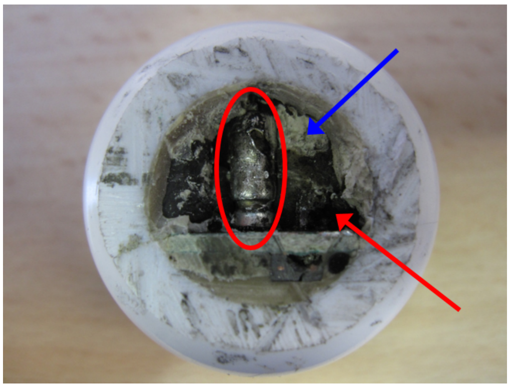

Figure 6.9: Photo of a disassembled group D bulb which failed after 2500 h of HT stress.

The visual inspection of the interior of the bulb highlighted the driver as the failed part (see Figure 6.9). In particular, the electrolytic capacitor, highlighted with red oval circles, shows a visible crack in the outer insulating layer. This is the typical damage signature which results as a consequence of the electrolyte evaporation, probably caused by power line surges or electrical and/or temperature-related overstress. The capacitor burst was so intense to cause the burn of the encasing material, which appears darkened (red arrow) rather than white as in the other regions (the blue arrow highlights the expected color of the filling material when the burned region is removed). These experimental results confirm that a proper design of the LED driver is needed not only to ensure high electrical conversion efficiency in a small form factor, but also to guarantee a long lifetime to the entire lighting source.

6.7 Conclusions

Within this chapter the degradation mechanisms that may affect the long-term reliability of commercially-available lamps have been evaluated. By means of lifetime tests carried out on four different groups of retrofit LED light bulbs, the importance of temperature as an accelerating factor for the degradation processes was confirmed. The main mechanisms which can lead to the decrease of the performance of the bulb were found to be following: (*i*) the darkening of the diffusive bulb, that impacts on the overall transmissivity of the dome and produces a distortion of the emitted spectrum, thus altering the perceived chromaticity of the emitted light; (*ii*) the variation of the chromatic properties of the phosphors and/or of the reflector, which reduces the efficiency of the lamp and also causes a strong change in the CCT; (*iii*) the worsening of the performance of the LED driver, which can lead to early failures of the entire system. All these effects concur in limiting the overall reliability of the system, whose expected lifetime is in the range of tens of thousands hours in nominal operating conditions.

Part II

Reliability of phosphorescent materials for laser-lighting applications

Introduction to Part II

The generation of white light by means of Phosphor-Converted LEDs based on a blue-emitting Gallium Nitride chip is the common approach adopted by modern SSL solutions in order to achieve reliable and efficient light sources for all kind of applications. However, alternative solid-state lighting solutions based on laser diodes instead of LEDs are starting to emerge. Compared to LEDs, lasers offer two main advantages: an increased efficiency at high driving current-densities, i.e. for high optical power single source operation, and a simplified and more effective design of the optical system. The first point is related to a reduced effect of the so-called *efficiency droop* phenomenon in LDs. The term efficiency droop describes the set of physical mechanisms responsible for the decrease in internal quantum efficiency of the device as the injected current increases: this phenomenon, typical for LEDs, is usually ascribed to Auger recombination [80] or carrier spill-over [81]. In laser diodes operated above threshold, the emission of coherent light is associated with the stimulated recombination of carriers, that, compared to the spontaneous emission process responsible for photon emission in LEDs, is a much faster process, less affected by the formerly cited loss mechanisms.

Efficiency droop limits the amount of optical power attainable from an LED for a given chip area, meaning that if high-brightness high-efficiency operation is to be reached, the area of the semiconductor chip needs to be increased. However, not only this approach would increase the manufacturing costs, but it would also worsen the optical performance of the lighting system in terms of light collimation. Since in an optical system the product of a source emitting area and the solid angle of the emitted beam does not decrease if the optical power is conserved, this means that the collimation of a (relatively) large area source (up to $4\,mm^2$) as an High-Power LED, featuring a large-aperture Lambertian emission pattern, would require an increase in the dimensions of the optical elements, thus increasing the complexity and the cost of the final illuminator. On the other hand, laser diodes feature a very small emitting area, in the orders of tens of square microns, which allows for the design of cheaper low-divergence LD-based light sources, like the ones employed in digital laser projectors.

When it comes to Laser-Activated Remote Phosphors (LARP) lighting systems, two main white-light generation approaches can be identified. These are either based on the partial conversion of blue light ($450-460nm$) through a yellow phosphor blend, or on the total phosphor conversion of near-UV light ($380-410nm$) into blue light, which is then partially converted to longer wavelengths in order to attain the desired chromaticity point. In principle, assuming phosphors and LDs with comparable efficiencies, the first approach shows an intrinsic advantage due to the reduced energy loss in the conversion process ($\approx 12.5\,\%$, considering excitation wavelengths of 400 and $450\,nm$). However, for high-power operation, the efficiency of the light source at high current densities is the dominant factor in determining the global efficiency of the LARP system. With regard to LEDs, this translates into a clear supremacy of NUV sources over convential blue emitters [82], determined by the higher efficiency droop of the latter at high injection currents. For laser diodes operating in stimulated emission regime, however, the intrinsic inefficiency of blue emitters is less pronounced, and the choice for a specific lighting approach becomes more bound to the technological limitations of state-of-the art devices and to the optical design of the illuminator rather than to the physical principles ruling the emission processes.

This work focuses on the reliability of blue-emitting phosphors for NUV ($405\,nm$) laser excitation. Devices featuring such emission wavelength have already proved their reliability and the capability for DC operation at output power in excess of 7 W [83]. The high light intensity generated by those devices requires phosphor morphologies with high thermal conductivity in order to face the self-heating due to Stokes loss and to the non unitary quantum efficiency, as well as an elevated chemical stability under high optical intensity/high temperature operating conditions. Aim of this work is to analyze the variation in the luminescence and of the chemical and morphological properties of blue phosphors under such operating conditions, in order to pinpoint the root cause of degradation and to determine a *safe operating area* for the material under analysis. The results of the investigation are reported in chapter 8, following a brief introduction on the fundamental properties of phosphorescent materials.

Chapter 7

Luminescent properties of phosphors for SSL

This chapter deals with the fundamental properties of luminescent material fol Solid-State Lighting (SSL) applications. Luminescent materials, also called phosphors, are typically inorganic crystalline materials, referred to as *host lattices*, that are intentionally doped with a small amount of impurities (*activators*), like rare earth ions or transition metal ions, usually responsible for the optical emission. Since the luminescence process involves both the host-lattice and the activators, the electronic transitions properties of those two components must be evaluated in order to fully understand the dynamics of luminescence for a specific phosphor. Aim of this chapter is to describe the physical fundamentals of luminescence in those materials, and to analyze the factors that can impact on their optical properties.

7.1 Fundamentals of luminescence

The term luminescence defines the physical process for which a medium, after it is excited by a specific type of external energy (EM radiation, electric field, e-beam,...), releases its excess energy in the form of electromagnetic radiation either immediately or over a long period. Like in semiconductor crystals, the luminescence process involves the excitation, energy transfer, and subsequent relaxation of the valence electrons from their excited states.

7.1.1 Excitation process

In a luminescent material composed of an host lattice and activators, two kinds of excitation processes mainly exist: direct and indirect excitation. In the case of direct excitation, the activators directly absorb the excitation energy, promoting atoms to the excited state of the activator ions. On the other hand, with indirect excitation the host lattice first absorbs the excitation energy, which is then transferred to the excited state of the activator ions. Since the energy levels of activator ions are usually located between the conduction and valence bands of the host material, the energy required for direct excitation is typically smaller. Thus, direct excitation processes are of primary importance for SSL applications, since the wavelength range for efficient laser or LED emission ranges from the near UV ($390\,nm$) to the blue ($460\,nm$), with corresponding photon energies much lower with respect to other excitation sources like then ones employed in fluorescence lamps or in cathode-ray tubes.

In order to interpret the excitation spectrum of a phosphor, the concept of configurational coordinate diagram must first be introduced.

The configurational coordinate diagram

The configurational coordinate diagram is usually employed to explain optical properties of a localized center in relation to electronic transitions, with particular focus on the effect of lattice vibrations.

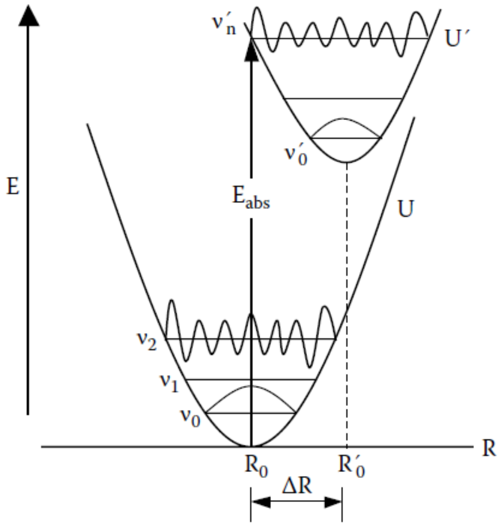

Figure 7.1: Example of configurational coordinate diagram, where $\mathcal{U}$ represents the ground state and $\mathcal{U}'$ the excited state.

In this model, shown in Figure 7.1, an absorbing center and the ions at its nearest neighbor sites are represented by plotting the total energy of the center in function of metal-lingand distance R, or, more generally, in function of a generic coordinate Q, called *configuration coordinate*, which represents an overall measure of the spatial configuration of the absorbing center and of its neighbor. The (vibrational) energy levels for the harmonic oscillator representing the activator-ion molecule are quantized. Those levels are reported in the diagram of Figure 7.1 as ν_0, $\nu_1\,\nu_2 ... \nu_n$ for the ground state $\mathcal{U}$, where we can also see that for the lowest vibration level ν_0 the system has the highest probability of being located in the center on the parabola, at R_0. The same considerations are also valid for the excited state $\mathcal{U}'$, whose minimum at R'_0 is shifted by a value ΔR due to differences in the chemical bond of the excited state with respect to the ground state.

The absorption of energy induces the transition from the lowest vibrational level ν_0 of the ground state $\mathcal{U}$ to some vibrational level ν'_n in the excited energy state $\mathcal{U}'$. Due to the Frank-Condon principle, electronic transitions are most likely to occur without changes in the positions of the nuclei in the molecular entity and its environment (vertical transitions), or, from a quantum mechanical point of view, the intensity of a vibronic transition is proportional to the square of the overlap integral between the vibrational wavefunctions of the two states that are involved in the transition. This means that the probability of the process is greatest for transitions starting from R_0, where the vibrational wave function has its maximum, and terminating at one of the edges of the excited state parabola, as shown by the solid arrow. That transition corresponds to the maximum of the absorption band of the phosphor.

With a reduced probability, transitions initiating from an R value different from R_0 can also occur. Since the energy required for the transition to occur depends on the relative position of R_0 and R'_0, and in particular on the relative position of the maxima of the vibrational wave-functions of the excited state with respect to R_0, the shape of the vibrational wave-function directly defines the excitation spectrum of a phosphor. Thus, in general, the larger the value of ΔR, the broader the excitation spectrum is.

Selection Rules The previously cited overlap between the wave-functions of ground and excited states is not the only factor determining the intensity of the absorption process. In fact, the transition probability is also governed by the so-called *selection rules*, derived from quantum mechanical principles. The two most important selection rules controlling the probability of electronic transitions, and their feasibility, are the following:

- *The spin selection rule.* Only electronic transitions between states of the same spin are allowed, meaning that the number of unpaired electrons in the external orbitals must be conserved.
- *The orbital selection rule.* Transitions involving only a redistribution of electrons within the same set of atomic orbitals are forbidden, that is $\Delta l = \pm 1$, where l is the orbital angular momentum quantum number.

7.1.2 The emission process

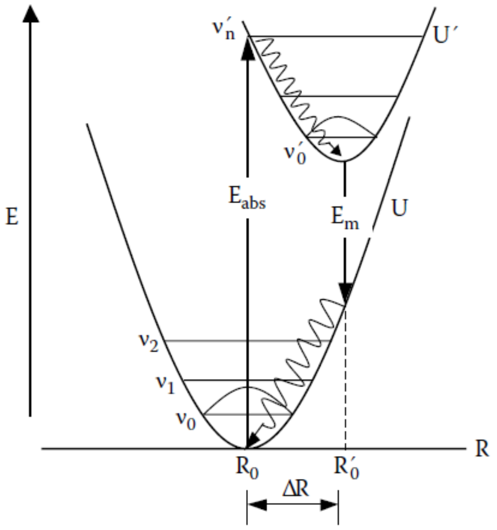

Figure 7.2: Configurational coordinate diagram describing the phases of the absorption/emission process.

After an electron is promoted to an excited vibronic state, the excited ion thermally releases (relaxation) some of its energy returning to the lowest vibrational level of the excited state, ν'_0, thus reaching an equilibrium state where the inter-atomic distances correspond to an equilibrium position. From this state, the excited ions can return to the ground state $\mathcal{U}$ by spontaneous emission of photons, reaching the vibrational state at the corresponding coordinate R'_0. Finally, with a second (non radiative) relaxation process, the ion reaches the lowest vibrational levels of the ground state.

As for the absorption process, a distribution of probabilities for the starting points of the emission transition exists, with a maximum in correspondence of R'_0. Since some energy is non-radiatively dissipated prior to the emission, the emitting photons have always a lower energy compared to the energy of the absorption process, which leads to an energy difference between the positions of the band maxima of the excitation and emission spectra (*Stoke's shift*). In the case of equally-shaped parabolas for the excited and ground states, the energy loss due to relaxation can be estimated to be equal to $Sh\nu$ for each parabola, where S is the *Huang-Rhys coupling factor* measuring the strength of the electron-lattice coupling ($S \propto (\Delta R)^2$) [84]. Hence, the Stokes shift (SS) can be expressed as:

$$SS = 2Sh\nu \tag{7.1}$$

where $h\nu$ is the energy difference between two vibrational levels. Equation 7.1 shows that a small value of ΔR is desirable in order to attain a smaller Stokes shift, thus increasing the luminous efficiency of the material for a given excitation wavelength. On the other hand, a non excessively small SS value is needed in order to avoid photon re-absorption and to reduce *thermal quenching*, as described in the following paragraph.

Temperature dependence of the emission process

Temperature affects the emission spectra both in terms of spectrum broadening and intensity (thermal quenching).

Spectrum broadening. An increase in the phosphor temperature generally leads to the broadening of the absorption and/or emission bands. By looking at Figure 7.1, we can see how the vibrational levels of both the ground and the excited stated are increasingly populated with increasing temperature, which means the a larger overlap factor between the vibrational wavefunctions of the electronic states can be attained. The effect of temperature on the spectral broadening ΔE can be approximated by the following equation:

$$\Delta E(T) \approx \Delta E(0)\sqrt{coth(h\nu/2kT)} \tag{7.2}$$

where $\Delta E(0)$ is the bandwidth at $0\,K$, and $h\nu$ is the energy of the coupling phonon.

Thermal quenching. Thermal quenching of emission is the phenomenon determining the decrease in emission efficiency with increasing temperature. Experimentally, the luminescence intensity at temperature T, $I(T)$, can be related to temperature according to

$$I(T) = \frac{I(0)}{1 + \frac{\Gamma_0}{\Gamma_\nu}\exp\left(-\frac{E_{tq}}{kT}\right)} \tag{7.3}$$

where Γ_ν is the probability of radiative transition, Γ_0 is a pre-exponential constant and E_{tq} is the energy barrier for thermal quenching. From equation 7.3, assuming that

$kT \gg E_{tq}$, the temperature dependence of the emission efficiency can be expressed as

$$\eta \approx c \exp\left(-\frac{E_{tq}}{kT}\right) \tag{7.4}$$

where c is a constant. For specific electronic configurations, thermal quenching of emission is mainly related to the *thermally activated non-radiative de-excitation* process, schematically represented in Figure 7.3.

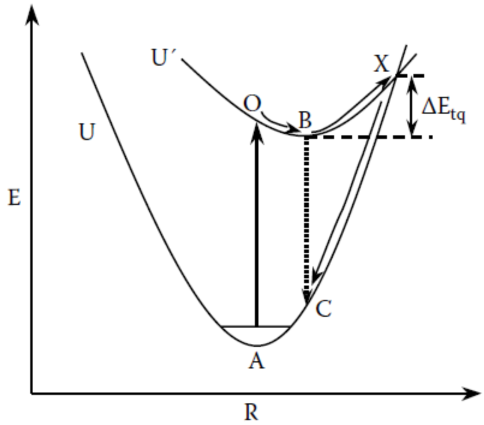

Figure 7.3: Configurational coordinate diagram representing a thermally-activated non-radiative transition.

The non-radiative transition can be explained by considering the existence of a crossing point X between the ground and excited states which is at higher energy level with respect to point O. In this situation, after the promotion to the excited state corresponding to point O, the luminescent center is relaxed non-radiatively to the lowest vibrational level corresponding to point B, as previously described. However, as temperature increases, the center can be thermally activated from point B to the crossover point X, from which it can reach the ground state and undergo thermal relaxation by multiphonon emission along the $X - C$ curve. This mechanism reduces the probability of emission due to direct transition from point B to point C, thus reducing the luminous efficiency of the phosphor.

Luminescent centers concentration dependence of the emission process

In principle, the emission intensity of a phosphor should increases with an increase in the concentration of a luminescent center in a given host lattice. This behavior, however, can be observed only up to a critical value for the concentration of the luminescent center: above this threshold value the luminescence intensity drops with increasing concentration (see Fig. 7.4).

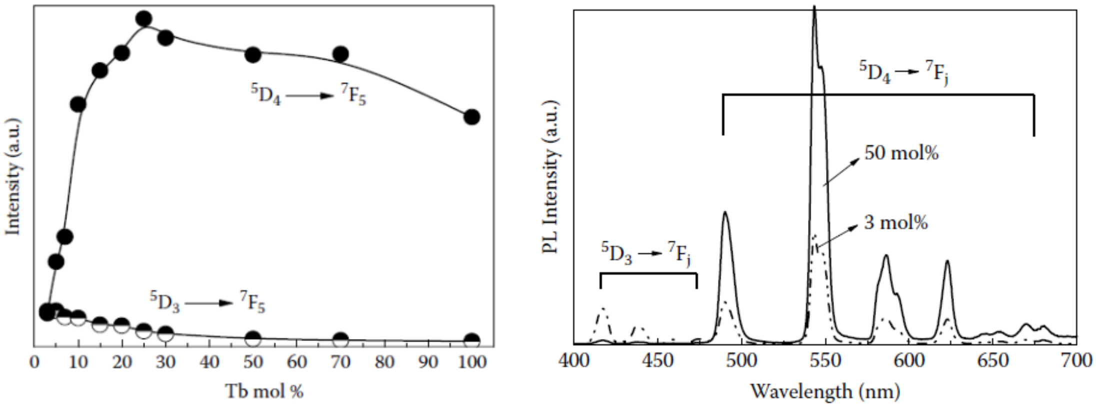

Figure 7.4: Emission intensity (left) and emission spectra (right) of Tb^{3+}-doped Ca-α-sialon in function of Tb^{3+} concentration.

The origin of this phenomenon, called *concentration quenching of luminescence*, is strictly related to the energy transfer between the luminescence centers: at the critical concentration, the distance between luminescent centers becomes so short that the efficiency of the energy transfer process starts decaying. The two main mechanisms responsible for that decay are the *donor-killer energy migration* and the *cross-relaxation.*

Donor-killer energy migration. In specific cases, the excess energy gained by the ion after excitation can be consecutively transferred to several centers before being radiatively released thanks to efficient energy transfer processes. However, energy transfer may also occurs towards acceptor/trap states originating from impurities or defects within the phosphor material. Since these acceptors then emit the absorbed excitation energy through non-radiative thermal relaxation processes, they eventually act as luminescence “killers”.

Cross-relaxation mechanism. This process describes the loss in energy transfer among luminescent centers due to resonant energy transfer between two identical adjacent centers with appropriate energy-level structure. This mechanism is responsible for the experimentally-observed concentration quenching of Tb^{3+} doped phosphors (Fig. 7.4), schematically reported in Figure 7.5.

The quenching process can be interpreted as follows: for low concentration values of Tb^{3+}, the radiative emissions due to the $^5D_3 \longrightarrow {}^7Fj$ transition dominates. With increasing concentration, a resonant interaction between two neighboring Tb^{3+} ions

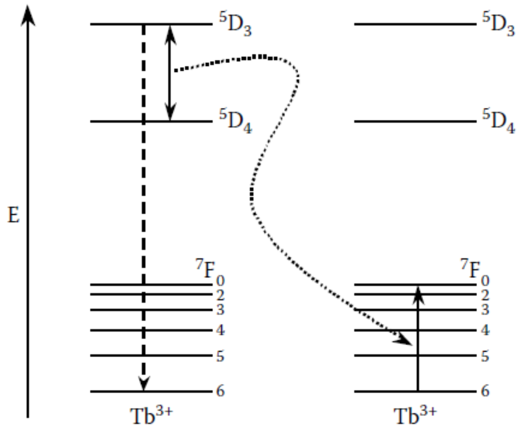

Figure 7.5: Quenching of the $^5D_3 \longrightarrow {}^7Fj$ emission due to cross-relaxation mechanism in Tb^{3+}-doped phosphors.

may take place, thus inducing the transfer of part of the energy of the $^5D_3$, $^5D_4$ levels of the excited (donor) ions to the $^7F_0$, $^7F_6$ levels of (acceptor) ions in the ground state. As a result of cross relaxation, the donor ions will be in the $^5D_4$ energy level, while the acceptor ions will be promoted to the $^7F_0$ level. Correspondingly, the luminescence due to the $^5D_3 \longrightarrow {}^7Fj$ transition is quenched, whereas the emission originating from the $^5D_4 \longrightarrow {}^7Fj$ transition is enhanced, as reported in the right plot of Figure 7.4.

Chapter 8

Reliability of blue phosphors for near-UV excitation

Within this chapter the operating limits of blue-emitting phosphors for 405 nm excitation are investigated. To this aim, several samples of Eu^{2+}-doped commercial phosphorescent material were first prepared by low-rpm spin coating and then submitted to thermal and/or optical stresses. The variation in the luminescence spectra and in the chemico-physical properties of the phosphors were evaluated by means of photo-luminescence measurements and advanced material analysis techniques. The experimental results, reported in the following sections, showed that both stress under high optical excitation and high-temperature (>400 °C) pure thermal stress can induce the oxidation of the the Eu^{2+} centers into Eu^{3+} ions, thus reducing the optical efficiency at the emission wavelength of interest.

The work presented in this chapter is partially supported by the New Energy and Industrial Technology Development Organization (NEDO), Japan, under the Strategic Innovation Program for Energy Conservation Technologies.

8.1 Characterization of blue-emitting phosphor

8.1.1 Chemico-physical analysis

The phosphorescent pigment under analysis is the SAB-L pigment, by Nemoto Industries. This material has been developed in order to attain a peak emission wavelength of $448nm$ (blue), whereas the excitation range, tuned for UV light sources, ranges from $200nm$ to $400nm$ (see Fig. 8.1).

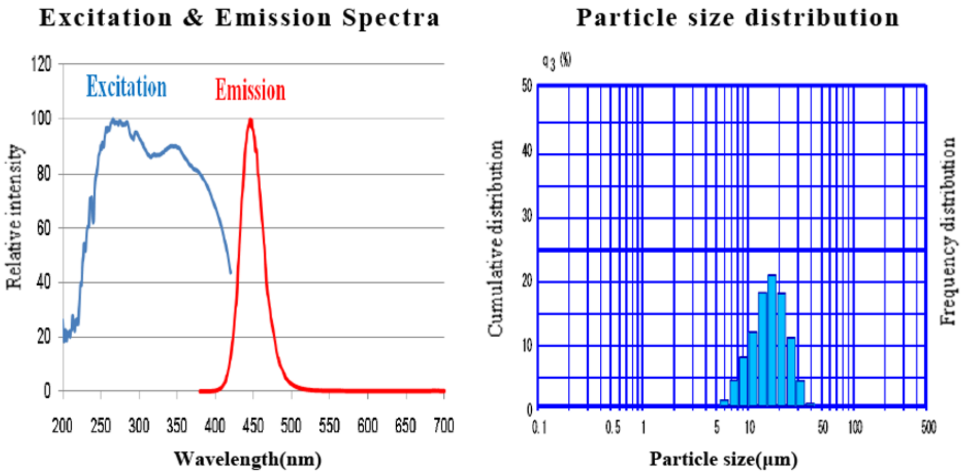

Figure 8.1: SAB-L pigment characteristics. On the left: emission and excitation spectra. On the right: particle size distribution. Data provided by the manufacturer.

From a physical point of view, the phosphorescent material is a white looking powder, whose typical grain size ranges from 5 μm to 40 μm, with an average of about 16 μm. For experimental purposes, the powder was deposited onto a thermally conductive sapphire substrate by a low rpm *spin-coating* technique. To be more specific, the powder was mixed in a 50:50 ratio with benzyl alcohol (employed as solvent/carrier fluid). A fixed amount of that mixture was then taken with a pipette and placed on top of the sapphire substrate, previously arranged in the spin-coater. After the spin-coating step, the phosphor-covered substrate was placed inside a thermal chamber at 250 °C for 7 minutes, in order to let the solvent evaporate. After this deposition procedure, the phosphor powder is spread in a solid phase across the surface of the substrate. Since after the evaporation of the alcohol no foreign materials are present in the sample, this procedure ensures that only the phosphor particles will be stressed and characterized. Despite the absence of an encapsulant material may increase the risk of contamination and degradation by external agents (moisture, oxygen, dust, etc...), the possibility of analyzing only the bare material offers far more advantages.

The quality of the deposition was evaluated by means of a profilometer with scanning red laser interferometer (model MSA-500 from Polytec).

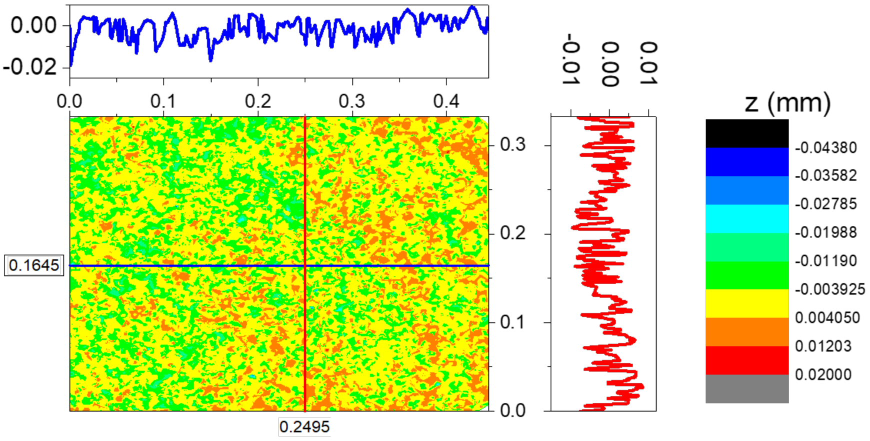

Figure 8.2: SAB-L Profiling of a 0.5 mm by 0.5 mm portion of the phosphor-coated surface. All units are in mm.

As can be seen from figure 8.2, the variation in the height of the deposition, which shows a peak to peak distance of $70\mu m$ with a variance of $5.3\mu m$, is compatible with the dimensions of the phosphor grains: this suggests that a very good level of deposition quality could be achieved with the adopted technique. That conclusion was further demonstrated by the ESEM images taken on an untreated sample, here reported in Fig. 8.3: the detected variations are mostly related to the different particles dimensions rather than to an improper deposition.

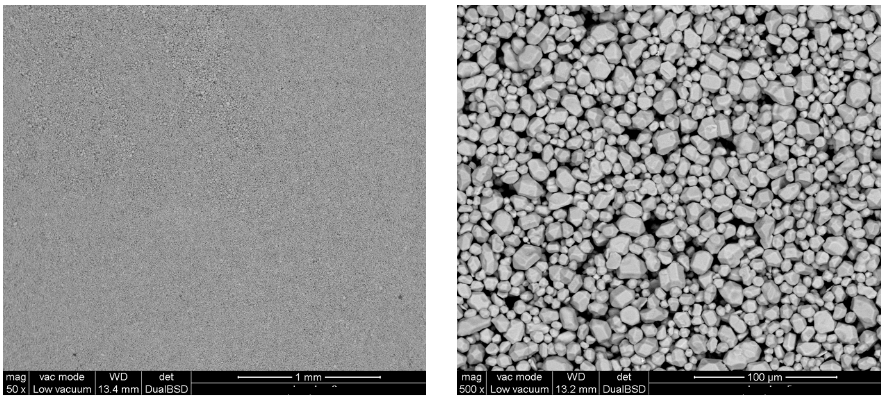

(a) (b)

Figure 8.3: Backscattered electroncs ESEM images of the phosphor surface taken at 50x (a) and 500x (b) magnification.

The same ESEM apparatus, equipped with an EDX (Energy Dispersive X-Ray) analysis module, was employed to retrieve some basic information regarding the chemical composition of the luminescent material. The EDX spectrum, reported in Fig. 8.4, reveals the presence of O, Sr, P, Ca, Cl and Ba.

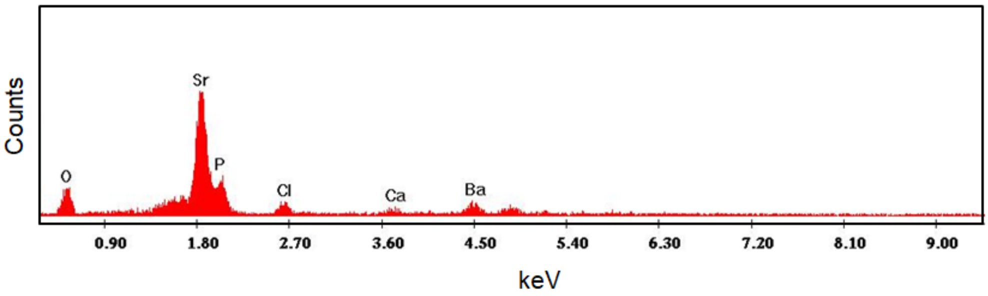

Figure 8.4: EDX spectrum of an untreated sample of SAB-L phosphor.

Considering that the optically active element within the phosphor structure is Eu^{2+}, the chemical analysis suggested that the composition of the phosphor under investigation, not disclosed by the manufacturer, should not be dissimilar to

$$(\mathrm{Sr}, \mathrm{Ba}, \mathrm{Ca})_5(\mathrm{PO}_4)_3\mathrm{Cl} : \mathrm{Eu}^{2+} \tag{8.1}$$

which identifies a large family of Eu^{2+}-activated alkaline-earth halophosphates usually employed in the past as luminescence materials for fluorescence lamps, and, more recently, for solid-state lghting [85]. By adjusting the relative concentration of the Sr, Ba, Ca and Eu species it is possible to tune, within specific limits, both the emission and excitation spectra, as well as to optimize the conversion efficiency of the material and its reliability. For this specific case of study, chemical analysis suggests the following concentration ranges: $0.66 \leq \mathrm{Sr} \leq 0.83$, $0.1 \leq \mathrm{Ba} \leq 0.2$, $0.05 \leq \mathrm{Ca} \leq 0.1$ and $0.02 \leq \mathrm{Eu} \leq 0.04$.

8.1.2 Optical properties

In order to characterize the emission properties of the luminescence material under investigation, a custom setup for PL (Photo-Luminescence) measurement was arranged. As visible in Fig. 8.5, the phosphor-coated sapphire substrate was placed on top of a temperature controlled chuck. Above the sample, a collimated $375nm$ power-controlled laser source was placed in orthogonal position (model LBX-375 from Oxxius, $16mW$ maximum power). For power density evaluation, the shape and dimensions of the laser beam were evaluated by direct imaging of the PL spot on the phosphor surface by

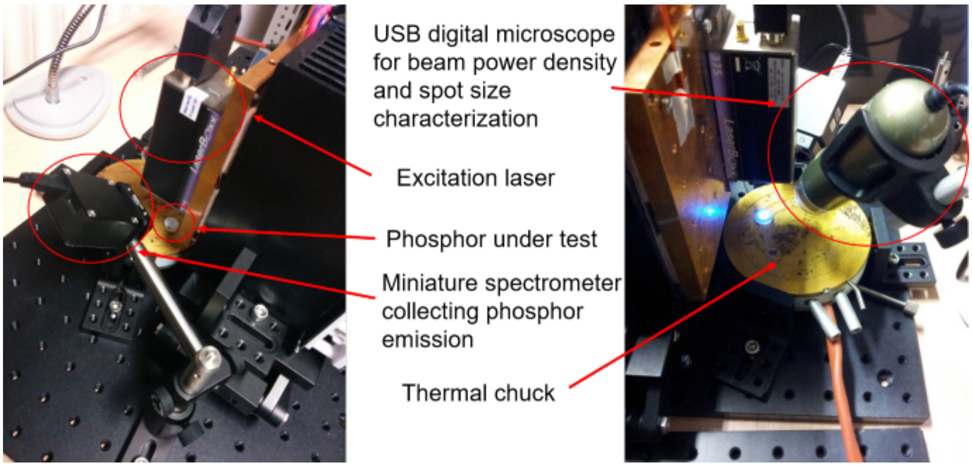

Figure 8.5: Experimental setup for the characterization of SAB-L phosphors.

means of a digital microscope. Finally, the PL spectra were collected with a Labview-controlled miniature spectrometer (model STS-VIS from Ocean Optics).

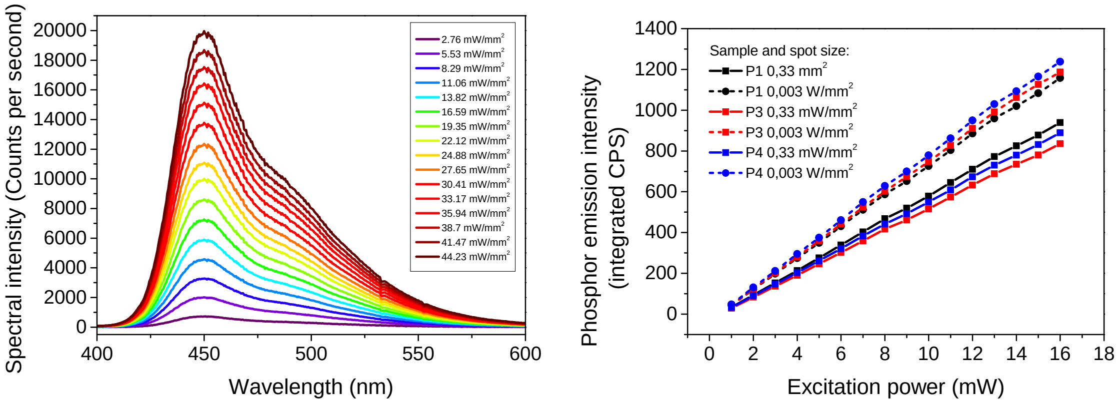

(a) (b)

Figure 8.6: PL spectra acquired under different 375 nm excitation densities at room temperature (25 ° C) (a). PL intensity in function of the laser excitation power for three different samples and two different spot sizes (b).

With regard to the dependence on excitation intensity, the material under analysis showed a good linearity over a wide excitation power density range (Fig. 8.6b), which testified than no saturation of the emission or thermal quenching were taking place. Interestingly, the PL spectra showed a broad shoulder around 500 *nm*, probably due to the specific tuning of the phosphor blend aimed at increasing the CRI and attaining a specific green-shifted color point of the emitted light. This can be achieved by increasing the ratio of the $Ca_5(PO_4)_3Cl : Eu^{2+}$ to $Sr_5(PO_4)_3Cl : Eu^{2+}$ species, which feature a typical emission peak of $460\,nm$ and $445\,nm$, respectively.

The behavior of the PL emission in function of temperature is reported in Fig. 8.7. Excitation wavelength and spot size employed are respectively 375 nm and 0.33 mm^2.

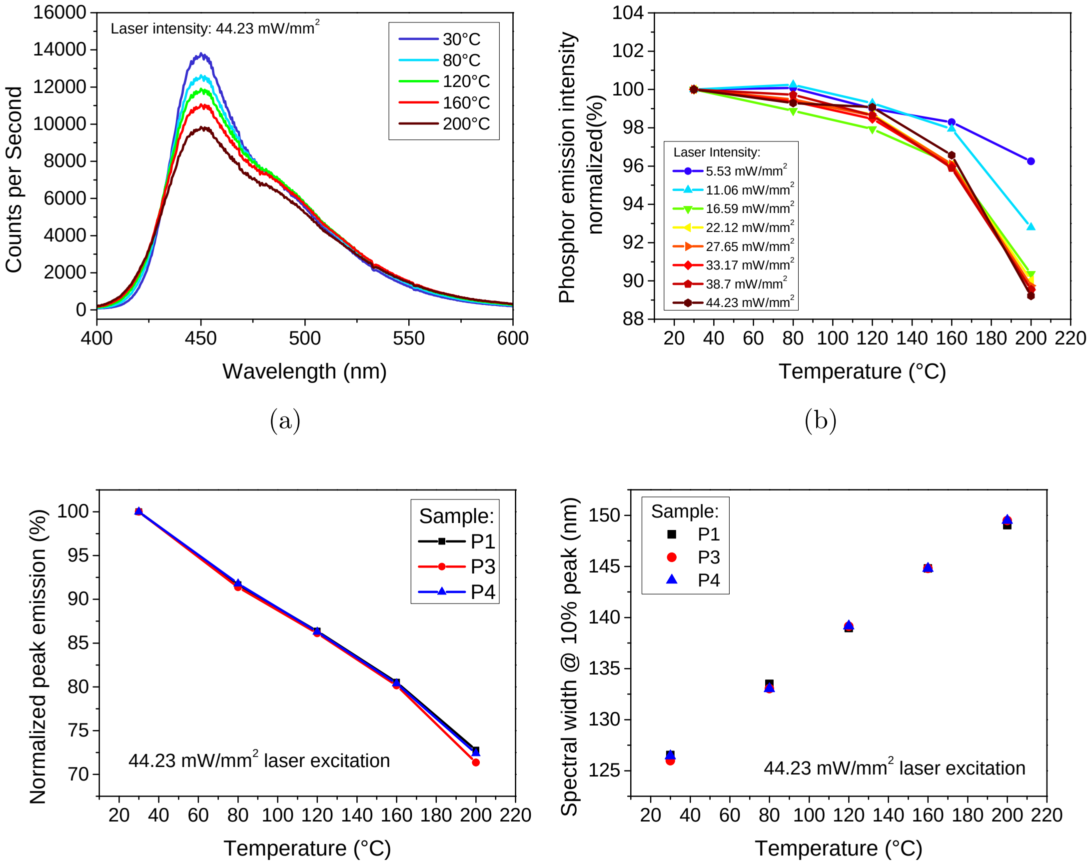

(a) (b)

(c) (d)

Figure 8.7: Temperature dependence of PL emission: PL spectra (a), total emission intensity (integrated counts per second) (b), peak intensity (c) and spectrum broadening at 10% maximum (d).

Under constant excitation intensity, the spectra exhibited the expected reduction in the peak intensity and the broadening of the spectral tails with increasing temperature (Fig 8.7a). The less than 4% peak intensity drop at 200 °C for low excitation densities reveals a very good thermal quenching behavior. Similar thermal droop was exhibited at various excitation power densities, though the reduction in the total luminescence was found to be more intense at higher excitation levels, but still within an acceptable maximum 11 % drop with respect to the emission at 30 °C (Fig, 8.7b).

The observed spectrum broadening is a minor effect compared to the measured spectral width of 150 nm (Fig, 8.7d), nonetheless the uneven decrease in PL signal across the whole range of emission caused the peak intensity, reported in Figure 8.7c, to follow a linear trend with temperature, whereas the integrated emission from 400 nm

to 650 nm followed a milder linear decay trend. The good consistency of the experimental data retrieved from the three different samples further validates the employed deposition method.

8.2 Effect of thermal stress

Due to the Stokes shift, and to the non unitary quantum yield, during high power density operation the luminescent material can reach very high temperatures that can negatively affect both the optical performance of the material and its long term reliability.

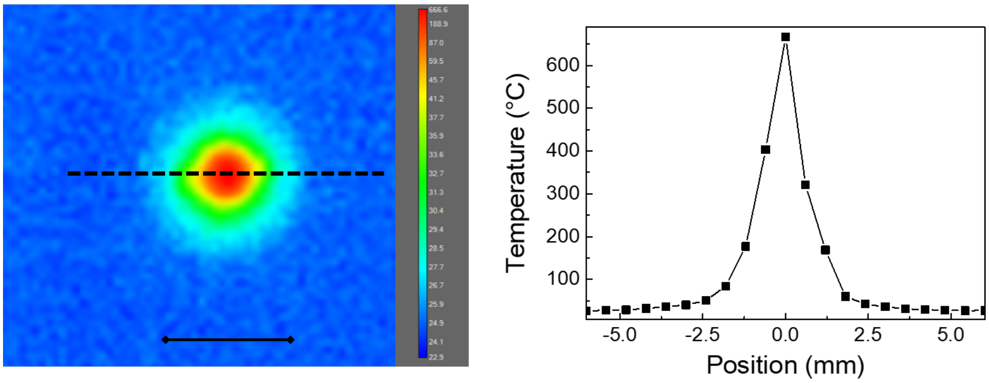

Figure 8.8: Thermography of the luminescent spot during 405 nm excitation at 3.2 W/mm^2 and T_{AMB}=25° C, with a spot size of 716 μm by 567μm.

For instance, the IR imaging of the stress spot during a 405 nm - 3.2 W/mm^2 excitation experiment reported in Figure 8.8 shows a peak phosphor temperature well in excess of 300 $^\circ C$. While the previously reported measurements showed that the luminescent material under analysis should not be operated in such a temperature regime, since the overall efficiency becomes limited by the thermal droop, a comprehensive analysis on the effects of thermal aging is due, in order to identify the limiting operating conditions in LARP luminaires with reduced thermal management capabilities.

To this aim, three sets of long-term degradation experiments have been arranged: *(a)* a pure thermal stress under moderate temperatures (110 °C to 300 °C); *(b)* a pure thermal stress at high temperature (450 °C to 500 °C) and *(c)* a low temperature stress in a moist environment (85 °C, 80% humidity). This latter stress was aimed at finding whether the oxidation processes that is typically responsible for the thermally-induced degradation of Eu-doped phosphors could be accelerated by humidity or not [86], thus proving the need for a proper phosphor encapsulant material.

In the aforementioned experiments different phosphor samples were submitted to extended thermal cycles in climate chambers or muffle ovens. The characterization of the samples, performed at regular intervals, was carried out by means of transmission PL measurements. The experimental setup for PL analysis was arranged as follows: the sample substrate was held vertically and placed in front of the spectrometer with the phosphor coated surface pointing towards a 405 nm high-power LED, which was chosen for this suite of tests as excitation source. In order to guarantee a constant excitation power density on the sample, a feedback photodiode, shielded from the PL radiation emitted by the phosphors, was employed in order to measure the LED intensity and implement the current-control loop of the LED. The results of the long-term aging experiments at constant (moderate) temperatures are summarized in figure 8.9.

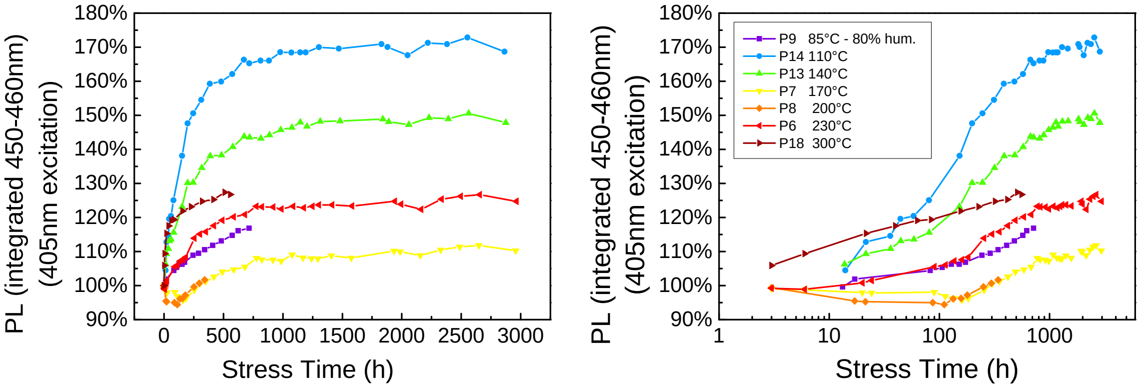

(a) (b)

Figure 8.9: Lorng-term aging at moderate temperatures: normalized trend over stress time of the (transmitted) PL signal in (a) linear and (b) semi-logarithmic scale.

The degradation kinetics show no tangible worsening of the PL emission across all the stress scenarios. By contrast, the material under investigation exhibited a noticeable increase in luminescence. This process was not found to be thermally activated, and did not induce significant changes in the spectral shape, aside from a minor decrease in the relative PL emission in the long wavelength region between 475 nm and 500 nm (see Fig. 8.10).

On the other hand, the degradation kinetics at high stress temperature reported in Fig. 8.11 show remarkable (and reproducible among different samples) PL signal degradation, even during the first 50 - 100 hours of stress. In this case, the degradation process was found to be thermally activated, with an activation energy for the $\mathrm{TTF}_{75\%}$, the time required by the sample to lose 25 % of its original PL signal strength, around 1.6 eV (preliminary estimation). As will be shown in the following sections, this be-

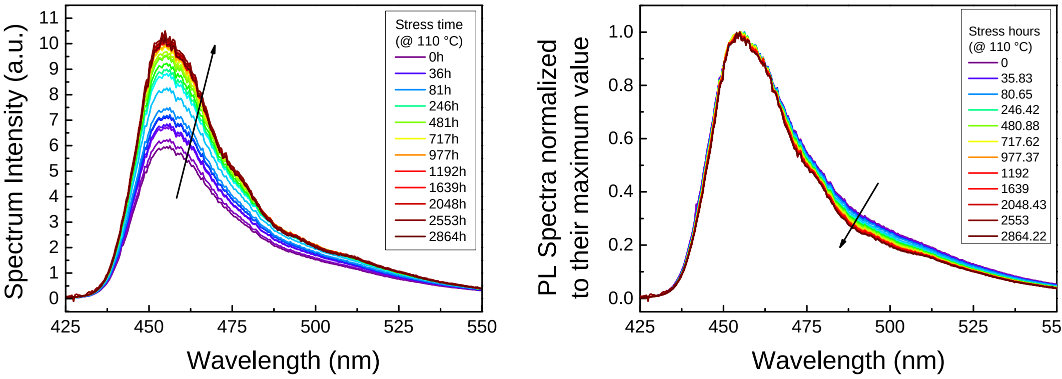

(a) (b)

Figure 8.10: PL spectra acquired during thermal aging at 110 ° C: absolute values (a) and (b) normalized to their maximum value.

havior may be explained by the thermally-induced ionization of Eu^{2+} centers due to high temperature baking in air environment.

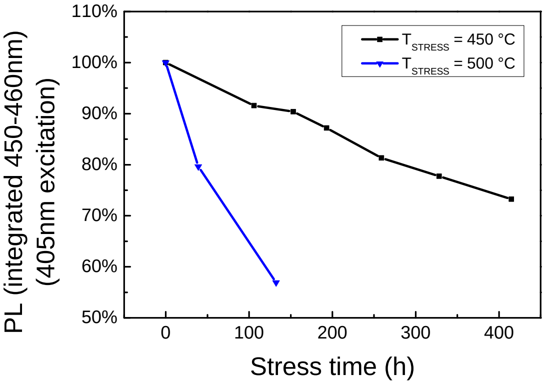

Figure 8.11: Lorng-term aging at high temperatures: normalized trend over stress time of the (transmitted) PL signal.

8.3 Stress under optical excitation

8.3.1 Stress under 375 nm excitation

Temperature is not the only accelerating factor for the degradation processes of Eu-doped luminescent materials. As testified by several reports, the prolonged exposure to high-intensity and high-energy radiation can promote multiple degradation mechanisms, including the photoinization of the Eu^{2+} centers [87], the creation of optically and electrically active traps [88] or the migration of Eu^{2+} centers toward different crystalline sites [89]. In order to explore the reliability of the phosphor under investigation towards high optical density operating conditions, we employed the same experimental setup formerly described in section 8.1.2. In this case the laser source was kept on at a fixed power (density) level for the entire course of the stress, while the PL spectra were regularly sampled by the spectrometer. The results of the short-term aging at very high excitation intensity, namely 25 W/mm^2, and substrate temperatures ranging from 30 °C to 230 °C are reported in figure 8.12.

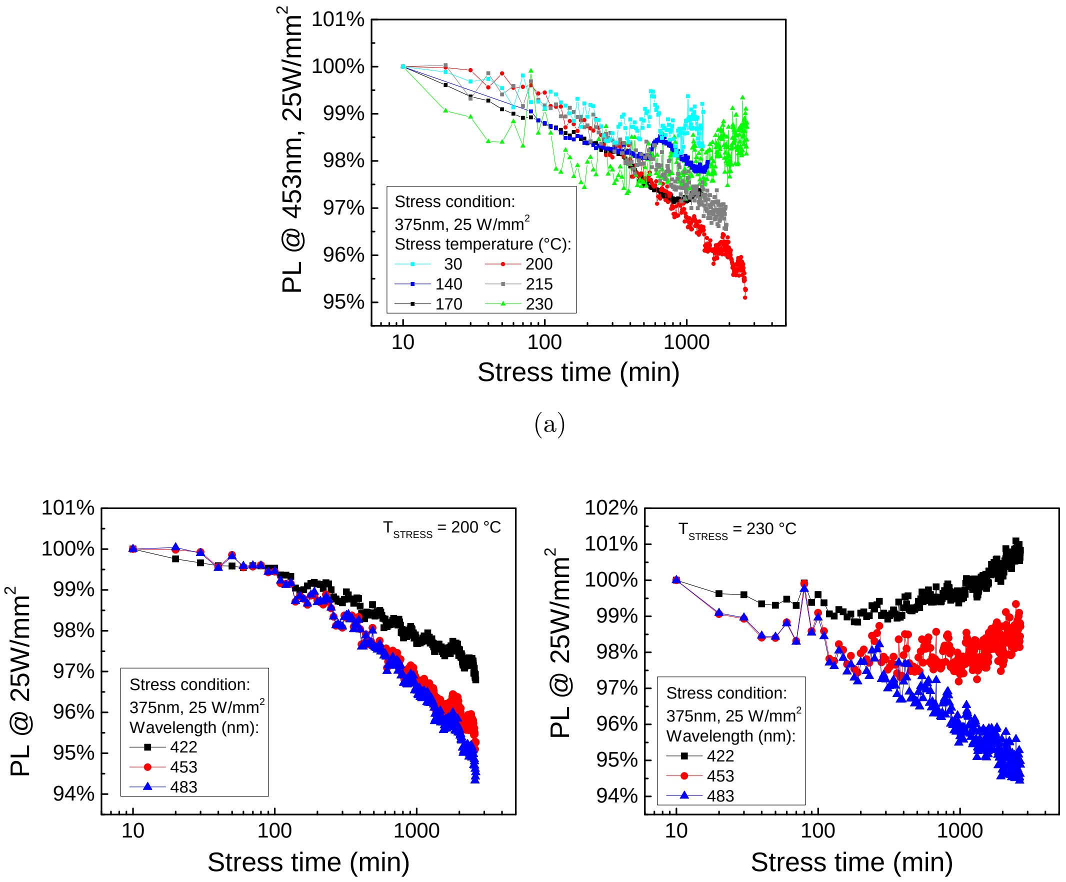

(a)

(b)

(c)

Figure 8.12: Stress under optical excitation at 375 nm - 25 W/mm^2. (a) PL trend during stress at different substrate temperatures. Wavelength-dependent PL trend during the stress experiments at 200 °C (b) and 230 °C (c).

The PL kinetics in plot 8.12a show that up to a substrate temperature of 200 °C the degradation process was positively affected by temperature. Moreover, plot 8.12b reveals a less prominent effect on the high-energy side of the spectra: since this peculiar trend in the short-wavelength range could also be observed as a consequence of pure thermal stress, we can conclude that probably the same temperature-driven degradation process was active during both stress experiments. Interestingly, above the 200 °C threshold, a competing mechanism responsible for the increase of the emission at the high-energy end of the spectra becomes visible (see Fig. 8.12c). Due to the presence of an antagonist degradation process, an to the fact that the actual stress temperature of the heavily excited phosphor spot is unknown, the positive aging trend registered during high-temperature and high optical excitation stress cannot be directly related to the annealing phenomenon showed by thermally treated samples. Nonetheless, additional information regarding the wavelength-dependent degradation process could be obtained by further analysis of the PL data reported in Figure 8.13, which revealed a strong correlation between the trends of the PL signal at high-energy and of the reflected laser signal.

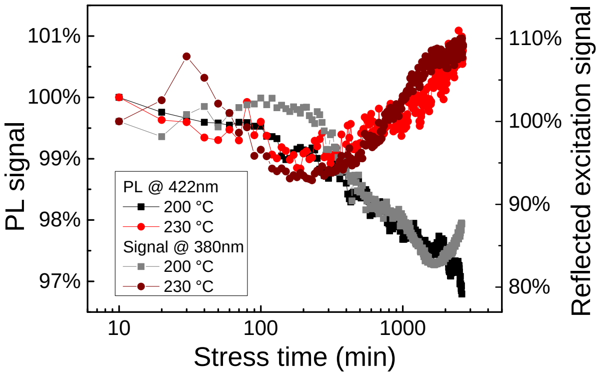

Figure 8.13: PL signal and reflected laser signal trends during stress at 375 nm excitation.

This correlation suggests that the PL trend, at least at the high-energy side of the spectra, can possibly be related to a process responsible for the variation of the layer reflectivity. This kind of degradation may be either due to the stress-induced opacization or oxidation of the surface, or to the spatial redistribution of the phosphor particles. In order to pinpoint the root cause for this change in reflectivity, spatially and wavelength-resolved photo-luminescence maps of the stress spot were taken.

Figure 8.14a reports the micrography of the stressed area, which clearly shows a redistribution of the phosphor particles around a hole, visually appearing as a dark spot. As shown by the PL map in Fig. 8.14b, the dark spot has a highly reduced luminescence at 453 nm, which correlates with the reduction in the global PL emission registered during aging at 200 °C and 25 W/mm^2. This variation in the (wavelegnth-dependent) optical properties of the stressed area, and of the sorrounding material, may be related to a decrease in the photon absorption and/or escape probability due to stress-induced changes in the refractive index or in the absorption coefficient of the material, as suggested by Klaassen in [90].

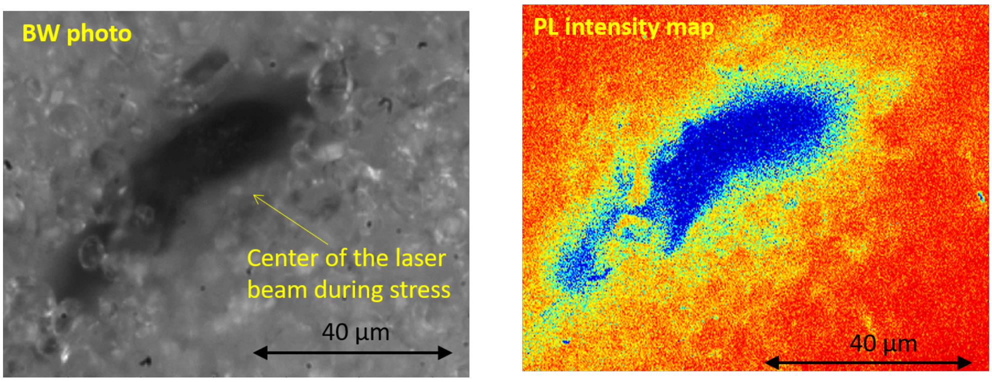

(a) (b)

Figure 8.14: Morphological changes induced by high temperature and high optical excitation stress on the phosphor deposition: micrography (a) and false color 375 nm excitation PL map selectively filtered at 453 nm (b).

8.3.2 Stress under 405 nm excitation

For the second series of degradation experiments under optical excitation, a 405 nm high-power laser diode was employed as optical source. Due the high availability and the high efficiency of modern 405 nm solid state sources, this excitation condition represents the sweet spot from an engineering point of view [82]. However, the reduced conversion efficiency of the phosphorescent material at this lower energy wavelength may pose different reliability issues, especially related to the increased self-heating of the material.

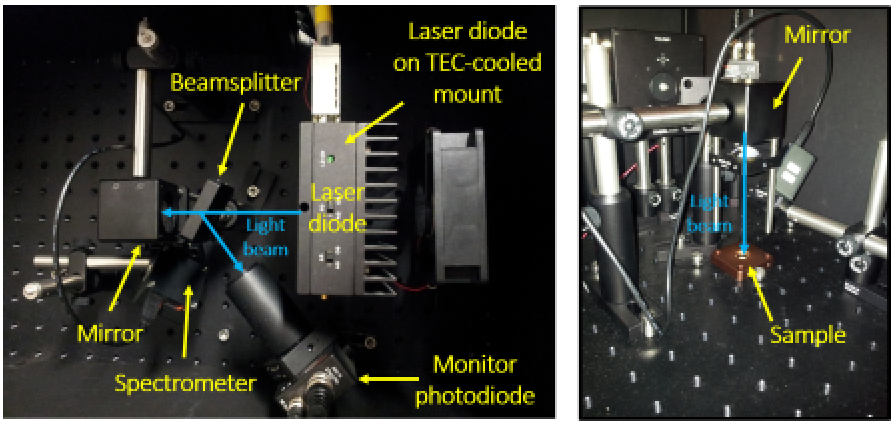

Figure 8.15: Experimental setup for stress and characterization of blue-emitting phosphors under high levels of optical excitation at 405 nm.

The characterization of the effects of prolonged exposure to 405 nm high-intensity radiation was carried out by means of the experimental setup reported in figure 8.15. The optical source, a high-power 405 nm LD capable of emitting up to 2.4 W at 1.5 A, was placed inside a thermo-controlled fixture and properly collimated. Optical feedback for constant-power operation was achieved by means of a monitoring photodiode and a beam-sampler, from which the outgoing excitation beam was redirected towards the horizontally-placed sample with a common 45°mirror, and focused onto the phosphor surface with a properly positioned lens. Finally, in order to attain complete power-calibration of the setup, the readings of a power meter (model S142C from Thorlabs) placed below the focusing lens were compared with the readings of the photodiode, which were then employed as actual set-points in the control loop. With this experimental apparatus we were able to replicate the same aging conditions employed for the stress tests at 375 nm excitation.

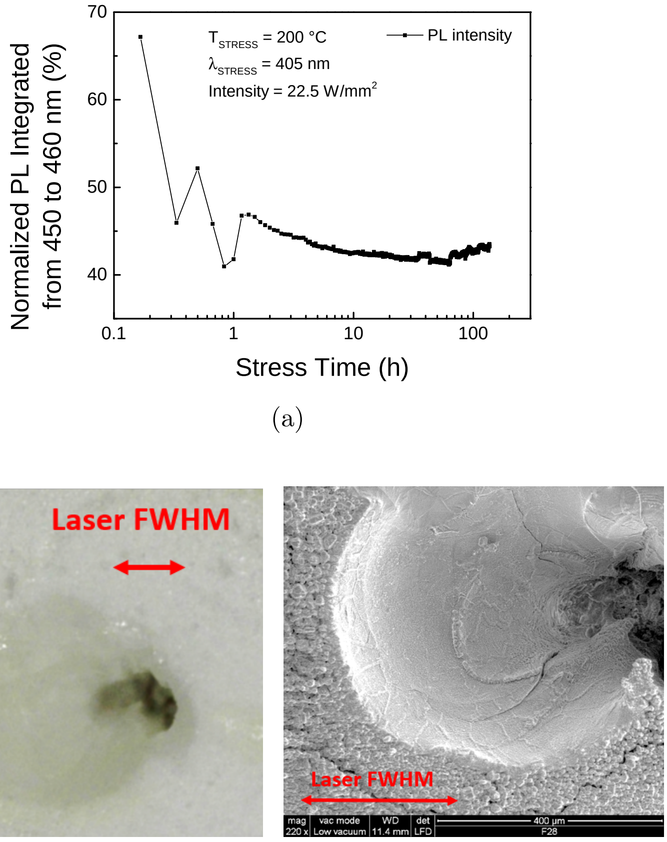

(a)

(b) (c)

Figure 8.16: Stress under optical excitation at 405 nm - 22.5 W/mm^2 - 200 °C. (a) trend during stress of PL signal. (b) Optical image and (c) secondary electrons ESEM image of the excitation spot after stress.

Figure 8.16 summarizes the results of the long-term stress performed under optical excitation at 22.5 W/mm^2 and 200 °C. The sample experienced a strong 55 % PL decay during the first 20 minutes of stress. As visibile from figures 8.16b and 8.16c, the extreme stress conditions induced a morphological degradation of the phosphorescent layer, which underwent a phase-change into a glass/ceramic-like material.

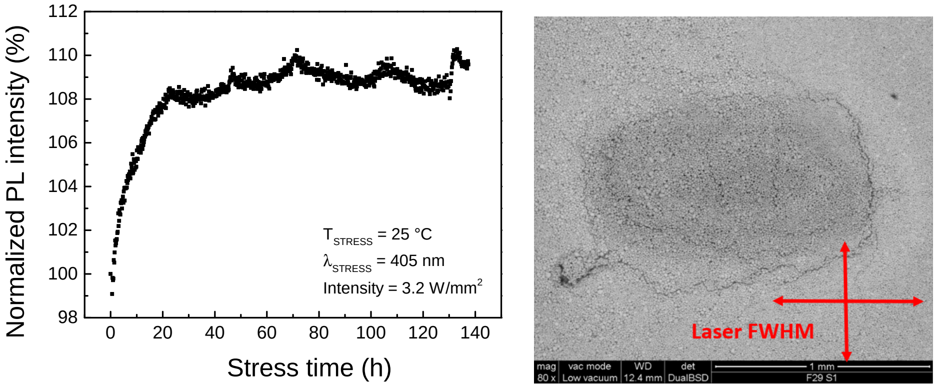

(a) (b)

Figure 8.17: Stress under optical excitation at 405 nm - 3.2 W/mm^2 - 25 °C. Trend during stress of PL signal (a) and backscattered electrons ESEM image of the excitation spot after stress (b).

For the following stress experiment, a milder 3.2 W/mm^2 excitation intensity and a substrate temperature of 25 °C were employed. In this case the PL trend exhibited a 10 % increase over stress time (Fig 8.17a). In contrast to that, optical inspection of the excitation spot revealed minor signs of morphological degradation of the phosphor layer, including small cracks and a slight browning of the grains around the stress spot. Degradation of the luminescent material was further confirmed by several other analysis. First, ESEM backscattered electrons imaging showed a variation in the chemical composition of the optically excited area and of its surroundings (8.17b). Secondly, very low intensity LED excitation of the phosphor coated substrate revealed a *dark spot* in correspondence of the stressed area (Fig. 8.18a).

Interestingly, the non-emissive spot could only be observed by direct excitation of the phosphor surface, whereas upward illumination induced a uniform photo-emission: considering that no complete absorption of the excitation radiation was taking place, and thus the upper portion of the material could still be pumped from the back, this behavior may suggest that only the upper layers of the phosphor were affected by degradation. Lastly, a reddish PL signal, absent in untreated areas of the sample, could be detected by low-intensity (0.21 W/mm^2) 405 nm laser excitation of the stressed spot (Fig. 8.18b). As reported in Figure 8.18c, the spurious red luminescence was found to have an emission linewidth ranging from about 609 nm to 624 nm, compatible with an increased presence of Eu^{3+} centers [91].

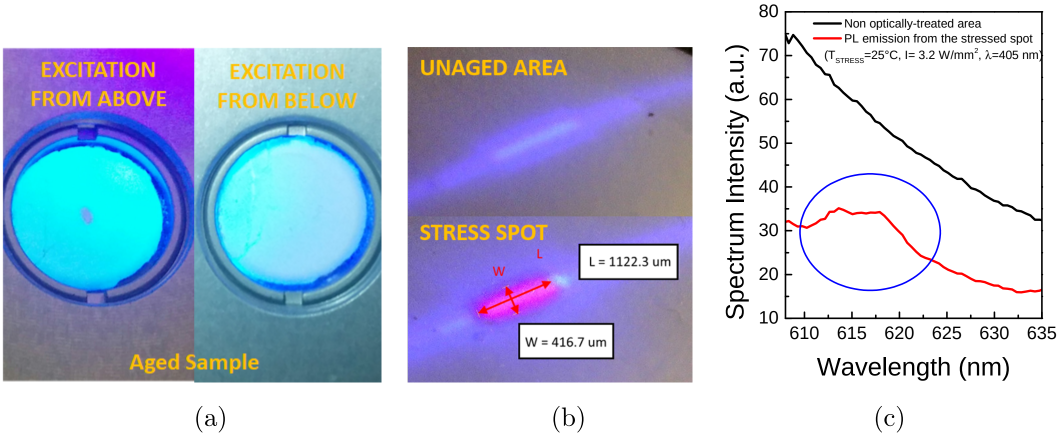

Figure 8.18: Stress under optical excitation at 405 nm - 3.2 W/mm^2 - 25 °C. (a) Comparison between the surface emission of the phosphor with low intensity excitation from above (left) and from below (right) the sample. (b) Emission from the stressed spot under low intensity excitation. (c) PL spectra in the low energy region of a treated and an untreated phosphor region.

In order to investigate step-by-step the spectral changes in the red spectral region and to acquire further details on the kinetics of this degradation phenomenon, the same stress experiment was repeated in a second spot of the same phosphor deposition.

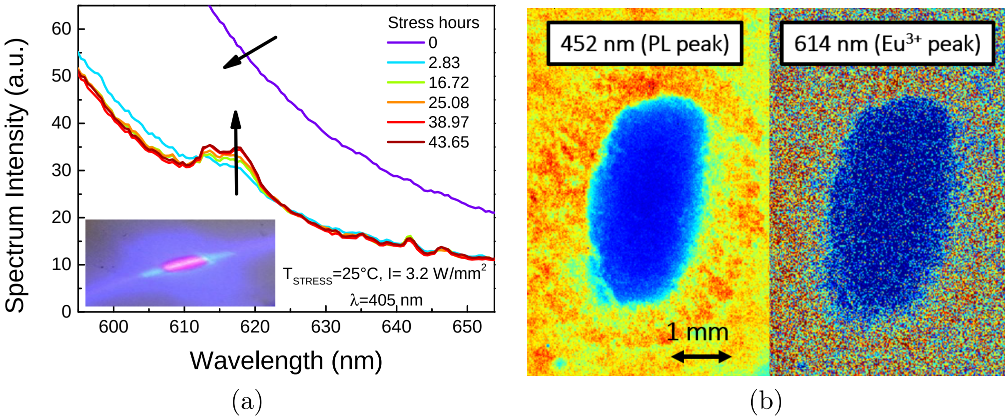

Figure 8.19: Stress under optical excitation at 405 nm - 3.2 W/mm^2 - 25 °C (second sample). Stress-induced variation of the PL spectra measured at 0.21 W/mm^2 in the low energy region, with inset image showing the red emission of the aged phosphor discernible by naked eye (a). Spatially and wavelength resolved PL map of the stressed spot (low-intensity excitation at 405 nm) (b).

As reported in figure 8.19a, the intensity of the red luminescence peak was found to gradually increase with stress time, in an almost linear fashion. The extension of the degraded red-emitting area was then evaluated by means of spatially and wavelength resolved PL measurements (Fig. 8.19b). The comparison between the monochromatic emission maps at 452 *nm* and 614 *nm*, respectively the peak emission wavelengths of the phosphors and of the red luminescence, showed no peculiar differences. Assuming from optical images that the red emission originates from the center of stress spot, this may indicate that under the very low (LED) excitation condition employed for the measurement the process responsible for the observed spurious emission is relatively weak. This reduced emission rate may either be due to a reduced concentration in the chemical species which serves as optically active element, previously assumed to be Eu^{3+}, or to an inherently low efficiency of the process itself, probably related to a non-optimized chemical configuration of the host lattice or the the increased Stokes shift related to the spurious emission process.

8.4 Advanced characterization of thermally and optically treated samples

The experimental results reported in the previous section showed that aging of the phosphorescent material under moderate power densities can induce a catastrophic degradation of its luminescence properties. Since the drop in the PL signal could be related to an increase in a characteristic red emission around 613 *nm*, the degradation mechanism was preliminarily ascribed to the photo- and/or thermally-induced auto-ionization of the Eu^{2+} centers into Eu^{3+} ions. In order to prove this hypothesis, several samples of thermally and optically stressed phosphors were analyzed by means of advanced characterization techniques, described in the following paragraphs.

8.4.1 High-sensitivity luminescence spectroscopy

By means of a high sensitivity spectrometer, model CAS 140CT by Instrument Systems, the emission spectrum of the luminescent material was further investigated.

The results of the analysis, reported in Figure 8.20, show that as a consequence of the thermal and/or optical stress, characteristic spectral lines become visible or disappear, depending on the wavelength region. In Region I, UV treatment and annealing at 650° C induced the increase in the emission centered around 615 *nm*, which is commonly ascribed to the $^5D_0 \longrightarrow {}^7F_2$ Eu^{3+} transition [91, 92]. Similarly, in region II stress generated a spurious emission peak around 695 *nm* and 705 *nm*, which can be related to the Eu^{3+} $^5D_0 \longrightarrow {}^7F_4$ transitions [91, 93]. Finally, while the luminescence peaks of region III can be associated with the $^5D_0 \longrightarrow {}^7F_6$ transition of the Eu^{3+} compounds,

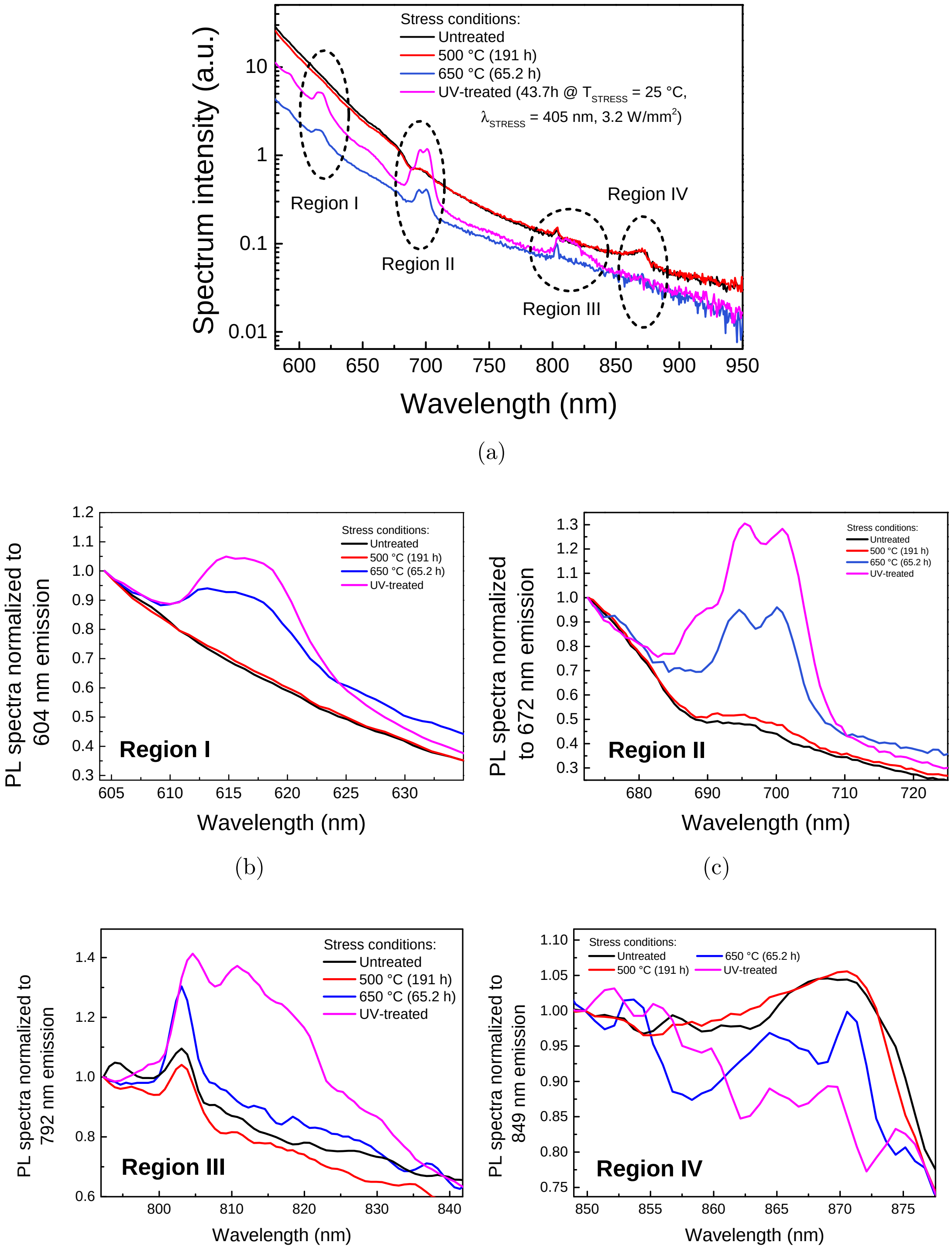

(a)

(b)

(c)

(d)

(e)

Figure 8.20: Low intensity normalized PL spectra in the long wavelength region acquired by the CAS 140CT spectrometer. The UV treatment referred to in the plot legend corresponds to the $405\,nm$ - $3.2\,W/mm^2$ - 25 °C - 44 hours stress described in Fig. 8.19.

no reference was found for the 870 nm peak located in region IV. These experimental results support the hypothesis that high-temperature or high optical excitation stress may induce degradation of the material due to the ionization of the optically active Eu^{2+} centers into Eu^{3+} ions.

8.4.2 Electron Paramagnetic Resonance(EPR)

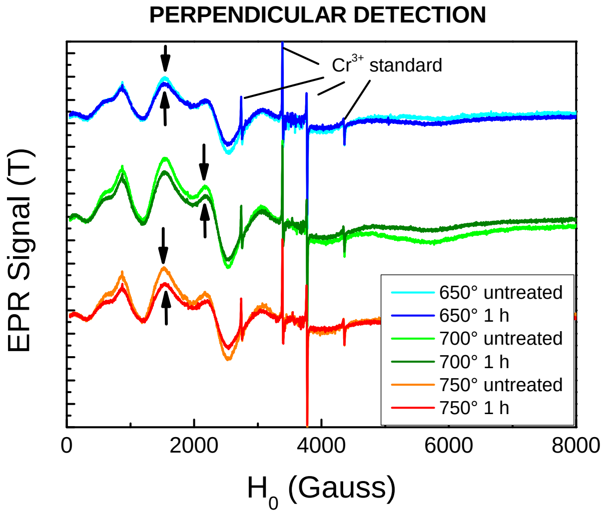

Figure 8.21: EPR analysis of three different phosphor samples thermally treated for 1 hour at 650 ° C, 700 ° C and 750 ° C.

Electron Paramagnetic Resonance (EPR) spectroscopy is a material analysis technique aimed at finding and identifying atoms, ions or molecules with unpaired valence electrons (free radicals). This technique leverages an external magnetic field to characterize the nature of the bond between those electrons and the chemical species those belong to. Since the optically active Eu^{2+} centers in the material feature an electronic structure with unpaired valence electrons in the $4f^7$ orbital, this technique proved to be suitable for our investigation. Although EPR is not a proper quantitative characterization technique, to ensure the highest possible repeatability the material was stressed and measured *in-situ* inside the EPR tube, which is a quartz-made tube-shaped holder that is inserted inside the resonant EPR cavity in order to probe solid and liquid-phase samples with high intensity magnetic field. Moreover, reference and post-stress measurements were both performed during the same day, with the EPR apparatus kept switched on and in the same configuration. To this aim, the degradation process was accelerated by performing 1 h long thermal stresses at the temperatures of 650 ° C, 700 ° and 750 ° C. Finally, unavoidable fluctuations of the EPR signal were taken into account by normalizing the spectra to the value of a reference (solid) Cr^{3+} standard introduced inside the tube prior to each measurement, then removed. The results of the EPR analyses are reported in Figure 8.21.

As a consequence to the thermal stress, the (Eu^{2+}) EPR signal within the 0 – 3000 Gauss region experienced a decrease in intensity. The relative decrease was greater for higher stress-temperatures. Thus, the analysis suggests that very high temperature short-term stress can induce a significant decrease in the concentration of the Eu^{2+} species of the phosphor. The thermally-induced decrease was also found to be compatible with previous reports on the degradation of Eu-doped phosphors submitted to high-temperature thermal aging [94].

8.4.3 X-Ray Photoelectron Spectroscopy(XPS)

In section 8.3.2 we showed how moderate optical stress only degraded the surface layers of the phosphorescent material. In order to further understand the effects of this localized degradation on the chemical composition of the material, XPS characterization of both treated and untreated samples was performed. XPS, or X-Ray Photoelectron Spectroscopy, is a surface analysis technique capable of quantitatively evaluate the chemical composition and the electronic state of the elements within the first $10\,nm$ layer of a specific material. This is achieved by irradiating the surface of the sample with X-rays and by measuring both the number and the kinetic energies of the electrons emitted from the material. An XPS spectrum is then obtained by plotting the number of detected electrons versus their binding energy. The number of electrons is proportional to the amount of a specific element inside the probing volume, whereas peaks in correspondence of specific binding energies identify the electrons configuration within the atoms, and thus the material under investigation.

The XPS characterization of the blue-emitting phosphors was performed in collaboration with an external laboratory. The measurement parameters employed are the following: Alk-α X-Ray source, $50\,eV$ pass energy, C1s reference signal and an approximate scan depth of $1\,nm$ to $5\,nm$. The results are reported in Fig. 8.22
Being the XPS a quantitative analysis technique, typically to the parts per thousand range, the experimental data suggest that thermal stress induced a variation in the amount of Eu centers near the surface of the material. In particular, thermal aging at 500 °C showed a comparable increase of the both the Eu^{2+} and Eu^{3+} XPS peaks, suggesting a thermally-driven diffusion of the two chemical species towards the surface. On the other hand, stress at 650 °C induced an increase in the relative amount of Eu^{3+} with respect to the concentration of Eu^{2+}: this observation is compatible with the oxidation of Eu^{2+}, assisted by high temperature and by the oxygen-rich environment

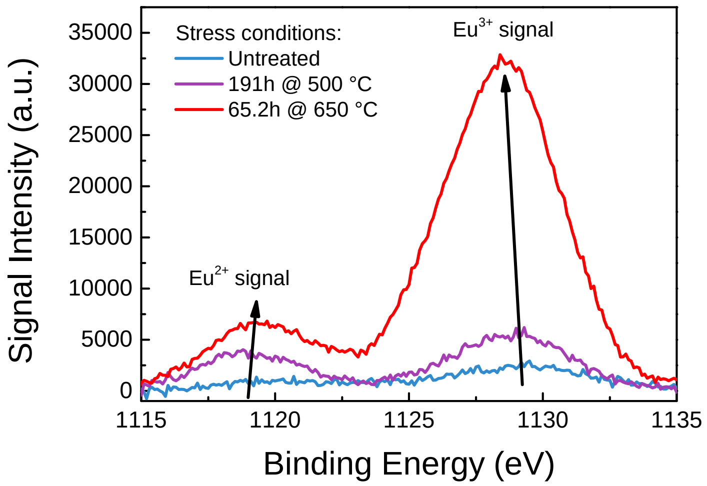

Figure 8.22: Variation of the phosphor XPS signature induced by thermal annealing at 500 °C and 650 °C.

near the surface of the sample [92]. The same relative increase in Eu^{3+} was previously observed in literature by means of XPS on both thermally and UV-treated phosphors, as reported in Figure 8.23.

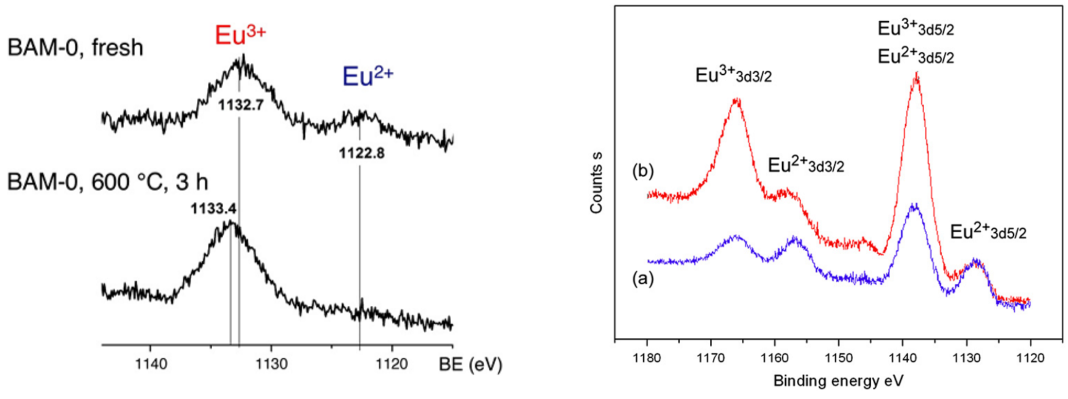

(a)

(b)

Figure 8.23: Literature reports of (a) thermally and (b) UV-induced Eu^{3+} oxidation investigated by means of XPS analysis on Eu-doped blue phosphors (from references [94] and [10]).

As suggested in [92], the degradation process may originate from the following reaction:

$$2\,\mathrm{Eu}^{2+} + \frac{1}{2}\mathrm{O}_2(\mathrm{g}) + \mathrm{V}_\mathrm{o} \longrightarrow 2\,\mathrm{Eu}^{3+} + {\mathrm{O}_\mathrm{o}}^{2-}$$

where $\mathrm{O}_2(\mathrm{g})$ is a gaseous oxygen molecule, V_o an oxygen vacancy and ${\mathrm{O}_\mathrm{o}}^{2-}$ is an oxygen ion in the lattice. During high-temperature stress, a gaseous oxygen atom is first adsorbed in an oxygen vacancy inside the phosphor lattice near the surface. Since the adsorbed oxygen has a different valence with respect to oxygen ions in the phosphor, the adsorbed oxygen atoms tend to reach a more stable electronic configuration by capturing electrons from the diffused Eu^{2+} ions near the surface, thus increasing the number of Eu^{3+} centers.

8.5 Fast optically-induced phosphor degradation

In section 8.3.2 the long-term stability of the luminescent material under moderate to high optical excitation was investigated. Interestingly, what we found is that despite the stressed phosphor in correspondence of the excitation spot exhibited severe PL degradation and a spurious red luminescence (Fig. 8.18a), the trend over stress time of the PL signal registered by the spectrometer showed an increase of the blue emission (Fig. 8.17a). In order to understand whether this behavior could have arisen from a very fast degradation process, undetectable with the relatively slow spectral acquisition system so far employed, the experiment was repeated with a slightly different setup. In order to attain an higher temporal resolution during the acquisition of the PL signal, the spectrometer was replaced with an amplified photodiode (model PDA36A-EC from Thorlabs), carefully shielded from the 405 nm laser light reflected from the sample and connected to an oscilloscope. Moreover, in order to discriminate between thermal quenching-induced PL decay and non-recoverable phosphor degradation, a reference PL measure at a safe $0.5\,W/mm^2$ excitation level was performed before and after each stress. The results of the $21\,h$ long stresses at $1.5\,W/mm^2$ and $3\,W/mm^2$ carried out with the improved setup are reported in Figure 8.24.

NOTE: The experimental data reported in this section refer to a different second-generation sample of luminescent material, which shares with the previously investigated one the (general) composition and the behavior under optical excitation.

With regard to the stress under $1.5\,W/mm^2$ excitation, the waveform of the PL signal during stress in Fig. 8.24a shows a 10.5 % difference between the peak and the steady-state value. Interestingly, only a $< 0.75\,\%$ decay in the reference PL measurement was registered (Fig. 8.24b). This suggests that the PL decay experienced by the sample is mostly related to a thermal quenching phenomenon and that $1.5\,W/mm^2$ is a safe pumping intensity for the given deposition conditions and the thermal management capabilities of the system. On the other hand, stress under $3\,W/mm^2$ excitation induced a 71.8 % decay in the steady-state PL with respect to peak value (Fig. 8.24c), as well as a (non-recoverable) 54.56 % decrease of the reference PL signal (Fig. 8.24d). By comparing the experimental data of the two experiments, the following statements

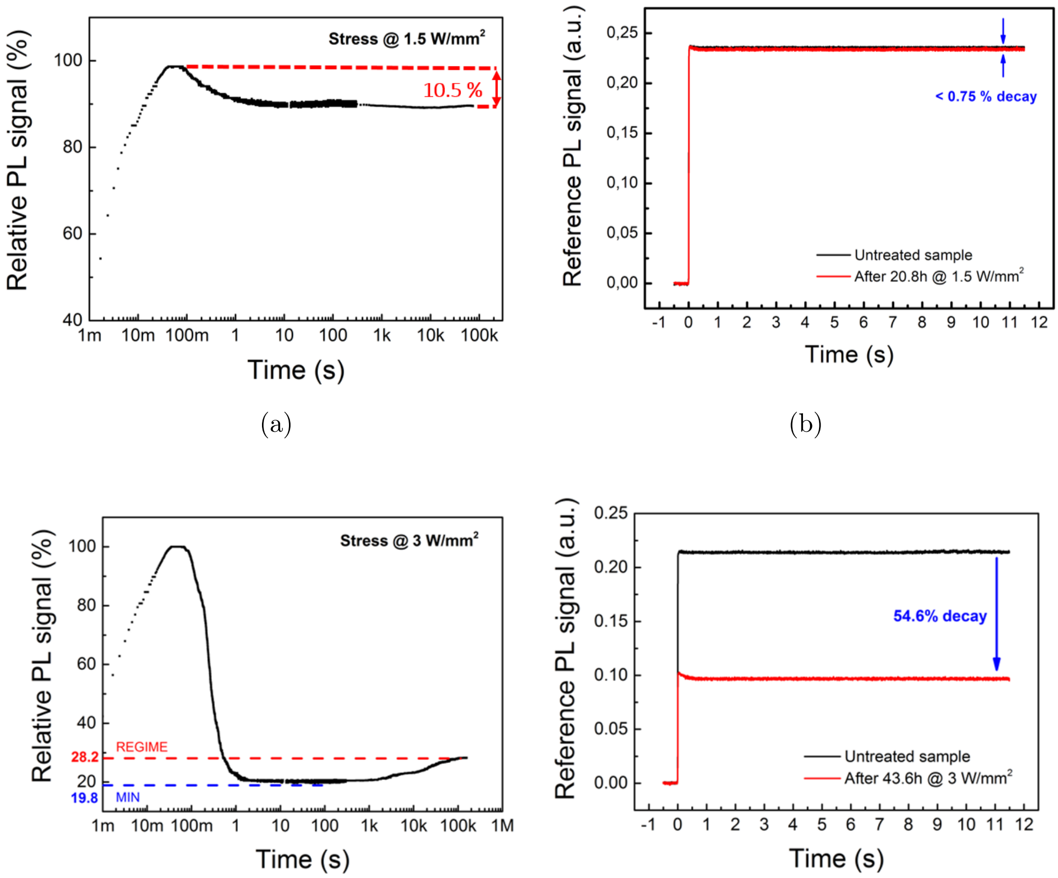

(a) (b)

(c) (d)

Figure 8.24: Short-term stress under 405 nm optical excitation at 1.5 W/mm^2 (a) and 3 W/mm^2 (c). Reference measurements taken before and after stress at 0.5 W/mm^2 are also reported in figures (b) and (d).

can be made: (i) the degradation process is very fast, most of the PL decay occurs during the first seconds of stress; (ii) a recoverable PL decay is present and can be ascribed to the thermal quenching experienced by the luminescence material; (iii) stress at 3 W/mm^2, with a relatively small 0.1mm^2 spot size, induces severe damage to the phosphorescent material.

Optical step-stress: $0.5 - 3.5\,W/mm^2$ (single spot)

The outcomes of the experiments described in the former section suggest that the phosphorescent material under investigation is not suitable for continuous operation at an excitation intensity of 3 W/mm^2, thus actual excitation intensity limits must be explored. To this aim, an optical step-sress experiment was arranged. A specific stress spot was submitted to 12 s long stress steps under increasing 405 nm optical excitation, from 0.5 W/mm^2 to 3.5 W/mm^2. A reference measurement at 0.5 W/mm^2 was taken before and after each stress step. A cool-down period of 300 s was employed before low-intensity characterization in order to let the sapphire substrate and the phosphors dissipate the heat accumulated during the stress. The results are reported in Figure 8.25. Plot 8.25b shows that a sudden PL decay occurred after 400 ms stress

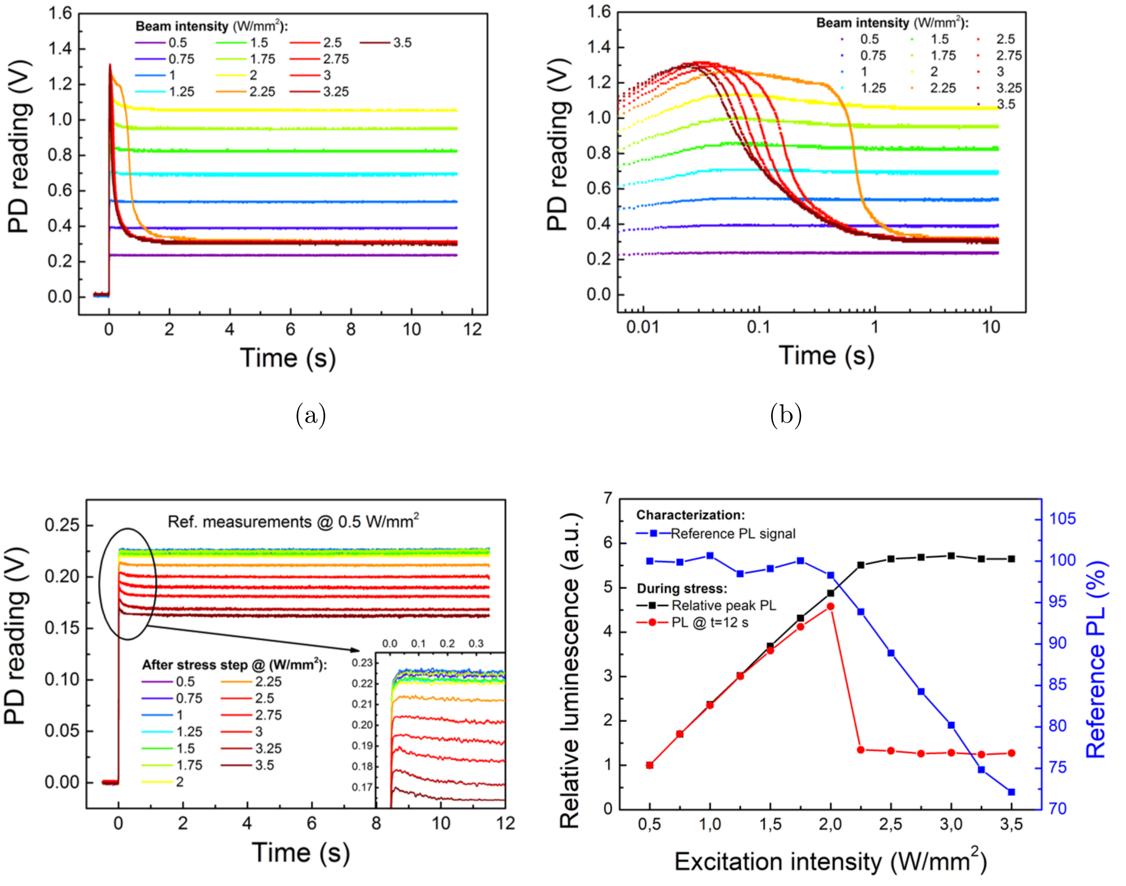

(a) (b)

(c) (d)

Figure 8.25: Short-term optical step-stress under increasing 405 nm optical excitation. PL transient in linear (a) and semilog scale (b), reference measurements waveforms taken at 0.5 W/mm^2 after stress (c) and magnitude after each stress step of the relevant PL signals (d).

at 2.25 W/mm^2. Above this excitation intensity the regime PL signal, i.e. the photoluminescence at the end of the 12 s stress step, drops to a fixed value corresponding roughly to the emission during 0.5 W/mm^2 stress, whereas the reference PL measurements starts decreasing in amplitude, meaning that stress above 2.25 W/mm^2 induced permanent degradation to the phoshor (Fig. 8.25d). The PL transients of the reference measurements reported in Figure 8.25c also show an increase of the initial PL decay rate at $0.5\,W/mm^2$, which suggests that permanent PL degradation was followed by an increase in the non-radiative phenomena, possibly a stronger thermal quenching or an increase in the concentration of traps inside the phosphor lattice, or by the worsening of the heat-conduction properties of the material.

Optical step-stress: $0.5 - 18\,W/mm^2$ (multiple spots)

In order to evaluate the effects of a specific excitation intensity, and to understand what is the variability introduced by the uneven morphology of the phosphor surface, the experiment described in the former paragraph was repeated by changing the excitation spot after each $12\,s$ stress step. This was accomplished by moving the substrate and adjusting the LD power to spot-size ratio. A second deposition, labeled sample 2 in Fig. 8.27a, was employed for excitation intensities greater than $5\,W/mm^2$.

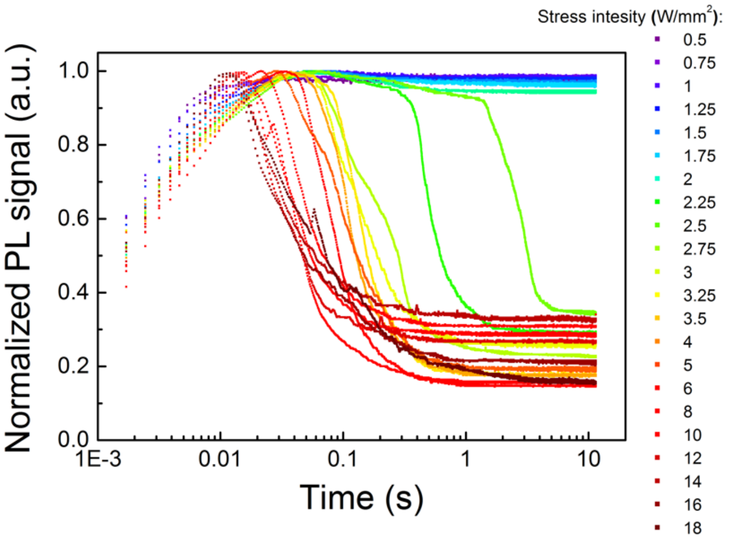

Figure 8.26: Normalized PL transients registered during short-term optical step-stress under increasing $405\,nm$ optical excitation.

Figure 8.26 shows the PL transients, normalized to their peak value, registered during each stress step (normalization was performed in order to compare the optical responses of different surface spots). For excitation intensities up to $2.25\,W/mm^2$ only a slight drop in the PL signal at $12\,s$ can be observed. As testified by the trend of the reference PL signal reported in Fig. 8.27a, this decay is mostly related to recoverable thermal quenching, despite some permanent material degradation is induced for optical intensities greater than $1.75\,W/mm^2$. Above $2.25\,W/mm^2$, a very fast decay of the PL signal occurs; in particular, the delay between the beginning of the stress and the peak PL decreases with increasing light intensity. This behavior can be explained considering that above a certain (power-dissipation) threshold, the self-heating of the material reduces the rate of optical emission, increasing even more the quantity of dissipated power. This positive feedback rapidly increases the temperature of the stress spot, thus annihilating the emission from this area and inducing permanent degradation of the phosphor particles located nearby. This hypothesis is further confirmed by the comparison between the trend of the reference PL measurement and the peak-to-regime PL (Fig. 8.27b), which shows that correlation between the two quantities is maintained for non-critical excitation intensities (up to 1.7 W/mm^2). When this critical stress intensity is reached, the PL becomes more dependent on the phosphorescent material surrounding the excitation spot, rather than on the severely heated (and partially degraded) excitation spot itself.

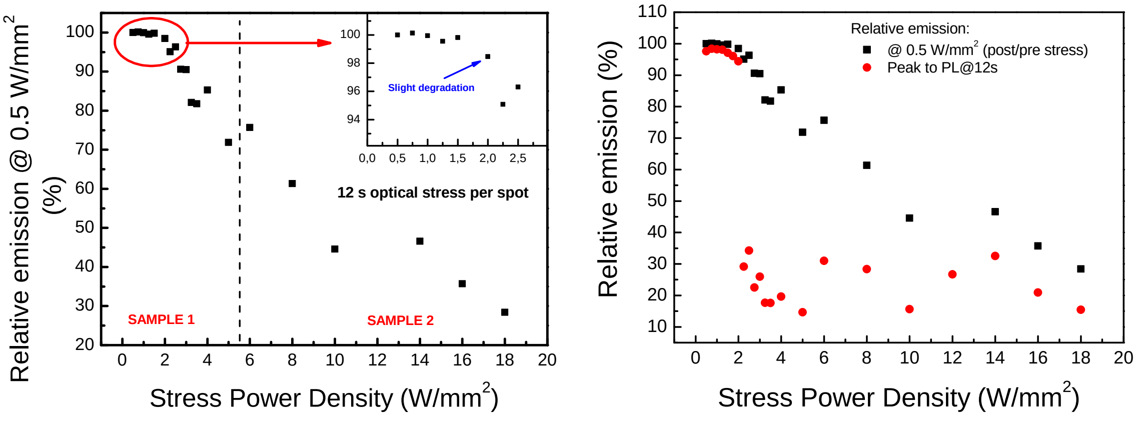

(a)

(b)

Figure 8.27: Short-term optical step-stress under increasing 405 nm optical excitation: reference PL signal trend at 0.5 W/mm^2.

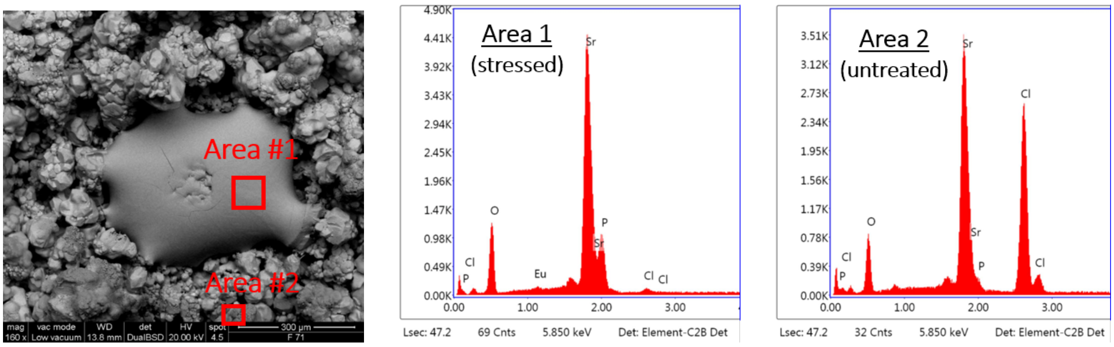

(a)

(b)

(c)

Figure 8.28: ESEM analysis of the excitation spot submitted to 12 s optical stress at constant 405 nm - 18 W/mm^2 excitation: backscattered electrons image (a) and EDX analyses of the surface spots marked respectively as (b) AREA 1 and (c) AREA 2.

The severe degradation of the phosphors in correspondence of the excitation spot was also confirmed by ESEM analysis, shown in Figure 8.28. For excitation intensities greater than $10\,W/mm^2$, fusion of the material and transition to a glass-like phase could be clearly observed. Aside from this morphological change, a reduction in the concentration of Chlorine for the stressed material was also found (Fig. 8.28b,8.28c).

8.6 Conclusions

In this chapter the robustness and the degradation mechanisms of blue-emitting phosphors for near-UV laser pumping were investigated. By means of a series of long-term aging and short-term stress experiments under optical excitation and/or high temperature environment, the limits for continuous operation of the luminescent material were found. In particular, the phosphors demonstrated good stability during pure thermal treatment in air up to 300 °C. For temperatures equal to or greater than 450 °C the material exhibited a time-dependent drop in the PL, which was attributed to the thermally-induced autoionization of the Eu^{2+} optically active centers. By means of different material characterization techniques, such as EPR, XPS and high-sensitivity optical spectroscopy, evidence of this degradation process were also found on samples stressed under moderate $3\,W/mm^2$ optical excitation. This indicated that the optically (and thermally) induced ionization of the Eu^{2+} species is the most critical degradation process for this family of phosphorescent material.

In addition to that, short term stress under $405\,nm$ optical excitation revealed that a threshold excitation intensity I_{TH} for continuous pumping of the 2nd generation luminescent pigment exists. The threshold value I_{TH} was found to be in the $1.5\,W/mm^2$ to $2\,W/mm^2$ range for the given deposition condition: this threshold excitation may depend on the specific morphology of the area under analysis, as well as on the thickness of the deposition and on the type of substrate employed. Above I_{TH}, decay of the steady-state PL intensity and/or degradation of the material occur with respect to lower excitation intensity, which suggests that the material is being operated in an unuseful excitation regime.

Part III

Degradation mechanisms of heterogeneous III-V/Silicon laser diodes

Introduction to Part III

Photonic Integrated Circuits (PICs) represent an excellent solution for improving the performance and reducing the cost of telecommunication and optical interconnection technologies in the $1.31\,\mu m$ and $1.55\,\mu m$ spectral ranges. The on-chip integration of both active (laser diodes, photodiodes) and passive (couplers, modulators, filters, multiplexers ...) photonic elements offers many advantages. The reduction in the size of the devices and in the number of optical and electrical interfaces allows for a decrease in the total system cost, also paving the way for large-scale manufacturing.

To this aim, the SOI (Silicon-On-Insulator) technology has been heavily explored by PICs researchers over the last decade [95, 96, 97]. Due to its maturity, this technology offers high yields and low manufacturing costs, while being fully compatible with standard CMOS processes. Owing to its indirect bandgap, silicon is not suitable for the fabrication of efficient optical sources. Despite numerous attempts made in this direction [98, 99, 100], many researchers and industries have now focused their attention on the heterogeneous integration of III-V based sources (lasers diodes (LDs) or light emitting diodes (LEDs)) on the SOI platform [101, 102, 103]. With this kind of approach the optical source can be separately grown through a III-V specific process, and then transferred to the SOI wafer by means of a wafer bonding process [104, 105, 106]. This procedure is performed at relatively low temperatures, usually below 350 °C, in order to minimize the issues related to the large mismatch between the thermal expansion coefficient of III-V semiconductors and silicon [107]. However, while these optimized wafer-bonding techniques and the introduction of Super-Lattice Structures (SLS) have greatly improved device reliability [108, 13], an in-depth investigation on the degradation mechanisms of such novel heterogeneous devices has not been presented to date in the literature.

The aim of the work reported in the following chapters is to improve the understanding of the degradation mechanisms that limit the reliability of future heterogeneous III-V/silicon laser diodes. For this purpose, a series of accelerated aging tests have been performed on experimental heterogeneous DBR LDs emitting at $1.55\,\mu m$, provided by the optoelectronics research group of the University of Santa Barbara (UCSB). An extensive characterization based on electro-optical measurements, capacitance-voltage (C-V) characterization, and Deep Level Transient Spectroscopy (DLTS) was carried out to identify the root cause of degradation.

The results of this analysis are described in Chapter 10, after a brief introduction on the fundamental properties of semiconductor lasers and on the working principles of the capacitance-DLTS technique.

Chapter 9

Laser diodes: working principles and advanced analysis techniques

This chapter briefly describes the fundamental properties of laser-diodes. By considering the separate contributions of the different recombination mechanisms inside a semiconductor device, and by taking into account the electro-magnetic amplification effect produced by stimulated recombination within a gain medium in an optical cavity, the basic output-power versus injection current relation of a Fabry-Perot laser diode is derived. The parametric dependencies highlighted by this equation, either above or below threshold, are of primary importance in addressing the degradation mechanisms responsible for the worsening of the optical performances of semiconductor lasers.

The second section of this chapter introduces the concept of deep-level transient spectroscopy as an experimental approach for the characterization of deep-levels within a semiconductor device, with particular emphasis on the working principles of the commonly-employed capacitance-DLTS technique.

9.1 Working principles of laser diodes

Efficient optoelectronic devices employ double-heterostrutures in order to spatially localize the carriers inside the active region, thus maximizing the rate of radiative recombination processes. If I is the current injected at the terminals of the device, and V is the volume of the active region, then $\eta_i I/qV$ electrons per second per volume unit are injected into the active region. The prefactor η_i, also called injection efficiency, takes into account the possible leakage and recombination paths that may operate in shunt with the active region, thus effectively reducing the population of injected carrier that could contribute to the generation of photons. Within the active region, the carrier density (N) is governed by a dynamic process. From a mathematical standpoint, the variation in the population of carrier can be expressed by the so-called *rate equation*, given by

$$\frac{dN}{dt} = G_{gen} - R_{rec} \tag{9.1}$$

where G_{gen} is the rate of injected electrons and R_{rec} is the rate of recombining electrons per unit volume. From what previously found, the term $\eta_i I/qV$ represents the generation rate G_{gen}, whereas the recombination rate R_{rec} takes into account all the possible radiative and non radiative recombination processes that contribute to consume the population of carrier injected within the active region.

Several mechanisms participate to the recombination process. Aside from the contribution of the spontaneous emission (R_{sp}), and of the non-radiative recombination processes (R_{nr}), a carrier leakage rate (R_l) that takes into account the fraction on injected carrier that escape from the active region due to poor lateral confinement must be taken into account. Finally, by also considering the net stimulated recombination, including both stimulated emission and absorption, the recombination rate R_{rec} can be written as

$$R_{rec} = R_{sp} + R_{nr} + R_l + R_{st} \tag{9.2}$$

where the first three terms describe the unstimulated recombination process, while the fourth one requires the presence of photons. With regard to the unstimulated recombination, a carrier lifetime τ related to a natural decay process can be defined considering that $dN/dt = N/\tau$, where $N/\tau = R_{sp} + R_{nr} + R_l$. Thus, the fundamental rate equation can be rewritten as

$$\frac{dN}{dt} = \frac{\eta_i I}{qV} - \frac{N}{\tau} - R_{st} \tag{9.3}$$

9.1.1 Stimulated recombination in semiconductor lasers

Above threshold, the main photon generation process in the device is the stimulated emission (R_{st}). Due to this process, when an electron-hole pair is stimulated to recombine, another photon is generated. Since the cavity volume occupied by photons (V_p) is usually larger than the volume of the active region populated by free electrons (V), the photon density generation rate will be reduced by factor of $[V/V_p]$ with respect to R_{st}. The aforementioned electron-photon overlap factor is generally referred to as the *confinement factor* Γ. For this reason, it is convenient to model the dimensions of the cavity by means of effective thickness (d_{eff}), width (w_{eff}), and length (L) that define the region where photons are propagating. Hence, if the active region populated by free carriers has dimensions d, w and L_a, the confinement factor can be expressed as $\Gamma = \Gamma_x\Gamma_y\Gamma_z$, where $\Gamma_x = d/d_{eff}$, $\Gamma_y = w/w_{eff}$ and $\Gamma_z = L_a/L$. This concept is reported in Figure 9.1.

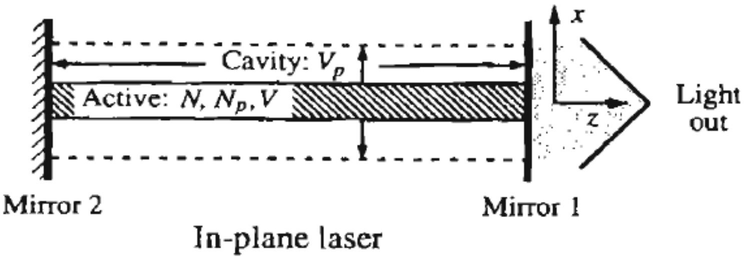

Figure 9.1: Schematic view of an in-plane laser cavity illustrating the active layer (cross-hatched) and the photon cavity (dashed lines) volumes. The reference coordinate system is reported as well (image taken from [109]).

Like injected carriers, also photons propagating inside the optical cavity are subjected to several loss mechanisms. Mainly, photons can be lost due to optical absorption and out of mode scattering, as well as due to the output coupling mirror, where a portion of the resonant mode is coupled to an output medium (air, fiber, waveguide,. . .). The net loss of photons can be characterized by a *photon (cavity) lifetime* τ_p, hence, similarly to the rate equation for carriers defined in 9.3, a rate equation for photons can be written considering the related generation and the loss terms:

$$\frac{dN_p}{dt} = \Gamma R_{st} + \Gamma\beta_{sp}R_{sp} - \frac{N_p}{\tau_p} \tag{9.4}$$

where N_p is the number of photons per unit volume and β_{sp} is the *spontaneous emission factor*, that for uniform coupling to all modes is the reciprocal of the number of optical modes in the bandwidth of the spontaneous emission process. Equations 9.3 and 9.4

can be solved to evaluate the steady-state and dynamic responses of a laser diode. To this aim, the dependence of the various terms on N and N_p must first be made explicit.

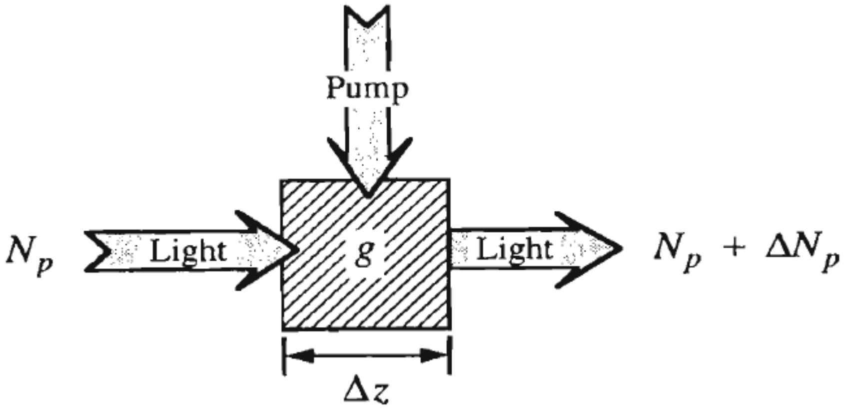

Figure 9.2: Photon gain per unit length for photons of density N traveling through a small portion of gain material ΔZ (from [109]).

The term R_{st} is a generation term for photons, since it represents the net photon-stimulated $e-h$ recombination which generates photons. The growth in photon density from an incoming value N_p to an exiting value of $N_p + \Delta_p$ as it propagates through a small length ΔZ of active region, schematically represented in Figure 9.2, can be described in terms of *gain per unit length* g, by considering that:

$$N_p + \Delta N_p = N_p e^{g\Delta z} \approx N_p g v_g \Delta t \tag{9.5}$$

where we assumed that for small values of Δz $\exp(g\Delta z) \approx 1 + g\Delta z$, and we employed the relation $\Delta z = v_g \Delta t$, with v_g being the group velocity. Thus, assuming a unitary confinement factor, the generation term form the photon rate equation 9.4 becomes

$$\left(\frac{dN_p}{dt}\right)_{gen} = R_{st} = \frac{\Delta N_p}{dt} = N_p g v_g \tag{9.6}$$

where the dependency of the term g on photon and carrier density is not explicated. This quantity can be evaluated by means of Einstein's approach to the description of the interaction between EM radiation and electronic states, as shown in the following paragraph.

Einstein's A and B coefficients and optical gain

The rate of absorption ed emission of photons between two generic energy levels in an atom can be described in terms of the rate equations based on Einstein's A and B coefficients. This approach consists in applying rate constants to the three radiative processes appearing in Eq. 9.4, assuming that these rates must be proportional to the carrier density. In this context, an A coefficient is associated with spontaneous processes (spontaneous emission $R_{sp}^{2\to1}$ from the higher (2) to the lower (1) energy level), whereas the B constants are associated with stimulated processes (stimulated emission $R_{st}^{2\to1}$ and absorption $R_{sp}^{1\to2}$). Einstein's constants can be interpreted from a physical point of view as transition probabilities (per unit time): that is, if N_2 is the number of excited electrons in level (2), the rate of spontaneous emission, which is the number of transitions per unit time, is given by

$$R_{sp}^{2\to1} = A_{21} N_2 \tag{9.7}$$

On the other hand, since stimulated processes have to take into account the density of available photons at the energy of interest, B rates are weighted by the radiation spectral density ρ_ν. At thermal equilibrium, this spectral density corresponds to the black-body radiation defined by Plank's law:

$$\rho_\nu = \frac{8\pi h\nu^3}{c^3}\frac{1}{e^{h\nu/kT}-1} \tag{9.8}$$

where c is the light speed in vacuum, h is Plank's constant and ν is the frequency of the EM radiation. Thus, the rates of absorption and of stimulated emission can be written as:

$$R_{st}^{2\to1} = B_{21}\rho_\nu N_2 \qquad R_{st}^{1\to2} = B_{12}\rho_\nu N_1 \tag{9.9}$$

where B_{21} and B_{12} are constants that represent the probability per unit time and unit frequency of stimulated emission and absorption, respectively.

At thermal equilibrium, the number of upwards transitions must equal the number of downwards transitions. By imposing $B_{21} + A_{21} = B_{12}$, and solving for ρ_{nu}, we obtain that

$$\rho_\nu = \frac{A_{21}/B_{21}}{(B_{12}/B_{21})(N_1/N_2)-1} \tag{9.10}$$

Since the population of the energy levels is dictated by the Boltzmann statistics, that means that the occupation of the j-th level is proportional to $N_j \propto g_j e^{-E_j/kT}$, where g_j is the degeneracy of the specific level, defining the number of electronic configurations associated with the same energy. From that observation, we can write that

$$\frac{N_1}{N_2} = \frac{g_1}{g_2} e^{(E_2 - E_1)/kT} = \frac{g_1}{g_2} e^{h\nu/kT} \tag{9.11}$$

If the quantity found in equation 9.11 is inserted into equation 9.10 and compared to 9.8, we can write that:

$$\rho_\nu = \frac{A_{21}/B_{21}}{(B_{12}/B_{21})(N_1/N_2) - 1} = \frac{A_{21}/B_{21}}{\dfrac{B_{12} g_1}{B_{21} g_2} e^{h\nu/kT} - 1} = \frac{8\pi h \nu^3}{c^3} \frac{1}{e^{h\nu/kT} - 1} \tag{9.12}$$

where the last identity is true for all temperatures only if the the following two equation hold:

$$B_{12} g_1 = B_{21} g_2 \qquad \frac{A_{21}}{B_{21}} = \frac{8\pi h \nu^3}{c^3} \tag{9.13}$$

While the second term establishes a fundamental link between stimulated and spontaneous emission processes, strictly dependent on the photon density, the first equation shows that if the degeneracy of the levels is equal, the probabilities of stimulated absorption and emission are equal, that is $B_{12} = B_{21}$. Hence, the ratio of the stimulated to spontaneous emission rates can written as

$$\frac{R_{st}^{2\to 1}}{R_{st}^{1\to 2}} = \frac{B_{21} \rho_\nu N_2}{B_{12} \rho_\nu N_1} = \frac{N_2}{N_1} \tag{9.14}$$

This is a fundamental outcome, since it revels that in order for stimulated emission to prevail on absorption, and thus attain Light Amplification by Stimulated Emission of Radiation (the LASER effect), a condition of inversion of population, $N_2 > N_1$, must be first reached.

At this point, a general form for the optical gain g in a two-levels system can be derived by considering from equation 9.6 that:

$$g = \frac{1}{v_g N_p} \frac{dN_p}{dt} \tag{9.15}$$

If we consider only the coherent photons emitted through the stimulated recombination process, then

$$\frac{dN_p}{N_p dt} = R_{st}^{2\to 1} - R_{st}^{1\to 2} = B_{21} \rho_\nu N_2 - B_{12} \rho_\nu N_1 = (N_2 - N_1) B_{21} \rho_\nu \tag{9.16}$$

where we assumed $B_{12} = B_{21}$. Hence, if we approximate the group velocity v_g with the speed of light in the medium c/n, and the photon density ρ_ν with the photon density around a central frequency ν_0 with band $\Delta\nu$ given by $\rho(\nu_0) = N_p h\nu_0/\Delta\nu$, we obtain that:

$$g(\nu_0) = \frac{1}{v_g N_p}(N_2 - N_1)B_{21}\rho(\nu_0) = (N_2 - N_1)B_{21}\frac{h\nu_0}{\Delta\nu}\frac{n}{c} \tag{9.17}$$

In semiconductor lasers, the population inversion is related the concentration of excess carriers N injected into the active region. Thus, equation 9.17 can be re-written in function of the carrier density, obtaining

$$g = g_{21} \approx a(N - N_{tr}) \tag{9.18}$$

where a is the differential gain coefficient and N_{tr} is the transparency carrier density. The linear relation presented in 9.18 approximates the logarithmic dependence of g on the carrier density that derives from a proper material-related quantum-mechanical extrapolation of the gain factor.

9.1.2 Threshold gain in lasers

Equation 9.18 shows that once a sufficient amount of population inversion is reached, the density of photons traveling through the gain medium, the active region of the semiconductor device, is progressively increased by the stimulated emission process. However, as summarized by equation 9.4, photons loss mechanisms within the cavity can reduce the optical field density, thus reducing the ratio of stimulated to spontaneous emission given by:

$$\frac{R_{st}^{2\to 1}}{R_{sp}^{2\to 1}} = \frac{B_{21}\rho_\nu N_2}{A_{21}N_2} = \frac{B_{21}}{A_{21}}\rho_\nu \tag{9.19}$$

which is directly proportional to the photon density term ρ_ν. In order to evaluate the internal (photon) losses of a laser, we can consider the schematic view of an optical cavity with gain medium reported in Figure 9.3.

The amplitude of an electric field that propagates longitudinally along the y-axis can be written as

$$\boldsymbol{E} = \hat{\boldsymbol{e}}_y E_0\, U(x, e)e^{j(\omega t - \hat{\beta} z)} \tag{9.20}$$

where $U(x, y)$ is the transverse field profile. In particular, the spatial dependence of the amplitude derives from the term $e^{-j\hat{\beta}z}$, where $\hat{\beta}$ is the propagation constant of the mode. This complex propagation constant includes both the incremental transverse modal gain $g_{xy} = g\Gamma_{xy}$ (assuming $g(x, y)$ to be constant in the active region) and the

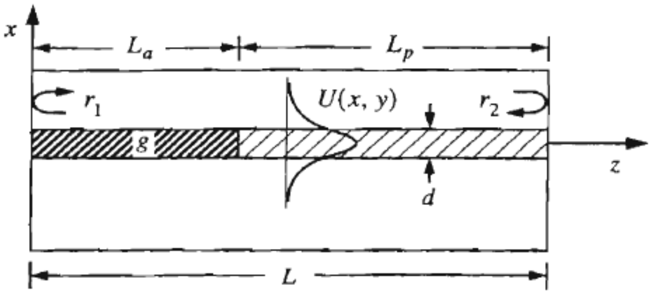

Figure 9.3: Simplified view of an EM mode longitudinally propagating in a laser cavity [109].

internal modal loss α_i. Hence,the progation constant can be written as:

$$\hat{\beta} = \beta + j\beta_i = \beta + \frac{j}{2}(g_{xy} - \alpha_i) \tag{9.21}$$

where $\beta = 2\pi n/\lambda$, g_{xy} and α_i are found from weighted averages of the gain and loss across the transverse mode shape, and the $1/2$ factor takes into account the dependence on power, rather than on amplitude, of these two coefficients.

From a simplified point of view, most laser cavities can be divided into two sections: an active ($g \neq 0, \alpha_{ia} \neq 0$) section of length L_a, and a passive ($g = 0, \alpha_{ip} \neq 0$) section of length L_p. The propagating mode is reflected by the end mirrors, which have reflection coefficients r_1 and r_2, respectively. The amount of transmitted power (non reflected and non absorbed) is potentially useful output. In order for a specific mode of the laser to reach threshold, the gain in the active section must be increased so that all the formerly mentioned propagation losses are compensated: in this condition the electric field exactly replicates itself after one round-trip in the cavity. From a mathematical perspective, this condition imposes the equality of the electric field at $z = 0$ and $z = 2L$, considering the reflection term due to the mirrors at $z = 0$ and $z = L$. By employing those boundary conditions in Equation 9.20, the following relation, valid at threshold, can be obtained:

$$r_1 r_2 e^{-2j\hat{\beta}_a L_a} e^{-2j\hat{\beta}_p L_p} = 1 \tag{9.22}$$

If we consider the magnitude terms of equation 9.22, and solve for $\Gamma_{xy} g_{th} L_a$, we obtain

$$\Gamma_{xy} g_{th} L_a = \alpha_{ia} L_a + \alpha_{ip} L_p + ln\left(\frac{1}{r_1 r_2}\right) \tag{9.23}$$

By defining the average internal loss $\langle\alpha_i\rangle$ as $(\alpha_{ia} L_a + \alpha_{ip} L_p)/L$, and by dividing the former equation for the total cavity length, we obtain that the average threshold gain is equal to

$$\langle g_{th} \rangle = \Gamma g_{th} = \langle \alpha_i \rangle + \frac{1}{L} ln \left(\frac{1}{r_1 r_2} \right) = \langle \alpha_i \rangle + \alpha_m \tag{9.24}$$

where we also considered that, for $L_a \gg \lambda$, $\Gamma_{xy} L_a / L \approx \Gamma_{xy} \Gamma_z = \Gamma$. Equation 9.24 provides the cavity loss parameters necessary to calculate the threshold gain for an in-plane cavity laser.

On the other hand, the phase term of equation 9.22 imposes the oscillating condition of the mode to be $\exp(2j\beta_a L_a) \exp(2j\beta_a L_a) = 1$, that is, $\beta_a L_a \beta_p L_p = m\pi$, with m being an integer number. In other terms:

$$\lambda_{th} = \frac{2}{m} [n_a L_a + n_p L_p] \tag{9.25}$$

If we assume equal refractive indexes n_a and n_p, which is generally not true since n depends on both carrier density and wavelength, equation 9.25 gives

$$L = m \frac{\lambda_{th}}{2n} \tag{9.26}$$

which specifies the modal oscillating condition inside a generic Fabry-Perot optical cavity.

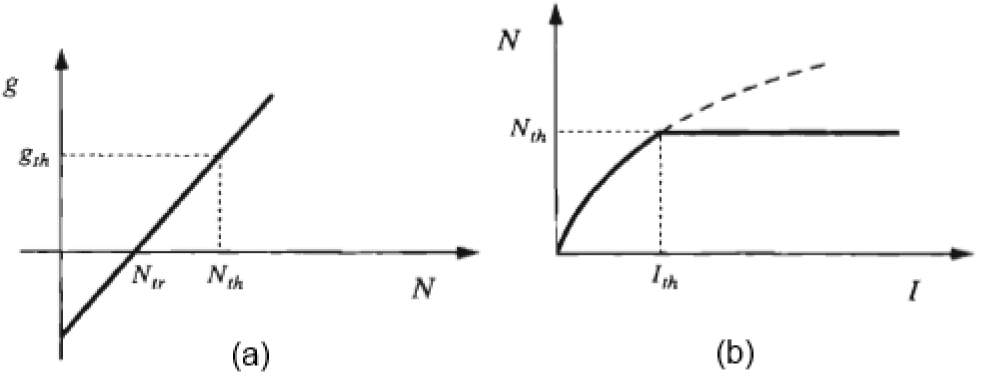

Figure 9.4: Approximate gain-carrier density relation (a) and carrier density Vs. current relation (b) in a laser diode (from [109]).

An important observation must be made on the behavior of the LD steady-state gain above threshold. In fact, once all the internal and mirrors losses are overcome, the gain value must remain fixed at the threshold value g_{th} defined in equation 9.24, otherwise the optical field would increase without any bound, which is a condition the cannot be physically sustained. Moreover, since the gain is monotonically related to the carrier density (see Eq. 9.18), this requires that also the carrier density must clamp at its threshold value. From these observations, the two following relations hold for above-threshold steady-state operation:

$$g(I > I_{th}) = g_{th} \qquad N(I > I_{th}) = N_{th} \tag{9.27}$$

as reported from the graphs of Figure 9.4. From a physical standpoint, the clamping of the threshold gain can be explained considering that as current density is increased above I_{th}, an initial increase of N and g occurs. However, since also the stimulated recombination rate is increased, the excess amount of carriers is rapidly (in the ns range) decreased by the recombination process, to the point where the conditions defined in 9.27 are again satisfied.

9.1.3 Output characteristic of a laser diode

In order to derive the output characteristic of the laser diode we should start by evaluating the rate equation given in 9.3 in steady-state ($dN/dt = 0$) at threshold ($N = N_{th}$, $I = I_{th}$, $R_{st} = 0$), thus obtaining:

$$\frac{\eta_i I_{th}}{qV} = (R_{sp} + R_{nr} + R_l)_{th} = \frac{N_{th}}{\tau} \tag{9.28}$$

Since the middle term depends monotonically on N, also its value clamps above threshold; hence by substituting Eq. 9.28 into the rate equation 9.3, and considering that from Eq. 9.6 we have that $R_{st} = N_p g v_g$, we obtain the above-threshold carrier rate equation and steady-state photon density, given by

$$\frac{dN}{dt} = \eta_i \frac{I - I_{th}}{qV} - N_p g v_g \qquad N_p = \eta_i \frac{I - I_{th}}{qV \nu_g g_{th}} \tag{9.29}$$

The value of N_p in 9.29 can be used to calculate the optical output power by multiplying the energy stored inside the optical cavity, given by $E_o = N_p h\nu V_p$, times the energy loss rate through the mirrors, equal to $1/\tau_m = v_g \alpha_m$, thus obtaining

$$P_o = v_g \alpha_m N_p h\nu V_p \tag{9.30}$$

By substitution of 9.29 and 9.24 into 9.30, and considering that $V_p = V_\Gamma$, we obtain the fundamental equation defining the L-I characteristic of a laser diode above threshold:

$$P_o = \eta_i \left(\frac{\alpha_m}{\langle \alpha_i \rangle + \alpha_m} \right) \frac{h\nu}{q} (I - I_{th}) \tag{9.31}$$

which dictates that for $I > I_{th}$ the output optical power (from both mirrors) linearly depends on the injection current (Fig. 9.5). This linearity holds as soon as the gain-current relation, the internal efficiency, the confinement factor, and the cavity losses remain constant with increasing current above threshold.

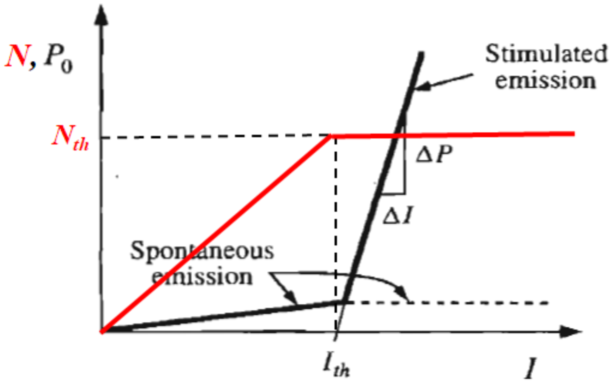

Figure 9.5: Output power characteristic of a laser diode.

LD slope efficiency In equation 9.31, the factor

$$\frac{h\nu}{q}\frac{\eta_i\alpha_m}{\langle\alpha_i\rangle+\alpha_m}=\frac{h\nu}{q}\eta_d \tag{9.32}$$

represents the slope of the L-I curve of the laser diode above threshold, also called *Slope Efficiency* (SE). This quantity can be interpreted as the efficiency of the injected carrier to coherent photons conversion process operated by stimulated emission, and is measured in W/A. Dividing the SE by the term $h\nu/q$ we obtain the number of photons exiting the laser per number of injected electrons, which is the *differential quantum efficiency* η_d.

The slope of the L-I curve below threshold has different dependencies. If we don't consider the stimulated emission term and solve the photon rate equation 9.4 for N_p under steady-state conditions, we can find that

$$N_p=\Gamma\beta_{sp}R_{sp}\tau_p \tag{9.33}$$

By combining the former equation with the relations found in 9.3, 9.30 and 9.24, the spontaneous emission into the lasing mode can be written as:

$$P_{o-sub}=\eta_r\eta_i\left(\frac{\alpha_m}{\langle\alpha_i\rangle+\alpha_m}\right)\frac{h\nu}{q}\beta_{sp}I \tag{9.34}$$

where η_r is the radiative efficiency of the spontaneous (LED-like) emission, defined as $R_{sp}/(R_{sp} + R_{nr} + R_l)$. Above threshold the sub-threshold emission clamps at the value determined by Eq. 9.34 with $I = I_{th}$, while the spontaneous emission increases as described by Eq. 9.31.

9.2 Deep-level transient spectroscopy (DLTS)

In a semiconductor crystal, a defect represents a (more or less) localized interruption of the periodic lattice structure. The loss in periodicity of the atomic structure, i.e. of the atomic potential, induces the formation of allowed energy states, called deep-levels, within the forbidden energy gap separating valence and conduction bands. According to the Shockley-Read-Hall (SRH) model [17, 18], the rate of non-radiative recombination through those deep-levels is strictly dependent of the characteristics on those energy levels, as well as on other extrinsic factors like the temperature and the carriers concentration. Since recombination trough deep levels, also called traps, reduces the amount of free carriers that can potentially participate to radiative (emission) processes, thus lowering the optical efficiency of the device, the identification and the reduction in the amount of traps within an opto-electronic (and electronic) device is of primary importance. To this aim, several analysis methods have been developed in the past. Among the non-destructive techniques, capacitance DLTS, or Deep-Level Transient Spectroscopy, is the most effective when dealing with defects in semiconductor structures featuring a depletion region. The working principle of this technique, which has been employed to characterize the IR lasers analyzed in chapter 10, will be presented in the following sections.

9.2.1 Capture and emission properties of deep-levels

In order to define a characterization technique capable of detecting and identifying deep-levels in semiconductor devices, the recombination dynamics that involve capture and emission of carriers through these states must first be explored. Generally speaking, a deep-level can interact with charge carries through four different processes, which involve the capture or the emission either of an electron or of a hole (see Fig. 9.6).

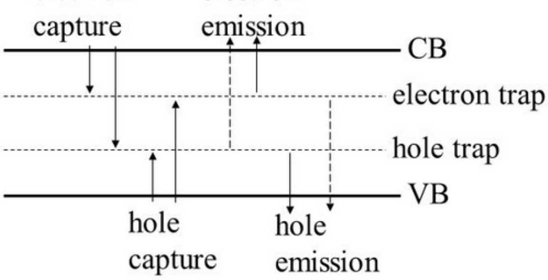

Figure 9.6: Possible interactions between localized energy states within the energy gap (traps) and free carriers.

Considering that at thermal equilibrium the rates of capture (c_n, c_h) and emission (e_n, e_h) of carriers must be equal, the following relations can be found [110]:

$$e_n = \frac{\nu_{th}\sigma_n N_c}{g}\exp\left(-\frac{E_C - E_T}{kT}\right) \qquad e_h = \frac{\nu_{th}\sigma_p N_v}{g}\exp\left(-\frac{E_T - E_V}{kT}\right) \tag{9.35}$$

and

$$c_n = \nu_{th}\sigma_n n \qquad c_h = \nu_{th}\sigma_p p \tag{9.36}$$

where ν_{th} is the electron (hole) thermal velocity, proportional to $\sqrt{8kT/\pi m^*}$ (m^* being the electron (hole) effective mass), $\sigma_{n,p}$ is the electron/hole capture cross section of the defect, n and p are the electron and hole concentrations, N_C and N_V are the effective densities of states in the conduction and valence bands, g is the degeneracy of the deep level, k is the Boltzmann constant, E_T,E_C and E_V are the energies of the deep level, the conduction and the valence bands, and T is the absolute temperature. The value ΔE represented by $E_T - E_V$ and by $E_C - E_T$ corresponds to the depth of the trap, or its *free energy*, from the band-edge to which the trapped carrier is emitted. In particular, equation 9.35 shows that the emission rates are proportional to a Boltzmann factor $\exp(-\Delta E/kT)$, and thus depend exponentially on the value of ΔE, also called *activation energy* of the deep-level (E_a). Considering that an *electron trap* is a trap that tends to be empty, and thus able to capture electrons, whereas an *hole trap* is a trap that tends to be full, thus able to capture holes, and assuming the capture rates to be zero, the former observations suggest that an electron trap is more likely to be found in the upper part of the energy gap, where the electron emission process proportional to

$$\propto \exp(-\Delta E/kT) \quad \textit{with} \quad \Delta E = E_C - E_T < E_g/2$$

is much faster than the hole emission process

$$\propto \exp(-\Delta E/kT) \quad \textit{with} \quad \Delta E = E_T - E_V > E_g/2$$

A corresponding inverted relation is valid for hole traps, which are more likely to be found in the lower part of the energy gap.

Capture cross-section σ and activation energy E_a are peculiar characteristics of a specific defect that define its emission properties. Equation 9.35 suggests that those two parameters can be measured by evaluating the temperature dependence of the emission rate of the deep-level. Once those experimental data have been acquired, the temperature dependencies in equation 9.35 can be explicitated by considering that

$$\nu_{th} \propto T^{\frac{1}{2}} \quad and \quad N_{c,v} = 2\left(\frac{2\pi m^*_{e,h} kT}{h^2}\right)^{\frac{3}{2}} \propto T^{\frac{3}{2}}$$

hence the quantity $N_{c,v}\, v_{th} \propto T^2$. Then, by dividing both terms for T^2 and by taking the natural logarithm, the following equation can be written:

$$ln(T^2/e_{n,h}) = ln\left(\frac{T^2}{\sigma_{n,h}\nu_{th}N_{c,v}}\right) + \frac{E_T}{kT} \tag{9.37}$$

Equation 9.37 shows that by plotting the emission rate-temperature relation as $ln(T^2/e_{n,h})$ versus $1/kT$ (Arrhenius plot), the activation energy of the trap corresponds exactly to the slope of the (ideally linear) resulting curve, whereas the capture cross-section is determined by the intercept with the y-axis. An example of an Arrhenius plot extrapolated from DLTS measurements on an AlInGaAs-based heterostructure is reported in Figure 9.7, from [111].

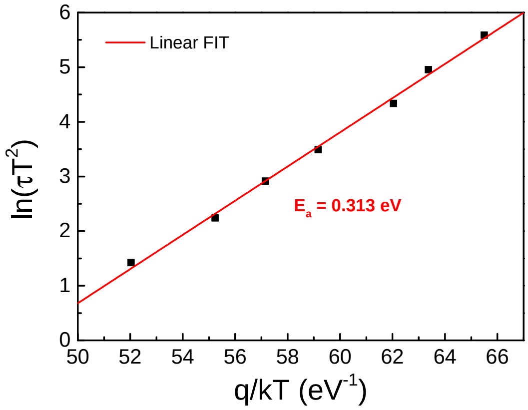

Figure 9.7: Example of an Arrhenius plot related to an electron trap in a quaternary AlInGaAs alloy.

With regard to the temperature dependencies of equation 9.35, two further considerations should be made. First, the electrons and holes capture cross-section are in general temperature-dependent. Even though some defects may not explicitly show this dependence, phenomena like carrier capture by multiphonon emission via lattice relaxation may occur [112]. In this case the capture cross-section has the form:

$$\sigma = \sigma_\infty \exp(-E_\sigma/kT) \tag{9.38}$$

where E_σ is the (thermal) activation energy of the cross section. Thus, the rate of emission of electrons to the conduction band can be re-written as follows:

$$e_n = \frac{\nu_{th}\sigma_\infty N_c}{g} \exp\left(-\frac{\Delta E + E_\sigma}{kT}\right) \tag{9.39}$$

which highlights the two different components for the activation energy of the emission process.

The second observation regards the physical meaning of the parameter ΔE. What was previously referred to as the thermal activation energy of the emission process, from a thermodynamical standpoint is the Gibbs free energy of the ionization reaction, defined as

$$E_C - E_T = \Delta E \equiv \Delta H - T\Delta S \tag{9.40}$$

where ΔH and ΔS are, respectively, the changes in enthalpy and entropy due to change in the charge state of the deep-level. By explicating these two quantities, the Boltzmann factor in equation 9.35 becomes

$$\exp\left(-\Delta E/kT\right) = \exp\left(-\Delta H/kT\right)\exp\left(\Delta S/k\right) \tag{9.41}$$

which shows the only the enthalpy of the deep-level can be extrapolated from the slope of the Arrhenius plot, not its free energy. Actually, the slope extrapolated from the Arrhenius plot represents the free energy at $T = 0K$, which differs from the free energy at the measuring temperature due to the (non-linear) temperature dependence of the energy-gap value. Therefore, the accurate estimation of the depth in energy of a trap requires the knowledge of the E_g-T relation for the specific semiconductor material under investigation. Moreover, since the entropy changes for ionization reactions in semiconductors is within $0 \leqslant S \leqslant 6k$, the added exponential prefactor may be as high as 400, thus leading to large errors in determining the capture cross-section of the Arrhenius plot.

9.2.2 Capacitance-DLTS

In the previous paragraph an analytic relation between the emission rate of a deep-level and temperature was presented. As this relation can be exploited to extrapolate important features of a deep-level, i.e. its capture cross-section and activation energy, a technique able to measure the (e, T) relation is needed. To this aim, several methods based on the measurement of the (small-signal) C-V characteristic were introduced in the past. These techniques track the variation induced by the presence of defects to the capacitance associated with the depletion region of a p-n junction or of a Schottky diode biased at a specific voltage. In particular, transient spectroscopy techniques evaluate the capacitance transient induced by varying the extension of the depletion region, thus inducing the capture/emission of carriers within the region on interest.

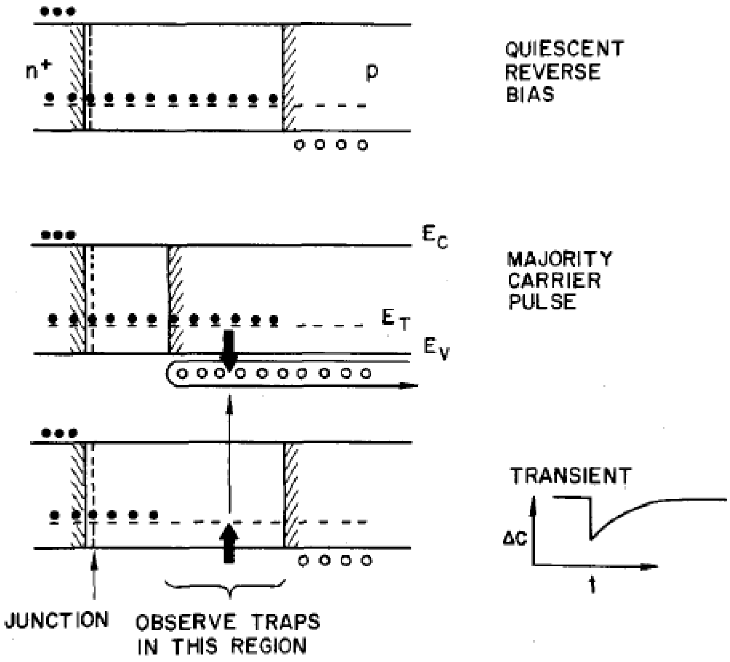

Figure 9.8: Filling pulse sequence adopted by capacitance DLTS in order to induce a capacitance transient related to a majority carrier trap. Electrons and holes are represented by black and white circles, respectively (from [113]).

For instance, we will now consider the case of a reverse-biased n^+p junction where a deep acceptor level exists at the p-side of the material, as reported in the first frame of Figure 9.8. Under reverse bias, the depletion region extends more towards the lightly doped p-side of the material. Within this region, the aforementioned acceptor (majority-carrier) traps are emptied of holes, due to relative position of the Fermi level with respect to the trap level. By rapidly reducing the applied reverse bias, the extensions of the depletion region is reduced, thus varying the electric field, and the Fermi level, in the device region that in the former bias condition was at the edge of the depleted semiconductor layer. The new relative position of the trap level with respect to the Fermi level induces the capture of holes. This time-dependent process is governed by the relation:

$$N(t) = N_T \left(1 - \exp^{-c_h t}\right) \tag{9.42}$$

where N_T is the trap concentration and c_h is the hole capture rate, previously defined in equation 9.36. After a sufficient amount of time, which may vary due to the measuring condition (temperature, voltage) and to the intrinsic properties of the deep-level under investigation, all the traps contained within the region of interest can be considered filled (frame two of Fig. 9.8). At this point, if the applied bias is brought back to the original quiescent value, emission of (majority) carriers from the recently filled traps occurs. Despite the change in the absolute energy level of the trap is immediate, the emission process may be a (relatively) slow phenomenon. In this case, the variation with time of the density of occupied trap states, and thus of the capacitance value, is given by

$$N(t) = N_T \exp^{-e_h t} \tag{9.43}$$

where e_h is the hole emission rate defined in equation 9.36. Due to the high electric field inside the depletion region, the carriers emitted to the valence band are rapidly swept away in a time frame the typically ranges from $10^{-12}\,s$ to $10^{-10}\,s$: this avoids the re-trapping of emitted carriers, thus ensuring an easier interpretation of the capacitance transient and an easier extrapolation of the emission rate. In equation 9.43, N_T represents the the total trap concentration only if the filling phase was long enough to permit the occupation of all the empty trap states. This topic will be further discussed in section 9.2.2.

The sign of the capacitance transient provides direct information on the type of carriers that are being emitted at a specific sample temperature. As reported in Figure 9.9, an increase in the diode capacitance after the filling phase is associated with the emission of majority carriers, whereas the emission of minority carriers induces a negative transient. Filling of minority carrier traps can be achieved by employing a forward-bias pulse during the filling phase, thus forcing the injection of minority carriers from the junction. This forces both majority and minority carriers traps to be filled, hence the observed capacitance transient is the net result of the emission of both types of carriers.

Deep-level profiling profiling

So far, the DLTS technique was showed to be capable of identifying the type (acceptor Vs. donor) and the intrinsic properties (activation energy and capture cross-section) of deep-levels within the (variable) depletion region of a semiconductor device. Since the magnitude of the capacitance transient during the emission process is proportional to the concentration of trapped carriers within the region of interest, the C-DLTS can be also employed to evaluate the concentration of the traps involved in the emission process. First, we must consider that the magnitude of the capacitance transients depends on the relative position of the trap with respect to the edges of the space

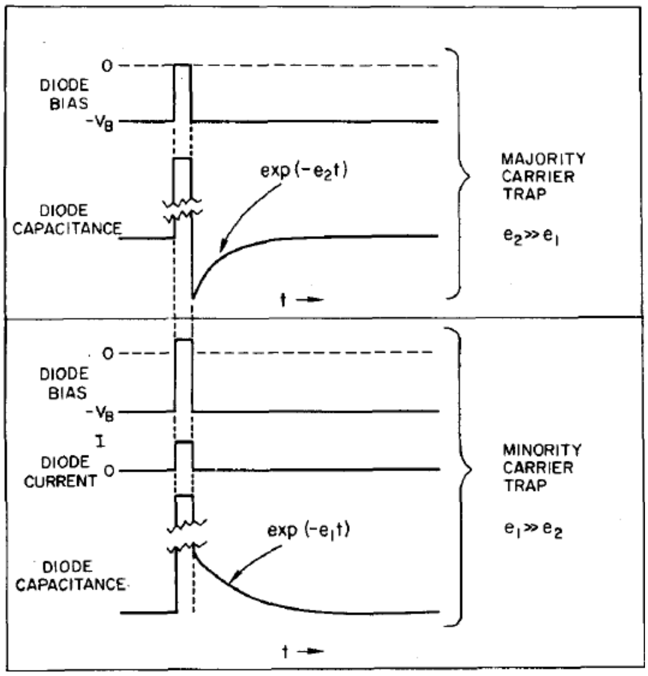

Figure 9.9: Effect of majority and minority carriers emission processes on the diode capacitance after the filling pulse. A forward bias filling pulse is employed in order to inject minority carriers from the junction to fill the minority carriers traps [113].

charge region, even for uniformly distributed traps and uniformly doped samples. If we consider a space charge layer which extends from 0 to W within a Schottky barrier or a p^+n junction, from Poisson's equation we can evaluate that the voltage change induced by trapping $n(x)$ electrons at position x in the interval Δx is given by:

$$\Delta V = \frac{e}{\varepsilon}\left[N_+ W \Delta W - n(x) x \Delta x\right] \tag{9.44}$$

where ε is dielectric constant of the semiconductor, and N_+ is the positive space-charge concentration at W. Since we are dealing with relative capacitance variation at constant bias, this quantity can be easily evaluated by setting ΔV to zero in equation 9.44, thus obtaining

$$\left(\frac{\Delta C}{C}\right)_x = -\frac{n(x)}{N_+ W^2} x \Delta x \tag{9.45}$$

Since the sensitivity of the junction capacitance to trapped charge reported in equation 9.45 varies linearly from zero a the junction ($x = 0$) to a maximum a the boundary of the SCR, this means that the for inhomogeneously distributed traps, capacitance-based deep-level profiling techniques are very insensitive for traps located closer to the junction.

In order to evaluate the magnitude of the total capacitance variation, equation 9.45

must be integrated over the entire region of the space-charge layer where the emission is taking place. If we consider the band-diagram of the asymmetric junction reported in figure 9.10, two different regions of interest can actually be identified. In particular, at the outer edge of the depletion layer there is a transition region between the free carrier-rich bulk material and the depleted semiconductor near the junction. This trap-specific region corresponds to the so-called edge region (or Debye tail), whose extension λ from the SCR boundary defines the point where the trap level E_T crosses the Fermi level E_F. If we consider a uniform carrier concentration in the bulk material (N_+), then it can be proved that

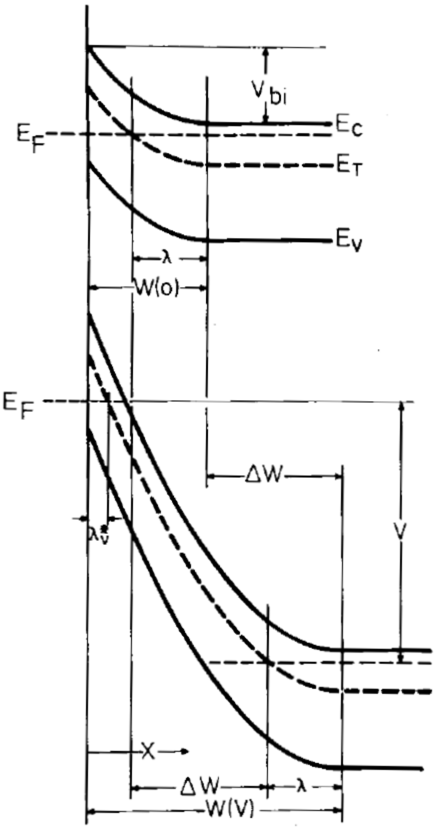

Figure 9.10: Band diagram of an n-type (asymmetric) Schottky-like junction at 0V (top) and under reverse bias (bottom) [114].

$$\lambda = \sqrt{\frac{2\epsilon\left(E_F - E_T\right)}{e^2 N_T}} \tag{9.46}$$

Within the edge region, at thermal equilibrium the trap level is below the Fermi level, and thus is filled with electrons: there are enough free carrier so that the capture rate is greater than the emission rate. In the remaining part of the depletion region the trap level falls above the Fermi level, and the trap occupancy after the filling pulse is defined by the thermal emission process described by equation 9.43. Although the concentration of free carriers has an impact on the trap occupancy, band bending is not affected, thus this region can be neglected for the calculation of the depletion width W. Given those assumptions, the total capacitance variation induced by a (majority-carrier) pulse, which brings the bias from the quiescent value V to zero bias in order to fill a trap whose concentration is N_T, can be evaluated by integrating equation 9.45 from $W(0)-\lambda$ to $W(V)-\lambda$, thus obtaining

$$\frac{\Delta C}{C} = -\frac{N_T}{2N_+}\left[1-\frac{\lambda}{2W(V)}\left(1-\frac{C(V)}{C(0)}\right)-\left(\frac{C(V)}{C(0)}\right)^2\right] \tag{9.47}$$

If the edge region is neglected, equation 9.47 turns into the widely-known relation

$$\frac{N_T}{N_+} \approx 2\frac{\Delta C}{C} \tag{9.48}$$

which may lead to a significant underestimation of the trap concentration if low reverse-bias voltages are employed.

The variation in extension of the depletion layer with the applied bias can be exploited in order to measure the trap concentration within the semiconductor. Once the shallow concentration profile is known, the trap profile can be measured by applying a series of (majority-carrier) filling pulse of increasing amplitude. With this method, the deep-level concentration is probed inwards from W as the deep level concentration is increased from zero. If we consider the case of an asymmetric junction, the incremental change in the junction capacitance due to the traps filled by the small change δV in the filling pulse voltage of amplitude V is given by:

$$\delta\left(\frac{\Delta C}{C}\right) = \left(\frac{\varepsilon}{eW^2N_+}\right)\frac{N_T(x)}{N_+(x)}\delta V \tag{9.49}$$

where x is the width of the space-charge layer during the pulse and C, W and N_+ are referred to the steady-state bias between the pulses. The former equation shows that a linear plot of ΔC Vs. V implies that the deep level and the shallow level have the same profile.

The rate-window concept

The rate-window concept was first introduced by Lang in [113] in order to evaluate the experimental data provided by the instrumentation employed to probe the thermally-stimulated deep-level related capacitance transients after the filling phase.

Older detection schemes were usually based on dual-gated signal averager (boxcar), that measured the capacitance transient at two different time t_1 and t_2: the time frame between t_1 and t_2 is called *rate window*. By applying a constant train pulse of $V_{MAX} = V_{FILL}$ and $V_{MIN} = V_{MEAS}$ (the quiescent reverse bias we previously referred to), it is possible to measure the difference in capacitance between t_1 and t_2 for a given sample temperature. By increasing this latter parameter, the emission rate from the deep-level increases, thus increasing the registered ΔC value. This concept is depicted in Figure 9.11.

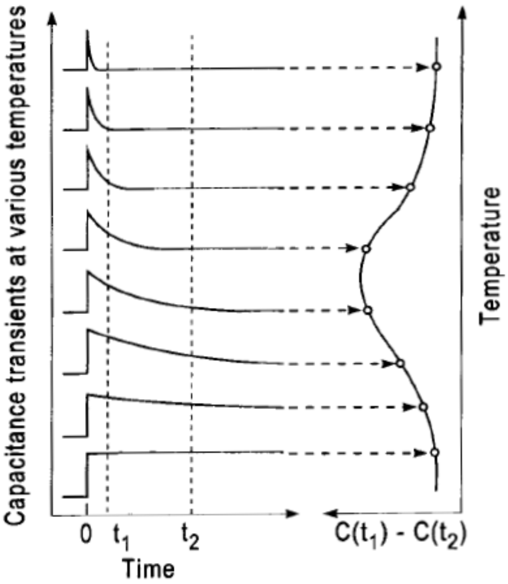

Figure 9.11: Graphic interpretation of the rate window concept [114].

The variation in capacitance is maximized once the the time constant of the emission process approaches the value of the adopted time window. Thus, a single point of the (e, T) relation can be extrapolated by plotting the ΔC Vs. T values, the so-called DLTS spectrum, and by evaluating the temperature for which the maximum ΔC is reached. If we assume a pure exponential dependence on time of the capacitance transient, the normalized DLTS signal in function of temperature is given by:

$$S(T) = \frac{C(t_1) - C(t_2)}{\Delta C(0)} = \exp\left(-\frac{t_1}{\tau}\right)\left[1 - \exp\left(\frac{\Delta t}{\tau}\right)\right] \tag{9.50}$$

where $\Delta C(0)$ is the magnitude of the capacitance transient at $t = 0$ and $\Delta t = t_1 - t_2$. By setting the derivative of Eq. 9.50 with respect to τ to zero, the maximum of the DLTS signal is obtained as

$$\tau_{max} = \frac{t_1 - t_2}{ln(t_1/t_2)} \tag{9.51}$$

By changing the values of t_1 and t_2 the DLTS peak shifts in temperature, hence the (e, T) relation in an extended temperature range can be extrapolated by performing several thermal scans at different rate windows. This produces a series of DLTS spectra, each one reporting a shifted (deep-level related) peak with respect to a longer (shift towards lower temperatures) or a shorter (shift towards higher temperatures) rate window. The position of the maxima and the current rate window value, i.e. the dominant emission rate, are then employed to build the Arrhenius plot of each deep-level, which shows up in the rate-window plot as a peak. An example of DLTS analysis performed at different rate windows is reported in Figure 9.12.

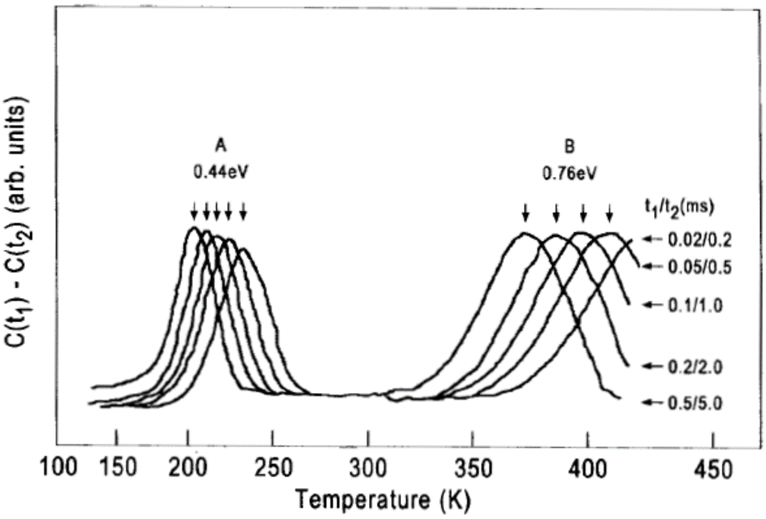

Figure 9.12: DLTS spectra showing two hole traps in n-GaAs [113].

Non-exponential transients and field-dependent emission

Under the low trap density approximation adopted so far, capacitance transients induced by the thermally stimulated emission of trapped carriers are assumed to be purely exponential. However, when dealing with large ($3N_T > N_+$) concentration of traps, comparable with the density of the shallow levels, the capacitance transients under constant voltage become nonexponetial. In this case, it can be demonstrated that by recording the voltage transient needed to maintain a constant capacitance rather than evaluating the capacitance transient at constant bias, exponential signal proportional to the trapped charge concentration can be obtained as well [115].

Nonexponential transient may also occur for a different set of reasons. For instance, the presence of multiple deep-levels responding in the same temperature range with similar emission rates. In this case, the resulting DLTS peak in the rate window plot is the result of the Gaussian convolution of the separate (theoretical) DLTS signal generated by each deep-level. By proper de-convolution methods it is possible to separate the two contributing signals, and proceed with the Arhhenius analysis of each deep-level. Alternatively, if the entire capacitance transient is recorded, fitting with multiple exponentials may be employed to separately extract the time constants of each contributing emission process.

Also deep-levels at the edges of the space-charge region may influence the shape of the capacitance transient: as previously stated, in the edge region the non-negligible free carrier concentration may induce the re-trapping of a small amount of the emitted carriers, thus slowing down and altering the capacitance transient.

Finally, nonexponetial transients may be detected when the emission rate of the specific defect under investigation has a strong field dependence, and thus varies depending on the position within the space-charge layer. A field dependent emission energy indicates that the carrier is trapped by a Coulombic potential well. According to the Poole-Frenkel effect [116], applying an electric field superimposes a linear potential onto the Coulombic potential, which reduces the effective potential barrier seen by the trapped carrier, thus reducing the amount of energy that needs to be (thermally) provided to the carrier in order to promote its emission. This effect is pictured in Figure 9.13.

The field dependence of the emission process can be easily evaluated by means pf the Double-Pulse DLTS (DDLTS technique), which employs a fixed pair of filling pulse

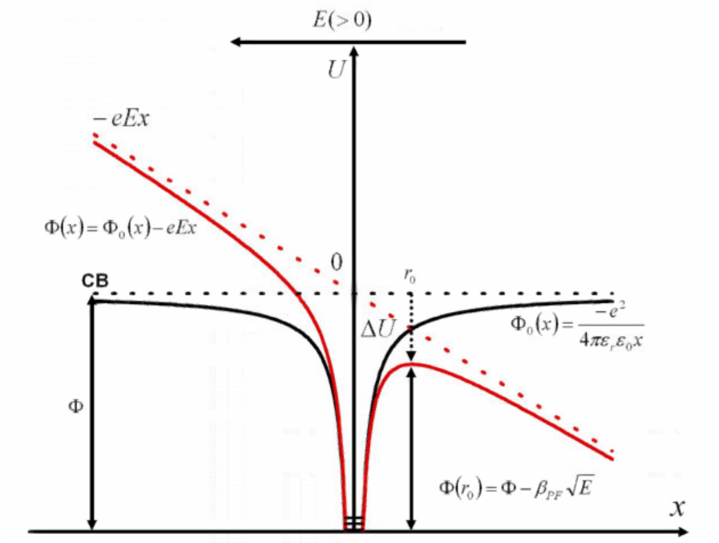

Figure 9.13: Influence of the Poole-Frenkel effect on the effective potential barrier seen by an electron trapped by a donor level. The reduction in the potential barrier is proportional to the square root of the local electric field ($\Delta U \propto \sqrt{E}$).

voltages while sweeping through a range of measurement voltages. For filling pulses sufficiently close together, the difference in emission transients that result from the two filling pulses is from a volume of the depletion region where the spread in electric field is limited. Thus, the dependence of the emission rate on the electric field can be determined by changing the measurement voltage and by evaluating the changes induced to the time constant (emission rate) extrapolated from the transient obtained by subtracting the two transient registered at two different filling pulses.

Capture kinetics

In the previous paragraphs the attention was focused on the dynamics of the emission process, and to the information that its temperature dependence provides regarding the defect-related deep level that is participating to the emission process. In particular, a relation was found between the variation in the normalized DLTS signal and the (relative) concentration of the deep-level generating the signal (see equation 9.48). This mathematical relation was derived assuming the all the traps contained in the depletion layer swept by the filling pulse are filled, i.e. that the duration of the filling pulse was long enough to saturate the capture process. For this reason, in order to quantitatively investigate the concentration of a specific trap, the duration of the filling phase must be tuned in order to ensure the complete filling of deep states. This can be easily achieved by evaluating the amplitude of the emission transient in function of the filling pulse amplitude, while keeping the sample at a reasonable fixed temperature for which the emission transient can be evaluated by the experimental apparatus. A threshold value for the duration of the filling pulse is then found, above which any increase in the duration of the filling phase does not further promote the filling of traps.

The dependence of the DLTS signal amplitude on the filling time, i.e. the time dependence of the capture process, also provides useful information regarding the physical nature of the defect. During a filling pulse, the capture rate is much greater than the emission rate. In terms of the filling time t_p, the time-dependent concentration of occupied defect states $n_T(t_p)$ by electrons in an n-type material can be expressed as:

$$n_T(t_p) = N_T + [n_T(0) - N_T]\exp(-c_n t_p) \tag{9.52}$$

where N_T is the total concentration of defects, and c_n is the capture rate defined in equation 9.36, valid only for a non interacting point defect. This translates into the following equation, which describes the variation in the capacitance at the end of the filling phase:

$$\Delta C(t_p) = \Delta C_{max} \left(1 - \exp(-c_n t_p)\right) \tag{9.53}$$

where ΔC_{max} is the amplitude of the transient. Since the DLTS signal is proportional to the initial concentration of occupied defect states, an exponential dependence of the normalized DLTS signal $\Delta C/C$ on the filling pulse width exists.

This theoretical trend of the of amplitude of the DLTS versus the filling pulse width can be altered by several factors. Firstly, capture of carriers may occur also at the edge region of the depletion layer, as depicted in Figure 9.14.

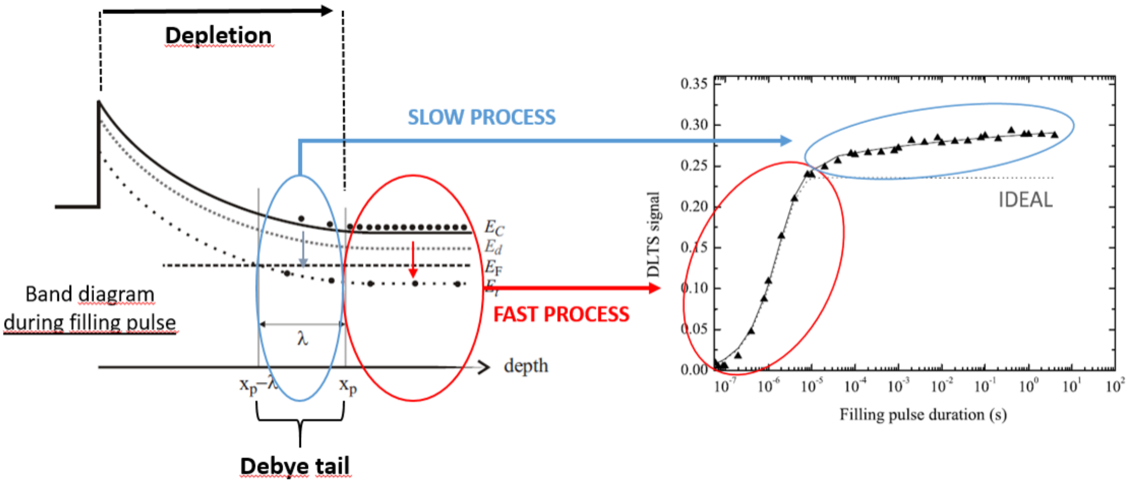

Figure 9.14: Effect of the Debye tail on the capture kinetics.

Since the capture rate is proportional to the concentration of free carriers n (9.36) within the Debye tail, where n is much lower with respect to bulk concentration, a slower trapping phenomenon takes place. As shown in the second plot of Figure 9.14, this effect can increase the filling time needed to reach complete trap saturation by several orders of magnitude (the variation in trap occupancy for an isolated point defect usually spans in a time interval which covers two to three orders of magnitude maximum).

For closely spaced defects, trapped electrons affect the electron capture process at neighboring defects by providing a repulsive time-dependent potential $\Phi(t)$ against electron capture (Fig. 9.15). In this situation, the electron capture rate equation can be re-written as:

$$\frac{dn_T}{dt} = c_n(N_T - n_T(t)) \exp\left(\frac{-e\Phi(t)}{kT}\right) \tag{9.54}$$

where we are assuming a linear spacing of defects, and $t_p \gg \tau$.

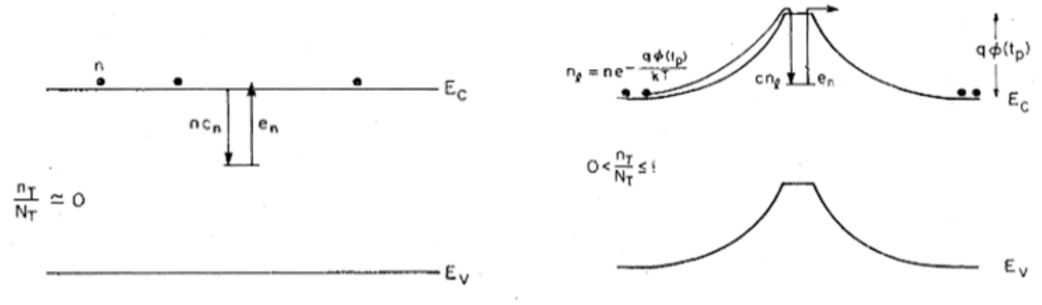

(a) (b)

Figure 9.15: Band-diagram model for an electron capture by a point defect located around a dislocation, in low (a) and high (b) trap occupancy condition [117]. The first case resembles the capture process by an isolated point defect, whereas for high $n_T(t)/N_T$ values a repulsive time-dependent potential $\Phi(t)$ rises.

From equation 9.54, the trap occupancy at time t_p can be written as:

$$n_T(t_p) = c_n \tau N_T ln(t_p/\tau) \tag{9.55}$$

where τ represents a characteristic time required for charge capture to begin influencing $\Phi(t)$. Equation 9.55 shows that trap occupancy for a linear arrangement of interacting defects depends logarithmically on fill pulse time, as depicted in Figure 9.16.

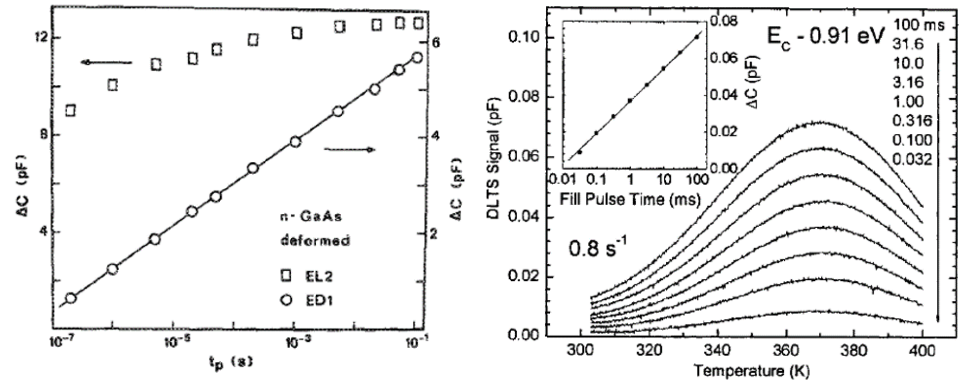

(a) (b)

Figure 9.16: Dependence of the amplitude of the DLTS signal on the filling pulse duration for a linear arrangement of point defects (a) in GaAs crystals [118], and (b) in MBE-grown n-GaN [119].

Linear arrangement of point defects can be further differentiated between (i) point defects arranged along a Threading Dislocation (TD) and (ii) TD cores. In the first case, a localized state within the energy gap exists, and the DLTS peak temperature is independent on t_p, since the trap occupancy dose not influence the trap level (see Fig. 9.16b). On the other hand, a band of states corresponds to defects related to TD cores (Fig. 9.17a). Since the lowest energy states are preferentially filled with electrons for short t_p values, the effective energy required to de-trap the carrier is reduced with increasing filling pulse width. This translates into a shift of the DLTS peak towards higher temperatures with decreasing t_p, as reported in Fig. 9.17b.

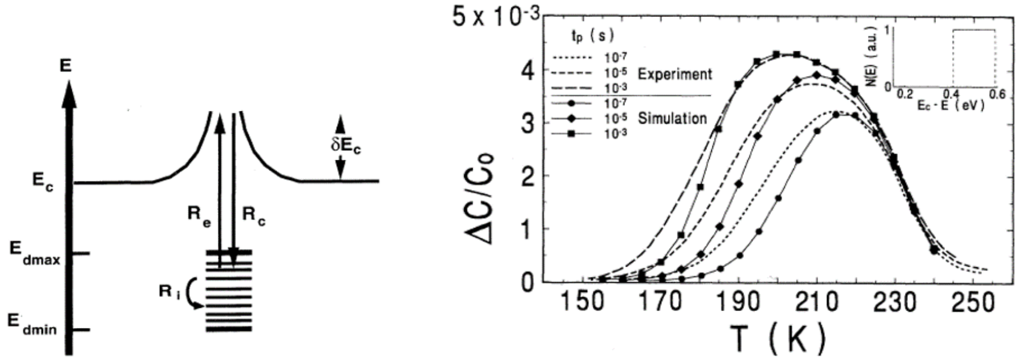

(a)

(b)

Figure 9.17: (a) Electron capture and emission from a band of states related to an extended defect. R_e, R_c and R_i are respectively the emission, capture and the internal equilibrium rates: if $R_i \gg R_e$, R_c the defect can be classified as bandlike. (b) Effect of the filling pulse width on the DLTS signal of Nichel-related dislocation cores in n-Si [120].

Finally, if a (fixed) capture barrier exists for the capture of electrons by a point defect, the capture process can be modeled by introducing an exponential term to the capture cross section according to:

$$\Delta C(t_p) = \Delta C_{max}\left(1 - \exp(-c_n t_p)\right) \qquad c_n = \nu n \sigma_e^{\infty} \exp\left(-\frac{\Delta E_b}{kT}\right) \tag{9.56}$$

where ΔE_b is the capture barrier energy, and σ_e^{∞} is the high-temperature electron capture cross section. The presence of a potential barrier slows down the capture process, introducing an additional temperature dependence to the kinetic of the process.

Chapter 10

Degradation Mechanisms of Heterogeneous III-V/Silicon 1.55 μm DBR Laser Diodes

This chapter reports an extensive analysis of the degradation processes of heterogeneous III-V/Silicon infrared (IR) laser diodes designed for integrated telecommunications and interconnects. By submitting the devices to a series of constant current stress tests, a gradual degradation of the main device parameters was observed. In particular, in every stress scenario the devices under test showed (*i*) an increase in the threshold current, (*ii*) a decrease of the turn-on voltage, and (*iii*) an increase in the apparent carrier concentration within the space charge region. The variation of the electrical parameters (turn-on voltage and apparent charge concentration) was found to be significantly correlated to the optical degradation for long stress times; the results support the hypothesis that degradation originates from an increase in the non-radiative recombination rate, possibly due to the diffusion of defects towards the active region of the devices. In order to investigate the physical origin of those defects, a capacitance DLTS analysis was performed. The results indicate the presence of five different deep levels, with a main trap located around $0.43\,eV$ above the valence band energy. This trap is compatible with an interface defect located between the $In_{0.53}Al_xGa_{0.47-x}As$ SCH region and the InP layer.

10.1 Devices and experimental details

The devices under analysis are heterogeneous III-V/Silicon Distributed Bragg Reflector (DBR) laser diodes with an emission wavelength of 1.55 μm. Typically, in heterogeneous photonics the III V region incorporates the light source, while the SOI region contains all the passives and wave guiding-related components, as well as some active silicon-based photonic devices [121]. For the samples under investigation, the integration of the two technologies was performed by means of low temperature molecular wafer bonding technique [122]. A cross-section of the whole structure is reported in Figure 10.1.

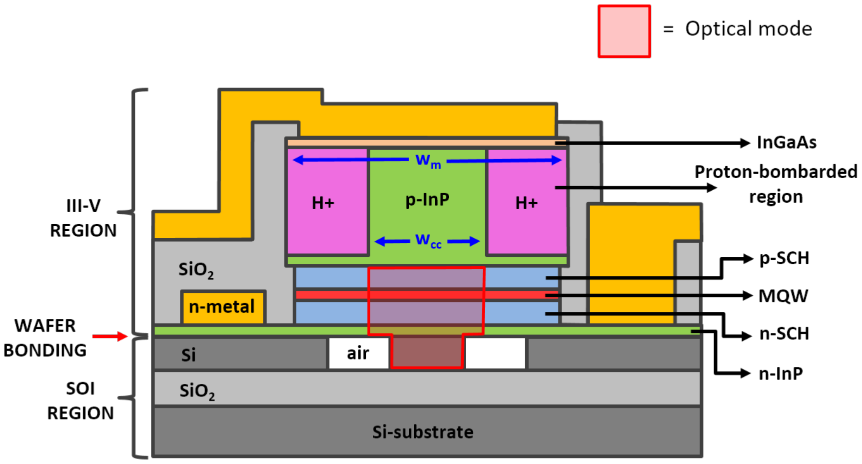

Figure 10.1: Cross section of the heterogeneous LDs under analysis. The red-shaded area highlights the preferential propagation region of the optical mode.

The red shading highlights the regions where the propagation of the optical mode takes place. The mode is longitudinally coupled to the silicon waveguide through a tapered mode converter [123] which ensures a low-loss and adiabatic (i.e. with no excitation of higher order transverse modes) optical field transfer. Optical feedback is granted by a DBR mirror, which also provides the high wavelength selectivity required by telecommunication channels [124].

As pictured in Fig. 10.2, the active layer of the devices is composed of seven InAlGaAs-based Multi Quantum Wells (MQWs) enclosed by two Graded Index Separate Confinement Heterostructure (GRIN-SCH) layers [125, 126]. These are employed to obtain high optical confinement while maintaining good overlap between the optical mode and the population of free carriers within the active region of the devices. Lattice matching between $In_{1-y}(Al_xGa_{1-x})_yAs$ confinement layers and InP was maintained by keeping the y mole fraction at a constant value of 0.47 [125]. An InGaAsP/InP superlattice structure was grown between the n-InP layer and n-contact in order to minimize

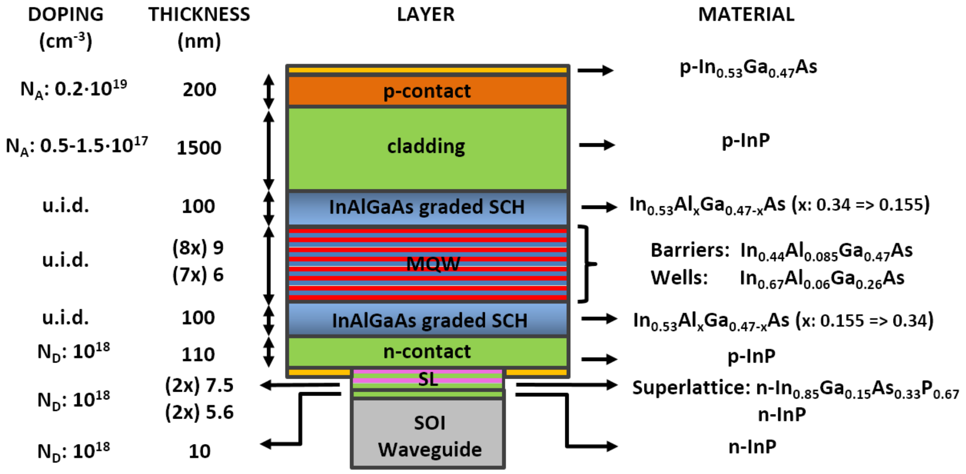

Figure 10.2: Detailed epitaxial structure of the III-V region reported in Figure 10.1.

the propagation of dislocations and defects through the active region of the devices. Finally, proton bombardment was employed in order to ensure lateral current confinement [109], thus reducing the effective carrier-injection area to about $8.16 \cdot 10^{-5}\,cm^2$. Device length (L_d), mesa width (W_m) and current channel width (W_{cc}) are respectively $L_d = 2040\,\mu m$, $W_m = 26\,\mu m$, and $W_{cc} = 4\,\mu m$.

For testing purposes, several identical slices of heterogeneous wafer were stressed and measured at a constant ambient temperature of 45 °C. The electrical characteristics were measured by a 4-wire configuration, in order to minimize the effects of series resistance. The C-V measurements were carried out with an HP 4284A LCR-meter. The light output signal was collected with an amplified Ge-based photodiode placed in front of the angled facet of the silicon waveguide.

10.2 Experimental results

10.2.1 Preliminary step-stress experiment

In order to rapidly evaluate the impact of DC aging on the electrical and optical performance of the devices, a current step-stress was performed at an ambient temperature of 45 °C. Each stage of the step-stress had a duration of 1 hour, with drive current increasing from 200 mA up to 950 mA, in 50 mA increments. A cool-down period of 120 s was introduced before each characterization step to let the device junction settle at the imposed cold-plate temperature, thus ensuring the repeatability and consistency of the measurements. The joint effect of current and temperature on the L-I characteristics of the devices is visible in Fig. 10.3a. A noticeable shift in the threshold current of the device is observed after each stage of the stress experiment. Interestingly, as shown in Fig. 10.3b, the threshold current increase has a quasi-linear dependence on stress time and current.

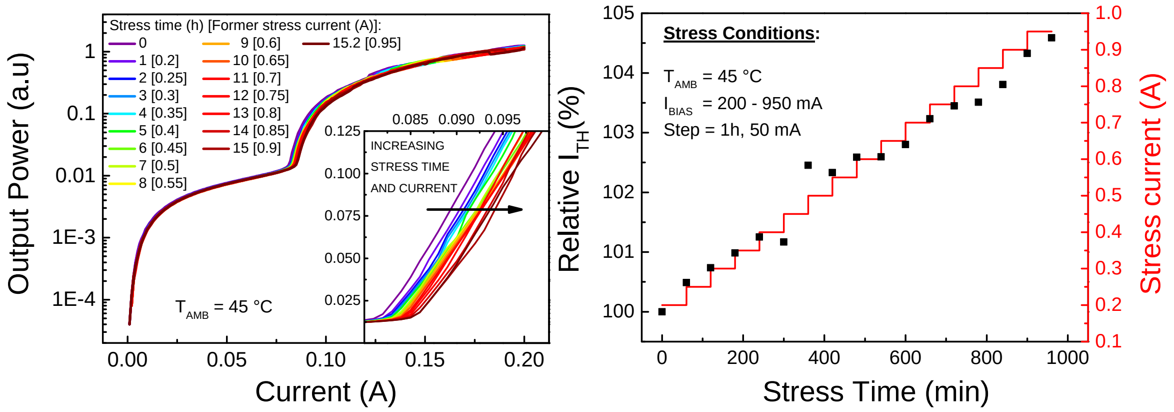

(a) (b)

Figure 10.3: Results of the optical characterization performed during the step-stress experiment. (a) Complete and near threshold L-I curves registered during the current step-stress performed at $T_{AMB} = 45\,°C$. The $950\,mA$ stress step was interrupted after 10 min due to the worsening of the mechanical contact between the sample and the tips. (b) Trend over time of the threshold current measured at the end of each 1h stress cycle. The "out-of-trend" threshold currents measured after the $400\,mA$ and $450\,mA$ steps are a consequence of the stress-induced instability of the position of a near-threshold optical kink experienced by the device.

10.2.2 Constant-current stress tests

Another outcome of this first stress test was the identification of the bias conditions to be used during long-term DC aging tests. With the aim of inducing a significant amount of degradation in a relatively short period, three current levels were chosen for the constant current experiments: $400\,mA$, $550\,mA$ and $700\,mA$, respectively equal to a current density flow through the active area of the device of $4.9\,kA/cm^2$, $6.74\,kA/cm^2$ and $8.59\,kA/cm^2$. The samples were aged for up to 500 hours. An ambient temperature of 45 °C was employed to slightly accelerate the degradation process. Finally, the measurement intervals were logarithmically-spaced, in order to properly monitor the evolution of the electrical (I-V, C-V) and optical (L-I) characteristics of the devices. Since the samples submitted to constant DC stresses behaved in a similar way, showing a common set of degradation processes but with different degradation rates, only the detailed evolution of the characteristics of the LD stressed at $550\,mA$ are reported in the following.

Variation of the optical parameters

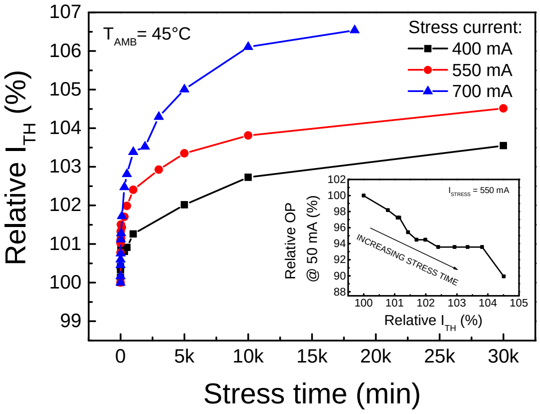

Figure 10.4: Threshold current degradation kinetics registered during the three different constant-current stresses performed at $T_{AMB} = 45\,°C$. Inset: correlation between the increase in threshold current and the decrease in sub-threshold emission, for the device stressed at $550\,mA$.

The degradation kinetics of the threshold current registered in the three different stress scenarios (Fig. 10.4) reveal a strong dependence of the degradation rate on the stress current level. Since the DUTs have a relatively low thermal resistance ($R_{TH} \approx 12\,K/W$), which produces a junction temperature shift between the stronger and the weaker stress conditions of about 7.4 °C, current flow appears to be the main driving force of the I_{th} increase.

A deeper investigation of the L-I curves revealed that no apparent variation of the Slope Efficiency (SE) was shown by the DUTs. For a laser diode the SE can be expressed as

$$SE = \eta_{inj} \frac{\alpha_m}{\alpha_m + \alpha_i} \tag{10.1}$$

where η_{inj} is the carrier injection efficiency and α_m and α_i are respectively the mirrors and the modal (cavity) losses [109]. The stability of SE demonstrates that the adopted aging conditions did not affect any of these parameters. In addition, the fact that SE is stable also indicates that the efficiency of the coupling between the III-V active layer and the SOI waveguide does not degrade significantly after stress.

On the other hand, the threshold current is proportional to

$$I_{th} \propto \frac{1}{\eta_{inj}} \frac{N_{th}}{\tau} \cong \frac{(A + BN_{th} + CN_{th}{}^2)N_{th}}{\eta_{inj}} \tag{10.2}$$

where N_{th}, τ, A,B and C are respectively the threshold carrier density, the carrier lifetime, the SRH recombination coefficient, the bimolecular recombination coefficient and C the Auger recombination coefficient. Finally, the increase in I_{th} was also found to be correlated with the decrease in the sub-threshold emission (defined as $OP_{sub} \propto N/\tau \cong (A + BN + CN^2)N$, see the inset of Figure 10.4). Since both parameters (threshold current and sub-threshold emission) depend on the balance between radiative and non-radiative recombination, the results support the hypothesis that degradation is due to an increase in the concentration of non-radiative recombination centers inside the active region of the devices, with subsequent increase in the "A" coefficient (under the hypothesis that the "B" and "C" coefficients are stable under stress).

Variation of the electrical parameters

In order to prove the hypothesis above, by demonstrating that defects are effectively generated during long-term stress, we analyzed the degradation of the electrical parameters of the devices. As shown in Fig. 10.5, stress induced an exponential decrease of the turn-on voltage of the laser diodes. This process was found to be well correlated with the increase in the threshold current for aging times longer than 50 min (see Figure 10.5 (b)).

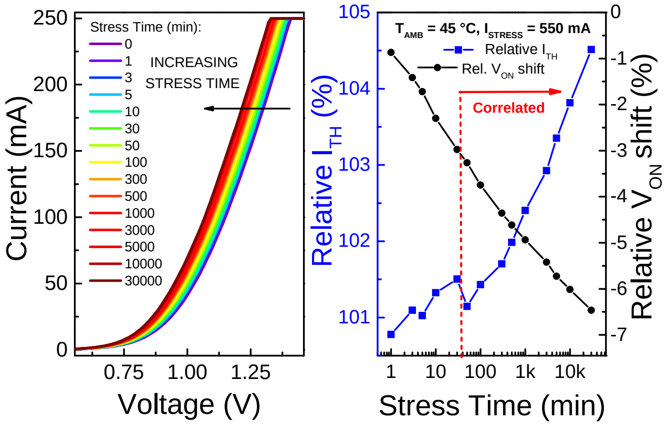

Figure 10.5: On the left: forward I-V characteristic measured during the constant current stress ($I_{STRESS} = 550\,mA$) performed at an ambient temperature of 45 °C. On the right: trend over-time of the LD turn-on voltage (V_{ON} was extrapolated as the LD voltage at $1\,mA$ current).

By considering that in the low forward-bias regime the I-V curves are dominated by defect-assisted conduction (i.e. by the trap-density in the p-n junction), Fukuda et al. [127] concluded that for their InGaAsP/InP laser diodes aged at constant current, this kind of correlation was compatible with a reduction of the lifetime of the injected carriers. This observation may further confirm what is suggested by the trend of the optical characteristics, i.e. that degradation is due to the generation of defects within the active layers.

Further evidence was collected by analyzing the ideality factor of the junction, as a function of the applied bias (Fig. 10.6).

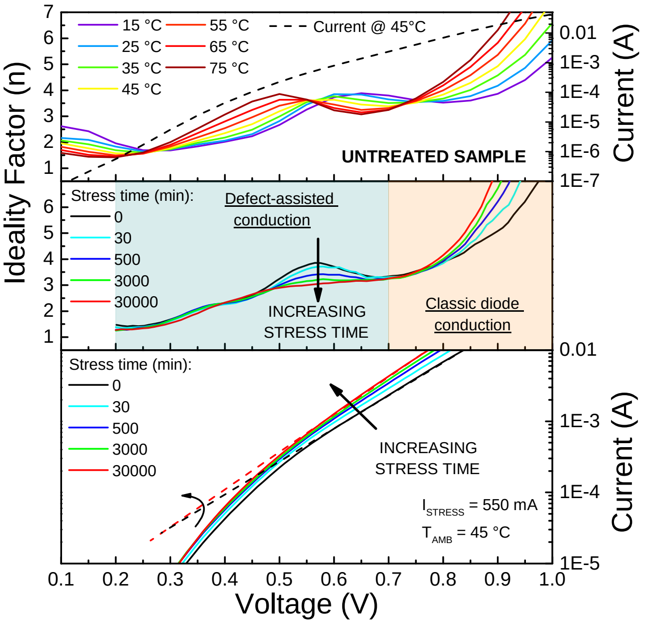

Figure 10.6: Bias-dependent diode ideality factor: temperature dependence measured for a generic untreated sample (top graph) and trend over time registered during the stress performed at 45 °C and at a bias current of 550 mA (middle graph). Bottom graph shows the variation of the semi-log I-V plot in the region of interest. Shaded areas highlight the dominant conduction mechanisms in the bias regimes of interest.

Interestingly, untreated samples exhibit a characteristic decrease in the ideality factor for voltages higher than 0.55 V (at 45 °C). Generally speaking, the reduction of the ideality factor indicates the turn-on of a new current conduction mechanism. Above a certain bias level (0.6 V at 45 °C in our case) the classic diode conduction, limited by the diffusion of carriers over the built-in potential barrier (and described by a ideality factor theoretically equal to 1), starts to prevail. At lower voltages, current conduction is dominated by defect-assisted tunneling [128, 129], leading to higher values of the ideality factor. This is also shown by the temperature-dependent curves in Figure 10.6 (a): as temperature increases, the turn-on voltage of the different conduction mechanisms decreases, leading to a left-wards shift of the n-V curves.

Device aging induced an increase in the slope of the I-V curves for voltages around 0.65 V (see Figure 10.6 (c)), possibly related to the creation of an additional set of defects or to an increase in the number of deep levels. This effect is consistent with the decrease in the ideality factor in the 0.45 V – 0.65 V voltage range experienced by the

DUTs. When the defect density increases, the corresponding tunneling current conduction mechanism becomes more efficient, leading to a higher current and to a lower value of the ideality factor. Those experimental observations suggest that the degradation of the electrical characteristics of the LDs is mainly driven by the increase in the concentration of deep-levels, i.e. of defects, within the active region, confirming what was previously suggested by the analysis of the optical characteristics during stress. This interpretation of the decrease in the ideality factor experienced by the DUTs is also supported by the degradation kinetics of the capacitance-voltage characteristics, that will be discussed in section 10.2.2.

Investigation of the origin of degradation: C-V analysis

In order to achieve a better description of the degradation process, we investigated the characteristics of the devices by means of capacitance-voltage measurements. The measurements were carried out in-situ, i.e. during the execution of the stress tests, in order to be able to correlate the variation of the optical parameters (I_{th}, SE) to the changes in junction capacitance. During constant-current aging, the small signal junction impedance, modeled as a capacitance in parallel with a conductance (C_p – G), was monitored by means of an LCR meter.

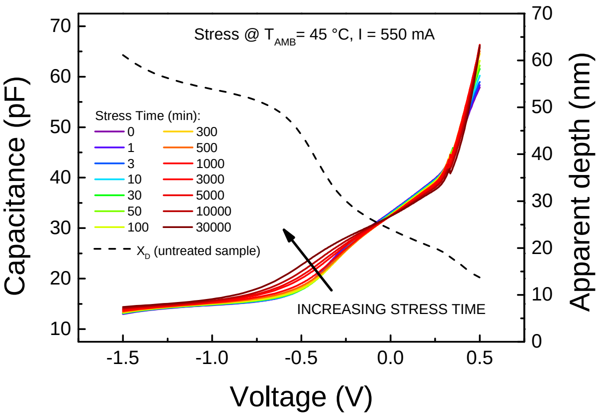

Figure 10.7: Evolution of the 1 MHz C-V measurements performed on the LD stressed at 550 mA with $T_{AMB} = 45\,°C$. Dashed line shows the apparent Space Charge Region extension, i.e. junction depth, in function of the LD voltage, for the unaged LD.

The evolution over time of the C-V characteristics, reported in Fig. 10.7, showed an increase of the junction capacitance for bias voltages between -1 V and 0 V. Since the value of C_p strictly depends on the concentration of free carriers within the Space Charge Region (SCR), C-V based carrier density profiling has been employed [110]. The results are plotted in Figure 10.8.

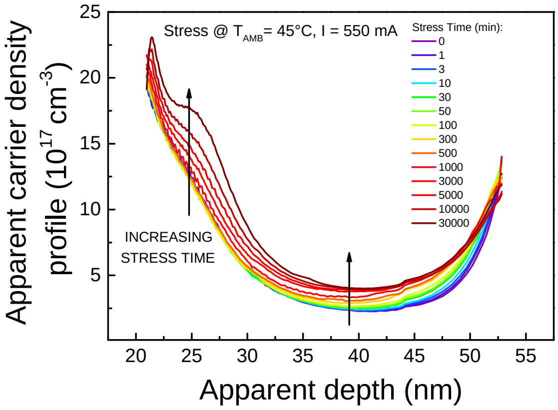

Figure 10.8: Apparent charge profile extrapolated from the C-V measurements reported in Fig. 10.7, performed during the 550 mA constant-current stress.

Considering that the doping concentrations of the InP layers closer to the active region are respectively $p = 5 \cdot 10^{17}\, cm^{-3}$ and $n = 10^{18}\, cm^{-3}$ (Fig. 10.2), we may treat the laser diodes under analysis as (weakly) $n^{+}p$ junctions. In such devices, the depletion region extends mostly towards the p-side, which corresponds in Fig. 10.8 to greater SCR extensions. By changing the bias level, the edges of the space-charge region are swept through different layers, whose apparent free charge concentration profiles can be estimated from the C-V curves.

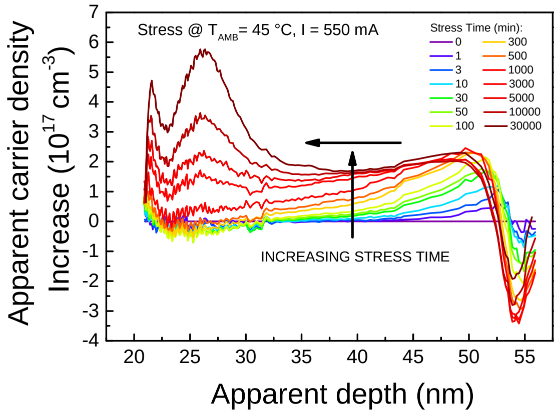

Figure 10.9: Relative variation of the apparent charge profiles reported in Fig. 10.8. All variations are referred to t=0 (flat line).

The interpretation of the apparent charge profiles reported in Fig. 10.8 can be simplified by looking at the overall variation of the apparent carrier density increase (plotted in Fig. 10.9). To be more specific, Figure 10.9 clearly shows a time-dependent and stress-induced re-localization of charge carriers towards the junction, which is located on the left-hand side. After redistribution, charge piles up in specific regions ($x_p \approx 22\, nm$ and $26\, nm$), possibly due to the presence of physical barriers to the observed diffusion-like process. In agreement with the epitaxial structure of our DUTs, those regions of preferential charge accumulation may be identified with the hetero-interfaces located within the active region of the LD, such as the QW/barrier or the QW/SCH interfaces, or at its edges, like the SCH/cladding border. As reported in Fig. 10.10, the increase in the junction charge was found to be well correlated with the increase in the threshold current for long stress times; this result confirms that the optical degradation is correlated to the redistribution of charge in the active region.

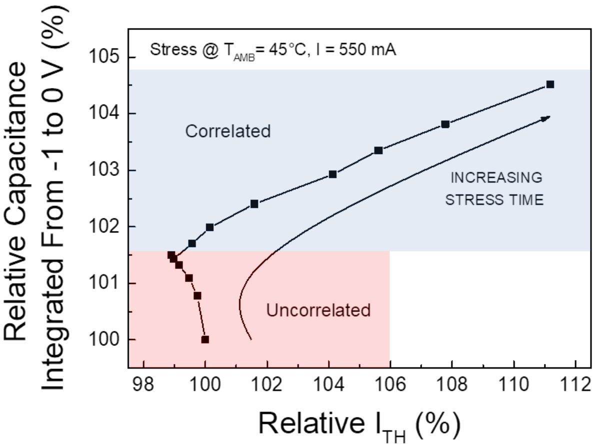

Figure 10.10: Correlation between the threshold current increase and the SCR free charge increase observed during the constant-current stress at 550 mA.

The results in Figure 10.9 are consistent with the diffusion of defects towards the active layer. Since some time is needed for the defects to reach this region (as testified by trend of the apparent charge increase for lower SCR extension), the reduction in the non-radiative lifetime due to defect-assisted recombination becomes relevant only after an initial period of stress, during which no apparent correlation between the variation of the threshold current and the increased free charge exists (see Figure 10.10). In particular, the peak carrier density in proximity of the active layer, i.e. for an apparent depth closer to 20 nm (Fig. 10.9), starts to increase only after about 100 min to 300 min of stress. After such amount of time, part of the diffused defects have relocated inside the active region of the device, where they start acting as non-radiative recombination centers. For longer stress times, the concentration of defects within the optically active layers of the device rapidly increases, thus reducing the non-radiative lifetime and increasing the amount of free charge inside the SCR.

With regard to the physical origin of those defects, we may consider that since the increase of the apparent free charge is in the order of $10^{17}\ cm^{-3}$ (Fig. 10.9), the diffusing species must be present inside the semiconductor device at least in this concentration.

Therefore, one hypothesis is that one of the dopants (Zn is more likely due to its high diffusivity [130, 131]), or native shallow defects, are moving towards the u.i.d. active region, thus increasing the density of free carriers and of non-radiative recombination centers [132, 133]. On the other hand, the source of those apparently diffusing defects may be located at one of the many hetero-interfaces present in proximity of the optically active layers. An imperfect control of the epitaxial growth may have led to a localized inclusion of impurities in the semiconductor crystal, or to the generation of extended defects. However, since with the exception of the MQW region the entire stack of the III-V epitaxy is lattice-matched, and since former studies on similar devices did not show any sign of the presence of misfit-related defects or of threading dislocations [13], the propagation of native or impurity-related point defects is more likely. Previous papers indicated that also extended Dark Line Defects (DLDs) may be generated after stress [134], leading to an increase in the losses and/or to the catastrophic failure of the devices. We suggest that DLD generation is not dominant in our devices, since the slope efficiency is stable during stress, and no catastrophic failure has been observed under the adopted aging conditions.

From the previous observations, we can conclude that the observed threshold current degradation process is driven by the diffusion of non-radiative defects towards the active region. Due to the quasi-symmetrical doping profile of the DUTs, the set of experimental data collected in our work is not sufficient to let us discriminate with a high degree of confidence the specific semiconductor layers which are undergoing degradation. Nonetheless, some insights into the physical origin of the diffusing species can be obtained by characterizing the defects present within the space-charge region of the devices. This goal has been achieved by means of a capacitance transient spectroscopy technique, as described in the following paragraph.

10.3 Deep-level transient spectroscopy

To further investigate the role of deep levels in the degradation of the devices under test, Capacitance Deep Level Transient Spectroscopy (C-DLTS) measurements were carried out. To this aim, thermal scans of capacitance transients in the range of 120 K – 350 K were measured with a DLTS apparatus built by SULA Technologies. As we are dealing with narrow-gap semiconductor materials, the selected thermal range allowed to identify the signatures of five different deep levels, reported in Figure 10.11 along with the specific quiescent and fill voltages employed for the measurements.

Following the assumption of a n^+p junction, and considering that a negative DLTS

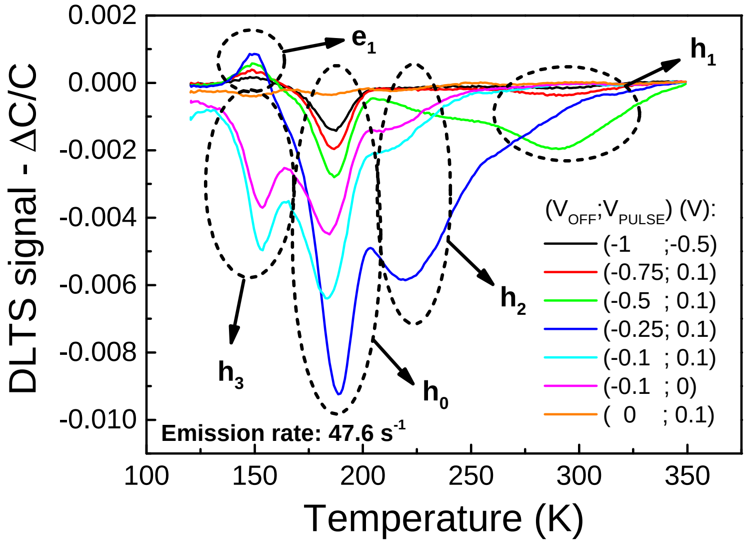

Figure 10.11: Overview of the deep levels observed by DLTS characterization at different bias conditions on an untreated sample. The figure shows the DLTS signal registered by the 5 ms correlator (time window), which corresponds to a carrier emission rate of approximately 47.6 Hz. The filling pulse voltage was limited to 0.1 V to avoid excessive levels of current injection.

peak corresponds to a majority-carrier trap [113], our characterization showed four hole traps (h_0,h_1,h_2,h_3) and one electron trap (e_1). Figure 10.12 reports the Arrhenius plot of the identified deep levels (due to the mutual influence of the DLTS signals of multiple deep levels, the activation energies of traps h_1 and h_2 could not be identified with accuracy and are not reported here).

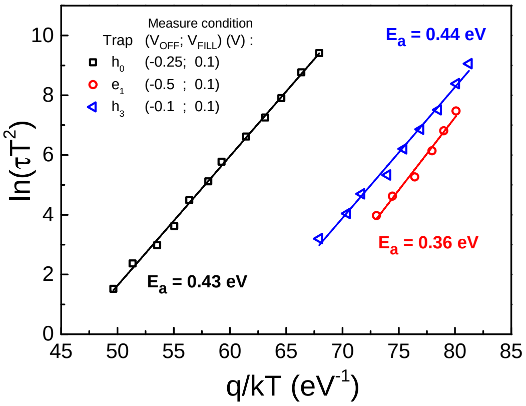

Figure 10.12: Arrhenius plot obtained by DLTS characterization on an untreated sample. The trap-specific measuring conditions, quiescent voltage (V_{OFF}) and fill voltage (V_{FILL}), are reported in the legend.

Further information could be obtained from the bias dependence of the peaks of the DLTS signal (Figure 10.11). The value of the quiescent voltage employed is proportional to the extension of the space-charge region under investigation, while the magnitude of those peaks is proportional to the concentration of the related defects [113]. The plot of Figure 10.11 shows that the maximum DLTS response is reached for $V_{OFF} = 0.25$ V by trap h_2, whereas trap h_1 responds more for lower quiescent voltages ($V_{OFF} =$-0.5 V), i.e. for greater SCR widths. This behavior suggests that the defect(s) associated with h1is probably located further from the active region with respect to trap h_2.

The Arrhenius plot of Fig. 10.12 shows that the main hole trap h_0 has an activation energy of $0.43\,eV$, and this value is constant across the entire quiescent voltage range adopted for our measurements. The Arrhenius signature of this trap is highly compatible with the E2 electron trap found by Schramm in Si-doped InAlGaAs Schottky contacts [135]. Considering that the devices grown with lower Al content exhibited a lower trap concentration, the authors suggested that the observed deep-level could be related to a native defect or an impurity related to Al incorporation. Thus, assuming trap h_0 to actually be an electron trap located on the p-side, the data reported by Schramm would suggest that the defect related to h_0 is located in the InAlGaAs SCH region closer to the InP cladding layer, where the Al content is maximum (x = 0.34). The presence of an intrinsic defect in high Al content $In_{0.53}Al_xGa_{0.47\text{-}x}As$ grown on InP has been documented by several other authors [136, 137, 138]. These papers report that the quaternary material exhibits a characteristic vacancy-related deep level whose activation energy linearly increases with Al content in the range $0.3\,eV - 0.8\,eV$. In particular, $0.43\,eV$ represents the activation energy commonly found for an aluminum concentration x = 0.34, which exactly matches the composition of the SCH graded layers at the InAlGaAs/InP interfaces of our DUTs.

Moving our attention on traps e_1 and h_3, we can notice from Fig. 10.12 that the two deep levels respond in the same temperature range, with slightly different activation energies and cross sections. Moreover, from Fig.10.11 we can see that while trap e_1 behaves as a (electron) minority carrier trap for lower quiescent voltages (hence for larger extensions of the SCR), in device regions closer to the active layer ($V_{OFF} =$ -0.1 V, 0 V) the DLTS signal is inverted, revealing a dominant presence of the majority carrier (hole) trap h_3. If we also consider that a minor influence of h_0 on the DLTS signal of h_3 exists, and that the emission properties of the traps can vary due to the local electric field [116], we suggest that the DLTS signatures of e_1 and h_3 are actually signatures of the same defect, but located at the two sides of the junction. To be more specific, under this assumption, trap e_1 signal originates from the probing this unknown defect at the n-side, whereas it responds with the h_3 signature at the p-side of the junction.

Finally, in-situ monitoring of the electrical characteristics of the devices inside

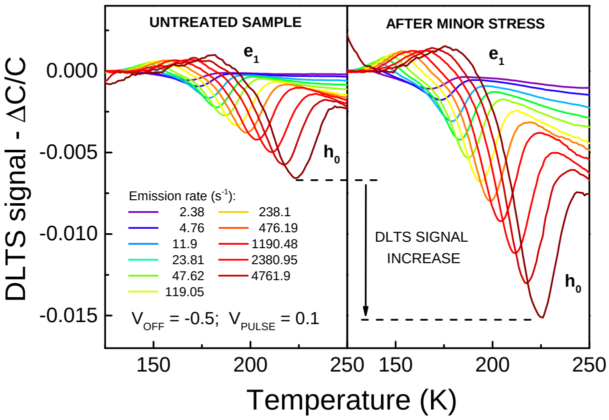

Figure 10.13: Full DLTS spectra of an LD sample measured before and after short-term aging and repeated optical (L-I) and electrical (I-V) characterization on the device.

the temperature-controlled sample holder employed for DLTS characterization let us identify another short-term aging-induced degradation process. In particular, after a preliminary characterization of the device performed at an ambient temperature of 45 °C with a maximum drive current of 250 mA, a noticeable variation in the magnitude of the DLTS peaks was observed. Since the magnitude of those peaks is proportional to the concentration of deep-levels, the experimental data show that stress induced the generation/propagation of defects inside the SCR of the LD. This phenomenon is visible in Fig. 10.13, which reports the DLTS spectra obtained for $\mathrm{V_{OFF}}$ = -0.5 V and $\mathrm{V_{FILL}}$= 0.1 V. The relevant increase of $\mathrm{h_0}$ signal suggests that, as a consequence of the short-term stress, an average increase of the defect concentration related to this deep-level is to be expected within the device.

10.4 Conclusions

In conclusion, with this work a preliminary analysis on the degradation mechanisms that may influence the lifetime of heterogeneous III-V/Silicon lasers was presented. To this aim, a series of accelerated aging experiments have been carried out on experimental 1.55 µm heterogeneous laser diodes. Long-term constant-current stress tests revealed the presence of several degradation processes, affecting both the optical and the electrical performance of the devices. In particular, the laser diodes showed an increase in the threshold current, compatible with the decrease of carrier lifetime, well correlated with the decrease in the operating voltage and the increase in the junction charge. These results support the hypothesis that degradation occurs through the diffusion of non-radiative defects towards the active region of the devices. The physical origin of those deep levels is most likely to be attributed to interface defects located at the AlInGaAs/InP interfaces or, less probably, to point defects generated as a consequence of the diffusion of the p-dopant Zn.

Chapter 11

Conclusions

The aim of this thesis was to identify and analyze the physical factors that limit the performance and reliability of innovative optoelectronic technologies based on nitrides and arsenides. More specifically, with this work we have extensively investigated the reliability of III-V lasers and LEDs for telecommunication and lighting applications, as well as the degradation mechanisms and operating limits of blue-emitting phosphorescent materials for near-UV excitation through solid-state III-N devices. By means of short-term stress tests it was possible to identify the dominant failure modes and mechanisms of GaN LEDs subjected to electrical over-stress, both in forward and reverse bias, and to correlate specific failures with the structure-related weaknesses of state-of-the-art LEDs. A series of accelerated life tests on mid-power GaN LEDs and on commercial retrofit bulbs employing this class of devices as emitters highlighted the presence of several gradual degradation mechanisms, either device or system-related, that were found to severely impact on the lifetime of the light sources when operated at the boundaries of their safe-operating area. Accelerated life test experiments have also been employed in order to pinpoint the root cause of optical degradation of III-V/Silicon heterogeneous laser diodes for integrated telecommunication applications and interconnects. Finally, the reliability investigation on blue-emitting phosphors successfully led to the identification of the dominant degradation mechanism under excessive optical excitation and operating temperature, whose non-reversible effect on the photo-luminescence efficiency can be avoided by pumping the material within an experimentally determinable excitation range.

The main outcomes of the research activity are briefly summarized in the following paragraphs.

Degradation of GaN LEDs

Visible Gallium Nitride LEDs temporary or continuously submitted to electrical overstress showed peculiar failure modes and mechanisms, related to the specific polarization regime and device structure.

- Under constant reverse bias, GaN LEDs exhibit a time-dependent degradation phenomenon, which promotes the increase of the leakage current of the device, eventually leading to the catastrophic failure. The Weibull-like distribution of the time-to-failure, and its exponential dependence on the stress voltage, closely resembles the statistics of a TDDB process, which suggests that highly-depleted GaN under reverse bias may behave like a partially-leaking dielectric that degrades over time due to a defect percolation process.
- Single high forward-current EOS events can induce the catastrophic failure of the device, with threshold overstress conditions that depend of the specific device structure and on the duration of the overstress event. In particular, flip-chip LEDs without metal lines showed the highest robustness among all devices, resulting the best choice whenever a high level of immunity towards electrically critical environment is required. Other families of LEDs, which shared common metal elements like bonding wires or current-spreading contact grids, faced failure at lower pulse current/power levels, due to the fusion of the bonding wires, the melting of the bonding pads or to the degradation of the surface metallization lines. This behavior suggests that EOS-related reliability issues tend to arise more from extrinsic elements of the LED system rather than from the GaN chip.
- The continuous exposure of high-power LEDs to bias currents greater that the absolute maximum rating induced different kinds of structure/layout-related failures, and the activation of a common set of epitaxy-related degradation processes. In particular, short-term high temperature and current stress induced the worsening of the conductivity of large portions of the semiconductor, by increasing the current crowding effect, and consequently power dissipation, in correspondence of the major current transport elements (vias, bonding pads and metal lines). As a consequence of the excessive levels of temperature reached during stress, those structures melted, causing the shorting and the catastrophic failure of the LED.

Due to the employed plastic package and non state-of-the-art semiconductor chips, mid-power white LEDs for lighting applications can be affected by several degradation mechanisms which may limit their long-term reliability. The experimental data gathered during a series of accelerated aging experiments allowed to identify degradation processes related both to the semiconductor chip (generation of defects within the active region of the devices, degradation of the electrical characteristics) and to the package/phosphors system (worsening of the chromatic properties of the emitted light). Despite those reliability issues, the LEDs under test showed a good robustness for junction temperatures belonging to the advised Safe Operating Area (SOA). Within these operating bounds, the analyzed devices are expected to have a useful lifetime adequate enough to fulfill nowadays market requirements.

The long-term reliability of mid-power LEDs was further investigated at system level by performing a lifetime analysis on commercial LED bulbs employing these devices as primary light sources. By means of long-term stress tests carried out on different groups of retrofit LED light bulbs, the importance of temperature as an accelerating factor for the degradation processes was confirmed. The main mechanisms that can lead to the decrease of the performance of the bulb were found to be (*i*) the darkening of the diffusive bulb, (*ii*) the variation of the chromatic properties of the phosphors and/or of the reflector, and (*iii*) the worsening of the performance of the LED driver, which can lead to early failures of the entire system. All these effects, mainly related to components of the bulb rather than to the LEDs, concur in limiting the overall reliability of the system, whose expected lifetime is in the range of tens of thousands hours in nominal operating conditions.

Reliability of blue-emitting phosphors for near-UV excitation

The investigation on the robustness and the degradation mechanisms of blue-emitting phosphors for near-UV laser pumping, performed by means of a series of stress experiments under optical excitation and/or high temperature environment, helped us identify the limits for continuous operation of the luminescent material. For pure thermal treatment temperatures greater than 450 °C the material exhibited a time-dependent drop in the PL, which was attributed to the thermally-induced autoionization of the Eu^{2+} optically active centers. By means of different material characterization techniques, evidences of this degradation process were also found on samples stressed under high levels of optical excitation, down to a moderate $3\,W/mm^2$ intensity. This indicated that the optically (and thermally) induced ionization of the Eu^{2+} species is the most critical degradation process for this family of phosphorescent material.

With regard to the actual operating limits of the luminescent material, the experimental data gathered on a second-generation improved phosphor showed that, for a given deposition condition, a threshold excitation intensity for continuous pumping exists. Above this threshold, decay of the steady-state photo-luminescence performance and irreversible degradation of the material were found to take place, which suggested that the material was being operated in an unuseful excitation regime, mainly limited by the thermal management capabilities of the carrier substrate rather than from intrinsic properties of the phosphor.

Gradual degradation mechanisms of III-V/Silicon heterogeneous lasers

A series of accelerated aging experiments on heterogeneous III-V/Silicon experimental lasers showed the presence of different gradual degradation processes, affecting both the optical and the electrical parameters of the devices. In particular, the worsening of the optical performances, compatible with the decrease in the non-radiative carrier lifetime, was found to be well correlated with the decrease in the operating voltage and the increase in the junction charge. These results support the hypothesis that the observed optical degradation occurs through the diffusion of non-radiative defects towards the active region of the devices.

With the aim of identifying the physical origin of the diffusing species, an extensive capacitance DLTS characterization was carried out. The results indicate the presence of several deep levels, with a main trap located around $0.43\,eV$ above the valence band energy. This trap was found to be compatible with an interface defect characteristic of the quaternary material employed to grow the active region of the device. Due to the lack of literature reports on defects related to AlInGaAs alloys, whose rate of adoption for the manufacturing of III-V emitters at $1.3\,\mu m$ and $1.55\,\mu m$ is currently growing, a clear identification of the deep-levels found within the device has yet to be achieved.

Bibliography

[1] S. Mokkapati and C. Jagadish, “III-V compound SC for optoelectronic devices,” *Materials Today*, vol. 12, pp. 22–32, apr 2009.

[2] D. A. Steigerwald, J. C. Bhat, D. Collins, R. M. Fletcher, M. O. Holcomb, M. J. Ludowise, P. S. Martin, and S. L. Rudaz, “Illumination with solid state lighting technology,” *IEEE Journal on Selected Topics in Quantum Electronics*, vol. 8, no. 2, pp. 310–320, 2002.

[3] M. Meneghini, A. Tazzoli, G. Mura, G. Meneghesso, and E. Zanoni, “A review on the physical mechanisms that limit the reliability of GaN-based LEDs,” *IEEE Transactions on Electron Devices*, vol. 57, no. 1, pp. 108–118, 2010.

[4] CREE Inc., “XLamp XQ-E HB-LEDs,” 2017.

[5] M. Buffolo, M. Meneghini, A. Munaretto, C. De Santi, G. Meneghesso, and E. Zanoni, “Failure of high power LEDs submitted to EOS: Dependence on device layout and pulse properties,” *IEEE Transactions on Device and Materials Reliability*, vol. 17, pp. 191–196, mar 2017.

[6] M. Buffolo, C. De Santi, M. Meneghini, D. Rigon, G. Meneghesso, and E. Zanoni, “Long-term degradation mechanisms of mid-power LEDs for lighting applications,” *Microelectronics Reliability*, vol. 55, pp. 1754–1758, aug 2015.

[7] K. A. Denault, M. Cantore, S. Nakamura, S. P. Denbaars, and R. Seshadri, “Efficient and stable laser-driven white lighting,” *AIP Advances*, vol. 3, p. 072107, jul 2013.

[8] J. Piprek, “Comparative efficiency analysis of GaN-based light-emitting diodes and laser diodes,” *Applied Physics Letters*, vol. 109, p. 021104, jul 2016.

[9] I. H. Cho, G. Anoop, D. W. Suh, S. J. Lee, and J. S. Yoo, “On the stability and reliability of $Sr_{1-x}Ba_xSi_2O_2N_2:Eu^{2+}$ phosphors for white LED applications,” *Optical Materials Express*, vol. 2, p. 1292, sep 2012.

[10] J. Zhang, M. Zhou, B. Liu, Y. Wen, and Y. Wang, "The ultraviolet irradiation degradation of fluorescent lamp used $BaMgAl_{10}O_{17}$:Eu^{2+},Mn^{2+} phosphor," *Journal of Luminescence*, vol. 132, pp. 1949–1952, aug 2012.

[11] J. M. Senior, *Optical Fiber Communications Principles and Practice.* Financial Times/Prentice Hall, 2009.

[12] J. Bowers, D. Liang, A. Fang, H. Park, R. Jones, and M. Paniccia, "Hybrid Silicon Lasers: The Final Frontier to Integrated Computing," *Optics and Photonics News*, vol. 21, p. 28, may 2010.

[13] S. Srinivasan, N. Julian, J. Peters, and J. E. Bowers, "Reliability of Hybrid Silicon Distributed Feedback Lasers," *IEEE Journal of Selected Topics in Quantum Electronics*, vol. 19, p. 1501305, jul 2013.

[14] S. Vaccari, M. Meneghini, A. Griffoni, D. Barbisan, M. Barbato, S. Carraro, M. La Grassa, G. Meneghesso, and E. Zanoni, "ESD characterization of multichip RGB LEDs," *Microelectronics Reliability*, vol. 53, no. 9-11, pp. 1510–1513, 2013.

[15] M. Dal Lago, M. Meneghini, C. De Santi, M. Barbato, N. Trivellin, G. Meneghesso, and E. Zanoni, "ESD on GaN-based LEDs: An analysis based on dynamic electroluminescence measurements and current waveforms," *Microelectronics Reliability*, vol. 54, pp. 2138–2141, sep 2014.

[16] Z. Zheng, Z. Chen, Y. Xian, B. Fan, S. Huang, W. Jia, Z. Wu, G. Wang, and H. Jiang, "Enhanced electrostatic discharge properties of nitride-based light-emitting diodes with inserting Si-delta-doped layers," *Applied Physics Letters*, vol. 99, p. 111109, sep 2011.

[17] W. Shockley and W. T. Read, "Statistics of the recombinations of holes and electrons," *Physical Review*, vol. 87, pp. 835–842, sep 1952.

[18] R. N. Hall, "Electron-hole recombination in germanium," *Physical Review*, vol. 87, p. 387, jul 1952.

[19] X. Li, P. W. Bohn, and J. J. Coleman, "Impurity states are the origin of yellow-band emission in GaN structures produced by epitaxial lateral overgrowth," *Applied Physics Letters*, vol. 75, pp. 4049–4051, dec 1999.

[20] J. M. Shah, Y. L. Li, T. Gessmann, and E. F. Schubert, "Experimental analysis and theoretical model for anomalously high ideality factors (n >> 2.0) in AlGaN/GaN p-n junction diodes," *Journal of Applied Physics*, vol. 94, pp. 2627–2630, aug 2003.

[21] T. Seong, *III-Nitride Based Light Emitting Diodes and Applications*, vol. 126 of *Topics in Applied Physics.* Dordrecht: Springer Netherlands, 2013.

[22] Z. Q. Fang, D. C. Reynolds, and D. C. Look, "Changes in electrical characteristics associated with degradation of InGaN blue light-emitting diodes," *Journal of Electronic Materials*, vol. 29, pp. 448–451, apr 2000.

[23] M. K. Kazuyuki Tadatomo, Hiroaki Okagawa, Youichiro Ohuchi, Takashi Tsunekawa, Yoshiyuki Imada and T. Taguchi, "High Output Power InGaN Ultraviolet Light-Emitting Diodes Fabricated on Patterned Substrates Using Metalorganic Vapor Phase Epitaxy," *Japanese Journal of Applied Physics*, vol. 40, pp. 583–585, jun 2001.

[24] S. Nakamura, M. Senoh, and T. Mukai, "P-gan/n-ingan/n-gan double-heterostructure blue-light-emitting diodes," *Japanese Journal of Applied Physics*, vol. 32, pp. L8–L11, jan 1993.

[25] V. Haerle, B. Hahn, S. Kaiser, A. Weimar, S. Bader, F. Eberhard, A. Plössl, and D. Eisert, "High brightness LEDs for general lighting applications using the new ThinGaN™-Technology," in *Physica Status Solidi (A) Applied Research*, vol. 201, pp. 2736–2739, WILEY-VCH Verlag, sep 2004.

[26] R. Degraeve, B. Kaczer, and G. Groeseneken, "Reliability: a possible showstopper for oxide thickness scaling?," *Semiconductor Science and Technology*, vol. 15, pp. 436–444, may 2000.

[27] T.-L. Wu, D. Marcon, B. De Jaeger, M. Van Hove, B. Bakeroot, S. Stoffels, G. Groeseneken, S. Decoutere, and R. Roelofs, "Time dependent dielectric breakdown (TDDB) evaluation of PE-ALD SiN gate dielectrics on AlGaN/GaN recessed gate D-mode MIS-HEMTs and E-mode MIS-FETs," in *2015 IEEE International Reliability Physics Symposium*, pp. 6C.4.1–6C.4.6, IEEE, apr 2015.

[28] I. Rossetto, M. Meneghini, O. Hilt, E. Bahat-Treidel, C. De Santi, S. Dalcanale, J. Wuerfl, E. Zanoni, and G. Meneghesso, "Time-Dependent Failure of GaN-on-Si Power HEMTs With p-GaN Gate," *IEEE Transactions on Electron Devices*, vol. 63, pp. 2334–2339, jun 2016.

[29] D. Marcon, T. Kauerauf, F. Medjdoub, J. Das, M. Van Hove, P. Srivastava, K. Cheng, M. Leys, R. Mertens, S. Decoutere, G. Meneghesso, E. Zanoni, and G. Borghs, "A comprehensive reliability investigation of the voltage-, temperature- and device geometry-dependence of the gate degradation on state-of-the-art GaN-on-Si HEMTs," in *2010 International Electron Devices Meeting*, pp. 20.3.1–20.3.4, IEEE, dec 2010.

[30] G. Onushkin, "Efficient Alternating Current Operated White Light-Emitting Diode Chip," *IEEE Photonics Technology Letters*, vol. 21, pp. 33–35, jan 2009.

[31] L. Li, J. Guan, D. Yan, G. Yang, S. Xiao, and X. Gu, "Current and light emission efficiency behaviors in GaN-based LEDS," in *2014 12th IEEE International Conference on Solid-State and Integrated Circuit Technology (ICSICT)*, pp. 1–3, IEEE, oct 2014.

[32] P. Kozodoy, J. P. Ibbetson, H. Marchand, P. T. Fini, S. Keller, J. S. Speck, S. P. DenBaars, and U. K. Mishra, "Electrical characterization of GaN p-n junctions with and without threading dislocations," *Applied Physics Letters*, vol. 73, p. 975, aug 1998.

[33] J. Kim, J. Kim, Y. Tak, S. Chae, J. Y. Kim, and Y. Park, "Effect of v-shaped pit size on the reverse leakage current of InGaN/GaN light-emitting diodes," *IEEE Electron Device Letters*, vol. 34, no. 11, pp. 1409–1411, 2013.

[34] Q. Shan, D. S. Meyaard, Q. Dai, J. Cho, E. Fred Schubert, J. Kon Son, and C. Sone, "Transport-mechanism analysis of the reverse leakage current in GaInN light-emitting diodes," *Applied Physics Letters*, vol. 99, no. 25, pp. 2009–2012, 2011.

[35] J. Cho, A. Mao, J. Kim, J. Son, Y. Park, and E. Schubert, "Analysis of reverse tunnelling current in GaInN light-emitting diodes," *Electronics Letters*, vol. 46, p. 156, jan 2010.

[36] T. Hino, S. Tomiya, T. Miyajima, K. Yanashima, S. Hashimoto, and M. Ikeda, "Characterization of threading dislocations in GaN epitaxial layers," *Applied Physics Letters*, vol. 76, p. 3421, jun 2000.

[37] A. Armstrong, T. A. Henry, D. D. Koleske, M. H. Crawford, K. R. Westlake, and S. R. Lee, "Dependence of radiative efficiency and deep level defect incorporation on threading dislocation density for InGaN/GaN light emitting diodes," *Applied Physics Letters*, vol. 101, p. 162102, oct 2012.

[38] X. A. Cao, P. M. Sandvik, S. F. LeBoeuf, and S. D. Arthur, "Defect generation in InGaN/GaN light-emitting diodes under forward and reverse electrical stresses," *Microelectronics Reliability*, vol. 43, no. 12, pp. 1987–1991, 2003.

[39] J. Cho, E. F. Schubert, J. K. Son, D. Y. Kim, and J. K. Kim, "Strong correlation between capacitance and breakdown voltage of GaInN/GaN light-emitting diodes," *Electronic Materials Letters*, vol. 10, no. 6, pp. 1155–1157, 2014.

[40] M. Ohring and L. Kasprzak, *Reliability and Failure of Electronic Materials and Devices*. 2015.

[41] Alexander Wilm, "LED tunnel lamp – A reality check: 50.000 hours field data and lifetime," in *LED Professional 2015 symposium*, 2015.

[42] J. Hu, L. Yang, and M. W. Shin, "Electrical, optical and thermal degradation of high power GaN/InGaN light-emitting diodes," *Journal of Physics D: Applied Physics*, vol. 41, no. 3, p. 035107, 2008.

[43] S.-C. Yang, P. Lin, C.-P. Wang, S. B. Huang, C.-L. Chen, P.-F. Chiang, A.-T. Lee, and M.-T. Chu, "Failure and degradation mechanisms of high-power white light emitting diodes," *Microelectronics Reliability*, vol. 50, no. 7, pp. 959–964, 2010.

[44] M. Meneghini, L.-R. Trevisanello, U. Zehnder, T. Zahner, U. Strauss, G. Meneghesso, and E. Zanoni, "High-Temperature Degradation of GaN LEDs Related to Passivation," *IEEE Transactions on Electron Devices*, vol. 53, pp. 2981–2987, dec 2006.

[45] C. D. Santi, M. Meneghini, M. L. Grassa, B. Galler, M. Goano, S. Dominici, M. Mandurrino, F. Bertazzi, G. Meneghesso, and E. Zanoni, "Role of defects in the thermal droop of InGaN-based Light Emitting Diodes," vol. 094501, 2016.

[46] M. Meneghini, C. de Santi, N. Trivellin, K. Orita, S. Takigawa, T. Tanaka, D. Ueda, G. Meneghesso, and E. Zanoni, "Investigation of the deep level involved in InGaN laser degradation by deep level transient spectroscopy," *Applied Physics Letters*, vol. 99, p. 093506, sep 2011.

[47] P. Appaiah, N. Narendran, I. U. Perera, Y. Zhu, and Y. wei Liu, "Effect of thermal stress and short-wavelength visible radiation on phosphor-embedded LED encapsulant degradation," *Optical Materials*, 2014.

[48] M. Dal Lago, M. Meneghini, N. Trivellin, G. Mura, M. Vanzi, G. Meneghesso, and E. Zanoni, "Phosphors for LED-based light sources: Thermal properties and reliability issues," *Microelectronics Reliability*, vol. 52, pp. 2164–2167, sep 2012.

[49] J. K. Kim, H. Luo, E. F. Schubert, J. Cho, C. Sone, and Y. Park, "Strongly Enhanced Phosphor Efficiency in GaInN White Light-Emitting Diodes Using Remote Phosphor Configuration and Diffuse Reflector Cup," *Japanese Journal of Applied Physics*, vol. 44, pp. L649–L651, may 2005.

[50] S. Buso, G. Spiazzi, M. Meneghini, and G. Meneghesso, "Performance degradation of high-brightness light emitting diodes under DC and pulsed bias," *IEEE Transactions on Device and Materials Reliability*, vol. 8, no. 2, pp. 312–322, 2008.

[51] S.-m. Moon and J. S. Kwak, "High-current Electro-optical Degradation of InGaN / GaN Light-emitting Diodes Fabricated with Ag-based Reflectors," vol. 55, no. 3, pp. 1128–1131, 2009.

[52] M. Meneghini, L.-R. Trevisanello, G. Meneghesso, and E. Zanoni, "A Review on the Reliability of GaN-Based LEDs," *IEEE Transactions on Device and Materials Reliability*, vol. 8, pp. 323–331, jun 2008.

[53] K. Kaschani, "What is Electrical Overstress? - Analysis and Conclusions," *Microelectronics Reliability*, vol. 55, pp. 853–862, may 2015.

[54] M. Meneghini, E. Zanoni, N. Trivellin, C. De Santi, M. Buffolo, M. Dal Lago, A. Munaretto, D. Barbisan, M. Ferretti, and G. Meneghesso, "Reliability of high power LEDs: from gradual to catastrophic failure," in *LED Professional 2015 symposium*, 2015.

[55] R. Tuttle, "Electrical Overstress Simulation and Failure Mechanisms of Light Emitting Diodes," in *LED Professional 2014 symposium*, 2014.

[56] OSRAM Opto Semiconductors, "The Basic Principles of Electrical Overstress (EOS)," tech. rep.

[57] CREE, "XLamp® LED Electrical Overstress," tech. rep.

[58] A. Griffoni, "EOS/ESD Challenges in LED Lighting," in *IEW 2016*, 2016.

[59] O. B. Shchekin, J. E. Epler, T. A. Trottier, T. Margalith, D. A. Steigerwald, M. O. Holcomb, P. S. Martin, and M. R. Krames, "High performance thin-film flip-chip InGaN-GaN light-emitting diodes," *Applied Physics Letters*, vol. 89, no. 7, 2006.

[60] Y. Xi and E. F. Schubert, "Junction-temperature measurement in GaN ultraviolet light-emitting diodes using diode forward voltage method," *Applied Physics Letters*, vol. 85, no. 12, pp. 2163–2165, 2004.

[61] Z. G. Ju, S. T. Tan, Z.-H. Zhang, Y. Ji, Z. Kyaw, Y. Dikme, X. W. Sun, and H. V. Demir, "On the origin of the redshift in the emission wavelength of InGaN/GaN blue light emitting diodes grown with a higher temperature interlayer," *Applied Physics Letters*, vol. 100, p. 123503, mar 2012.

[62] J. Hu, L. Yang, L. Kim, and M. W. Shin, "The ageing mechanism of high-power InGaN/GaN light-emitting diodes under electrical stresses," *Semiconductor Science and Technology*, vol. 22, pp. 1249–1252, dec 2007.

[63] M. Dal Lago, M. Meneghini, N. Trivellin, G. Mura, M. Vanzi, G. Meneghesso, and E. Zanoni, ""Hot-plugging" of LED modules: Electrical characterization and device degradation," *Microelectronics Reliability*, vol. 53, no. 9-11, pp. 1524–1528, 2013.

[64] M. Meneghini, M. Dal Lago, N. Trivellin, G. Meneghesso, and E. Zanoni, "Degradation mechanisms of high-power LEDs for lighting applications: An overview," *IEEE Transactions on Industry Applications*, vol. 50, no. 1, pp. 78–85, 2014.

[65] X. Cao, E. Stokes, P. Sandvik, S. LeBoeuf, J. Kretchmer, and D. Walker, "Diffusion and tunneling currents in GaN/InGaN multiple quantum well light-emitting diodes," *IEEE Electron Device Letters*, vol. 23, pp. 535–537, sep 2002.

[66] F. Rossi, M. Pavesi, M. Meneghini, G. Salviati, M. Manfredi, G. Meneghesso, A. Castaldini, A. Cavallini, L. Rigutti, U. Strass, U. Zehnder, and E. Zanoni, "Influence of short-term low current dc aging on the electrical and optical properties of InGaN blue light-emitting diodes," *Journal of Applied Physics*, vol. 99, no. 5, 2006.

[67] B. Hamon, B. Bataillou, L. Mendizabal, A. Gasse, and G. Feuillet, "N-contacts degradation analysis of white flip chip LEDs during reliability tests," in *2014 IEEE International Reliability Physics Symposium*, pp. FA.1.1–FA.1.6, IEEE, jun 2014.

[68] E. Jung, M. S. Kim, and H. Kim, "Analysis of Contributing Factors for Determining the Reliability Characteristics of GaN-Based White Light-Emitting Diodes With Dual Degradation Kinetics," *IEEE Transactions on Electron Devices*, vol. 60, pp. 186–191, jan 2013.

[69] M. Meneghini, M. Dal Lago, N. Trivellin, G. Meneghesso, and E. Zanoni, "Thermally Activated Degradation of Remote Phosphors for Application in LED Lighting," *IEEE Transactions on Device and Materials Reliability*, vol. 13, pp. 316–318, mar 2013.

[70] G. Mura, G. Cassanelli, F. Fantini, and M. Vanzi, "Sulfur-contamination of high power white LED," *Microelectronics Reliability*, vol. 48, pp. 1208–1211, aug 2008.

[71] C.-C. Tsai, W.-C. Cheng, J.-K. Chang, S.-Y. Huang, J.-S. Liou, G.-H. Chen, Y.-C. Huang, J.-S. Wang, and W.-H. Cheng, "Thermal-Stability Comparison of Glass- and Silicone-Based High-Power Phosphor-Converted White-Light-Emitting Diodes Under Thermal Aging," *IEEE Transactions on Device and Materials Reliability*, vol. 14, pp. 4–8, mar 2014.

[72] Lightingprize.org (website), "L-Prize - Bright Tomorrow Lighting Prizes – Competition Overview."

[73] F. P. Vahl, L. M. Campos, and N. Casarotto Filho, "Sustainability constraints in techno-economic analysis of general lighting retrofits," *Energy and Buildings*, vol. 67, pp. 500–507, dec 2013.

[74] M. Cai, D. G. Yang, S. Koh, C. A. Yuan, W. B. Chen, B. Y. Wu, and G. Q. Zhang, "Accelerated testing method of LED luminaries," in *2012 13th International Thermal, Mechanical and Multi-Physics Simulation and Experiments in Microelectronics and Microsystems, EuroSimE 2012*, pp. 1/6–6/6, IEEE, apr 2012.

[75] S. Ishizaki, H. Kimura, and M. Sugimoto, "Lifetime Estimation of High Power White LEDs," *Journal of Light & Visual Environment*, vol. 31, no. 1, pp. 11–18, 2007.

[76] N. Narendran, Y. Gu, J.-P. Freyssinier, H. Yu, and L. Deng, "Solid-state lighting: Failure analysis of white LEDs," *Journal of Crystal Growth*, 2004.

[77] E. Jung, M. S. Kim, and H. Kim, "Analysis of contributing factors for determining the reliability characteristics of GaN-Based white light-emitting diodes with dual degradation kinetics," *IEEE Transactions on Electron Devices*, vol. 60, pp. 186–191, jan 2013.

[78] LUMILEDS; OSRAM; CREE; LedEngin; Seoul Semiconductor, "Figures from commercially-available LED datasheets: Cree XREROY, LedEngin LZ4-00B210, Lumileds LXML-PR01, Osram LD W5SM, Seoul Semiconductor D42180."

[79] Yuege Zhou, Xiang Li, Xuerong Ye, and Guofu Zhai, "A remaining useful life prediction method based on condition monitoring for LED driver," in *Proceedings of the IEEE 2012 Prognostics and System Health Management Conference (PHM-2012 Beijing)*, pp. 1–5, IEEE, may 2012.

[80] Y. C. Shen, G. O. Mueller, S. Watanabe, N. F. Gardner, A. Munkholm, and M. R. Krames, "Auger recombination in InGaN measured by photoluminescence," *Applied Physics Letters*, vol. 91, p. 141101, oct 2007.

[81] L. Wang, C. Lu, J. Lu, L. Liu, N. Liu, Y. Chen, Y. Zhang, E. Gu, and X. Hu, "Influence of carrier screening and band filling effects on efficiency droop of InGaN light emitting diodes," *Optics Express*, vol. 19, p. 14182, jul 2011.

[82] J. McKittrick, M. E. Hannah, A. Piquette, J. K. Han, J. I. Choi, M. Anc, M. Galvez, H. Lugauer, J. B. Talbot, and K. C. Mishra, "Phosphor Selection Considerations for Near-UV LED Solid State Lighting," *ECS Journal of Solid State Science and Technology*, vol. 2, pp. R3119–R3131, dec 2012.

[83] M. Kawaguchi, O. Imafuji, S. Nozaki, H. Hagino, S. Takigawa, T. Katayama, and T. Tanaka, "Optical-loss suppressed InGaN laser diodes using undoped thick waveguide structure," p. 974818, feb 2016.

[84] B. Henderson and G. F. Imbusch, *Optical Spectroscopy of Inorganic Solids*, vol. 3. Clarendon Press, 2006.

[85] D. Kim, S.-C. Kim, J.-S. Bae, S. Kim, S.-J. Kim, and J.-C. Park, "Eu^{2+}-Activated Alkaline-Earth Halophosphates, $M_5(PO_4)_3X:Eu^{2+}$ (M=Ca,Sr,Ba; X=F,Cl,Br) for NUV-LEDs: Site-Selective Crystal Field Effect," *Inorganic Chemistry*, vol. 55, pp. 8359–8370, sep 2016.

[86] Y. Kim and S. Kang, "Investigation of the degradation mechanisms in $BaMgAl_{10}O_{17}:Eu^{2+}$ phosphor: on the influence of thermal process on operational durability," *Applied Physics B*, vol. 98, pp. 429–434, feb 2010.

[87] Y. Li, Y. Wang, Y. Gong, X. Xu, and F. Zhang, "Photoionization behavior of Eu2+-doped BaMgSiO4 long-persisting phosphor upon UV irradiation," *Acta Materialia*, vol. 59, pp. 3174–3183, may 2011.

[88] B. Moine and G. Bizarri, “Degradation mechanism of phosphors by vacuum ultraviolet excitation,” *Optical Materials*, vol. 28, pp. 587–591, may 2006.

[89] Z. H. Zhang, Y. H. Wang, X. X. Li, Y. K. Du, and W. J. Liu, “Photoluminescence degradation and color shift studies of annealed $BaMgAl_{10}O_{17}$:Eu^{2+} phosphor,” *Journal of Luminescence*, vol. 122-123, pp. 1003–1005, jan 2007.

[90] D. Klaassen, D. de Leeuw, and T. Welker, “Degradation of phosphors under cathode-ray excitation,” *Journal of Luminescence*, vol. 37, pp. 21–28, apr 1987.

[91] K. Binnemans, “Interpretation of europium(III) spectra,” *Coordination Chemistry Reviews*, vol. 295, pp. 1–45, jul 2015.

[92] M. Ma, D. Zhu, C. Zhao, T. Han, S. Cao, Y. Lei, and M. Tu, “Thermal degradation of BaAl2Si2O8:Eu2+ phosphor excited by near ultraviolet light,” *Chinese Science Bulletin*, vol. 57, pp. 1728–1732, may 2012.

[93] Q. Liu, Y. Yuan, J. Li, J. Liu, C. Hu, M. Chen, L. Lin, H. Kou, Y. Shi, W. Liu, H. Chen, Y. Pan, and J. Guo, “Preparation and properties of transparent Eu:YAG fluorescent ceramics with different doping concentrations,” *Ceramics International*, vol. 40, pp. 8539–8545, jul 2014.

[94] A. Lacanilao, G. Wallez, L. Mazerolles, P. Dubot, L. Binet, B. Pavageau, L. Servant, V. Buissette, and T. Le Mercier, “Structural analysis of thermal degradation and regeneration in blue phosphor $BaMgAl_{10}O_{17}$:Eu^{2+} based upon cation diffusion,” *Solid State Ionics*, vol. 253, pp. 32–38, dec 2013.

[95] R. Soref, “The Past, Present, and Future of Silicon Photonics,” *IEEE Journal of Selected Topics in Quantum Electronics*, vol. 12, pp. 1678–1687, nov 2006.

[96] T. Kita, M. Abe, Y. Ohtera, and H. Yamada, “Practical integration method of active devices on SOI photonic integrated circuits,” in *IEEE International Conference on Group IV Photonics GFP*, pp. 275–277, IEEE, sep 2010.

[97] M. Nadenkov and B. Jalali, “Advances in Silicon-on-Insulator Photonic Integrated Circuit (SOIPIC) Technology,” *IEEE International SOI Conference*, pp. 1–11, 1999.

[98] J. D. E. B. D. Liang, “Recent progress in lasers on silicon,” *Nature Photonics*, vol. 4, pp. 511–517, aug 2010.

[99] J. Liu, X. Sun, R. Camacho-Aguilera, L. C. Kimerling, and J. Michel, "Ge-on-Si laser operating at room temperature," *Optics Letters*, vol. 35, p. 679, mar 2010.

[100] J. M. Ramírez, F. Ferrarese Lupi, O. Jambois, Y. Berencén, D. Navarro-Urrios, A. Anopchenko, A. Marconi, N. Prtljaga, A. Tengattini, L. Pavesi, J. P. Colonna, J. M. Fedeli, and B. Garrido, "Erbium emission in MOS light emitting devices: from energy transfer to direct impact excitation," *Nanotechnology*, vol. 23, p. 125203, mar 2012.

[101] M. J. R. Heck, H.-W. Chen, A. W. Fang, B. R. Koch, D. Liang, H. Park, M. N. Sysak, and J. E. Bowers, "Hybrid Silicon Photonics for Optical Interconnects," *IEEE Journal of Selected Topics in Quantum Electronics*, vol. 17, pp. 333–346, mar 2011.

[102] S. Srinivasan, Y. Tang, G. Read, N. Hossain, D. Liang, S. J. Sweeney, and J. E. Bowers, "Hybrid silicon devices for energy-efficient optical transmitters," *IEEE Micro*, vol. 33, pp. 22–31, jan 2013.

[103] A. W. Fang, H. Park, R. Jones, O. Cohen, M. J. Paniccia, and J. E. Bowers, "A continuous-wave hybrid AlGaInAs - Silicon evanescent laser," *IEEE Photonics Technology Letters*, vol. 18, pp. 1143–1145, may 2006.

[104] D. Pasquariello and K. Hjort, "Plasma-assisted InP-to-Si low temperature wafer bonding," *IEEE Journal on Selected Topics in Quantum Electronics*, vol. 8, no. 1, pp. 118–131, 2002.

[105] K. Schjølberg-Henriksen, S. Moe, M. M. V. Taklo, P. Storås, and J. H. Ulvensøen, "Low-temperature plasma activated bonding for a variable optical attenuator," *Sensors and Actuators A: Physical*, vol. 142, no. 1, pp. 413–420, 2008.

[106] D. Liang, A. W. Fang, H. Park, T. E. Reynolds, K. Warner, D. C. Oakley, and J. E. Bowers, "Low-Temperature, Strong SiO2-SiO2 Covalent Wafer Bonding for III–V Compound Semiconductors-to-Silicon Photonic Integrated Circuits," *Journal of Electronic Materials*, vol. 37, pp. 1552–1559, oct 2008.

[107] U. Gösele, G. Cha, and R. Gafiteanu, "Low Temperature Wafer Direct Bonding," *Journal of Microelectromechanical Systems*, vol. 3, pp. 29–35, mar 1994.

[108] M. Sugo, H. Mori, Y. Sakai, and Y. Itoh, "Stable cw operation at room temperature of a 1.5-μm wavelength multiple quantum well laser on a Si substrate," *Applied Physics Letters*, vol. 60, pp. 472–473, jan 1992.

[109] L. A. Coldren, “Diode Lasers and Photonic Integrated Circuits,” *Optical Engineering*, vol. 36, no. 2, p. 616, 1997.

[110] R. S. Muller, T. I. Kamins, and M. Chan, *Device Electronics for Integrated devices.* John Wiley & Sons, 2002.

[111] F. Ducroquet, G. Jacovetti, K. Rezzoug, S. Ababou, G. Guillot, J. P. Praseuth, F. Olivier-Martin, and L. Giraudet, “Deep trap characterisation and conduction band offset determination of AI 0.48 In 0.52 As/(Ga 0.7 AI 0.3) 0.48 In 0.52 As heterostructures,” *Materials Science and Technology*, vol. 13, pp. 971–973, nov 1997.

[112] C. H. Henry and D. V. Lang, “Nonradiative capture and recombination by multiphonon emission in GaAs and GaP,” *Physical Review B*, vol. 15, pp. 989–1016, jan 1977.

[113] D. V. Lang, “Deep-level transient spectroscopy: A new method to characterize traps in semiconductors,” *Journal of Applied Physics*, vol. 45, pp. 3023–3032, jul 1974.

[114] P. Mooney, “Chapter 2 Defect Identification Using Capacitance Spectroscopy,” *Semiconductors and Semimetals*, vol. 51, pp. 93–152, 1999.

[115] G. Goto, S. Yanagisawa, O. Wada, and H. Takanashi, “An improved method of determining deep impurity levels and profiles in semiconductors,” *Japanese Journal of Applied Physics*, vol. 13, pp. 1127–1133, jul 1974.

[116] J. Frenkel, “On pre-breakdown phenomena in insulators and electronic semiconductors [3],” *Physical Review*, vol. 54, pp. 647–648, oct 1938.

[117] P. Omling, E. R. Weber, L. Montelius, H. Alexander, and J. Michel, “Electrical properties of dislocations and point defects in plastically deformed silicon,” *Physical Review B*, vol. 32, pp. 6571–6581, nov 1985.

[118] T. Wosiński, “Evidence for the electron traps at dislocations in GaAs crystals,” *Journal of Applied Physics*, vol. 65, pp. 1566–1570, feb 1989.

[119] A. Hierro, A. R. Arehart, B. Heying, M. Hansen, J. S. Speck, U. K. Mishra, S. P. DenBaars, and S. A. Ringel, “Capture kinetics of electron traps in MBE-grown n-GaN,” *Physica Status Solidi (B) Basic Research*, vol. 228, pp. 309–313, nov 2001.

[120] W. Schröter, J. Kronewitz, U. Gnauert, F. Riedel, and M. Seibt, "Bandlike and localized states at extended defects in silicon," *Physical Review B*, vol. 52, pp. 13726–13729, nov 1995.

[121] J. K. Doylend and A. P. Knights, "The evolution of silicon photonics as an enabling technology for optical interconnection," jul 2012.

[122] D. Liang, G. Roelkens, R. Baets, and J. E. Bowers, "Hybrid Integrated Platforms for Silicon Photonics," *Materials*, vol. 3, pp. 1782–1802, mar 2010.

[123] M. L. Davenport, S. Skendzic, N. Volet, J. C. Hulme, M. J. Heck, and J. E. Bowers, "Heterogeneous silicon/III-V semiconductor optical amplifiers," *IEEE Journal on Selected Topics in Quantum Electronics*, vol. 22, pp. 78–88, nov 2016.

[124] A. W. Fang, B. R. Koch, R. Jones, E. Lively, D. Liang, Y. H. Kuo, and J. E. Bowers, "A distributed Bragg reflector silicon evanescent laser," in *2008 5th International Conference on Group IV Photonics, GFP*, pp. 58–60, IEEE, 2008.

[125] J. Thompson, R. M. Ash, N. Maung, A. J. Moseley, and D. J. Robbins, "Long wavelength GRIN-SCH MQW lasers incorporating graded GaAlInAs confinement layers," *Journal of Electronic Materials*, vol. 19, pp. 349–355, apr 1990.

[126] C. Zhang, S. Srinivasan, Y. Tang, M. J. R. Heck, M. L. Davenport, and J. E. Bowers, "Low threshold and high speed short cavity distributed feedback hybrid silicon lasers," *Optics Express*, vol. 22, p. 10202, may 2014.

[127] M. Fukuda and G. Iwane, "Degradation of active region in InGaAsP/InP buried heterostructure lasers," *Journal of Applied Physics*, vol. 58, pp. 2932–2936, oct 1985.

[128] M. Auf der Maur, B. Galler, I. Pietzonka, M. Strassburg, H. Lugauer, and A. Di Carlo, "Trap-assisted tunneling in InGaN/GaN single-quantum-well light-emitting diodes," *Applied Physics Letters*, vol. 105, p. 133504, sep 2014.

[129] M. Mandurrino, G. Verzellesi, M. Goano, M. Vallone, F. Bertazzi, G. Ghione, M. Meneghini, G. Meneghesso, and E. Zanoni, "Physics-based modeling and experimental implications of trap-assisted tunneling in InGaN/GaN light-emitting diodes," *Physica Status Solidi (A) Applications and Materials Science*, vol. 212, pp. 947–953, may 2015.

[130] N. Otsuka, M. Ishino, and Y. Matsui, "Stability of Zn doping profile in modulation-doped multiple quantum well structure," *Journal of Applied Physics*, vol. 80, p. 1405, 1996.

[131] M. Glade, J. Hergeth, D. Grützmacher, K. Masseli, and P. Balk, "Diffusion of Zn acceptors during MOVPE of InP," *Journal of Crystal Growth*, vol. 108, no. 3, pp. 449–454, 1991.

[132] T. Sasaki, H. Yamada, S. Takano, M. Kitamura, I. Mito, T. Suzuki, and H. Hoshino, "Doping optimization in InGaAsP DH lasers and improved characteristics in BH lasers grown by MOVPE," *Journal of Crystal Growth*, vol. 93, no. 1-4, pp. 838–842, 1988.

[133] Y. Huang, X.-B. Zhang, J.-H. Ryou, R. D. Dupuis, F. Dixon, N. Holonyak, and M. Feng, "InAlGaAs/InP light-emitting transistors operating near 1.55μm," *Journal of Applied Physics*, vol. 103, p. 114505, jun 2008.

[134] M. Fukuda, K. Wakita, and G. Iwane, "Dark defects in InGaAsP/InP double heterostructure lasers under accelerated aging," *Journal of Applied Physics*, vol. 54, pp. 1246–1250, mar 1983.

[135] C. Schramm, H. G. Bach, H. Künzel, and J. P. Praseuth, "Molecular Beam Epitaxy Grown Al(Ga)InAs: Schottky Contacts and Deep Levels," *Journal of The Electrochemical Society*, vol. 138, no. 9, p. 2808, 1991.

[136] K. Rezzoug, F. Ducroquet, G. Guillot, L. Giraudet, and J. Praseuth, "Deep trap characterization of $Al_{0.48}In_{0.52}As/In_{0.52}(Ga_{0.7}Al_{0.3})_{0.48}As$ heterostructures," in *Proceedings of Semiconducting and Semi-Insulating Materials Conference*, pp. 291–294, IEEE, 1996.

[137] D. Biswas, A. Chin, J. Pamulapati, and P. Bhattacharya, "Traps in molecular-beam epitaxial $In_{0.53}(Ga_xAl_{1-x})_{0.47}As/InP$," *Journal of Applied Physics*, vol. 67, pp. 2450–2453, mar 1990.

[138] Z. C. Huang, C. R. Wie, J. C. Chen, and G. Davis, "Interface traps in InP/InAlGaAs p-n junctions by metal organic chemical vapor deposition," *Journal of Applied Physics*, vol. 77, pp. 5736–5738, jun 1995.